# Microstructure-informed modeling of hydrogen diffusion in zirconium polycrystals

Alireza Tondro, *The University of Western Ontario*

Supervisor: Abdolvand, Hamidreza, *The University of Western Ontario*
A thesis submitted in partial fulfillment of the requirements for the Doctor of Philosophy degree in Mechanical and Materials Engineering
© Alireza Tondro 2023

# Abstract

Zirconium alloys are widely used in the core of various types of nuclear reactors. During service, the hot water coolant reacts with zirconium and releases hydrogen atoms that ingress into the lattice of the metal alloy. With time, hydrogen concentration exceeds its terminal solid solubility limit in zirconium, and a brittle phase known as zirconium hydride forms. This phase severely deteriorates the mechanical properties of zirconium alloys, leading to safety concerns regarding the integrity of nuclear pressure tubes. This thesis uses a crystal plasticity finite element model coupled with diffusion equations to study the effects of localized deformation at the grain scale on the hydrogen diffusion and hydride precipitation in zirconium. Attention is given to the effects of crystals elastic and plastic anisotropy, texture, microstructure, and plastic deformation by slip as well as twinning.

By considering the effects of the transformation strain associated with the formation of hydrides, it is shown that, hydrides tend to grow from their tips and are more probable to grow within mechanically "harder" grains. It is further shown that parallel hydrides are more probable to interlink than perpendicular ones. The effects of hydride shapes are also investigated where the results indicate that hydrides have an optimum width of 1 µm.

A three-point bending set-up is used to deconvolute the contributions of texture, microstructure, and external strains to the diffusion of hydrogen atoms towards micro-scale notches. While it is shown that grain-grain interactions significantly affect the distribution of hydrogen atoms, it is revealed that as the acuity of the notch increases, the effect of texture on hydrogen transport towards the notch root becomes less significant.

Lastly, the contribution of dislocations to hydrogen diffusion is studied using a novel non-local crystal plasticity finite element model coupled with diffusion equations. It is shown that slip bands and heavily deformed regions could greatly contribute to the hydrogen embrittlement of metals.

# Keywords

Hydrogen embrittlement, coupled diffusion and crystal plasticity, hydrogen diffusion, hydride precipitation, CANDU pressure tube, texture, grain morphology, hydride interactions, localized deformation zones, trapped hydrogen concentration

# Summary for Lay Audience

Nuclear industry is one of the biggest contributors to low-emission energy supply to reach net zero carbon emission. In Canada, as a tier one nuclear nation, over 60% of Ontario's electricity is generated through nuclear power plants across the province. One of the major problems that the nuclear community is facing in Canada, and all over the world, is called "hydrogen embrittlement". This phenomenon occurs when a metal is exposed to hydrogen-rich environments, which happens to nuclear pressure tubes. During service, the hot water coolant reacts with zirconium-alloy pressure tube and releases hydrogen into zirconium. Hydrogen atoms are highly mobile at the operating temperature of nuclear reactors (~330 °C). Following the diffusion and redistribution of hydrogen atoms within the metal lattice, and in case of reactor shutdown, a new phase called zirconium hydride might form within the metal. Hydrides, due to their brittleness, significantly deteriorate the mechanical behavior and the integrity of zirconium alloys. In this research, different factors which contribute to the probability of hydride formation and its consequences on propagation of hydrides are studied in detail.

# Co-Authorship Statement

This thesis is presented in an integrated article format with four manuscripts, which are published in the journals listed below.

**Chapter 3**: A. Tondro, H. Abdolvand, Quantifying hydrogen concentration in the vicinity of zirconium hydrides and deformation twins, Journal of the Mechanics and Physics of Solids, 148 (2021), 104287. https://doi.org/10.1016/j.jmps.2020.104287

Author Contribution: AT conducted all simulations and prepared the first draft of the manuscript and all figures presented. HA designed and planned the research, supervised, and contributed to writing the manuscript as well as the interpretation of the results.

**Chapter 4**: A. Tondro, H. Abdolvand, On the effects of texture and microstructure on hydrogen transport towards notch tips: A CPFE study, International Journal of Plasticity, 152 (2022), 103234, https://doi.org/10.1016/j.ijplas.2022.103234

Author Contribution: Alireza Tondro: Conceptualization, Formal analysis, Investigation, Methodology, Visualization, Writing - original draft. Hamidreza Abdolvand: Conceptualization, Methodology, Investigation, Writing - review & editing, Resources, Funding acquisition, Supervision.

**Chapter 5**: A. Tondro, B. Bidyk, I. Ho, H. Abdolvand, Modelling the interaction of zirconium hydrides, Materials Today Communication, 32 (2022), 103933, https://doi.org/10.1016/j.mtcomm.2022.103933

Author Contribution: AT, BB, and IH conducted all simulations, prepared all figures, and the first draft of the manuscript. HA designed, planned, and supervised the research, and contributed to writing the manuscript as well as the interpretation of the results.

**Chapter 6**: A. Tondro, M. Taherijam, H. Abdolvand, Diffusion and redistribution of hydrogen atoms in the vicinity of localized deformation zones, Mechanics of Materials 177 (2023), 104544, https://doi.org/10.1016/j.mechmat.2022.104544

# Acknowledgment

First and foremost, I would like to sincerely thank my supervisor Professor Hamid Abdolvand for giving me the opportunity to work on this project. His hardworking attitude, conscientious, friendship, and expertise in this field of study will always remain exemplary in my life. Working in his group has helped me shape the future path of my professional and personal life. I will be always indebted to him for this amazing experience.

I would like to acknowledge Drs. Sterling St Lawrence and Michael Bach at Canadian Nuclear Laboratories for supporting this research.

This thesis wouldn't have been possible without the help from many people; to all my fellow lab mates. Thank you everyone for your teamwork and all the memorable time we have had together over the last few years in London. A big thanks to my former colleagues Ivan and Brooke for their dedication and hard work during their research assistantship in our group which ended up being a part of my thesis. To my sincere friends in Canada; Karim, Bolin, Ivan, Ahmed, AmirReza, Amir, Saiedeh, Masoud, Amirhosein, and especially Brooke. I have learned a lot from every single one of you and will miss your company so much (unless we hopefully reunite sometime soon…). To my cousin, Mohsen, who was of great support throughout my stay in London. And of course, to my best friends back home; Ali Mohammadi, Ali Farrokhi and Mohammad Mahzoon for their immense support, even from 10,000 km away.

Last but not least, I would like to thank my parents, Abdolreza and Maryam, back in my beautiful hometown, Shiraz (where I truly miss to live in again), and also my sister, Atena, without whose help I would have never been able to pursue my aspirations in life.

# Dedication

*To those whom I will eternally love...*

# Table of Contents

# List of Tables

# List of Figures

# List of Abbreviations

| | |
|---|---|
| BC | Bi-crystal / Boundary condition |
| BCC | Body-centered cubic |
| CANDU | Canada deuterium uranium |
| CD | Coupled temperature displacement |
| CF | Concentration factor |
| CPFE | Crystal plasticity finite element |
| CPFEM | Crystal plasticity finite element method |
| CRSS | Critical resolved shear stress |
| D-CPFE | Diffusion-crystal plasticity finite element |
| DD | Dislocation dynamics |
| DDD | Discrete dislocation dynamics |
| DDP | Discrete dislocation plasticity |
| DH | Dual hydride |
| DHC | Delayed hydride cracking |
| EBSD | Electron backscatter diffraction |
| FCC | Face-centered cubic |
| FE | Finite element |
| GB | Grain boundary |
| GND | Geometrically necessary dislocation |
| HCP | Hexagonal close-packed |
| HE | Hydrogen embrittlement |
| HEDE | Hydrogen-enhanced degradation |
| HELP | Hydrogen-enhanced localized plasticity |
| HITS | Hydride induced transformation strain |
| HR-EBSD | High angular resolution electron backscatter diffraction |
| HS | Hydrostatic stress |
| IP | Integration point |
| LD | Loading direction |
| MD | Molecular dynamics |
| NILS | Normal interstitial lattice sites |
| RD | Radial direction |
| ROI | Region of interest |
| RSS | Resolved shear stress |
| SAD | Stress-assisted diffusion |
| SC | Single crystal |
| SDV | Solution dependent state variables |
| SEM | Scanning electron microscopy |
| SH | Single hydride |
| SS | Steady state |
| SSD | Statistically stored dislocation |
| TC | Tri-crystal |

| | |
|---|---|
| TD | Transverse direction |
| TEM | Transmission electron microscopy |
| TSS | Terminal solid solubility |
| UMAT | User material subroutine |
| UMATHT | User material heat transfer subroutine |
| XRD | X-ray diffraction |

# Chapter 1

## 1 Introduction

## 1.1 Background

Nuclear energy contributes to about 60% of power generation in Ontario and to about 15% in Canada. Zirconium (Zr) and its alloys with a hexagonal close-packed (HCP) crystal structure have been widely used in the core of various types of nuclear reactors. Good mechanical properties, high corrosion resistance at elevated temperatures, and most importantly, low neutron absorption cross-section are among the good characteristics of zirconium alloys. Hydrogen embrittlement (HE) of zirconium alloys is one of the major concerns in nuclear industry, including in CANada Deuterium Uranium (CANDU) nuclear reactors. To develop accurate predictive models and enhance the in-service performances of core components, it is important to understand the underlying mechanisms that contribute to hydrogen embrittlement.

A section view of the fuel channel assembly of CANDU reactors is shown in Fig. 1-1. During the reactor operation, the hot water coolant reacts with zirconium, resulting in the formation of zirconium oxides and the release of hydrogen atoms which subsequently ingress into zirconium lattice. This reaction can be expressed as:

$$2\,D_2O + Zr \rightarrow ZrO_2 + 2\,D_2$$
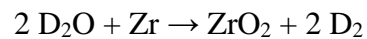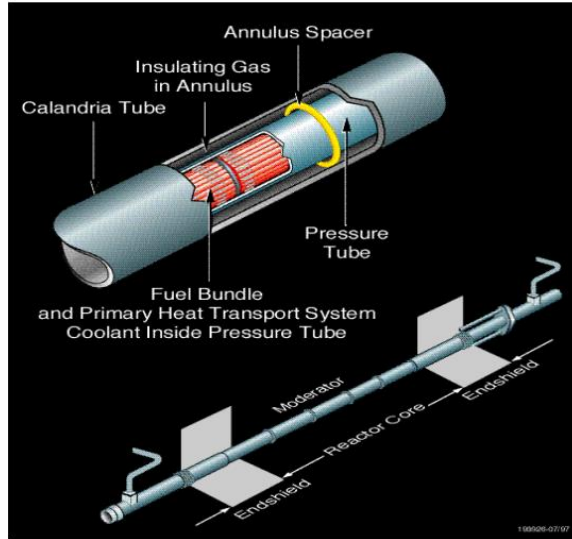
**Fig. 1-1 – Section View of Fuel Channel Assembly (Ontario Power Generation Darlington Fuel Channel Fitness for Service Report, 2015)**

The diffusion of hydrogen atoms into zirconium lattice is detrimental to the performance of reactor core components as at lower temperatures, when the hydrogen concentration in zirconium exceeds its solubility limit, a brittle phase called zirconium hydride forms. Such low temperatures happen during reactor shut down or during maintenance. Following the diffusion of hydrogen and surpassing the terminal solid solubility (TSS) of hydrogen in zirconium, different types of zirconium hydrides are likely to form. Fig.1-2a depicts an example of Zr-H phase diagram in which different phases of zirconium (α and β) as well as zirconium hydrides (δ, γ and ε) are shown with their associated temperature and hydrogen content. Fig.1-2b locates a few hydrides in the zirconium matrix. These hydrides reduce the fracture toughness of zirconium and under mechanical load, turn into microcracks that in long term lead to the failure of the nuclear pressure tubes. This process is known as hydrogen embrittlement and can lead to a failure process known as Delayed Hydride Cracking (DHC).

a.                                          b.
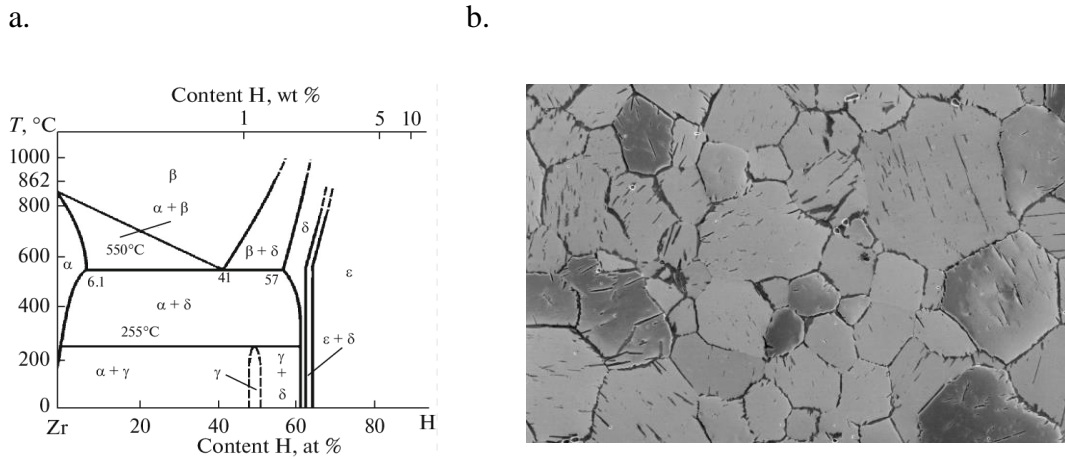


**Fig. 1-2 – (a) Phase diagram of the Zr-H system. (b) Precipitated hydride precipitates shown as dark phase in zirconium microstructure (Chernov et al., 2017).**

The zirconium alloys used in nuclear industry mainly consist of α-Zr phase with an HCP crystal structure. This crystal structure inherently possesses high elastic and plastic anisotropy. The elastic and plastic anisotropy of zirconium crystals considerably affect localized stresses, the patterning of which subsequently alters distribution of hydrogen atoms. A multi-scale representation of a zirconium specimen, cut from a portion of a pressure tube, modelled from macroscale down to grain-scale is shown in Fig. 1-3.
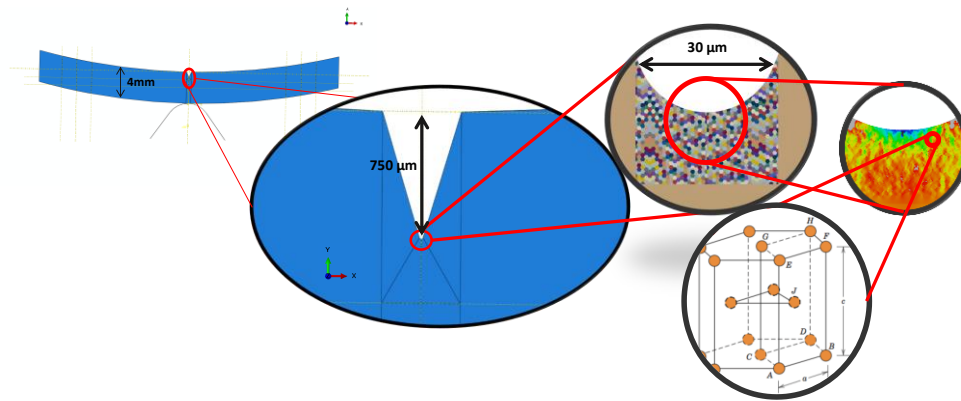


**Fig. 1-3 - Multi-scale analysis of hydrogen diffusion in zirconium alloys used in CANDU pressure tubes.**

Mechanistic understanding of hydrogen embrittlement is of great importance to the nuclear industry. Such insights help develop guidelines for the safe operation of reactors core components. Hence, this research focuses on understanding the micro-mechanism of hydrogen diffusion and hydrogen embrittlement in zirconium alloys.

## 1.2 Motivation

Ontario will be relying on the power generated by its CANDUs for decades to come. Refurbishment and maintenance of these reactors require detailed investigation of failure micro-mechanisms and understanding the state of material deformation at microscopic scale. For instance, the excessive sag of pressure tubes can lead to contact between the calandria tube and the pressure tube. This contact leads to excessive diffusion of H atoms within the pressure tube and acceleration of DHC and premature failures.

This research uses an in-house crystal plasticity finite element (D-CPFE) model coupled with mass diffusion modules to study the effects of deformation and phase transformation on the distribution of hydrogen atoms at microscopic scales. As such, a User MATerial (UMAT) subroutine is coupled with a UMAT Heat Transfer (UMATHT) subroutine, both of which are written in Fortran and run through SIMULIA Abaqus to study stress-assisted diffusion (SAD) of hydrogen atoms.

## 1.3 Objectives

This research aims to investigate various case studies related to hydrogen diffusion and hydride precipitation in zirconium. Attention is given to understanding the fundamentals of load sharing at the grain scales, and their effects on hydrogen redistribution in the lattice and dislocations, hydride precipitation and propagation, as well as the interactions of hydrides. Therefore, the following research objectives are defined for this thesis:

1) Understanding the effects of crystal misorientations and their effects on the diffusion of hydrogen atoms in the presence of zirconium hydrides and deformation twins.

2) Studying the effects of stress concentration on accelerated transport of hydrogen atoms towards micro-scale notches and the effects of texture and grain morphology on peaks of hydrogen concentration.

3) Studying the interactions of zirconium hydrides in different configurations on the formation of "macro-hydride".

4) Studying the effects of hydride geometry on their propagation.

5) Investigating the contribution of dislocations to hydrogen concentration using an in-house non-local D-CPFE model.

## 1.4 Structure of the thesis

A brief introduction on the importance and application of this research is presented in Chapter 1. In Chapter 2, a brief literature review is provided while the current knowledge gaps are stated. A comprehensive literature review is presented in each of the following chapters. Chapter 3 focuses on the effects of crystal orientation on the SAD of hydrogen atoms towards zirconium hydrides (Tondro and Abdolvand, 2021). A progressive modeling approach to address hydrogen distribution in the vicinity of hydrides and grains with different crystallographic orientations is presented in this paper. Chapter 4 focuses on the effects of grain morphology and texture on the transport of hydrogen towards micro-scale notches (Tondro and Abdolvand, 2022). Simulations are conducted to deconvolute the effects of notch geometry, grain morphologies, grain size, texture and external loading condition on distribution of hydrogen within the region of interest (ROI) near the notch tip. Chapter 5 discusses the interactive effects of neighboring hydrides formed in different directions of the pressure tube (Tondro et al., 2022). This paper also discusses the effects of hydride geometry on further propagation of hydrides. Chapter 6 studies trapping of hydrogen atoms within dislocation trap sites and presents a statistical analysis of hydrogen distribution at different microstructure sites, including triple points and grain boundaries (Tondro et al., 2023).

# Chapter 2

## 2 Literature review

This chapter focuses on providing an overview of the works previously conducted to understand different aspects of hydrogen embrittlement, both experimentally and numerically. More detailed and comprehensive literature review is presented in the beginning of chapters 3 to 6. Here, after investigating the tool used in this thesis, focus is given to recent studies in this field and identification of knowledge gaps, on which different chapters of this thesis are built upon.

## 2.1 Advantages of crystal plasticity finite element modelling approach

CPFE is a robust tool to study various aspects of microstructural behavior of the materials. One of the biggest advantages of CPFE over other macroscopic techniques, such as conventional FE, is its capability to capture crystallographic slip as well as twinning and incorporate such effects into calculation of plastic strain. Further, CPFE models the material as a collection of grains and is able to understand the interaction between individual crystals, each with a distinct orientation and anisotropic mechanical behavior. Therefore, it is necessary to use CPFE compared to FE in order to study hydrogen embrittlement at grain scale.

## 2.2 Hydrogen diffusion and hydride precipitation - experiments

There have been extensive experimental and numerical studies over the past decades on the processes of hydrogen diffusion and hydride precipitation. Studies on different alloys, including zirconium alloys, have shown that the presence of tensile stresses, e.g., at the crack tips, enhances the diffusion of hydrogen atoms through a process known as stress-assisted diffusion (SAD) (Eadie et al., 1991). It is also known that phase transformation from zirconium to hydrides is dependent on the microstructure of zirconium (Motta et al., 2019; Wang et al., 2019). Vizcaíno et al. (2014), for example, investigated the effects of parent grain orientation on the hydride precipitation. They highlighted the dependency of

hydride formation on the parent grain orientation where they reported that the precipitation of hydrides commonly occurs in HCP grains with their c-axis oriented towards the hoop direction of the tube or an intermediate direction in hoop-radial plane of the pressure tube.

Studies in the literature have also reported different types of hydrides with different crystal structures. For instance, Daum et al. (2009) used X-ray diffraction to identify different types of hydrides in zirconium alloys, among which γ-hydrides and more dominantly, δ-hydrides are the most frequent types of hydrides. γ- and δ-hydrides are shown to have face-centered tetragonal (FCT) and face-centered cubic (FCC) crystals, respectively (Mani Krishna et al., 2006). However, δ-hydrides precipitate when a higher concentration of hydrogen atoms exists, and when slow cooling rates are used ($< 2$ °C/min). These hydrides are shown to precipitate at three different sites: (i) along the grain boundaries, known as intergranular hydrides, (ii) within the grains, known as intragranular hydrides, and (iii) twin boundary hydrides. The transformation of HCP α-zirconium to FCC δ-hydride at any of these sites is accompanied by 17.2% volumetric strain reported in Carpenter (1973), which is known as hydride-induced transformation strain (HITS). Therefore, formation of hydrides could significantly influence the state of deformation in the vicinity of the hydride.

In terms of crystallographic terminologies, the shared plane between α-zirconium and hydride phase is called the habit plane. The habit plane of δ-hydride in pure zirconium and zirconium alloys, including Zircaloy-2 and -4, are respectively shown to be $\{1\,0\,\bar{1}\,0\}$ and $\{1\,0\,\bar{1}\,7\}$ (Perovic et al., 1983). Hydride platelets are also known to precipitate close to the basal plane of zirconium lattice (Puls, 1988), such that the orientation relationship of α (0 0 0 1)// δ (1 1 1) and α [1 1 -2 0]// δ [1 -1 0] is satisfied. Formation of hydrides along different directions has been shown to directly affect the toughness and the lifetime of zirconium where more radially oriented hydrides are more critical than circumferential hydrides within the pressure tubes (Kiran Kumar and Szpunar, 2011). More relevant studies about different aspects of hydride formation are discussed later in sections 3.1 and 5.1.

## 2.3 Hydrogen diffusion and hydride precipitation - modeling

The strong dependency of hydride formation on parent zirconium crystal has also been studied using numerical techniques. For example, Qin et al. (2014) showed that hydrides tend to connect and form an interlinked structure. Han et al. (2019), using a phase-field model, showed that hydrides grow from their tips. Phase-field modeling was also used to study the nucleation of hydrides (Welland and Hanlon, 2020). Discrete dislocation dynamics (DDD) can also be used to study the precipitation of hydrides. For instance, Gu and El-Awady (2018), using this method, studied the interaction of hydrogen atoms and dislocations. In another study using the same method, Tummula et al. (2018) quantified the state of stress in the surrounding regions of the hydride.

Crystal plasticity finite element (CPFE) is also another useful method to study material deformation at grain scale. This method was previously used and validated using the experimental observation for considerable number of grains (Abdolvand et al., 2018; Abdolvand et al., 2020). This is one of the advantages of CPFE over DDD which is computationally costly for large number of grains. Coupling CPFE with diffusion modules enables the calculation of hydrogen concentration fields as a result of stress acting as a driving force (Ilin, 2014). This technique uses the resemblance of diffusion and heat transfer equations to calculate hydrogen concentration which is held equivalent to temperature after the use of heat transfer subroutines.

Although recent studies have focused on the modeling and experimentation of hydrogen diffusion and hydride precipitation, less attention is given to modeling the effects of stress-assisted hydrogen diffusion. Moreover, few number of studies have modelled phase transformation from α-zirconium to zirconium hydride phases and its associated accompanied strains and stresses, as this would considerably affect the deformation fields in the vicinity of hydrides and further hydrogen diffusion and hydride propagation (Motta et al., 2019).

## 2.4 Hydrogen diffusion towards notch tips - experiments

The process of SAD could be intensified by the presence of micro-scale notches and flaws (Scarth et al., 2002) as a result of excessive deformation and stress concentration (Cui et al., 2009). The existence of such flaws helps the transport of highly mobile hydrogen atoms at the operating temperatures of the nuclear reactor and hence increases the likelihood of hydride formation and causes premature failures of the material. Through such repetitive process, commonly known as delayed hydride cracking (DHC), the pressure tube gradually loses its fitness for continued service. There are plenty of parameters that contribute to this process. For example, texture and grain morphology play an important role in determining the state of deformation near highly deformed regions because of the inherent anisotropy of zirconium alloys (Kim, 2006). Texture may also affect the susceptibility of zirconium to hydrogen embrittlement by accelerating hydrogen transport towards notches. Wang et al. (2007) showed that higher hydrogen concentrations lead to a lower fracture stress. Furthermore, geometry of the flaw, and specifically the acuity of the notch might contribute to hydrogen diffusion (Shek et al., 2005). More relevant studies on the effects of notches and stress risers on hydrogen embrittlement of materials are discussed in section 4.1.

## 2.5 Hydrogen diffusion towards notch tips – modeling

Numerical methods are used to investigate hydrogen transport towards notch tips. Studies on hydrogen diffusion are also performed on materials other than zirconium, as steels, e.g., 304, 316L, 310S and nickel-based alloys are also susceptible to hydrogen embrittlement (Martínez-Pañeda et al., 2016). Some numerical studies have investigated the effects of experimental parameters using multiple simulations. For instance, Krom et al. (1999) studied the effects of strain rate on SAD of hydrogen towards notches. They concluded that higher strain rates lead to a smaller number of hydrogen atoms residing at normal interstitial lattice sites (NILS). Numerical simulations have also shown that hydrostatic stress is directly correlated with lattice hydrogen concentration (Di Leo and Anand, 2013), such that regions with higher tensile hydrostatic stress have more lattice hydrogen concentration and vice versa. Some other studies developed brittle fracture models which correlates the mutual effects of hydrogen transport and hydrogen-assisted fracture (Duda et al., 2008). It should be noted that the models mentioned above are mostly conducted on

isotropic materials and are unable to take anisotropy of zirconium alloys into account. Therefore, the contribution of strong texture, elongated grains and the geometry of the notch to the hydrogen embrittlement of CANDU pressure tubes are barely addressed in the literature, especially using numerical methods.

## 2.6 Hydrogen in highly localized deformation zones

Dissolved hydrogen atoms could reside in NILS or inside crystal imperfections, such as vacancies, dislocations or grain boundaries, all of which are referred to as "trap sites". Oriani (1970) suggested that the concentration of hydrogen in trap sites and NILS are governed through equilibrium equations. Based on this theory, Sofronis and McMeeking (1989) developed a model which indicates that the trapped hydrogen concentration is directly proportional to plastic strain and dislocation density. Oriani's theory has been consistently used in various studies ever since (Dadfarnia et al., 2014). The works of Di Leo and Anand (2013) and Krom and Bakker (2000) showed that effects of traps on hydrogen content can be significant for FCC metals. However, these effects have not been thoroughly addressed for HCP materials.

## 2.7 Coupling diffusion and crystal plasticity finite element

Abdolvand (2019) has recently developed a series of diffusion subroutines that are coupled with CPFE. The mentioned work is used to simulate the effects of thermal residual stresses on governing diffusion equations. However, before presenting results and simulation input models, Abdolvand presents a fundamental case study – a single crystal simulation with a linearly increasing stress profile along the x-axis, shown in Fig. 2-1, which is used to validate the developed diffusion module against Abaqus mass transfer solver as well as a closed form solution presented in Puls (2012):

$$C = C_0 * \exp(\frac{\bar{V}_H * \sigma_H}{RT})$$

(2-1)

It is shown in Fig. 2-1 that a linear stress is imposed along the crystal x-axis and the resulting hydrogen concentration (shown in Fig. 2-1 c) follows the same profile as that of the hydrostatic stress. This case study shows that the model generates consistent results

with the ones from closed-form solution and Abaqus mass transfer solver and is validated for further and more complex simulations. This model is used later in this thesis to study different aspects of hydrogen diffusion.

a.
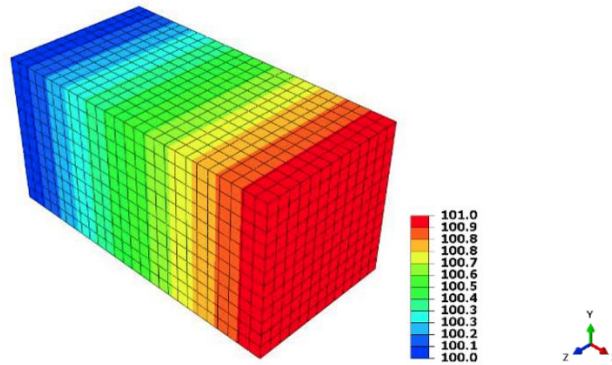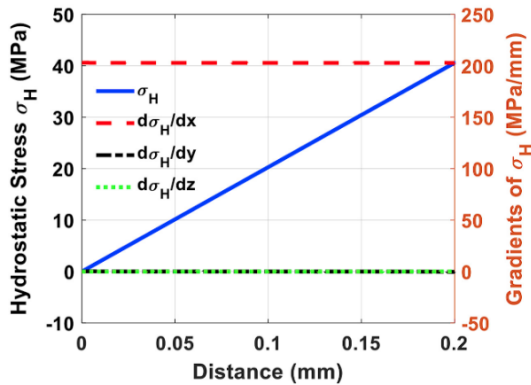


b.                                                    c.
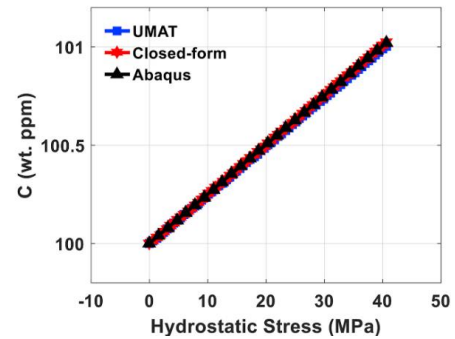


**Fig. 2-1- (a) The concentration distribution shown along the single crystal. (b) The distribution of hydrostatic stress along the crystal x-axis. (c) The comparison conducted between the predicted concentration profile using developed diffusion module, Abaqus mass transfer solver and closed-form solution. All figures are taken from Abdolvand (2019)**

## 2.8 Knowledge gaps

Hydrogen embrittlement is a long-standing issue in nuclear industry. Although numerous numerical and experimental studies have addressed hydrogen embrittlement of zirconium alloys, there still remain many unaddressed questions. In this section, based on the literature review provided earlier in this chapter, a list of knowledge gaps is described that

could be addressed using the modeling approach adopted in this thesis. Each of the following chapters presented in the rest of this thesis attempts to fill a specific knowledge gap.

I) Recent numerical studies for simulating stress-assisted hydrogen diffusion and the effects of material deformation to hydrogen embrittlement are mostly focused on macroscopic scales. Therefore, the significant contributions of crystals anisotropy, secondary phases (zirconium hydrides in this specific case), dislocation pile-ups and grain boundary are neglected. In this thesis, a crystal plasticity finite element model is used to understand grain-grain interaction at microscopic scale as well as the effects of crystal anisotropy.

II) In terms of solving diffusion equations, Abaqus mass transfer solver is incapable of considering the contribution of stresses and thermal gradients. This thesis, on the other hand, uses a diffusion module which is coupled with the CPFE. The diffusion-CPFE (D-CPFE) model is capable of solving for stress-assisted diffusion equations.

III) Hydride precipitation in zirconium alloys is accompanied with considerable volumetric strain and therefore imposes a significant deformation on the surrounding zirconium matrix. The effects of this volumetric strain and its correlation with crystal orientations which directly influences the propagation of hydride is barely discussed in the literature.

IV) Zirconium hydrides form in different directions of the pressure tube. Their interactive effects are not thoroughly discussed in previous works.

V) Highly localized deformation zones are accompanied by generation of dislocations. According to an equilibrium previously introduced in the literature, hydrogen atoms reside within lattice or trap sites. This condition, which could be quite important in solving diffusion equations, has not been addressed for zirconium alloys.

In summary, in this thesis, a coupled diffusion and crystal plasticity model is used to shed light on the knowledge gaps listed above. This tool is used to investigate various case studies, each of which is presented in the format of a journal paper in the following chapters.

# Chapter 3

# 3 Quantifying hydrogen concentration in the vicinity of zirconium hydrides and deformation twins

This study focuses on investigating the effects of the localized stresses that develop during formation of zirconium hydrides on the redistribution of hydrogen atoms in the zirconium matrix. A coupled mass diffusion and crystal plasticity finite element approach is used. The effects of the transformation strain associated with the formation of hydrides within various combinations of soft-hard grains and tri-crystals are studied. In addition, the interaction between intergranular and intragranular hydrides with grain boundaries is investigated. It is shown that hydrogen atoms tend to diffuse towards the tips of hydrides and away from their sides due to the tensile and compressive hydrostatic stresses that respectively develop at these two locations. This results in the propagation of a hydride along its axial direction. It is further shown that under a tensile applied stress, hydrides tend to form and propagate within hard grains, where stress hotspots with high tensile hydrostatic stresses develop. Lastly, it is shown that hydrogen atoms tend to diffuse towards twin tips, particularly when the twin tip is located near a harder grain.

## 3.1 Introduction

Zirconium (Zr) and its alloys have been widely used in the core of various types of nuclear reactors. Good mechanical properties, high corrosion resistance at elevated temperatures and most importantly, low neutron absorption cross-section are among the good characteristics of zirconium alloys. The diffusion of hydrogen atoms into zirconium lattice can be detrimental to the performance of reactor core components as at lower temperatures, when the hydrogen (H) concentration in zirconium exceeds its solubility limit, a brittle phase called zirconium hydride can form. Such low temperatures happen during reactor shut down or during maintenance. Following the diffusion of hydrogen and surpassing the terminal solid solubility (TSS) of hydrogen in zirconium, different types of hydrides are likely to precipitate. The zirconium alloys used in the core of reactors consist of mainly the α-Zr phase with hexagonal close packed (HCP) crystal structure and with high elastic and plastic anisotropy. In HCP crystals, c-axis is the one that is normal to the basal plane and

a-axis is the one that lies within the basal plane. Previous studies have shown that the presence of tensile stresses, e.g., at the crack tips, enhances the diffusion of hydrogen atoms through a process known as stress-assisted diffusion (SAD) (Eadie et al., 1991, Blackmur et al., 2016, Courty et al., 2014, Motta et al., 2019). It is also known that formation of hydrides depends on the microstructure of zirconium (Wang et al., 2019). This study focuses on formation of microscale hydrides and on the numerical simulation of SAD of hydrogen atoms and its correlation with the microstructure of zirconium as well as with the macroscopic loads.

Many studies have focused on using experimental methods to understand different aspects of hydrogen diffusion in zirconium alloys. Motta et al. (2019) have recently outlined that the distribution of hydrogen atoms in zirconium is mainly affected by the total concentration of hydrogen atoms, temperature, and the state of the stress, as well as their gradients within the material. According to a study conducted by Simpson and Ells (1974), tensile residual stresses are suggested to be one of the main parameters affecting hydrogen diffusion and hydride redistribution. Using X-ray diffraction, Vizcaíno et al. (2014) studied the effects of the parent grain orientations on the precipitation of $\delta$-hydrides ($ZrH_{1.66}$). It was reported that the precipitation of $\delta$-hydrides occurs mostly in two groups of HCP grains: (i) those having their c-axis oriented towards the hoop direction of the pressure tube, and (ii) those having their c-axis pointed towards an intermediate direction in hoop-radial plane of the tube. In nuclear pressure tubes, the c-axis of most of the HCP crystals are oriented towards the hoop direction. Further, zirconium hydrides are perceived to have four different crystal structures. The stability of the hydride phases has been extensively studied in the literature (McRae and Coleman, 2018; Breen et al., 2018; Lumley et al., 2014). It is generally accepted that $\delta$-hydrides with face-centered cubic (FCC) crystals and $\gamma$-hydrides with face-centered tetragonal (FCT) crystals are frequently formed (Suman et al. 2017), but $\delta$-hydrides are probably not in equilibrium with $\alpha$-zirconium matrix. Daum et al. (2009) used X-ray diffraction to identify different types of hydrides in zirconium alloys. $\gamma$-hydrides, and more dominantly, $\delta$-hydrides are reported to be the most frequent types in their study. It is reported in the same study that new types of hydrides are observed when the initial H concentration is increased. Root et al. (2003) showed that the

transformation from δ- to γ- phase happens slowly at lower temperatures. The type of hydride studied in the current work, δ-hydrides, precipitates when a higher concentration of hydrogen atoms exists, and when slow cooling rates are used (< 2 °C/min). The transformation of HCP α-zirconium to FCC δ-hydride is accompanied by 17.2% volumetric strain reported in Carpenter (1973), which is known as hydride-induced transformation strain (HITS). This phenomenon imposes a stress field on the surrounding regions within the matrix, which can subsequently alter the distribution of hydrogen atoms. Han et al. (2019) showed that δ-hydrides form in stacks that are nearly parallel to the basal plane of the zirconium matrix. They also developed a model that predicts that pre-existing hydrides tend to grow from their tips where the driving force for nucleation of hydrides is the highest.

The growth of zirconium hydrides has been the focus of many studies. For example, even though δ- and γ-hydrides have different crystal structures, they grow in the same direction that has been determined to be [1 1 $\bar{2}$ 0] in different studies (Weatherly, 1980; Westlake, 1968; Ells, 1968). The crystallographic plane shared between the parent α-zirconium crystal and the hydride phase is called the habit plane. It is suggested that {1 0 $\bar{1}$ 0} are the δ-hydride habit planes in pure zirconium, and {1 0 $\bar{1}$ 7} are the habit planes in zirconium alloys, e.g. Zircaloy-2 and 4 (Weatherly, 1980; Wang et al., 2019; Bailey, 1963; Ells, 1968). In addition, some studies have reported {1 0 $\bar{1}$ 2}, {1 1 $\bar{2}$ 2} and {1 0 $\bar{1}$ 1} as other possible habit planes (Shinohara et al., 2009; Westlake, 1968; Barrow et al., 2013). Both experimental and numerical studies have reported that hydrides generally tend to nucleate at the grain boundaries (Ma et al. 2002; Wang et al., 2019). For instance, Bradbrook et al. (1972) used electron microscopy and observed that grain boundaries are the main sites for the precipitation of δ-hydrides. It was also mentioned that the presence of an externally applied stress or the internal stresses induced during manufacturing could affect the process of hydride precipitation. δ-hydrides can be categorized into three main groups, reported in Wang et al. (2019): (1) intergranular hydrides which are seen at grain boundaries, (2) twin boundary hydrides and (3) intragranular hydrides which are observed within the grains. Wang et al. (2019) reported that the last group of hydrides possesses a higher proportion within larger grains as a result of higher area to grain boundary ratio. Similarly, El Chamaa

et al. (2018) used EBSD to study effects of grain sizes and grain boundaries on the nucleation of intergranular and intragranular δ-hydrides. They reported that intergranular δ-hydrides form in specimens with smaller grain sizes. However, more intragranular hydrides were observed in bigger grains. Furthermore, it is reported by Cox (1990) that intergranular hydrides could cause rapid intergranular fracture under tensile stresses. The work by Lee and Hong (2002) suggests that the size and distribution of hydrides are greatly affected by the cooling rate where homogeneously distributed γ-hydrides were formed in air-cooled tubes. Conversely, furnace-cooled tubes led to the formation of long bands of γ-hydrides within the tube. In another study by Qin et al. (2014), it was shown that δ-hydrides tend to connect to each other and form an interlinked structure. They also reported the presence of tensile stresses at the tips of the pre-existing δ-hydrides and their contribution to the growth of the δ-hydride into other grains or grain boundaries. Additionally, Kearns and Woods (1966) studied the effect of texture and grain size on the orientation of hydrides. They reported that hydrides are favorably oriented such that hydride habit plane is perpendicular to the tensile stress axis. Nath et al. (1975) studied the effects of cooling rate on the nucleation of both δ- and γ-hydrides and observed that increasing the H concentration and decreasing the cooling rate increases the probability of formation of δ-hydrides in comparison to γ-hydrides.

Understanding the mechanism of hydrogen diffusion and hydride precipitation have been the focus of many numerical studies as well. Some of the models are concerned with the effects of temperature on the precipitation of hydrides. For instance, Xiao et al. (2015) developed a model to predict the probability of δ-hydride precipitation as a function of temperature. The local stresses resulting from HITS contribute to redistribution of hydrogen atoms which may lead to propagation of existing hydrides. For instance, Ma et al. (2006) studied the interaction between hydrostatic stress (HS) and H concentration assuming a constant initial H concentration field. They used an FEM-based model to show that the tensile stresses that develop at the notch tips enhance the diffusion of hydrogen atoms. Strain rate is another parameter affecting the process of hydrogen diffusion. For example, Krom et al. (1999) showed that higher strain rates result in lower levels of H concentration within the lattice. A coupled diffusion and elastic-plastic finite element

approach was employed in their work, where it was found that the lattice is filled with hydrogen if there is enough time for hydrogen transport. Similarly, using a model called DFM, McRae et al. (2010) predicted that due to the gradient of chemical potential imposed by the tensile stresses that develop around a crack, hydrogen atoms diffuse toward the crack tip. Using an atomistic model for H-H interaction, Von Pezold et al. (2011) showed that micro-cracks are likely to form at dislocation pile-ups. Phase-field modeling has also been used to study different aspects of hydrides precipitation (Welland and Hanlon, 2020); Wook et al., 2019; Martínez-Pañeda et al., 2018). For example, Lin and Heuser (2019) developed a phase-field model to simulate hydrogen solvus in Zr solution where it was shown that δ-hydrides tend to precipitate within the grains having lower strain energy. Recently, Kristensen et al. (2020) developed a phase-field model to study hydrogen embrittlement in elastic-plastic solids. They showed that the gradients of plastic strain elevate the stress and H concentration at the crack tips and reduces the fracture energy. Discrete dislocation dynamics (DDD) simulation is also used to study the effects of hydrogen and hydrides. For instance, Gu and El-Awady (2018) developed a DDD framework to study the interaction between hydrogen atoms and dislocations. The distribution of hydrogens as a function of the stress fields associated with dislocations as well as the stress induced by hydrogen inclusion were studied. Tummala et al. (2018) proposed a DDD model to quantify the stresses in the vicinity of δ-hydrides and showed that the dislocations nucleated at the hydride-matrix interface may act as nucleation sites for new hydrides. Yu et al. (2019) used a DDD and discrete dislocation plasticity (DDP) approach to study hydrogen effects in BCC materials. It was shown that in the presence of hydrogen more slip steps form on the surface of studied microcantilevers indicating enhanced dislocation activity.

Crystal Plasticity Finite Element Modeling (CPFEM) is another method used to study the state of deformation and local stresses at the grain scale (Abdolvand et al., 2015a; Abdolvand et al., 2015b; Alawadi and Abdolvand, 2020; Bronkhorst et al., 2007; Cheong and Busso, 2006). For example, Cheng and Ghosh (2017) used CPFEM to study formation of discrete twins in polycrystalline magnesium. Busso et al. (2000) implemented crystallographic formulations into CPFE to study the behavior of crystals of nickel-based superalloys. Wu and Zikry (2015) used CPFE, coupled with a fracture formulation, to study

hydrogen-assisted cracking. They reported that hydrogen accumulation can accelerate crack growth and embrittlement and induce significant reduction of critical fracture stress. CPFEM has also been used to study the effects of stress fields on the diffusion of hydrogen atoms. For example, Ilin et al. (2014) studied stress-assisted hydrogen diffusion in steel and showed that hydrogen segregation occurs within the grains with higher HS. Abdolvand (2019) used a coupled diffusion-CPFE model to study the effects of thermal residual stresses on the nucleation of δ-hydrides. It was shown that grain-scale stresses result in nonuniform distribution of hydrogen atoms which affects the sequence of hydride nucleation.

This study focuses on the stress-assisted redistribution of hydrogen atoms during formation of microscale δ-hydrides. Formation of intragranular and intergranular δ-hydrides as well as precipitation in the vicinity of twin boundaries is investigated using a coupled diffusion and CPFE model. After describing the implemented materials constitutive equations and FE input models, the results of the model for H concentration in bi- and tri-crystals as well as in the vicinity of twin boundaries are discussed.

## 3.2 Modeling

### 3.2.1 Crystal plasticity formulation

In the following mathematical formulation, tensors are presented with bold fonts and vectors with an arrow on the top. The coupled Diffusion-CPFE model (D-CPFE) developed by Abdolvand (2019) is used for numerical simulations. The key equations used in the model are presented in this section. A detailed discussion of the formulations can be found in Abdolvand (2019). A User MATerial (UMAT) subroutine is coupled with UMATHT for simulating diffusion of atoms in an anisotropic polycrystal. The UMAT subroutine calculates stress increments and updates the solution dependent state variables based on the inputs provided by the FE solver, i.e., strain, rotation, time, and temperature increments. The total strain increment ($\Delta \boldsymbol{\varepsilon}$) can be written as:

$$\Delta \boldsymbol{\varepsilon} = \Delta \boldsymbol{\varepsilon}^{el} + \Delta \boldsymbol{\varepsilon}^{pl} + \Delta \boldsymbol{\varepsilon}^{trH} \tag{3-1}$$

where $\Delta\boldsymbol{\varepsilon}^{el}$ and $\Delta\boldsymbol{\varepsilon}^{pl}$ respectively represent the increments of elastic strain and the plastic strain resulting from crystallographic slip. $\boldsymbol{\varepsilon}^{trH}$ is the HITS which is incrementally applied to the domain that undergoes phase transformation during precipitation of hydrides. For calculating the plastic strain increment, the plastic part of deformation rate ($\boldsymbol{D}^{pl}$) is integrated over each time increment, i.e.:

$$\dot{\boldsymbol{\varepsilon}}^{pl} = \boldsymbol{D}^{pl} = \sum_{\alpha=1}^{N^{spl}} \boldsymbol{P}^{\alpha}\dot{\gamma}^{\alpha} \tag{3-2}$$

$$\boldsymbol{P}^{\alpha} = sym(\boldsymbol{S}^{\alpha}) \ where \ \boldsymbol{S}^{\alpha} = \vec{d}^{\alpha} \otimes \vec{n}^{\alpha}$$

where $\boldsymbol{P}^{\alpha}$ is the symmetric part of the Schmid tensor ($\boldsymbol{S}^{\alpha}$), $\dot{\gamma}^{\alpha}$ is the shear rate on the slip system $\alpha$, and $\vec{d}^{\alpha}$ and $\vec{n}^{\alpha}$ are respectively slip direction and normal to the slip plane for the same slip system. The following equation is used to calculate shear rates (Needleman et al., 1985):

$$\dot{\gamma}^{\alpha} = \dot{\gamma}_0 \left| \frac{\tau^{\alpha}}{g^{\alpha}} \right|^n sign\left( \frac{\tau^{\alpha}}{g^{\alpha}} \right) \tag{3-3}$$

where $\dot{\gamma}_0$ is a reference shear strain rate and $n$ controls the rate dependency. $\tau^{\alpha}$ and $g^{\alpha}$ are the resolved shear stress on the slip system $\alpha$ and the strength of this system, respectively. An extended Voce hardening law is used for $g^{\alpha}$:

$$g^{\alpha} = g_0^{\alpha} + (g_1^{\alpha} + \theta_1^{\alpha}\Gamma)\left( 1 - exp\left( -\frac{\theta_0^{\alpha}\Gamma}{g_1^{\alpha}} \right) \right) \tag{3-4}$$

where $g^{\alpha}$ is the current critical resolved shear stress (CRSS), $g_0^{\alpha}$ is the initial CRSS, $\Gamma$ is the shear accumulated on all slip systems, $\theta_0^{\alpha}$ is initial hardening rate, and $g_1^{\alpha}$ and $\theta_1^{\alpha}$ determine asymptotic characteristics of hardening.

The resolved shear stress used in Eq. 3-3 is proportional to the Kirchhoff stress ($\boldsymbol{\Psi}$) through (Peirce et al., 1983):

$$\tau^{\alpha} = \boldsymbol{P}^{\alpha} : \boldsymbol{\Psi} \tag{3-5}$$

The Jaumann rate of Kirchhoff stress ($\breve{\Psi}$) correlates with the elastic part of the deformation rate tensor ($\boldsymbol{D^{el}}$) and the elastic stiffness tensor ($\mathbb{C}$) through the following equation:

$$\breve{\Psi} = \mathbb{C}:\boldsymbol{D^{el}} \ where \ \breve{\Psi} = \dot{\Psi} - \boldsymbol{\Omega^{el}}\boldsymbol{\Psi} + \boldsymbol{\Psi}\boldsymbol{\Omega^{el}} \tag{3-6}$$

where $\boldsymbol{\Omega^{el}}$ is the elastic part of the spin tensor. The unconstrained misfit strain associated with the formation of δ-hydrides were calculated to be 4.58% and 7.2% along the HCP crystal a-axis and c-axis, respectively (Carpenter, 1973) :

$$\boldsymbol{\varepsilon^{trH}} = \begin{bmatrix} 0.0458 & 0 & 0 \\ 0 & 0.0458 & 0 \\ 0 & 0 & 0.072 \end{bmatrix} \tag{3-7}$$

This transformation strain was applied incrementally over the time period of 3600 seconds to the domain that undergoes phase transformation.

## 3.2.2 Stress-assisted hydrogen diffusion

The flux of hydrogen atoms ($\vec{J}$) within zirconium matrix depends on the concentration (C) and the velocity of hydrogen atoms ($\vec{v}$ ):

$$\vec{J} = \vec{v}C \tag{3-8}$$

The velocity of hydrogen is proportional to its mobility ($\boldsymbol{M}$) and the gradient of the chemical potential ($\mu$):

$$\vec{v} = -\boldsymbol{M}\vec{\nabla}\mu$$
$$\boldsymbol{M} = \frac{\boldsymbol{D}}{RT} \tag{3-9}$$

where R is the universal gas constant, $\mu$ is the chemical potential of hydrogen in zirconium, and T is the absolute temperature ($K$). The diffusivity of hydrogen atoms along the a-axis ($D_a$) and c-axis ($D_c$) of the HCP zirconium crystals for the temperature range of 300K-1100 K is (Zhang et al., 2017):

$$D_c = 1.08 \exp\left(-\frac{0.46}{8.6 \times 10^{-5}T}\right)$$

$$D_a = D_c(-3.3 \times 10^{-7}T^2 + 7 \times 10^{-4}T + 0.8298)^{-1}$$

(3-10)

in which diffusivities are in units of mm/s². The chemical potential of the diffusing hydrogen can be written as:

$$\mu = \mu_0 + RT\ln C - \frac{\sigma_{kk}}{3}\bar{V}_H$$

(3-11)

where $\mu_0$ is the reference chemical potential, $\frac{\sigma_{kk}}{3}$ represents the HS, and $\bar{V}_H$ is the partial molar volume of the hydrogen atoms in the Zr lattice and is 1670 mm³/mol. Combining Eqs. 3-8, 3-9 and 3-11, the equation for hydrogen flux can be rewritten as:

$$\vec{J} = -\boldsymbol{D}.\left[\vec{\nabla}C + C.\ln C \frac{\vec{\nabla}T}{T} - C\frac{\bar{V}_H}{3.RT}\vec{\nabla}\sigma_{kk}\right]$$

(3-12)

where $\frac{\vec{\nabla}\sigma_{kk}}{3}$ represents the gradient of HS. According to Eq. 3-12, the three parameters affecting mass flux are the gradient of mass concentration, the gradient of temperature (known as temperature-driven diffusion), and the gradient of HS (known as stress-assisted diffusion). When diffusion happens under constant temperature, the second term on the right-hand side of Eq. 3-12 will be zero. In this work we only focus on the effects of stress on mass diffusion, i.e., we solve for isothermal case where the gradient of temperature is zero. The general form of diffusion equation derived from a control volume can be written as:

$$\frac{\partial C}{\partial t} = -\nabla.\vec{J}$$

(3-13)

For the steady state condition, the derivative of concentration with respect to time will be zero.

The format of Eqs. 3-12 and 3-13 is very similar to the conductive heat transfer equations used for calculating temperature distribution in the presence of heat sinks and sources. In

Abaqus FE solver, UMATHT can be used for modeling coupled temperature-displacement problems, but with replacing temperature with concentration (C), this subroutine can be used for coupled diffusion-displacement problem. Following the method discussed in Abdolvand (2019), Eqs. 3- 9 to 3-13 are implemented in a UMATHT subroutine to solve for H concentration.

For calculating mass flux in Eq. 3-12, it is necessary to calculate the gradient of HS. This is done in the UMAT by using the element shape function through the following equations (Abdolvand, 2019):

$$3HS = \sigma_{kk} = \sum_{a=1}^{a=no.Nodes} N^a\, \sigma_{kk}^a$$

$$\vec{\nabla}\sigma_{kk} = \frac{\partial \sigma_{kk}}{\partial x_i} = \sum_{a=1}^{a=no.Nodes} \frac{\partial N^a}{\partial x_i} \sigma_{kk}^a$$

(3-14)

where $N^a$ is the shape function of an element with "$a$" nodes.

To summarize, the total strain and time increments provided at the beginning of each time increment are used to calculate stress increment using Eqs. 3-1 to 3-6 (Abaqus Documentation, 2020). If a domain undergoes hydride formation, the HITS provided in Eq. 3-7 is applied to the domain to replicate the strain fields around the δ-hydride. The updated stress matrix at each IP is then used to calculate HS, and with the use of current coordinates of the same IP, the gradients of HS are calculated (Eq. 3-14). The calculated $\vec{\nabla}\sigma_{kk}$ is subsequently sent to UMATHT to calculate H concentration using Eqs. 3-12 and 3-13. The use of UMATHT and the calculation of $\vec{\nabla}\sigma_{kk}$ within the UMAT enforce mass continuity across grain boundaries within single phase zirconium polycrystal as there is no need to calculate stress and mass independently. Mass discontinuity may happen in decoupled displacement-diffusion analysis causing numerical instability.

### 3.2.3 Input models

Since the diffusivity of hydrogen at the operating temperatures of nuclear reactors is quite high, and since the concentration of hydrogen at the (grain) micro-scale is the subject of this study, we focus on the distribution of hydrogen for the steady state case. A comparison between the steady state and transient responses is presented in section 3.4.3. The diffusion length of hydrogen atoms at 330 °C is about 100 µm over one minute which is much higher than the average grain size reported for typical zirconium pressure tubes used in nuclear reactors. Similarly, only the effects of stress gradients on the distribution of hydrogen atoms are studied, i.e., the effects of temperature gradients on the redistribution of hydrogen are simply ignored because the variation of temperature over a few grains is negligible. As such, in all simulations presented, it is assumed that the entire model stays at 330 °C, unless otherwise stated.

In all simulations presented, it is assumed that the initial concentration of hydrogen is 100 wt.ppm which is applied to the model boundaries. The effects of boundary conditions are discussed in section 3.4.2. The choice of 100 wt.ppm is because the solubility limit of hydrogen in the zirconium lattice at operative temperatures of nuclear reactors (~330 °C) is about 100 wt.ppm, although at the microscale, for $\delta$-hydride to form, 18,200 wt.ppm of hydrogen is required according to hydride stoichiometry (Courty et al., 2014). It is also shown that the driving force for hydride precipitation is low when hydrogen concentration is lower than 300 wt.ppm (Lumley et al., 2014) . For modeling the plastic behavior of zirconium crystals, the Voce hardening parameters reported in Abdolvand and Daymond (2013) are used. These parameters are listed in Table 3-1. It can be seen that the CRSS for prism and basal slip systems are lower than that of pyramidal <c+a> system. This means that grains with their c-axis parallel to the loading direction are "hard" grains while those having their c-axis perpendicular to the loading direction are "soft" grains. Also, the elastic moduli of the single crystal Zr used here are the ones determined by Fisher and Renken (1964): $C_{11}$=143.5 GPa, $C_{33}$=164.9 GPa, $C_{12}$=72.5 GPa, $C_{13}$=65.4 GPa, and $C_{44}$=32.1 GPa. In addition, the Euler angles presented in this work follow the Bunge convention for $\varphi_1, \varphi$, and $\varphi_2$ with crystals rotating about Z, X and Z axes, respectively.

Four input models are prepared to simulate the distribution of hydrogen atoms within zirconium single, bi- and tri-crystals. Steps used in each model are explained below.

**Table 3-1 – The single crystal parameters used for zirconium (Abdolvand and Daymond (2013))**

| Slip system | n | $\dot{\gamma}_0(s^{-1})$ | $g_0^{\alpha}$(Gpa) | $g_1^{\alpha}$(GPa) | $\theta_0^{\alpha}$(GPa) | $\theta_1^{\alpha}$(GPa) |
|---|---|---|---|---|---|---|
| Prism $< 11\bar{2}0 >$ | 20 | $3.5 \times 10^{-4}$ | 0.12 | 0.33 | 0.01 | 0 |
| Basal $< 11\bar{2}0 >$ | 20 | $3.5 \times 10^{-4}$ | 0.168 | 0.22 | 0.05 | 0 |
| Pyramidal <c+a> | 20 | $1.0 \times 10^{-4}$ | 0.331 | 0.27 | 0.62 | 0.28 |

## 3.2.3.1 Input model: Zirconium bi-crystals

The bi-crystal model is used to study the effects of crystal anisotropy on the distribution of hydrogen atoms. A schematic of the model is shown in Fig. 3-1. To study the effects of applied strain on the distribution of hydrogen, the bi-crystal model is strained uniaxially to 1%, 2% and 4% along the x-axis as shown in Fig. 3-1. These strains are applied using a constant strain rate of $5 \times 10^{-5} \, s^{-1}$ to replicate quasi-static loading. Also, there is no hydride in the model. The size of the model is 200 µm with each grain being 100 µm. Symmetric boundary conditions are applied to the three free surfaces presented by x=0, y=0, and z=0. The concentration of hydrogen on the Y-Z surface on left side of the model, at x=0, is assumed to be constant at 100 wt.ppm for all simulations conducted. As illustrated in Fig. 3-1, the orientation of the grain located in the left side of the figure is kept constant with the crystal c-axis parallel to the loading direction to simulate the behavior of a "hard" grain. However, the c-axis of the other grain is rotated from 0° to 90° around the Y-axis every 15°. The Euler angles assigned to each grain as well as the labels of the models tested are provided in Table 3-2. The variation of stresses and H concentration at the end of each simulation are studied.

**Table 3-2 - The set-up of the bi-crystal model**

| Case no. | Figure number | Grain#2<br><br>Euler Angles | Grain#1<br><br>Euler Angles | Misorientation angle θ (degrees) |
|---|---|---|---|---|
| BC-1 | Fig. 3-1 | (90 90 0) | (90 90 0) | 0 |
| BC-2 | Fig. 3-1 | (90 90 0) | (75 90 0) | 15 |
| BC-3 | Fig. 3-1 | (90 90 0) | (60 90 0) | 30 |
| BC-4 | Fig. 3-1 | (90 90 0) | (45 90 0) | 45 |
| BC-5 | Fig. 3-1 | (90 90 0) | (30 90 0) | 60 |
| BC-6 | Fig. 3-1 | (90 90 0) | (15 90 0) | 75 |
| BC-7 | Fig. 3-1 | (90 90 0) | (0 90 0) | 90 |
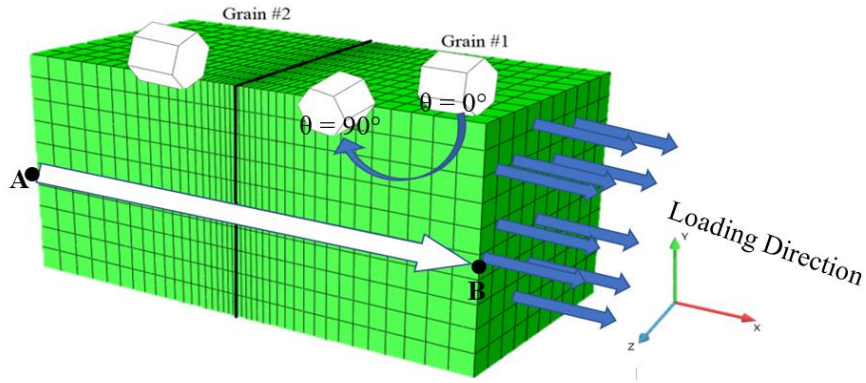


**Fig. 3-1 – The zirconium bi-crystal model. θ represents the misorientation angle between the two neighboring grains.**

## 3.2.3.2 Hydride precipitation within a single crystal

The second input model is to simulate the distribution of hydrogen atoms around a δ-hydride that is precipitated within a single crystal of α-Zr (Fig. 3-2). This model is designed to study the effects of local stresses around the hydride domain on the diffusion of hydrogen and how the hydride tends to grow. Electron microscopy studies conducted on hydrides have revealed that the habit plane of hydrides is nearly parallel to the basal plane of the parent zirconium crystals (Westlake, 1968; Motta et al., 2019; Wang et al., 2019). Hence,

a hydride is embedded within the single crystal such that the δ-hydride habit plane is perpendicular to the c-axis of the parent crystal (see Fig. 3-2). The length of hydride generally depends on the size of the parent grain. As the modelled single crystal is relatively big, considering the habit plane relationship, the hydride length is approximately 70 μm. The following approximate relationship between hydride length ($l$) and thickness ($t$), reported in Puls (2012), is used to determine the hydride thickness- which is set to be 0.5 μm:

$$l \approx 270 * t^{5/3} \qquad\qquad (3\text{-}15)$$

Two steps are used in the model:

Step-1: mechanical boundary conditions are applied to the model (see Table 3-3).

Step-2: applying the HITS onto the domain determined as δ-hydride. The concentration of hydrogen is shown at the end of this step.
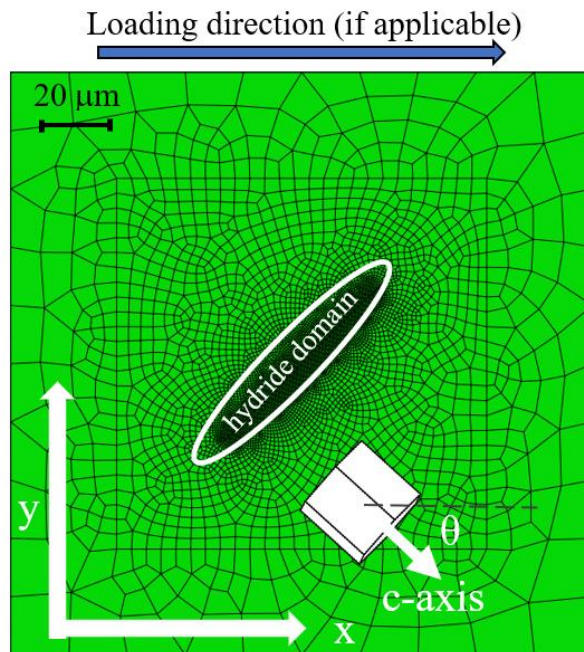


**Fig. 3-2 – The single crystal model and the embedded hydride domain under uniaxial loading. θ is the angle between the c-axis of the parent grain and the loading direction.**

To study the effects of crystal anisotropy on the localized stresses around the hydride, the c-axis of the parent crystal is rotated about the Z-axis as shown in Fig. 3-2. The details of all single crystal models with their labels are provided in Table 3-3. The model is extruded along the Z-axis for 1 μm which is 0.5% of the parent grain size. In the Step-1 of all simulations, both Y-Z surfaces were subjected to zero strain along x, except for the model SC-4 in which the single crystal is deformed to 0.3% of $\varepsilon_x$ at the strain rate of $5 \times 10^{-5} \ s^{-1}$. The boundary conditions on the left and bottom surfaces of the model are symmetry X and Y, respectively. Also, a Z symmetry boundary condition was applied to the top edge of the model. These boundary conditions remain active throughout all simulation steps. In Step-2 of the simulation, the δ-hydride misfit strain, i.e. HITS, is applied incrementally to the area that is densely meshed. This strain was applied over the period of 3600s to replicate the volumetric strain rate of $5 \times 10^{-5} \ s^{-1}$. In all of the models presented in this chapter, the HITS was applied under constant applied strain, i.e., in Step-2 the velocity applied to the right and left Y-Z surface was set to zero. This will result in zero applied displacement and strain during the phase transformation. All four external surfaces perpendicular to x and y axis are set to have constant hydrogen concentration of 100 wt.ppm throughout the simulation.

The determination of the mechanical properties of zirconium hydrides has been the focus of many studies (Puls et al., 2005; Yamanaka et al., 1999; Rico et al., 2014; Puls, 2012) . In this work, the material property of δ-hydride is considered to be linear elastic and isotropic with E = 100 GPa and ν = 0.33 as reported in Puls et al. (2005), Puls (2012) and Weck et al. (2015).

**Table 3-3 - The single crystal model undergoing hydride precipitation**

| Case no. | Figure number | Grain Euler Angle | θ (degrees) | Applied Strain |
|----------|---------------|-------------------|-------------|----------------|
| SC-1 | Fig. 3-2 | (90 90 0) | 0 | No load |
| SC-2 | Fig. 3-2 | (30 90 0) | 60 | $\varepsilon_x$=0.3% |
| SC-3 | Fig. 3-2 | (45 90 0) | 45 | No load |
| SC-4 | Fig. 3-2 | (45 90 0) | 45 | $\varepsilon_x$=0.3% |
| SC-5 | Fig. 3-2 | (0 90 0) | 90 | No load |

## 3.2.3.3 Hydride precipitation in a zirconium tri-crystal

This model adds the effects of grain boundary and crystal misorientation to the previous model. As shown in Fig. 3-3, this model consists of three grains and a δ-hydride domain embedded within the middle grain to replicate the role of an intragranular hydride. In order to study the interaction between the hydride and grain boundaries as well as with the neighboring grain, the hydride domain is set to terminate at the grain boundaries. Also, the width and the length of the hydride are the same as the ones used in the single crystal model. The main purpose of this model is to understand how the misorientation of neighboring grains can enhance or suppress the propagation of hydrides. In addition, this model will help understand at which grain misorientation, the concentration of hydrogen is maximum. Fig. 3-3b shows the tri-crystal model and illustrates how the orientations of the three grain changes with respect to the loading direction. As shown, the model is extruded along the Z axis for 1 μm which is 2.5 % of the size of each grain along X axis. The thickness of the model is exaggerated in this figure. Table 3-4 provides a list of the Euler angles assigned to each grain. In this table, θ represents the angle between the c-axis of the Grain#3 and the loading direction. Similarly, λ represents the angle between the c-axis of Grain #2 with the loading direction. In all simulations, the habit plane of the hydride domain is kept perpendicular to the c-axis of Grain#2. All modeling steps are similar to the ones used for the single crystal presented in the previous section. That is, the first step includes loading, followed by hydriding in the second step, and calculation of H concentration at the end of the Step-2. The mechanical boundary conditions used are

similar to the ones explained in the previous section. In all models 0.3% strain is firstly applied to the right-hand side of the model along the x-axis, which is followed by applying HITS to the hydride domain under constant applied strain. The choice of 0.3% applied strain is to ensure that no macroscopic plasticity is induced by this strain, yet the resulting macroscopic stress is close to the onset of plasticity. The effects of macroscopic plasticity are studied in the discussion section. The mass transfer boundary condition is similar to the one used for the single crystal model where H concentration was assumed to be 100 wt.ppm on the surrounding elements of the model. All three grains are surrounded by a layer of elements to reduce the effects of boundary conditions on the calculation of stress fields. The properties of this layer are the same as Grain #2. Only four combinations of misorientations are selected to discuss since the results obtained from the rest of the models follow similar trends.

a.

b.
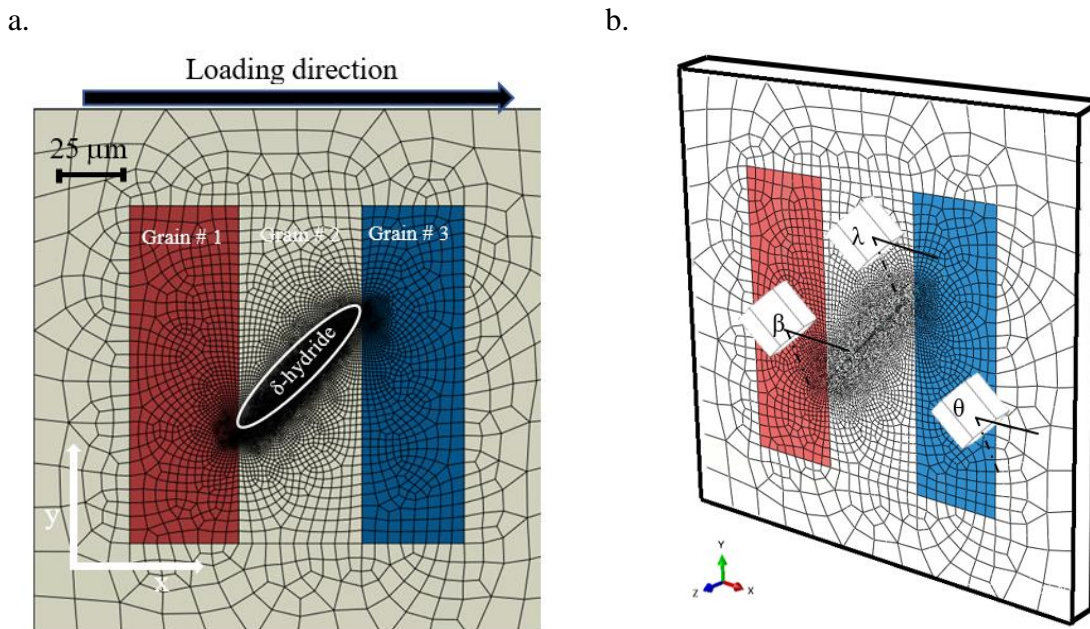


**Fig. 3-3 – The input model used for simulating the effects of grain orientation on redistribution of hydrogen around a hydride: (a) the tri-crystal model and (b) an isometric view of the model. β, λ and θ are the angles between the c-axis of the Grain #1, #2, and #3 with the loading direction respectively.**

**Table 3-4 - The tri-crystal models for intragranular hydride**

| Case no. | Simulation figure | Grain#1&2 | Grain#3 | θ (degrees) | β (degrees) | λ (degrees) | Applied Strain |
|----------|-------------------|-----------|---------|-------------|-------------|-------------|----------------|
| TC -1 | Fig. 3-3b | (30 90 0) | (90 90 0) | 0 | 60 | 60 | $\varepsilon_x$=0.3% |
| TC -2 | Fig. 3-3b | (45 90 0) | (90 90 10) | 0 | 45 | 45 | $\varepsilon_x$=0.3% |
| TC -3 | Fig. 3-3b | (60 90 0) | (45 90 0) | 45 | 30 | 30 | $\varepsilon_x$=0.3% |
| TC -4 | Fig. 3-3b | (90 90 0) | (45 90 0) | 45 | 0 | 0 | $\varepsilon_x$=0.3% |

## 3.2.3.4 Hydride precipitation along the grain boundary

The tri-crystal model is modified in this section to simulate formation of intergranular hydrides at the boundary of two neighboring grains. The steps used for modeling intergranular hydrides are the same as those explained in the previous section for intragranular hydrides, yet the hydride domain is located at the grain boundary. As shown in Fig. 3-4a and Fig. 3-4b, the hydride nucleates at the boundary of Grains #2 and #3. Table 3-5 provides a summary of the Euler angles used for each grain. The orientations of Grain #1 and Grain #2 are considered to be the same. The model set-up and boundary conditions are similar to those explained in section 3.2.3.3.
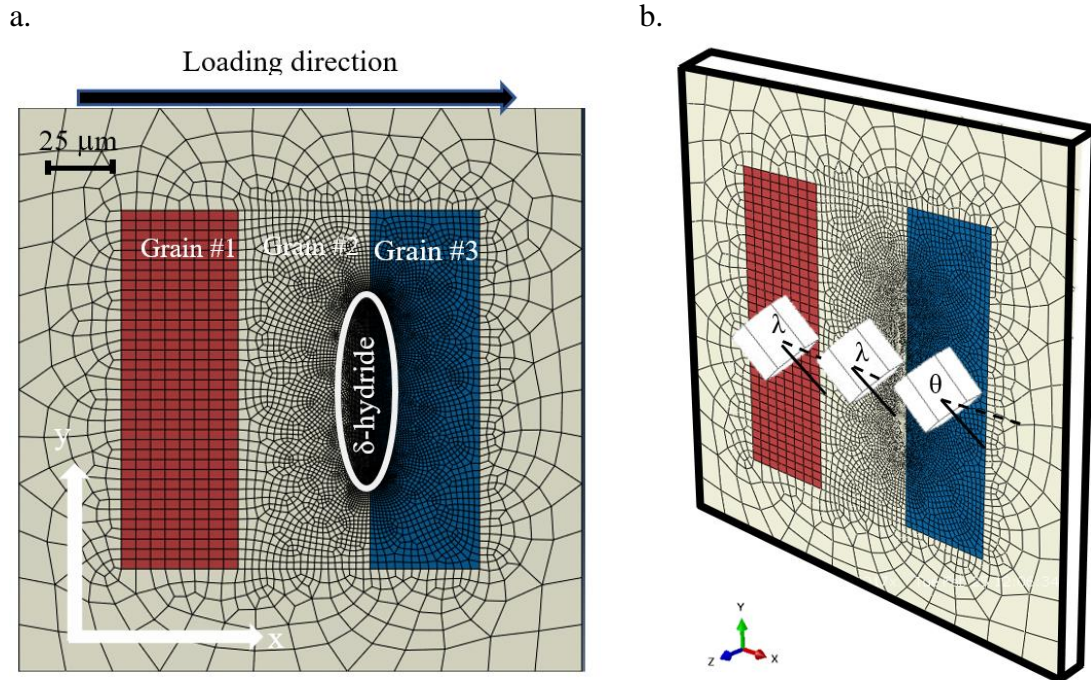
**Fig. 3-4 – The tri-crystal model for hydride precipitation along a grain boundary. θ is the angle between the c-axis of the Grain #3 and the loading direction. λ is the angle between the c-axes of the Grain #1 and #2 with the loading direction.**

**Table 3-5 - The tri-crystal models for intergranular hydride**

| Case no. | Simulation figure | Grain#1&2 | Grain#3 | λ(degrees) | θ(degrees) | Applied Strain |
|----------|-------------------|-----------|---------|------------|------------|----------------|
| TC -5 | Fig. 3-4b | (45 90 0) | (90 90 0) | 45 | 0 | $\varepsilon_x$=0.3% |
| TC -6 | Fig. 3-4b | (90 90 0) | (0 90 0) | 0 | 90 | $\varepsilon_x$=0.3% |
| TC -7 | Fig. 3-4b | (90 90 0) | (45 90 0) | 0 | 45 | $\varepsilon_x$=0.3% |

## 3.2.4 Deformation twinning and hydrogen diffusion

This model is to study the effects of deformation twinning on the redistribution of hydrogen atoms. Steps followed to create a twin are similar to hydride precipitation, except that twinning is accompanied by reorientation of the parent grain. Steps used in these simulations are shown in Fig. 3-5a. Following the method discussed in Abdolvand and Wilkinson (2016) and Arul Kumar et al. (2015), the twin domain is firstly reoriented using

31

the crystallographic orientation relationship of twin and parent and then, the 16.9% twinning shear is applied to the twin domain under the same boundary conditions used for hydriding, i.e., constant displacement on two Y-Z surface as shown in Fig. 3-6. In these simulations, the orientations of Grain#1 and Grain#2 are kept the same. Similar to the hydride modeling, the twinning domain is embedded in Grain #2 and terminates at the grain boundaries. Each of the models are simulated using two different externally applied strains to study how stress levels affect the distribution of hydrogen. The simulations configurations conducted in this section are summarized in Table 3-6.

**Table 3-6 - The bi-crystal model for twin and hydrogen interactions**

| Case no. | Simulation figure | Grain#1&2 | Grain#3 | Twin orientation | Applied Strain |
|----------|-------------------|-----------|---------|------------------|----------------|
| BC-tw-1 | Fig. 3-6 | (95 85 65) | (1 90 0) | (4 90 0) | $\varepsilon_x$=1.0% |
| BC-tw-2 | Fig. 3-6 | (95 85 65) | (90 90 0) | (4 90 0) | $\varepsilon_x$=1.0% |
| BC-tw-3 | Fig. 3-6 | (95 85 65) | (1 90 0) | (4 90 0) | $\varepsilon_x$=2.0% |
| BC-tw-4 | Fig. 3-6 | (95 85 65) | (90 90 0) | (4 90 0) | $\varepsilon_x$=2.0% |

To understand how further loading affects the hydrogen field around the twin, an extra 1% of strain is applied to the model after the twin shear transfer step. It is assumed that the twin does not grow or thicken over this step. Steps used in models BC-tw3 and tw4 are shown in Fig. 3-5b.
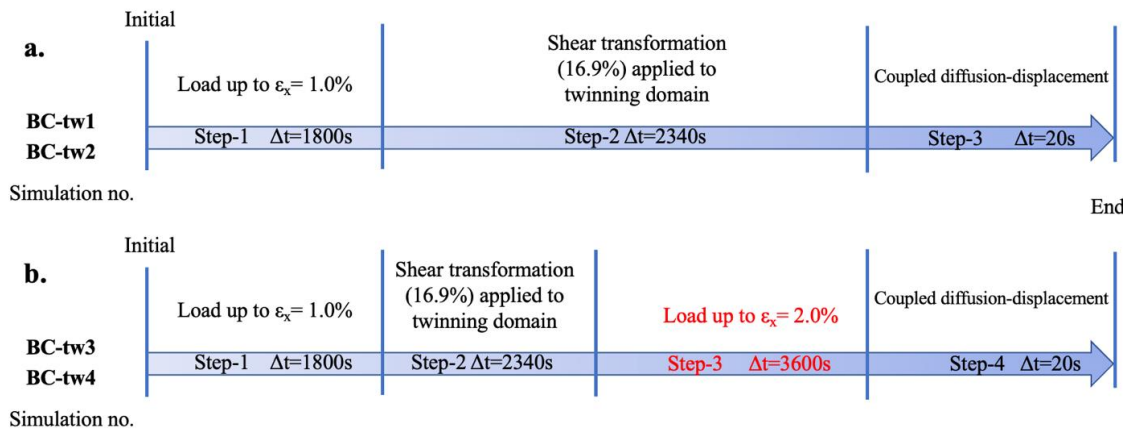
**Fig. 3-5 – Steps used in modeling hydrogen concentration around the twin domain: BC-tw3 and BC-tw4 have one extra step after the shear transfer step.**

The following steps are used in twinning-diffusion models:

Step-1: mechanical boundary conditions are applied to the model, including a 1% strain along the global x-axis, with a strain rate of $5 \times 10^{-5} \ s^{-1}$.

Step-2a: reorientation of the twinning domain using a reflection against the $\{10\bar{1}2\}$ plane.

Step-2b: twin transformation strain of 16.9% is applied incrementally to the twin domain.

Step-3: (for BC-tw3 and BC-tw4 only) applying further strain to 2%, along global x-axis with the same strain rate and boundary conditions as Step-1. Concentration of hydrogen is calculated at the end of this step.

33
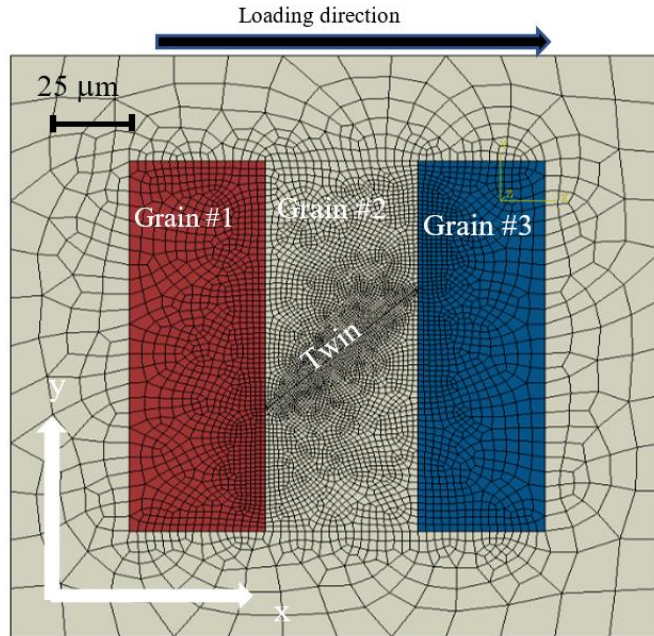
**Fig. 3-6 – 2D view of the bi-crystal model with a twin embedded within Grain #2. Orientation of Grain#1 and #2 are the same.**

## 3.3 Results

### 3.3.1 Bi-crystal model with no hydride

Fig. 3-7a demonstrates the normalized concentration of hydrogen under 4% of applied strain, along the path A-B shown in Fig. 3-1. The path A-B is selected far from the mechanical boundary conditions. This path plot is only selected to show how H concentration varies along the surface of the bi-crystal, but due to elastic and plastic anisotropy of zirconium, trends presented might change along other paths. All concentrations are normalized with respect to the one assigned as the boundary condition, i.e. $C_0$=100 wt.ppm. In all the simulations the left grain is the "hard" grain where the c-axis of the crystal is always parallel to the loading direction. The redistribution of hydrogen atoms is a result of the load sharing between the two grains. Also, different slip systems become active with rotating Grain #1. For instance, in the case of 90° misorientation, the right grain is considered to be soft where most of the applied strain is accommodated by crystallographic slip on prism systems. For the case that both grains have the same orientation, no stress gradient develops in the model and consequently, no hydrogen

34

redistribution takes place, i.e. for all nodes $C_{final} = C_0 = 100$ wt.ppm. Fig. 3-7b shows the distribution of normalized HS for all misorientation angles under 4% of applied strain, where $\sigma_{H0}$ is the HS on the back side of the model, at x=0. $\sigma_{H0}$ values for different misorientation angles are presented in Table 3-7. Also, misorientation angle of 75° has the steepest change in HS in the right grain, which results in steeper change in H concentration in this grain accordingly. On the other hand, HS for 15° misorientation changes smoothly within the right grain, resulting in almost no change in H concentration in the right grain. This is due to the fact that the dominant active slip system in the right grain at 15° misorientation is pyramidal <c+a>, which is the only active system in the left grain. This causes negligible change in HS and HS gradient at this angle over the model. In Fig. 3-7c and 3-7d the variations of H concentrations for the applied strains of 2% and 1% are respectively presented. As expected, applying higher strain leads to higher stress and higher variations in H concentration across the model. This can be seen by comparing the $C_{max}$-$C_{min}$ values at different applied strains. The maximum and minimum of H concentration occur respectively within the hard and soft grains. The values of $C_{max}$-$C_{min}$ at applied strains of 1% and 4% are respectively 9 wt.ppm and 11 wt.ppm. In addition, it can be seen that the concentration of hydrogen highly depends on the orientation of both grains as well as on the applied strain. In Fig. 3-7c and Fig. 3-7d, it is shown that the highest peaks of H concentration take place at 30° and 45° of misorientation, depending on the applied strain. This is due to the steep change of HS and HS gradient over the grain boundary compared to the other misorientation angles. Fig. 3-7e shows the effects of temperature on the redistribution of hydrogen at 75° misorientation, under 1% of applied strain. These temperatures are assigned to all nodes of the model to avoid temperature gradients. Both diffusivity and the stress-assisted term of Eq. 3-12 are a function of applied temperature where at higher temperatures, the effects of the stress gradients are weaker. It is shown in Fig. 3-7e that at lower temperatures the effects of stress-assisted term are more pronounced.

**Table 3-7 - Hydrostatic stress ($\sigma_{H0}$) values on the left side of the bi-crystal model for different misorientation angles**

| Misorientation angle (°) | 15° | 30° | 45° | 60° | 75° | 90° |
|---|---|---|---|---|---|---|
| $\sigma_{H0}$ (MPa) | 264 | 225 | 192 | 128 | 73 | 96 |

Results shown in this section are in agreement with those reported by Lin and Heuser (2019) where it was shown that the H concentration is higher within the grain which has its c-axis under higher levels of tensile stresses. These results were obtained using a phase-field model of a bi-crystal zirconium and, similar to the current study, the harder grain had its c-axis along the loading direction which facilitated the precipitation of hydrides. The same trend is also observed in an experiment conducted by Une et al. (2004) where hydrides precipitated early in the grains having their c-axis under tensile loadings.
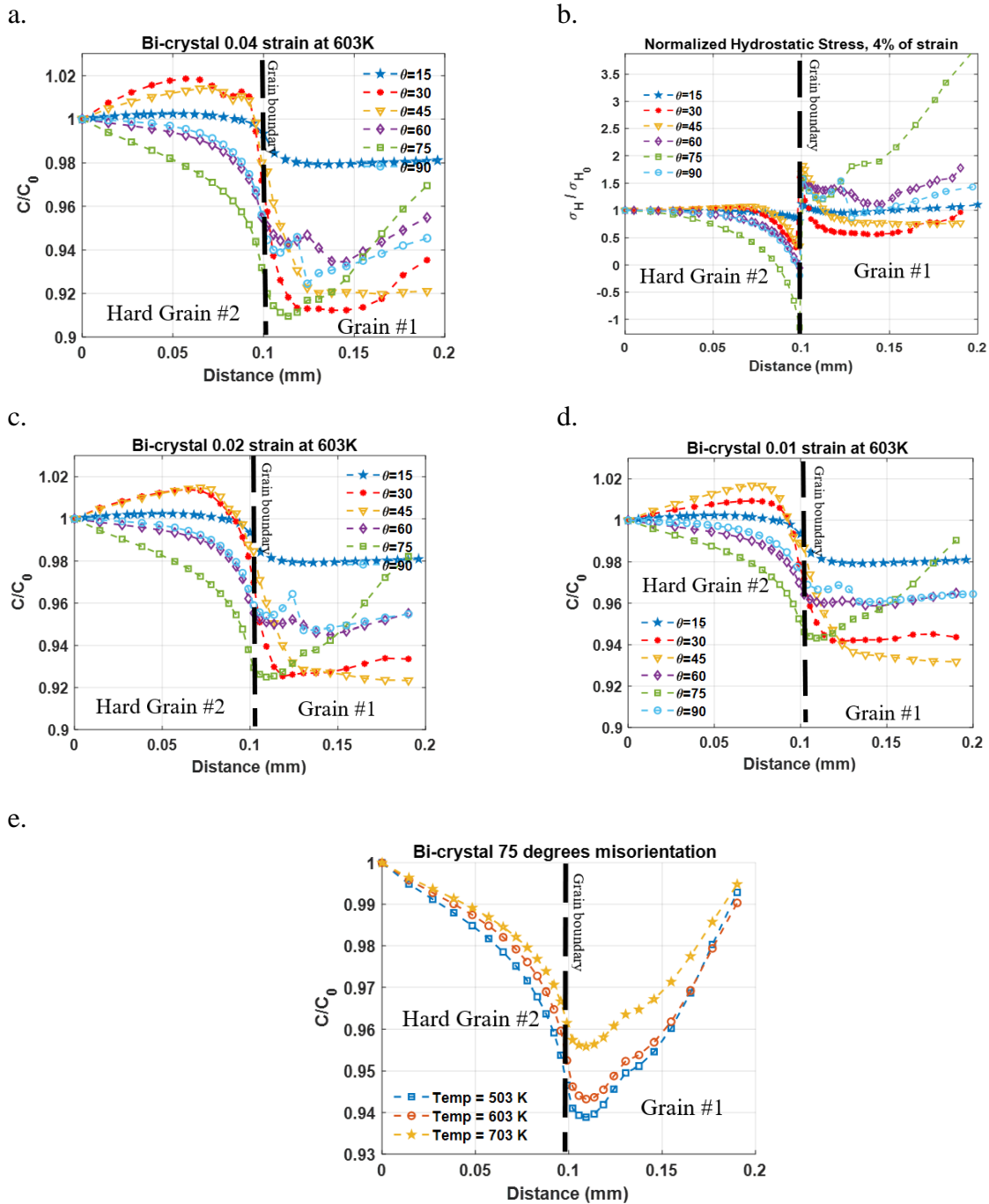
**Fig. 3-7 – Normalized hydrogen concentration along the line A-B in the bi-crystal model: (a) at 4% applied strain for different misorientation angles (c) at 2% and (d) 1% applied strains. (b) normalized hydrostatic stress along the line A-B at 4% applied strain. (e) Normalized hydrogen concentration along the line A-B at 1% applied strain for θ=75° of misorientation using three different temperatures. In all figures points A and B coincide with 0 and 0.2 mm, respectively.**

## 3.3.2 Hydride in a single crystal

The results of the simulations for the embedded δ-hydride within a single crystal are presented in Fig. 3-8 and Fig. 3-9. Results obtained on the x-y plane of the model are presented in this and the following sections. The c-axis and the orientation of the crystals are shown schematically in each figure with the labels of each model presented in Table 3-3. The right and left columns in Fig. 3-8 respectively represent the distribution of HS and H concentration at the last step of simulation. Fig. 3-8a and 8b show the results of the model SC-3 where no external strain was applied, i.e. HITS is the only reason for the developed stress fields. It is shown that the HS is tensile near the tip of the hydride, yet it is compressive along its sides. This leads to diffusion of hydrogen atoms toward the tips of the hydride and helps hydride grow axially. Further, there is a significant reduction of H concentration from the sides which indicates that the hydride does not tend to thicken. It should be noted that δ-hydride reluctance to thicken might stem from effects of coherency along different faces of hydride, which is not accounted for in these simulations. Also, it should be noted that at nanoscale, stresses at the tips of hydride are so high that cause significant flux of hydrogen towards hydride. The size of the representative volume element in CPFE simulations presented here is such that the model cannot capture these effects. These results are in agreement with the in-situ observations of hydride growth in Zr alloys using electron microscopy (Long et al., 2017; Singh et al., 2004; Arunachalam et al., 1967).

Hydrogen Concentration (wt.ppm)          Hydrostatic Stress (MPa)
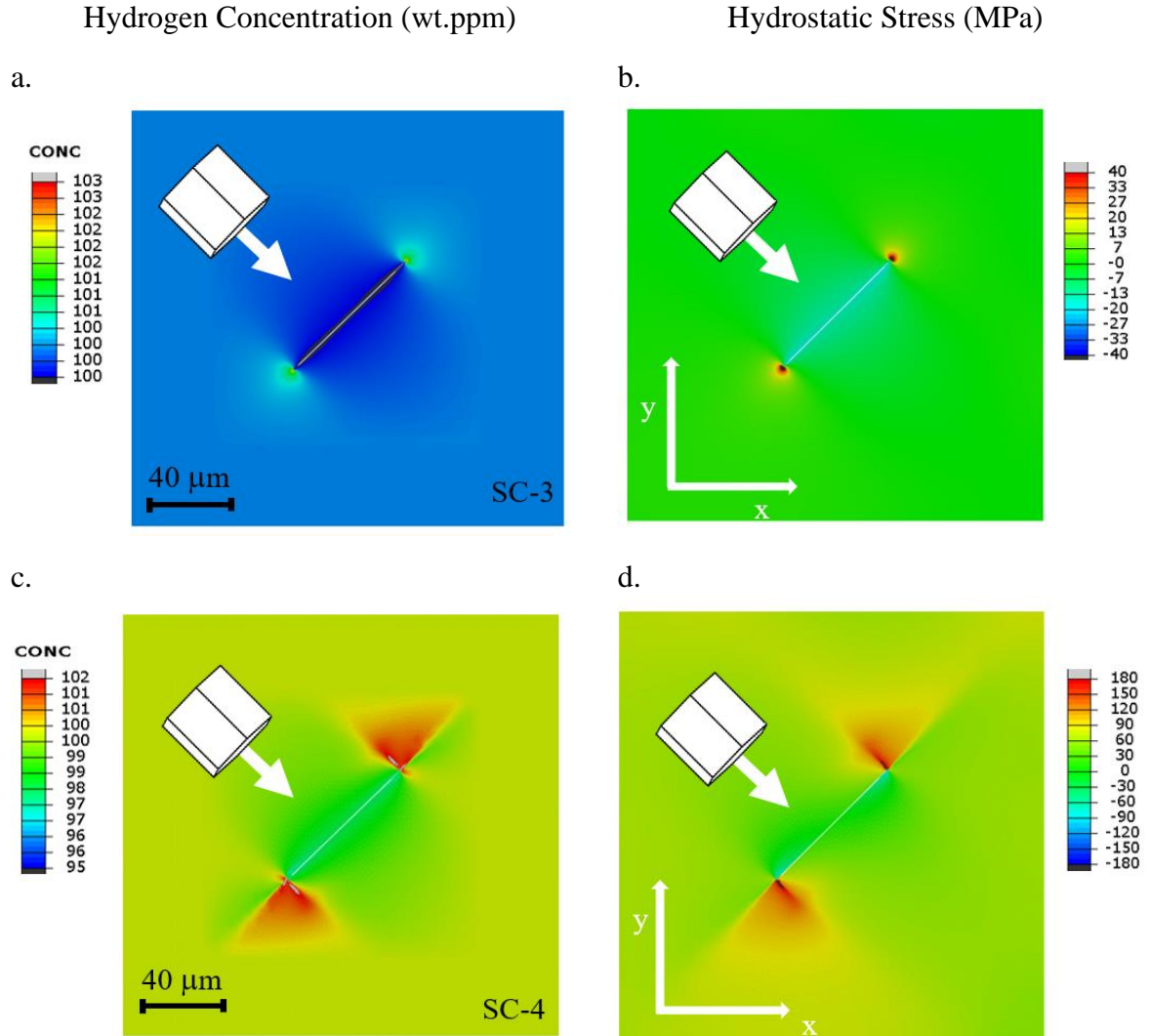


**Fig. 3-8 – The zirconium single crystal model undergoing hydride induced transformation strain in the hydride domain: (a) hydrogen concentration and (b) hydrostatic stress under no applied strain (c) hydrogen concentration and (d) hydrostatic stress after 0.3% applied strain followed by hydriding. The Euler angles of the single crystal is (45, 90, 0).**

Fig. 3-8c and 3-8d show the results of the model SC-4 where 0.3% strain is firstly applied to the model, followed by HITS applied to the hydriding domain under constant applied strain- velocity along x on the two external faces at x=0 and x=200 µm is set equal to zero. Although the distributions of H and HS around the hydride are changed, results of both SC-3 and SC-4 models indicate that hydrogen atoms tend to diffuse towards the tips of hydride. In addition, higher stresses develop in the vicinity of hydride in SC-4 model implying that under a tensile load, more hydrogen atoms diffuse towards the hydride tips.

The accumulation of hydrogen near the hydride tips increases the probability of surpassing the terminal solid solubility limit of hydrogen in zirconium and further precipitation of the hydride phase. The same trend was captured in the numerical study conducted by Guo et al. (2008) on single crystals of zirconium having a γ-hydride domain in the middle of a grain, where tensile and compressive HS were reported at the hydride tips and hydride sides, respectively. They reported that the observed trends are applicable for δ-hydrides as well. McRae et al. (2010) also showed that hydrogen atoms diffuse from the zones with compressive HS to the ones with tensile HS. Further, Kubo and Kobayashi (2013) studied the propagation of the hydrides near a crack tip and showed that under an applied tensile load, higher stresses develop near the tips of the hydrides. This finding is also in agreement with the results reported here.

Parent crystals with different orientations are studied to investigate the validity of the results provided above. Fig. 3-9 shows the results for H concentration and HS for the models SC-5, SC-2, and SC-1. In all models, the position of the hydride is kept perpendicular to the c-axis of the parent grain. It is shown that in all models, the highest tensile HS and H concentration occur in the vicinity of the δ-hydride tips. Further, between all models, the hardest grain, i.e., model SC-1, develops the highest HS and H concentration for a given applied strain. Results presented here also show that the hydrogen and stress fields around the δ-hydride tips are not always symmetric. For example, the results of SC-1, 3, and 5 reveal a symmetric hydrogen field at the δ-hydride tips, yet a rather different hydrogen field is observed in the results of SC-4 and SC-2. Nevertheless, the highest concentration of hydrogen in all models is calculated along the hydride axial direction. This is shown in the enlarged subfigure of Fig. 3-9c. As seen, the two paths labeled as A-B, along the hydride axial direction, and A-C have the highest H concentration at the hydride tip. The maximum H concentration along A-B and A-C are respectively 110 and 102 wt.ppm which indicate that the hydride will most probably grow along the path A-B.

Hydrogen Concentration (wt.ppm)          Hydrostatic Stress (MPa)

a.

b.

c.

d.

e.

f.

SC-5

SC-2

SC-1
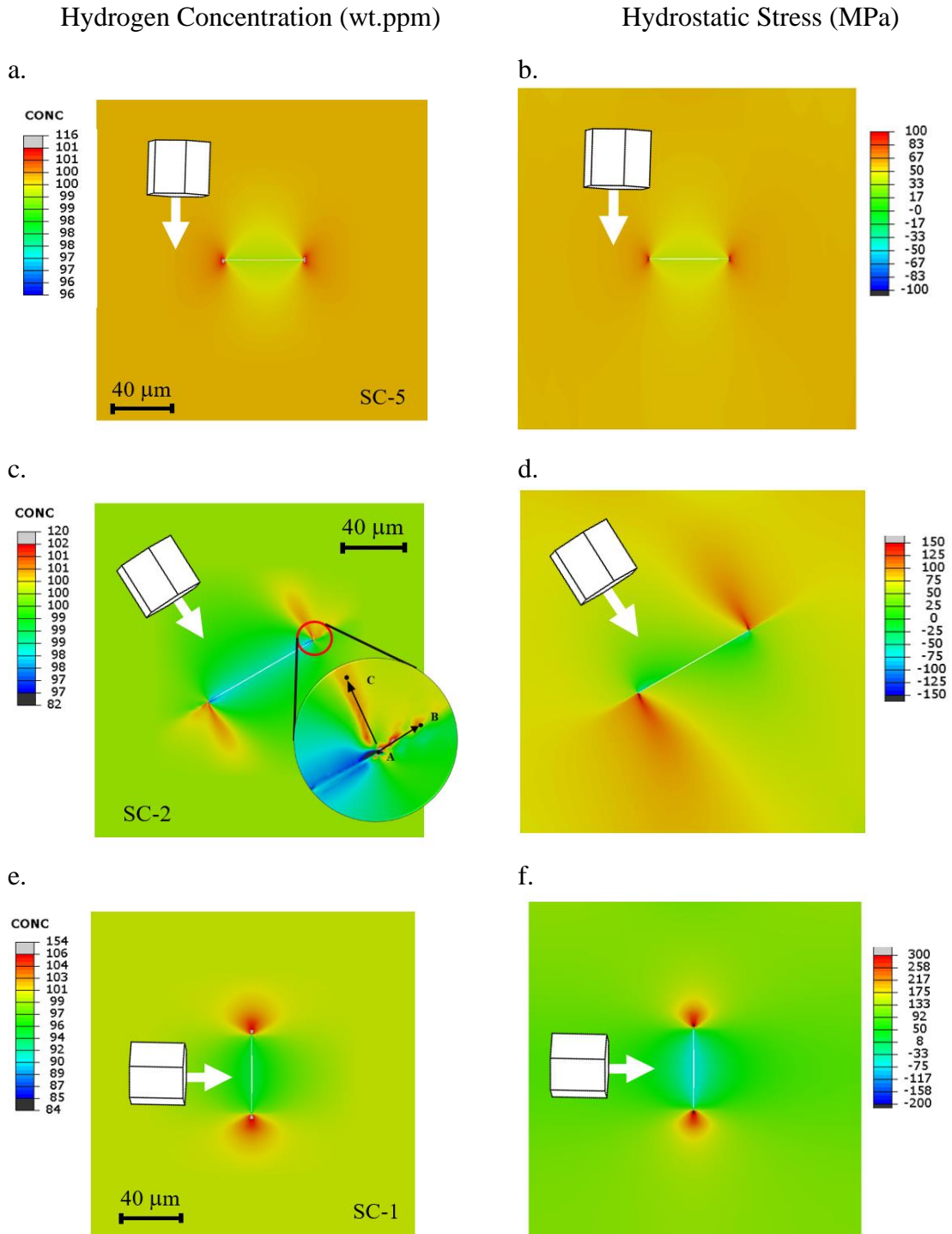
**Fig. 3-9 – The zirconium single crystal model: hydrogen concentrations are shown in the left column and hydrostatic stresses are shown in the right column. The orientation of the parent crystals are (a,b) (0,90,0), (c,d) (30,90,0) and (e,f) (90,90,0).**

### 3.3.3 Tri-crystal model

### 3.3.3.1 Intragranular hydrides

Results of the tri-crystal α-Zr model where a hydride is embedded within the middle grain are discussed in this section. Fig. 3-10 shows the distribution of HS and H concentration at the last step of simulation for models TC-1, 2 and 4. The orientations of the grains used in these models are provided in Table 3-4.

It is shown in Fig. 3-10 that H concentration and HS is much higher at the tips of the hydride, particularly in the vicinity of the harder grain. This suggests that hydrogen atoms preferentially diffuse towards the tip of the δ-hydride located in the harder neighboring grain. Thus, the alignment of crystal c-axis with the tensile loading direction leads to higher HS and higher likeliness of hydride growth within the hard grain. This can clearly be seen in Fig. 3-10e and Fig. 3-10f, where the hotspots are the tips of the hydride within the hard grain. These results are in agreement with those reported by Vicente Alvarez et al. (2012, 2011) and Vizcaíno et al. (2014), where it was shown using XRD that hydrides tend to precipitate within hard grains, i.e., the grains having their c-axis undergoing tensile stresses. In addition, Fig. 3-10e shows a depletion of hydrogen atoms in the softer grain and diffusion towards the harder one. Comparing the hotspots in Fig. 3-10c and Fig. 3-10e, higher value of H concentration is captured at the hotspot located in the harder grain (Grain#2 of TC-4). The above trend is also captured for the model TC-3 which is not presented here to avoid busy figures.

Hydrogen Concentration (wt.ppm)  Hydrostatic Stress (MPa)
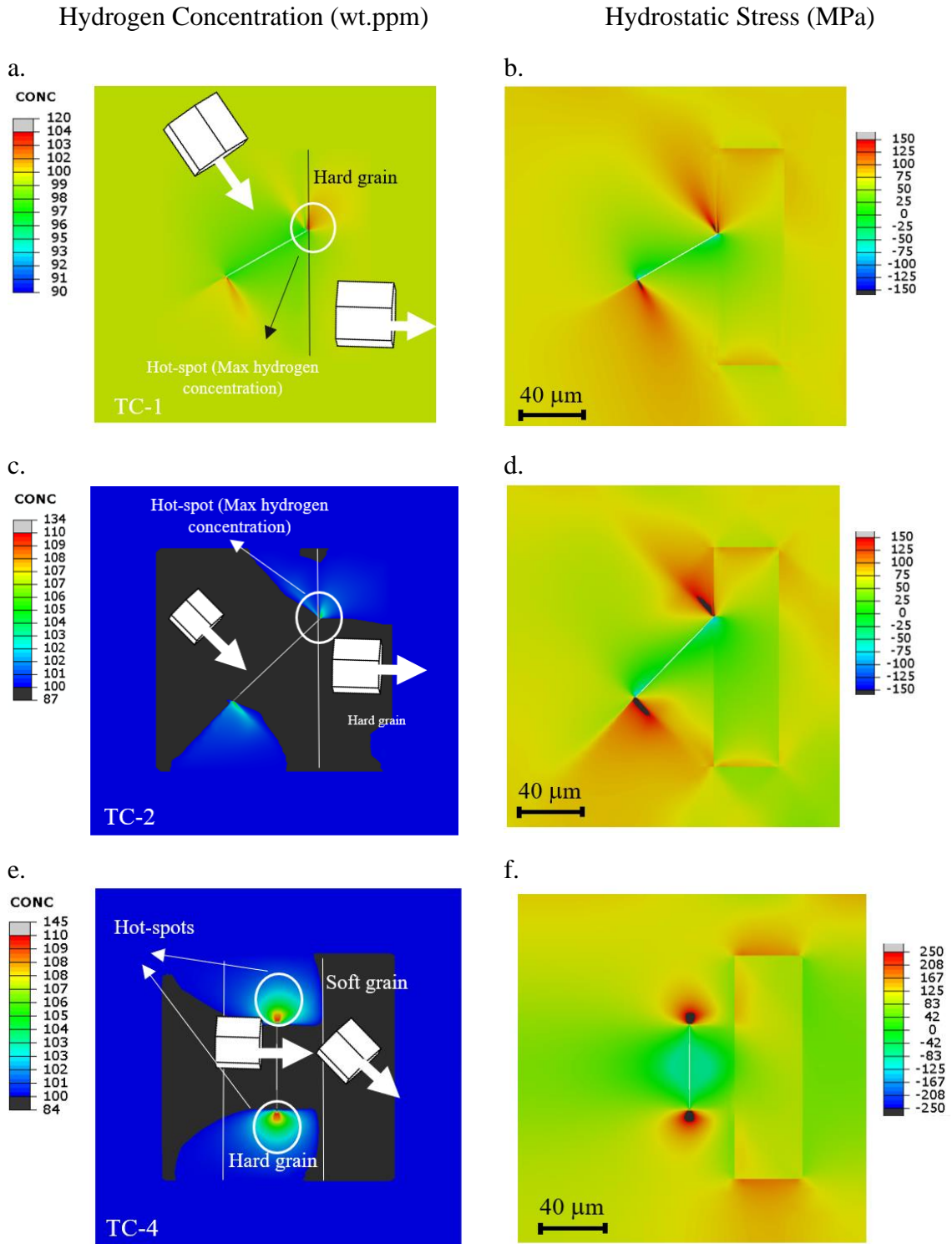


**Fig. 3-10 – Hydrostatic stress and hydrogen concentration fields around intragranular hydrides: Models (a, b) TC-1, (c, d) TC-2, and (e, f) TC-4. The orientation of each crystal is provided in Table 3-4.**

## 3.3.3.2 Intergranular hydrides

The steps used for modeling intergranular hydrides are the same as those explained in the previous section for intragranular hydrides, yet the hydride domain is located at the grain boundary. Fig. 3-11 shows the distribution of H concentration for the models TC-5, 6 and 7. The distribution of hydrogen is such that the hydride may propagate both along the grain boundaries and towards the grain interior, yet higher H concentration is calculated within the harder grain in comparison to the soft one. Fig. 3-11c shows the H concentration of the model TC-7 within Grain #2 and Grain #3. Higher H concentration is captured along the grain boundary and within the harder grain. Two separate path plots, as shown in the enlarged subfigure, are plotted to investigate the variation of H concentration across (Path#3) and along (Path#4) the grain boundary. The former starts from Grain #2 and crosses the grain boundary, near the tip of the hydride and terminates in Grain #3, whereas the latter (Path#4) is extended along the left side of the grain boundary. Variations of H concentration along Path #3 and Path #4 are shown in Fig. 3-11e and Fig. 3-11d, respectively. It is shown that H concentration peaks along the grain boundary, as opposed to within the harder grain. Hence, the existing hydride will most probably grow along the grain boundary. The same trend is captured for the TC-5 and 6 as well.

Hydrogen Concentration (wt.ppm)
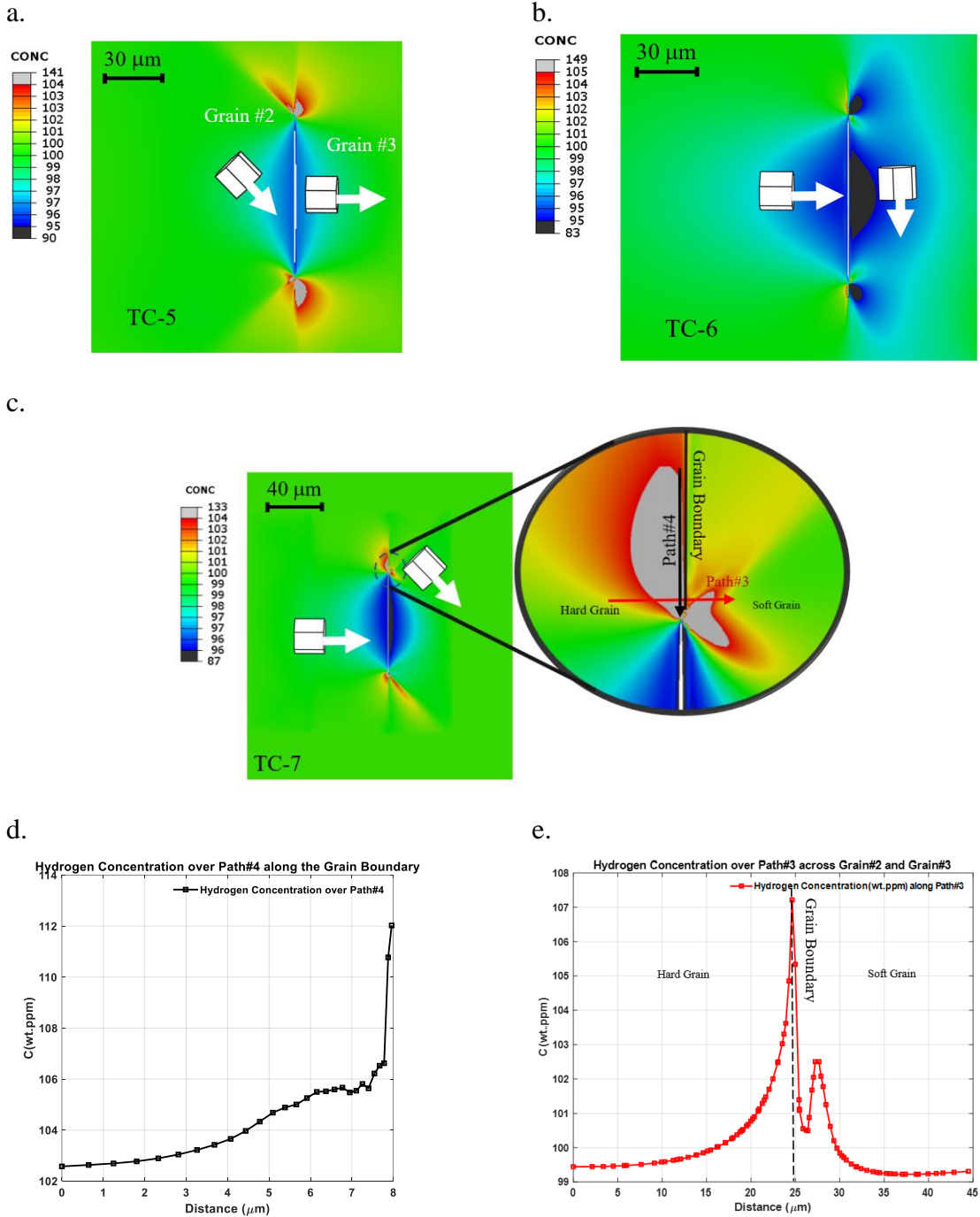


**Fig. 3-11 – Hydrogen concentration fields around intergranular hydrides: Models (a) TC-5, (b) TC-6 and (c) TC-7. The orientation of each crystal is provided in Table 3-5. The variation of hydrogen concentration as a function of distance from the hydride for (d) the Path #4 and (e) the Path # 3. Paths #3 and #4 are shown in (c).**

### 3.3.4 Twinning and hydrogen diffusion

The results of the bi-crystal model consisting of a twin domain are represented in Fig. 3-12 with the steps used in modeling the twin and hydrogen diffusion shown in Fig. 3-5. H concentration is calculated at the end of twin shear transfer. It can be seen in Fig. 3-12 that the twin tips are the hotspots, in terms of both HS and H concentration. The hotspot closer to the harder grain, i.e., BC-tw-2, is more susceptible to hydride precipitation due to having a higher HS and H concentration compared to the other end of the twin domain. Fig. 3-12c and Fig. 3-12d demonstrate an almost uniform distribution of hydrogen and HS, far from the tips of the twin domain. This is because the c-axes of all the grains are almost aligned with the loading direction. Moreover, the tips of the twin have higher H concentration and HS values compared to the inner regions of the matrix.

The twin-matrix interfaces are also possible locations for hydride precipitation as the H concentration along the twin-matrix interface is higher compared to parent grain interior. This region is highlighted using dashed arrow in Fig. 3-12c. This is in agreement with the experimental observation of Kim et al. (2016) where it was shown that hydrides precipitate at the interface of twin and parent grain.

Hydrogen Concentration (wt.ppm)          Hydrostatic Stress (MPa)
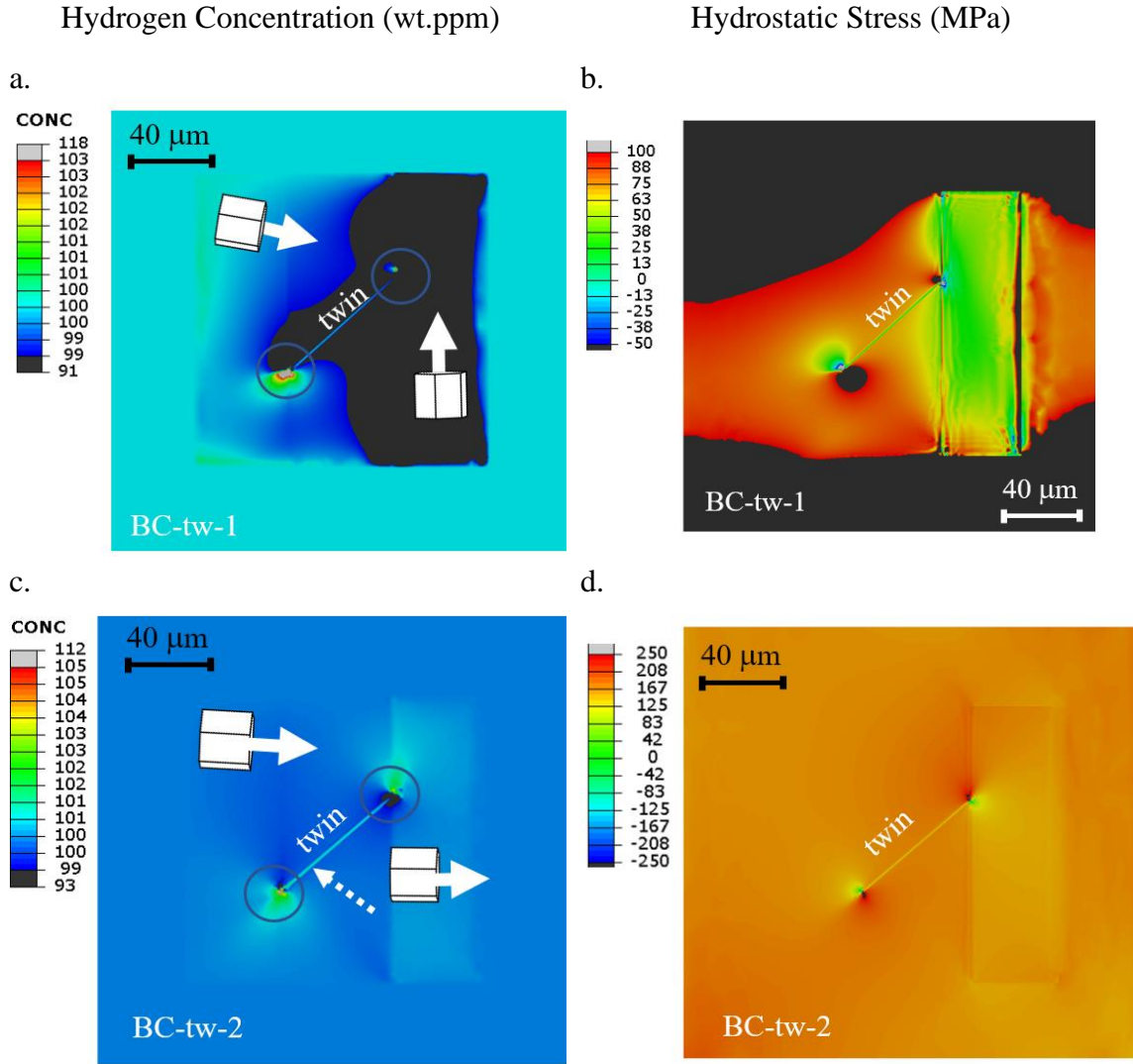


**Fig. 3-12 – Hydrogen concentration and hydrostatic stress for the bi-crystal model with a twin domain: (a,b) BC-tw-1 (c,d) BC-tw-2. Model labels and grain orientations are provided in Table 3-6.**

Fig. 3-13 shows the results of BC-tw-3 and BC-tw-4 models where after twin formation, the models were further strained. The new models maintain the same crystal orientations as the previous ones (see Table 3-6).

It is shown in Fig. 3-13 that with further loading, the effects of twins on alternating the distribution of hydrogen atoms weaken, although twin tips are still hydrogen hotspots. This can be seen by comparing the areas within the dashed circles in Fig. 3-13a and Fig. 3-13b

to those in the solid circles in Fig. 3-12a and Fig. 3-12c. In addition, the H concentration is still higher in harder grains in both BC-tw2 and BC-tw4 models.

Hydrogen Concentration (wt.ppm)
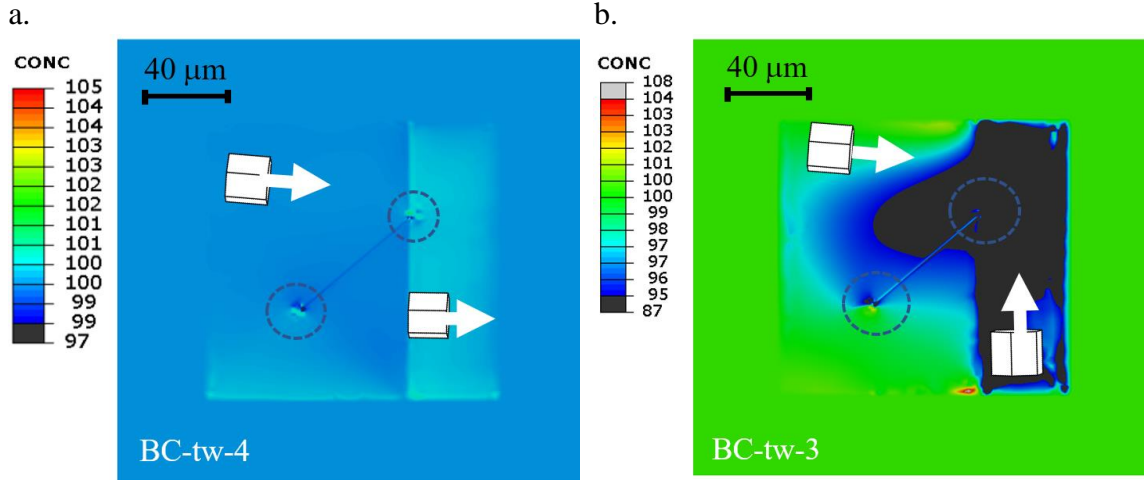


**Fig. 3-13 – Hydrogen concentration of the bi-crystal model with a twin domain after applying 2% strain. Model labels and grain orientations are provided in Table 3-6.**

## 3.4 Discussion

### 3.4.1 The effects of applied strain on hydrogen concentration

In this section the effects of the applied strain on the redistribution of hydrogen atoms and HS are discussed. The stress−strain curves of zirconium single crystals under a uniaxial tensile strain are shown in a. In this figure, θ is the angle between the crystal c-axis and the loading direction. At θ=0°, pyramidal <c+a> is the active slip system, but with increasing θ, slip on the basal planes will become active with maximum activity recorded at θ=30°. With further increase of θ, slip on the prism planes will become active. Since the CRSS of the pyramidal <c+a> is the highest and that of prism slip system is the lowest (Table 3-1), the hardest and softest responses in Fig. 3-14 are recorded for θ=0° and 90°, respectively. Results shown in the previous section are either for no applied strain or $\varepsilon_x = 0.3\%$, both of which belong to the elastic zone. In this section, results for $\varepsilon_x = 1\%$ and 2% are discussed to investigate the effects of plasticity on the trends reported. A summary of the models used for this study is presented in Table 3-8. The tri-crystal model is used. For the first batch of models, Grain #3 is considered to be hard, whereas for the second batch, it is considered to

be soft. The orientations of Grains #1 and #2 are kept constant. For the last batch of models, the orientations of all three grains are changed.

**Table 3-8 - Simulation cases of zirconium tri-crystal with different orientations**

| Case no. | Simulation figure | Grain#1 | Grain#2 | Grain#3 | θ (°) | Applied Strain | |
|---|---|---|---|---|---|---|---|
| TC -8 | Fig. 3-3b | (45 90 0) | (45 90 0) | (90 90 0) | 0 | $\varepsilon_x$=0.3% | Batch#1 |
| TC -8b | Fig. 3-3b | (45 90 0) | (45 90 0) | (90 90 0) | 0 | $\varepsilon_x$=1.0% | Grain #3 |
| TC -8c | Fig. 3-3b | (45 90 0) | (45 90 0) | (90 90 0) | 0 | $\varepsilon_x$=2.0% | is hard |
| TC -9 | Fig. 3-3b | (45 90 0) | (45 90 0) | (0 90 0) | 90 | $\varepsilon_x$=0.3% | Batch#2 |
| TC -9b | Fig. 3-3b | (45 90 0) | (45 90 0) | (0 90 0) | 90 | $\varepsilon_x$=1.0% | Grain #3 |
| TC -9c | Fig. 3-3b | (45 90 0) | (45 90 0) | (0 90 0) | 90 | $\varepsilon_x$=2.0% | is soft |
| TC -10 | Fig. 3-3b | (0 90 0) | (45 90 0) | (90 90 0) | 0 | $\varepsilon_x$=0.3% | |
| TC -11 | Fig. 3-3b | (75 90 0) | (45 90 0) | (90 90 0) | 0 | $\varepsilon_x$=0.3% | |
| TC -12 | Fig. 3-3b | (90 90 0) | (45 90 0) | (30 90 0) | 60 | $\varepsilon_x$=0.3% | Batch#3 |
| TC -13 | Fig. 3-3b | (90 90 0) | (45 90 0) | (90 90 0) | 0 | $\varepsilon_x$=0.3% | |

To study the effects of the applied strain, models TC-8 and TC-9 are firstly selected. In model TC-9, Grain#3 is a soft grain, whereas in model TC-8, it is a hard grain compared to Grain #2. As shown in Fig. 3-14c, a path is selected along the axial direction of the hydride to study how H concentration varies with distancing from the hydride tip. It can be seen in Fig. 3-14b and Fig. 3-14d that for all applied strains, H concentration increases towards the hydride tip. Comparing the soft and hard grains in Fig. 3-14b and Fig. 3-14d, it can be seen that higher levels of stresses lead to more depletion of hydrogen within the

soft grain and higher H concentration within the harder grain. This trend is consistent with the ones shown in the previous sections.

a.
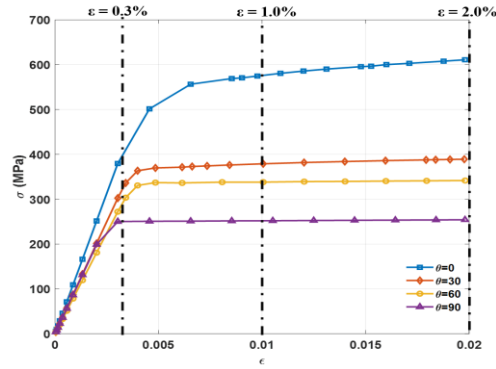


b.
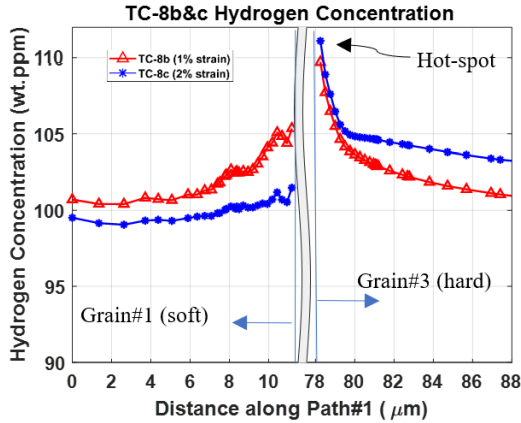


c.
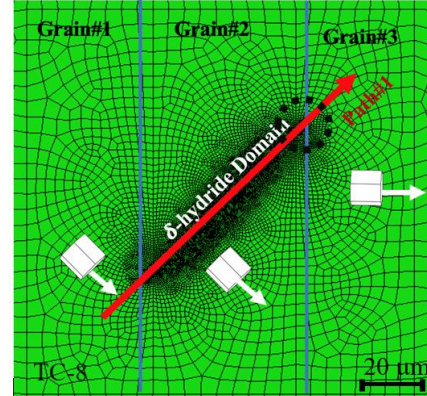


d.
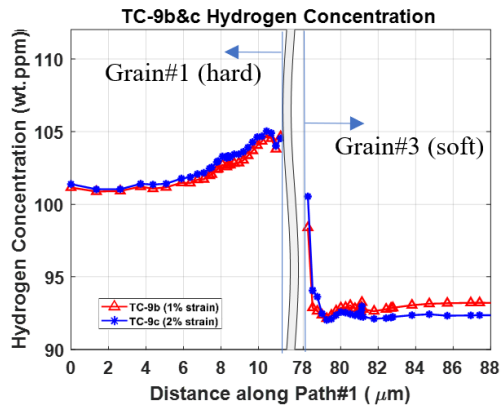


e.
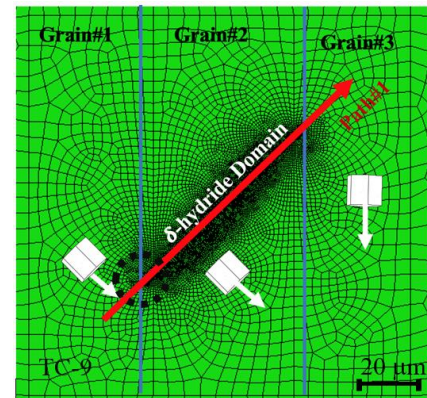


**Fig. 3-14 – (a) Stress–strain curves of zirconium single crystals. θ is the angle between the tensile loading direction and crystal c-axis. The effects of applied strain on hydrogen concentration of (b) TC-8b and TC-8c and (d) TC-9b and TC-9c. The grain orientations for the model TC-8 are shown in (c) and for the model TC-9 in (e). Path plots follow the red arrows and the hydride domains are excluded from the plots.**

Three different orientations are assigned to each crystal in the third batch of models. This is because the orientation of Grain #1 is set equal to that of Grain #2 in all simulations presented so far. Results of H concentration distribution for models TC-10, 11, 12 and 13 are presented in Fig. 3-15. In all of the tri-crystal models, higher tensile HS and H concentration develop within the harder grain. For example, in model TC-10 shown in Fig. 3-15a, the H concentration within the soft grain (Grain#1) as well as in the vicinity of the hydride tip in Grain#1 is significantly lower than the one calculated at the other end of the hydride. This can also be observed in Grain#3 of TC-10, where the maximum H concentration is at the tip of the hydride located in this grain. In addition, results from the models TC-11 and TC-12 indicate that as the c-axis of the crystal is more aligned with the loading direction, higher H concentration is captured at the tip of the hydride located in the harder grain.

Hydrogen Concentration (wt.ppm)
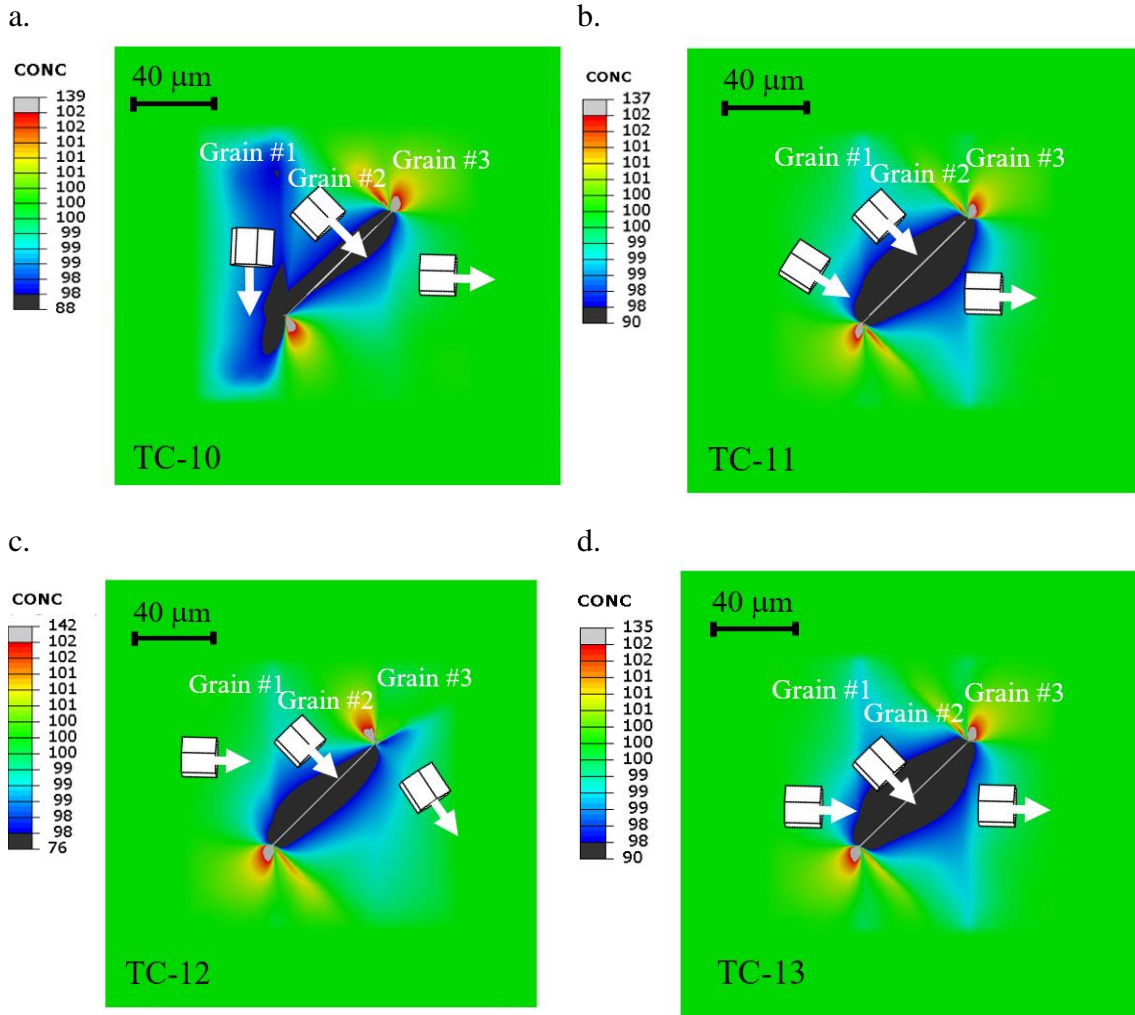


**Fig. 3-15 – Hydrogen concentration fields around the intragranular hydrides. Results for models (a) TC-10, (b) TC-11, (c) TC-12, and (d) TC-13.**

The concentration of hydrogen for model TC-8 along Path#2 is shown in Fig. 3-16a. Path#2 and the orientation of each grain in this model are shown in Fig. 3-16b. It can be seen that the H concentration decreases towards the hydride domain since compressive HS stress field develop along the sides of the hydrides. With distancing from the hydride, H concentration increases inside Grain #3, which is a hard grain. The H concentration value in this grain exceeds the maximum value of H concentration calculated within the other two grains.

a.



b.
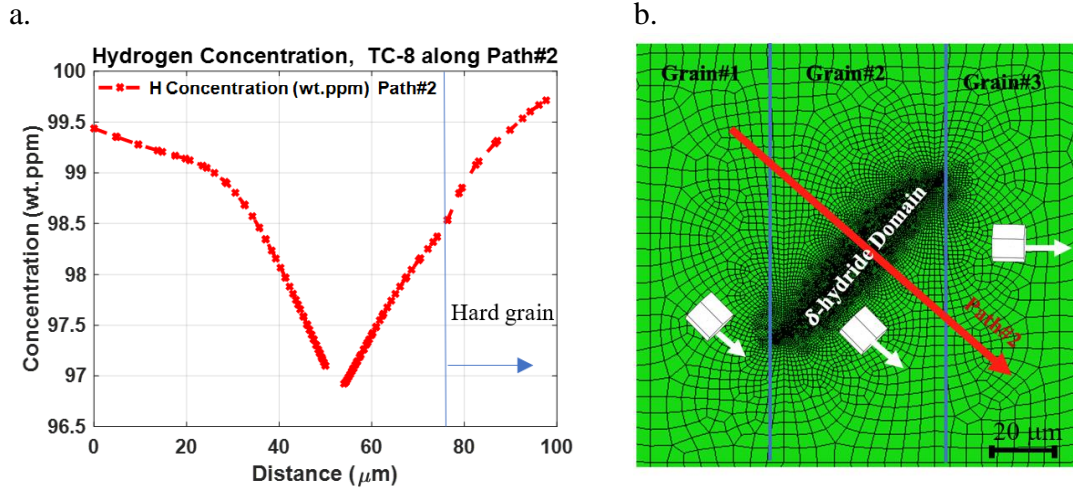


**Fig. 3-16 – (a) Hydrogen concentration along Path#2 for TC-8. Path#2 is shown in (b).**

## 3.4.2 The effects of boundary conditions

In all TC simulations presented so far, the H concentration was set to 100 wt. ppm along the four exterior boundaries at the two sides of the x and y planes. Here the effects of boundary conditions are studied for the model TC-8 by applying constant H concentration only to the left surface, i.e. x=0. Fig. 3-17 shows the variations of H concentration along Path#1 for the two cases, when all four exterior boundaries have constant hydrogen (case-1) and when only the left surface has such condition (case-2). As shown in Fig. 3-17, this change only has some minor effects on the distribution of H concentration.
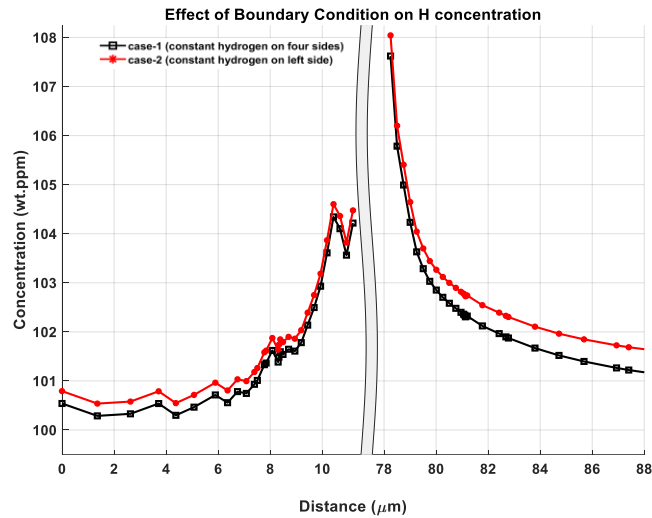
**Fig. 3-17– The effects of boundary conditions on hydrogen concentration for model TC-8 along Path#1, defined in Fig. 3-14c.**

## 3.4.3 Transient vs. steady state

In this section, a comparison between the steady state and transient responses of the single crystal model is presented. The single crystal model shown in Fig. 3-2 is used. A summary of the model set-up is presented in Table 3-9.

**Table 3-9 - Single crystal models undergoing hydride precipitation: transient vs. steady state analysis**

| Case no. | Analysis type | Figure number | Grain Euler Angle | θ (degrees) | Applied Strain |
|----------|---------------|---------------|-------------------|-------------|----------------|
| SC-6-ss | Steady State | Fig. 3-2 | (45 90 0) | 45 | $\varepsilon_x$=1.0% |
| SC-6-tr | Transient | Fig. 3-2 | (45 90 0) | 45 | $\varepsilon_x$=1.0% |

In the transient simulation, the element size and time increments are selected such that the convergence of the results are guaranteed. Total step time of the transient mass diffusion in SC-6-tr is 3060s.

Mechanical boundary conditions and steps for both SC-6-ss and SC-6-tr are the same as those in SC-4. Mass diffusion boundary conditions of the model SC-6-ss are the same as the ones presented in section 3.3. However, for the transient analysis, the model is set to have zero H concentration at time t=0s. The left surface of the model is then set to have 100 wt. ppm of hydrogen supply throughout the 3060 seconds simulation time. As soon as the left mass diffusion boundary condition is activated, the hydrogen atoms diffuse across the model in which the hydrogen flux ($\vec{J}$) is a function of gradient of concentration ($\vec{\nabla}C$), the diffusivity tensor ($\boldsymbol{D}$) and the existing hydrostatic stress field from previous mechanical steps. Fig. 3-18a represents the H concentration field after 120 seconds of the transient simulation which shows that the hydrogen flux is tilted toward the hydride tips (shown with white arrows). H concentration field at the end of the simulation for the transient model matches with the steady state response, both shown in Fig. 3-18b.

a.                                              b.
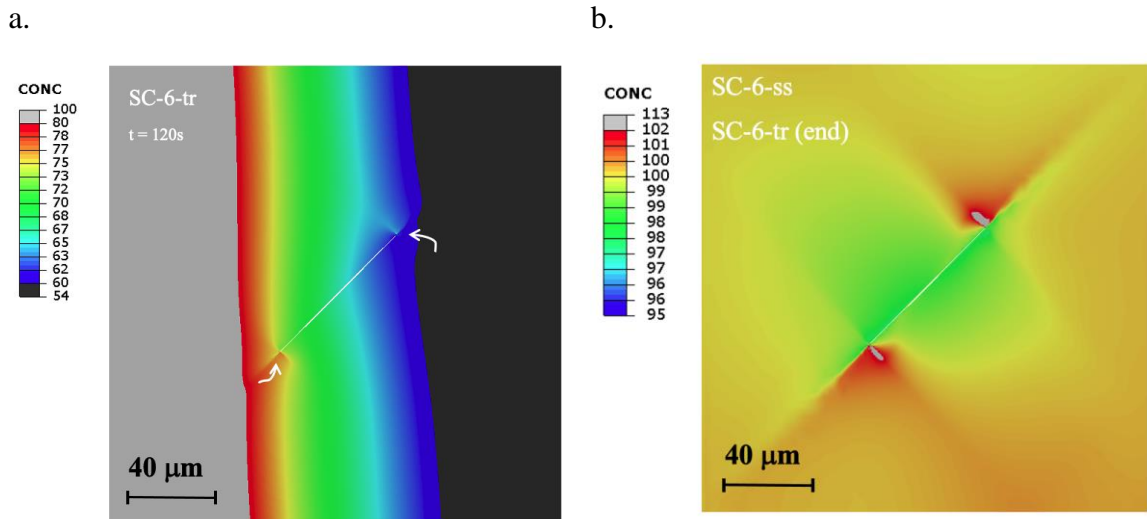


**Fig. 3-18 – Hydrogen concentration fields for (a) SC-6-tr at t=120s and (b) both SC-6-ss and SC-6-tr at the end of the simulation.**

In this work, some simplifying assumptions are made in simulating the diffusion of hydrogen and the precipitation of hydrides. For example, the effects of pipe diffusion resulting from dislocation-hydrogen interaction as well as the effects of accelerated diffusion at the grain boundaries are neglected. Also, the effects of trapping sites as well as the reduced hydrogen diffusivity inside the hydride phase are neglected. In addition, a conventional CPFE model is used in this study and the strain gradient effects are ignored. The magnitudes of the stresses at the locations with high strain gradients will be different from those calculated here, so as the calculated hydrogen concentrations, but the reported trends are not expected to change (Sedaghat and Abdolvand, 2021). These effects are the focus of our future studies.

## 3.5 Conclusions

The effects of δ-hydride precipitation on the redistribution of hydrogen atoms in α-Zr crystals are studied. A coupled mass-diffusion and crystal plasticity finite element approach is used to simulate the effects of hydride-induced-transformation strain on the stress-assisted diffusion of hydrogen atoms. The formation of δ-hydrides at the grain boundaries, in the vicinity of twins, and within single crystals is investigated. It is shown that:

1. the load sharing between different combinations of hard-soft grains alters the distribution of hydrogen atoms. With using a bi-crystal model under a tensile load, it is shown that the hydrogen concentration within the hard grain peaks when the c-axis misorientation between the two crystals is 30° or 45°, depending on the applied load.

2. formation of a hydride within a single crystal zirconium induces a tensile hydrostatic stress field at the hydride tips and a compressive one along the hydride sides. This stress field enhances the diffusion of hydrogen atoms towards hydride tips while suppresses further diffusion towards hydride sides. Therefore, hydrides tend to grow axially.

3. harder single crystals develop higher tensile hydrostatic stresses and higher hydrogen concentration under a tensile load. This is shown numerically by rotating the c-axis of the zirconium single crystals with respect to the loading direction while embedding a hydride domain within the crystal.

4. intragranular hydrides tend to grow into harder grains under a uniaxial tensile loading condition. This was shown using a tri-crystal model with a hydride embedded in the middle grain. It was shown that under a tensile load, both tensile hydrostatic stress and hydrogen concentration are higher in the vicinity of the hydride tip in the harder grain.

5. for intergranular hydrides, the peak of hydrogen concentration takes place along the grain boundary, preferentially at the interface of the hydride with the harder grain. This suggests that intergranular hydrides are more likely to grow along the grain boundary as opposed to growing into the grains.

6. due to the stress field induced by twin shear strain, the concentration of hydrogen is much higher in the vicinity of twin tips, especially the ones that are near the grains having their c-axis aligned with the loading direction.

# Chapter 4

## 4 On the effects of texture and grain morphology on hydrogen transport towards notch tips: A CPFE study

Hydrogen embrittlement is an important degradation mechanism affecting the lifetime of engineering components. The diffusion of hydrogen atoms into the metal lattice can be affected by the localized stresses that develop around service-induced flaws. In addition, the magnitudes of flaw tip stresses are affected by the flaw geometry, as well as the texture and microstructure of the metal. Microstructural effects can be significant, particularly in metals such as zirconium with a high degree of elastic and plastic anisotropy. This study uses a coupled diffusion-crystal plasticity finite element approach to conduct a comprehensive study on the redistribution of hydrogen atoms in the vicinity of service-induced flaws in zirconium polycrystals. The effects of texture, grain size, and notch tip geometry on the concentration of hydrogen atoms in the lattice sites are investigated. The results indicate that material texture can significantly affect the distribution of hydrogen atoms as well as the location of maximum hydrostatic stress and maximum hydrogen concentration. The modelled highly textured microstructures have connected regions of peak hydrogen concentration. It is shown that as the notch tip becomes sharper, the effects of texture on the hydrogen localization near the notch becomes less significant. It is also shown that with changing grain orientations, it is possible to move the location of peak hydrogen concentration away from the notch tip.

## 4.1 Introduction

Due to their low neutron absorption cross section and good mechanical properties, zirconium (Zr) and its alloys are widely used in the core of various types of nuclear reactors. During service, the hot water coolant reacts with zirconium-alloy pressure tube and releases hydrogen (H) into the zirconium lattice. With time, hydrogen atoms diffuse to stress concentration sites and their mass concentrations increase and exceed the solid solubility limit of hydrogen in zirconium. This leads to the formation of a brittle phase known as zirconium hydride that reduces the fracture toughness of the alloy. Hydrogen diffusion is generally intensified in the vicinity of service induced flaws, e.g., scratches

caused by fuel bundle or debris fretting flaws. In addition, the stress field around the flaws is significantly affected by the texture and microstructure of the alloy as these alloys are mainly comprised of the hexagonal close packed (HCP) α-zirconium crystals with a high degree of elastic and plastic anisotropy. There is a lack of information on the interactive relationships of texture and microstructure with the stress fields around the flaw tip and their subsequent effects on hydrogen diffusion. This study focuses on addressing this knowledge gap through the use of a coupled hydrogen diffusion and crystal plasticity finite element model.

Different aspects of hydrogen transport and embrittlement have been addressed in the literature using experimental methods (Sung et al., 2017; Oudriss et al., 2012; 2012b). For instance, it is shown that the severity of embrittlement could be influenced by the state of stress and temperature (Singh et al., 2006; Courty et al., 2014). In addition, Desquines et al. (2014) and Raykar et al. (2012) showed that hydrogen concentration could influence the ductility and critical stress intensity factor of materials. Desquines et al. (2014) further reported that Zr specimens with 100 wt.ppm of hydrogen had the lowest ductility. Similarly, Wang et al. (2007) showed that the use of higher hydrogen concentration leads to a lower fracture stress. Formation of hydrides can impose significant strains within the microstructure, especially near stress risers such as notch tips (Kerr et al., 2009; Kerr et al., 2010; Shiman et al., 2018). Stress-assisted hydrogen transport towards a notch tip was studied by Gong et al. (2018) where both finite element (FE) numerical modeling and neutron radiography were used to calculate hydrogen concentration around the notch tip region. The notched samples in their study were exposed to thermo-mechanical loads to allow hydrogen to diffuse under an applied load. It was shown that the maximum hydrogen concentration does not occur exactly at the tip of the notch.

The formation of hydrides at the notch tip can trigger a process known as delayed hydride cracking (DHC). This process involves cracking of the hydride located at the notch tip and further diffusion of hydrogen towards the new crack tip which results in further hydrogen embrittlement and the repetition of this process. DHC velocity is controlled by the thermomechanical history of the material such as cooling rate from the reactor temperature. Kim et al. (2004), for instance, showed that the incubation time for DHC is affected by

both cooling rate and the notch tip radius, where the incubation time gradually increases with increasing the notch tip radius. Also, it was shown that the incubation time decreases with faster cooling rates. Texture is also shown to play an important role in hydrogen embrittlement of metals. For example, Kim (2006) showed that the threshold stress intensity factor for hydride formation ($K_{IH}$) depends on the texture of Zr-2.5Nb samples. Similarly, the effects of texture on $K_{IH}$ were discussed in the work by Soo Kim and Suk Kim (2000) where it was shown that by changing the texture from the commercial CANDU pressure tube to a radial texture tube, $K_{IH}$ can be increased by 70%. In later studies, Cui et al. (2009) and Shek et al. (2005) investigated the likelihood of a DHC initiation from service-induced flaws to determine the fitness of pressure tubes for continued service. Their results indicate that resistance to fracture depends on several parameters, including hydrogen concentration and the flaw geometry. In addition, the role of plasticity in predicting a DHC initiation was studied by Scarth and Smith (2002), where it was shown that DHC predictions could be overly conservative if plasticity is not taken into account.

Numerical methods are also used to investigate hydrogen transport towards notch tips. Studies on hydrogen diffusion are not confined to zirconium alloys, as many other types of steels, e.g., 304, 316L, 310S and nickel-based alloys are also susceptible to hydrogen embrittlement (Martínez-Pañeda et al., 2016). For example, Shi and Puls (1994) developed a numerical method to determine the relationship between bulk hydrogen concentration and $K_{IH}$ through critical hydride length calculation. It was reported that $K_{IH}$ increases as hydrogen concentration decreases. One of the numerical methods used for studying materials deformation at the grain scale is crystal plasticity finite element (CPFE), which has been used in many studies in the literature (Busso et al., 2000; Baudoin et al., 2019; Abdolvand et al., 2011; Sedaghat and Abdolvand, 2021; Abdolvand et al., 2020). CPFE can be coupled with damage models to study crack nucleation and propagation near notches (Abdolvand, 2022). This method can also be coupled with diffusion equations to study the effects of localized stresses on the diffusion of atoms such as hydrogen (Ilin et al., 2014). For instance, Tondro and Abdolvand (2021) used a coupled diffusion and CPFE approach to study stress-assisted hydrogen diffusion and its effects on hydride propagation. It was concluded that harder grain orientations have higher hydrogen concentration and therefore are more susceptible to hydride precipitation and propagation. In a similar study by Hussein

et al. (2021), distribution of hydrogen atoms was studied using an FEM based model coupled with diffusion. They showed that hydrostatic stress (HS) leads to depletion of hydrogen atoms from compressive to tensile regions, consistent with the results of another study by Hassan et al. (2019) using the same technique. Furthermore, hydrogen induced localized plasticity (HELP) was studied by Aslan (2015) where the relationship between distribution of hydrogen concentration with hydrostatic stress was investigated. Diffusion equations could also be incorporated into phase-field modeling to study stress-assisted diffusion of hydrogen atoms as well as hydrogen-assisted cracking (Martínez-Pañeda et al., 2018; Klinsmann et al., 2015; Duda et al., 2014). For instance, Duda et al. (2018) studied hydrogen-assisted cracking (HAC) by developing a brittle fracture model using a phase-field model for solids with interstitial solutes such as hydrogen. This model describes the mutual effects of solute migration and solute-assisted fracture.

Other numerical methods have also been used to understand the fundamentals of hydrogen transport. For instance, Yokobori et al. (1996) used a finite difference model to show that hydrogen accumulation increases with yield stress. There are several reports indicating that the concentration of hydrogen in the lattice ($C_L$) is proportional to hydrostatic stress (Dadfarnia et al., 2009; Di Leo and Anand, 2013). For instance, Wang et al. (2006) showed that the peak of hydrogen concentration in steel is increased with time, but eventually follows the trends observed for hydrostatic stress. It was also shown that critical hydrogen concentration not only depends on the strength of the base material, but also on the stress concentration factor. Similarly, in another study, Wang et al. (2016) showed that as the simulation time approaches that of the steady state condition, the location of the peak hydrogen concentration coincides with that of the hydrostatic stress. Another parameter affecting hydrogen embrittlement in metals is the loading condition. For instance, Kotake et al. (2008) used an elastoplastic model to study the effects of various loading conditions on hydrogen diffusion near a crack tip. It was shown that the concentration of hydrogen near the notch highly depends on the loading frequency and the loading time. In a later study, Kanayama et al. (2008) showed that increasing the loading time provides more time for the hydrogen atoms to diffuse and leads to higher values of hydrogen concentration at the notch tip. Sofronis and McMeeking (1989) also used a coupled diffusion and elastic-plastic FE model to investigate the underlying mechanism of hydrogen transport near a

blunting crack tip. It was shown that the amount of hydrogen residing at normal interstitial lattice sites (NILS) near the crack is very small compared to that of trapping sites such as dislocations and vacancies. Also, it was shown that hydrogen concentration in lattice increases with distance from the crack tip but reaches its maximum at the location where the hydrostatic stress peaks. In a later study, Krom et al. (1999) studied the effects of strain rate on hydrogen diffusion. It was shown that as the strain rate increases, hydrogen atoms tend to fill the trap sites while the lattice sites are emptied. The effects of dislocation densities on local hydrogen concentration was studied by Dadfarnia et al. (2014). It was concluded in their study that dislocations could help deliver hydrogen atoms to the fracture process zone at concentrations much higher than those delivered by lattice diffusion. On the other hand, Ayas et al. (2014) analyzed samples with different hydrogen concentrations and showed that the hydrogen concentration in lattice sites increases the susceptibility to hydrogen embrittlement while the hydrogen content of trapping sites have a negligible contribution.

The significant effects of grain-grain interactions as well as crystals elastic and plastic anisotropy are not explicitly accounted for in most of the numerical studies available in the literature. In addition, the coupled effects of materials texture, microstructure, and notch tip geometry are hardly examined using mesoscale models. In this study, the effects of such parameters on the development of stress fields, and their subsequent effects on the hydrogen transport near notch tips are studied in detail for the first time using a coupled diffusion (D)-CPFE approach. The contribution of each parameter on hydrogen transport is deconvoluted from the rest of the parameters, which allows us to determine when the effects of one parameter overcomes those from the rest of the parameters. Two types of notch geometries with various combinations of soft-hard grains as well as polycrystals with different grain shapes, sizes and textures are studied. This study aims to understand (a) the importance of anisotropy of zirconium crystals on hydrogen redistribution close to the notch tips and (b) the effects of grain morphologies on hydrogen diffusion. First, the implemented constitutive equations are described, followed by the results of the model for hydrogen concentration and the state of stress in the vicinity of the two notch tips. The effects of different parameters on hydrogen transport in the lattice are investigated and discussed.

## 4.2 Modeling

### 4.2.1 Crystal Plasticity Finite Element

A brief description of the D-CPFE model is provided here, and a comprehensive description can be found in Abdolvand (2019). In the following formulations, a bold font is used for tensors while vectors are denoted by using an arrow. The D-CPFE model developed by Abdolvand (2019) is used for numerical simulations. A User MATerial (UMAT) subroutine is coupled with a UMATHT subroutine to account for the stress-assisted diffusion of hydrogen atoms. The UMAT subroutine calculates the stress increment and updates solution dependent state variables based on the inputs provided by the FE solver, i.e., strain, rotation, time, and temperature increments. The total strain increment can be decomposed to

$$\Delta \varepsilon = \Delta \varepsilon^{el} + \Delta \varepsilon^{pl} + \Delta \varepsilon^{trH} \tag{4-1}$$

where $\Delta \varepsilon^{el}$ and $\Delta \varepsilon^{pl}$ respectively represent the increments of elastic strain, and the plastic strain resulting from crystallographic slip. $\Delta \varepsilon^{trH}$ is the strain induced by formation of hydrides which is set to zero in this study as no precipitation is allowed by assuming that the diffusion takes place at elevated temperatures, i.e., 330 °C which is the nominal operative temperature of nuclear reactors. A comprehensive study of the effects of this strain tensor on hydrogen diffusion and hydride formation is provided in Tondro and Abdolvand (2021).

For calculating the plastic strain increment, the plastic part of deformation rate ($\boldsymbol{D}^{pl}$) is integrated over each time increment, i.e.:

$$\dot{\varepsilon}^{pl} = \boldsymbol{D}^{pl} = \sum_{\alpha=1}^{N^{spl}} \boldsymbol{P}^{\alpha} \dot{\gamma}^{\alpha} \tag{4-2}$$

$$\boldsymbol{P}^{\alpha} = sym(\boldsymbol{S}^{\alpha}) \; where \; \boldsymbol{S}^{\alpha} = \vec{d}^{\alpha} \otimes \vec{n}^{\alpha}$$

where $\boldsymbol{P}^{\alpha}$ is the symmetric part of the Schmid tensor ($\boldsymbol{S}^{\alpha}$). In this equation, $\dot{\gamma}^{\alpha}, \vec{d}^{\alpha}$ and $\vec{n}^{\alpha}$ are respectively the shear rate, slip direction and normal to the slip plane for the slip system $\alpha$. The following equation is used to calculate shear rates:

$$\dot{\gamma}^\alpha = \dot{\gamma}_0 \left| \frac{\tau^\alpha}{g^\alpha} \right|^n sign \left( \frac{\tau^\alpha}{g^\alpha} \right) \tag{4-3}$$

where $\dot{\gamma}_0$ is a reference shear strain rate and $n$ controls the rate dependency. $\tau^\alpha$ and $g^\alpha$ are respectively the resolved shear stress and the strength of slip system $\alpha$. An extended Voce hardening law is used for $g^\alpha$:

$$g^\alpha = g_0^\alpha + (g_1^\alpha + \theta_1^\alpha \Gamma) \left( 1 - exp \left( -\frac{\theta_0^\alpha \Gamma}{g_1^\alpha} \right) \right) \tag{4-4}$$

where $g^\alpha$ and $g_0^\alpha$ are the current and initial critical resolved shear stress (CRSS). $\Gamma$ is the shear accumulated on all slip systems, $\theta_0^\alpha$ is the initial hardening rate, and $g_1^\alpha$ and $\theta_1^\alpha$ determine the asymptotic characteristics of hardening.

The resolved shear stress used in Eq. 4-3 is proportional to the Kirchhoff stress ($\boldsymbol{\Psi}$) through (Peirce et al. (1983)):

$$\tau^\alpha = \boldsymbol{P}^\alpha \colon \boldsymbol{\Psi} \tag{4-5}$$

The Jaumann rate of Kirchhoff stress ($\breve{\boldsymbol{\Psi}}$) correlates with the elastic part of the deformation rate tensor ($\boldsymbol{D}^{el}$) and the elastic stiffness tensor ($\mathbb{C}$) through the following equation:

$$\breve{\boldsymbol{\Psi}} = \mathbb{C} \colon \boldsymbol{D}^{el} \ where \ \breve{\boldsymbol{\Psi}} = \dot{\boldsymbol{\Psi}} - \boldsymbol{\Omega}^{el} \boldsymbol{\Psi} + \boldsymbol{\Psi} \boldsymbol{\Omega}^{el} \tag{4-6}$$

where $\boldsymbol{\Omega}^{el}$ is the elastic part of the spin tensor which can be calculated by subtracting the provided total spin tensor from the FE solver and the plastic part of the spin tenor.

## 4.2.2 Stress-assisted hydrogen diffusion

In this section, the diffusion equations that are coupled with the CPFE model for simulating stress-assisted diffusion of hydrogen atoms are presented. The flux of hydrogen atoms ($\vec{J}$) within the lattice of zirconium depends on the concentration (C) and the velocity of hydrogen atoms ($\vec{v}$):

$$\vec{J} = \vec{v}C \tag{4-7}$$

The velocity of hydrogen is proportional to its mobility ($\boldsymbol{M}$) and the gradient of the chemical potential ($\mu$) through the following equations:

$$\vec{v} = -\boldsymbol{M}\vec{\nabla}\mu \tag{4-8}$$

$$\boldsymbol{M} = \frac{\boldsymbol{D}}{RT} \ where \ \boldsymbol{D} = \begin{bmatrix} D_a & & \\ & D_a & \\ & & D_c \end{bmatrix} \tag{4-9}$$

where R is the universal gas constant, $\mu$ is the chemical potential of hydrogen in zirconium, $\boldsymbol{D}$ is the diffusivity tensor in the crystal coordinate system, and T is the absolute temperature ($K$). As reported in Zhang et al. (2017), the diffusivity of hydrogen atoms in the zirconium lattice varies along the HCP crystal a-axis and c-axis and depends on temperature:

$$D_c = 1.08 \exp\left(-\frac{0.46}{8.6 \times 10^{-5}T}\right)$$
$$D_a = D_c(-3.3 \times 10^{-7}T^2 + 7 \times 10^{-4}T + 0.8298)^{-1} \tag{4-10}$$

in which diffusivities are in units of mm/s$^2$. The chemical potential of the diffusing hydrogen can be written as:

$$\mu = \mu_0 + RTlnC - \frac{\sigma_{kk}}{3}\bar{V}_H \tag{4-11}$$

where $\mu_0$ is the reference chemical potential, $\frac{\sigma_{kk}}{3}$ represents the hydrostatic stress, and $\bar{V}_H$ is the partial molar volume of hydrogen atoms in the Zr lattice which is 1670 mm$^3$/mol. In this work, a constant reference chemical potential is used in all the simulations and the variation of initial chemical potential at the grain boundaries is disregarded.

Combining Eqs. 4-8, -9 and -11, the equation for hydrogen flux can be rewritten as:

$$\vec{J} = -\boldsymbol{D} \left[ \vec{\nabla} C + C lnC \frac{\vec{\nabla}T}{T} - C \frac{\bar{V}_H}{3RT} \vec{\nabla}\sigma_{kk} \right] \tag{4-12}$$

in which $\frac{\vec{\nabla}\sigma_{kk}}{3}$ represents the gradient of hydrostatic stress. It can be seen that stress affects the diffusion equations by contributing to the chemical potential (Xie et al., 2020; Singh and Pal, 2020). According to Eq. 4-12, the three parameters affecting mass flux are the gradient of mass concentration, the gradient of temperature (known as temperature-driven diffusion), and the gradient of hydrostatic stress (known as stress-assisted diffusion). When diffusion happens under constant temperature, the second term on the right-hand side of Eq. 4-12 will be zero. Since we are focusing on stress and diffusion fields a in few micrometers around the notch tips, temperature gradients can be considered negligible, i.e., we solve for the isothermal case where $\vec{\nabla}T = 0$.

The general form of diffusion equation derived from a control volume can be written as:

$$\frac{\partial C}{\partial t} = -\nabla.\vec{J} \tag{4-13}$$

In a steady state problem, the derivative of concentration with respect to time will be zero. Hence, the spatial derivative of hydrogen flux will be also zero and the gradient of concentration will subsequently correlate with the hydrostatic stress and its gradients.

Eqs. 4-12 and 4-13 are very similar to the conductive heat transfer equations used for calculating temperature distribution in the presence of heat sinks and sources. In the Abaqus FE solver, UMATHT can be used for modeling coupled temperature-displacement problems, so by replacing the temperature with concentration (C), this subroutine can be used for coupled diffusion-displacement problems. Following the method discussed in Abdolvand (2019), Eqs 4-9 to 4-13 are implemented in a UMATHT subroutine to solve for hydrogen concentration.

It should be noted that the concentration of hydrogen in the zirconium lattice ($C_L$) is calculated in Eq. 4-13. The total hydrogen concentration ($C_H$) can be decomposed to hydrogen concentration at normal lattice sites ($C_L$) and that at trapping sites ($C_T$) (Oriani,

1970; Taha and Sofronis, 2001). $C_T$ generally depends on the density and distribution of crystal defects, e.g., dislocations or vacancies. In this study, only the hydrogen concentration in the normal lattice sites is calculated, and the contribution of dislocations to $C_T$ is discussed in section 4.4.5.

The gradient of hydrostatic stress used in Eq. 4-12 is derived using the element shape function through the following equation:

$$\frac{\sigma_{kk}}{3} = \sum_{a=1}^{a=no.IPs} N^a \, \sigma_{kk}^a$$

$$\vec{\nabla}\sigma_{kk} = \frac{\partial \sigma_{kk}}{\partial x_i} = \sum_{a=1}^{a=no.IPs} \frac{\partial N^a}{\partial x_i} \sigma_{kk}^a$$

(4-14)

where $N^a$ is the shape function of an element with "$a$" number of integration points (IPs). The details of the implemented formulation for calculating the spatial gradients of hydrostatic stress are presented in Abdolvand (2019).

To summarize, the total strain and time increments provided by Abaqus (2020) at the beginning of each time increment are used to calculate the stress increment using Eqs. 4-1 to 4-6. The updated stress matrix at each IP is then used to calculate hydrostatic stress, and with the use of current coordinates of the same IP, the gradients of hydrostatic stress are calculated (Eq. 4-14). The calculated $\vec{\nabla}\sigma_{kk}$ is subsequently sent to UMATHT to calculate hydrogen concentration using Eqs. 4-12 and 4-13.

## 4.2.3 Input models

### 4.2.3.1 Macroscopic setup and notch tip geometry

Three point bending of notched curved specimens cut from nuclear pressure tubes is one of the most common configurations used for characterizing hydrogen embrittlement and studying failure mechanisms of zirconium alloys. Here, a three-point bending setup similar to the experimental setup reported in Cui et al. (2009) is used for D-CPFE modeling. This setup is shown in Fig. 4-1a. The dimensions of the curved specimen represent the actual

dimensions of a typical CANDU Zr-2.5Nb pressure tube and the boundary conditions (BC) used are representative of a typical 3-point bending experiment. The specimen is deformed by applying an external displacement while the stress and hydrogen concentration fields in the vicinity of the notch tip area are studied (Fig. 4-1a). The applied mesh to the model is shown in Fig. 4-1a. The width of the sample along the Z-axis (AB in Fig. 4-1a) is 6 mm. Other dimensions are shown in Fig. 4-1b. The macroscopic setup as well as the mechanical and mass diffusion boundary conditions are the same for all the input models, all of which are shown in Fig. 4-1a-c. In this figure, $C$ represents hydrogen mass concentration in the zirconium lattice in wt.ppm and $U_i$ represents displacement BCs along the $i^{th}$ direction where i=1, 2, and 3 represent the global X, Y, and Z-axis shown in Fig. 4-1a.

In all simulations presented in this work, the temperature of the model is kept at 603K to replicate the in-reactor condition while preventing any hydride precipitation. The surface on the outer diameter of the tube, far away from the notch tip, is kept at 100 wt.ppm throughout the simulation. This is the only, and necessary, diffusion boundary condition applied to the model. This surface is chosen because we focus on how the state of stress affects the uniform distribution of hydrogen atoms when hydrogen atoms are constantly supplied to the matrix. The choice of 100 wt.ppm is because the solubility limit of hydrogen in zirconium lattice at the operative temperature of nuclear reactors (~330° C) is about 100 wt.ppm. The specimen is modelled as a 3D deformable part. The properties of HCP zirconium crystals used in this study are the single crystal properties of the HCP α-phase of Zr-2.5Nb reported in Cai et al. (2009), the summary of which is listed in Table 4-1. The use of crystal parameters presented in Table 4-1 results in a very low strain hardening. Further, the effects of hydrogen concentration on the mechanical properties of the metal alloy are not considered here because the probability of hydride formation at high temperatures, e.g., 603 K in this study, is quite low. The terminal solid solubility limit for precipitation of hydrides in zirconium is almost 220 wt.ppm at this temperature, which is much higher than the concentration of hydrogen in our case studies, i.e., 100 wt.ppm. Also, at such temperatures, the mechanical properties of zirconium alloys are very weakly affected by the hydrogen content (Tung et al., 2016). For the sake of simplicity, the effects of the cubic β-phase are ignored as the volume fraction of this phase is low (Aldridge and Cheadle, 1972; Fong, 2013). The elastic moduli of the single crystal zirconium used here

are the ones determined by Fisher and Renken (1964): $C_{11}$=143.5 GPa, $C_{33}$=164.9 GPa, $C_{12}$=72.5 GPa, $C_{13}$=65.4 GPa, and $C_{44}$=32.1 GPa.

**Table 4-1 - The single crystal parameters used for Zr-2.5Nb (Cai et al., 2009)**

| Slip system | n | $\dot{\gamma}_0(s^{-1})$ | $g_0^\alpha$(GPa) | $g_1^\alpha$(GPa) | $\theta_0^\alpha$(MPa) | $\theta_1^\alpha$(GPa) |
|---|---|---|---|---|---|---|
| Prism | 20 | $3.5 \times 10$-4 | 0.12 | 0.001 | 10 | 0.05 |
| Basal | 20 | $3.5 \times 10$-4 | 0.15 | 0.001 | 10 | 0.05 |
| Pyramidal <c+a> | 20 | $1.0 \times 10$-4 | 0.3 | 0.001 | 10 | 0.2 |

The elements used for meshing the model are second order coupled "displacement-concentration" brick elements (C3D20RT). The sample is meshed using ~80k elements. The region near the notch tip is densely meshed while a coarser mesh is used for the areas further away from the notch (Fig. 4-1a).

Two types of blunt 45-degree notch geometries are used here which are referred to as "U-notch" and "V-notch" models. The geometry and dimensions of the notches are shown in Fig. 4-1d and e. For the rest of this chapter, the model names starting with "U" and "V" refer to the notch shapes in the corresponding model. The radius used for the notch tip in the U model is 15µm and is the one reported in the experiment by Cui et al. (2009), but the one used for the V-notch is 2 µm, and is only to show the effects of notch tip sharpness on the stress and hydrogen distributions.

a.

b.

41.8 mm

R 103.4 mm

Notched area

W = 4.1 mm

Y (RD)

X (TD)

External displacement
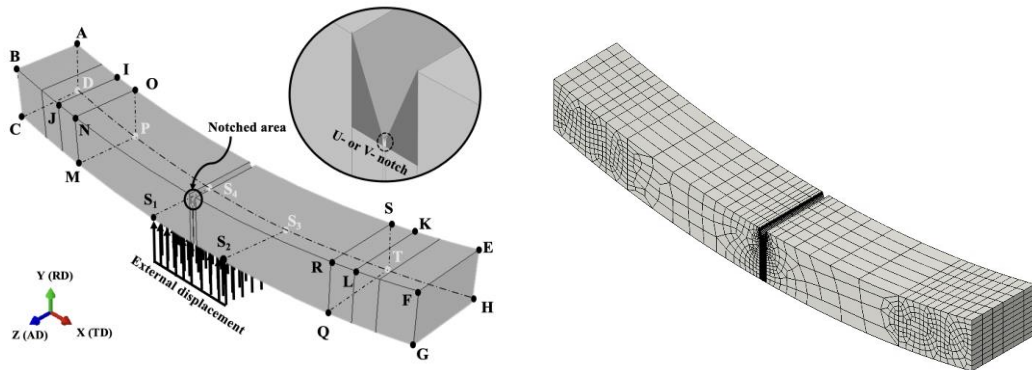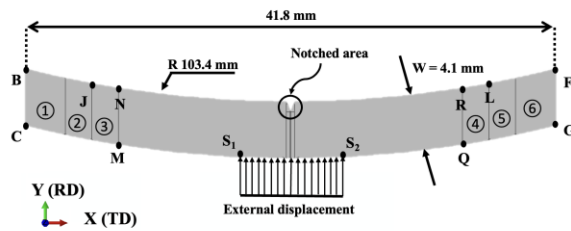
c.

**Mechanical & Mass Diffusion Boundary Conditions**

$U_3^{CG} = 0$

$U_1^{GH} = 0$

$U_2^{IJ} = U_3^{IJ} = U_2^{KL} = U_3^{KL} = 0$

$C_0^{model} = 100 \, wt.ppm$

$C^{CDHG} = 100 \, wt.ppm$

d.

45°

Notch depth = 750 μm

Notch radius=15μm

U-notch

e.

45°

Notch depth = ~765 μm

V-notch

Notch radius=2μm
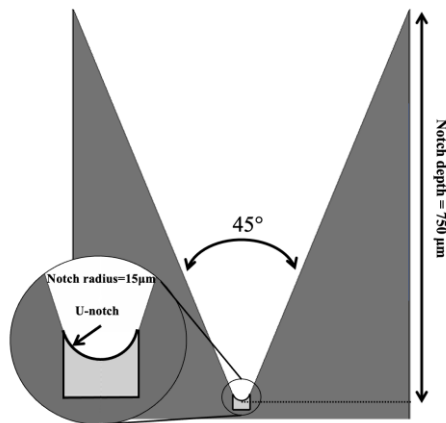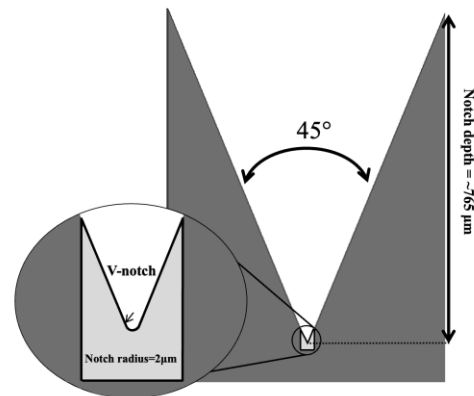
**Fig. 4-1 – (a) An isometric view and mesh discretization of the model. White letters are used for points on the back side of the specimen. (b) The front view (X-Y plane) of the model. (c) The mechanical and mass diffusion boundary conditions used in the model. The notch tip geometries used in (d) the U-notch, and (e) the V-notch models. The regions with light grey colors are the regions of interests where grain morphologies and microstructures are assigned. Grain morphologies and microstructures are shown in Fig. 4-2.**

In all the models presented below, the orientations of c-axis of all elements outside the notch tip region are set parallel to the global X-axis, except the ones in the vicinity of the notch tip (see below). This is to be consistent with the texture measured for CANDU pressure tubes (Cai et al., 2009), where the crystals c-axes are mainly parallel to the transverse direction (TD), which coincides with the global X-axis at the center of Fig. 4-1a. It should be noted that the crystal orientations outside the notch tip region do not follow the curvature of the specimen. In addition, this setup enforces that the variations observed in the results are only due to the changes made to the notches or to the microstructure around the notch. Unless otherwise stated, all models are deformed by the external displacement ($\Delta Y_{external}$) set to 42µm, using the quasi-static displacement rate of $0.19 \frac{\mu m}{s}$. All simulations are conducted in one diffusion-displacement step, and it is assumed that hydrogen diffusion has reached its steady state condition. The state of stress and hydrogen concentration field at the tip of the notch are investigated at the end of the simulation step.

## 4.2.3.2 Microstructure models

Throughout this chapter, various microstructure configurations near the notch tips are numerically studied in detail. The main goal here is to separate and characterize the contribution of microstructure to hydrogen diffusion from that of notch geometry. For this purpose, the notch tips of both U-notch and V-notch models are partitioned with different grain geometries that represent different textures. Each model examines the effects of one of the contributing parameters, i.e., grain geometry, texture, and grain size. Fig. 4-2a-h show the different microstructures assigned to U- and V-notched models. The region of interest (ROI) where individual grains are partitioned and assigned is 30µm along X, and depending on the notch tip, it is approximately 30µm along the Y-axis for U-notch models and 45µm for V-notch models. This is 3x the size of the biggest notch radius, where most of the stress concentrations take place. We start with the simplest case where a single crystal (SC) is assigned to the entire ROI (Fig. 4-2a and e) partition. The orientation is changed to study its effects on the distribution of stress and hydrogen fields around the notch tip (section 4.3.1). This is followed by assigning two grain orientations to the ROI to replicate a bi-crystal (BC) model (Fig. 4-2b and f) where the "grain size" is half that of the SC model. To separate the effects of grain geometry from those of texture, two types of

71

polycrystals are studied in this chapter; one with equiaxed hexagonal grains (Fig. 4-2c and g) and another with elongated rectangular grains (Fig. 4-2d and h). The hexagonal grains are to represent "equiaxed" polycrystalline grains and are to study the effects of triple points and their contribution to stress and hydrogen concentration. These models are addressed as "Poly" in the rest of this chapter (see Fig. 4-2i). The rectangular grains are to "resemble" the microstructure of CANDU pressure tube. Since pressure tubes are manufactured by extrusion, grains are elongated in the axial direction (Z-axis) and are much smaller in the transverse-radial surface (X-Y plane). The average grain size in pressure tubes is observed to be about 1µm x 4µm along the radial and transverse directions of the tube, respectively (Judge et al., 2017), hence, the same dimensions are assigned to the rectangular grains on the X-Y plane (see Fig. 4-2k). Models with rectangular grains are called "Rec" in the rest of this chapter. The size of the hexagonal grains in Polys is decided to be 1µm- to be consistent with the smallest dimension of the rectangular grains. In all models, grains are fully extruded along the Z-axis. That is, while the plasticity is modelled in 3D, the microstructure is modelled in quasi-3D such that all grain boundaries are extruded in the Z-direction. Mesh discretization and size for the Poly and Rec models are respectively shown in Fig. 4-2i-l. Table 4-2 provides a summary of the input models and their associated microstructure (shown in Fig. 4-2) assigned to the notch tip. The names SC, BC, Poly and Rec assigned to each model refer to single crystal, bi-crystal, polycrystals with hexagonal and rectangular-grain polycrystals, respectively. U and V refer to the notch shape geometry. It should be noted that the Euler angles defined in Table 4-2 follow the Bunge convention for $\varphi_1, \varphi,$ and $\varphi_2$ with crystals rotating respectively about Z, X, and Z axes.
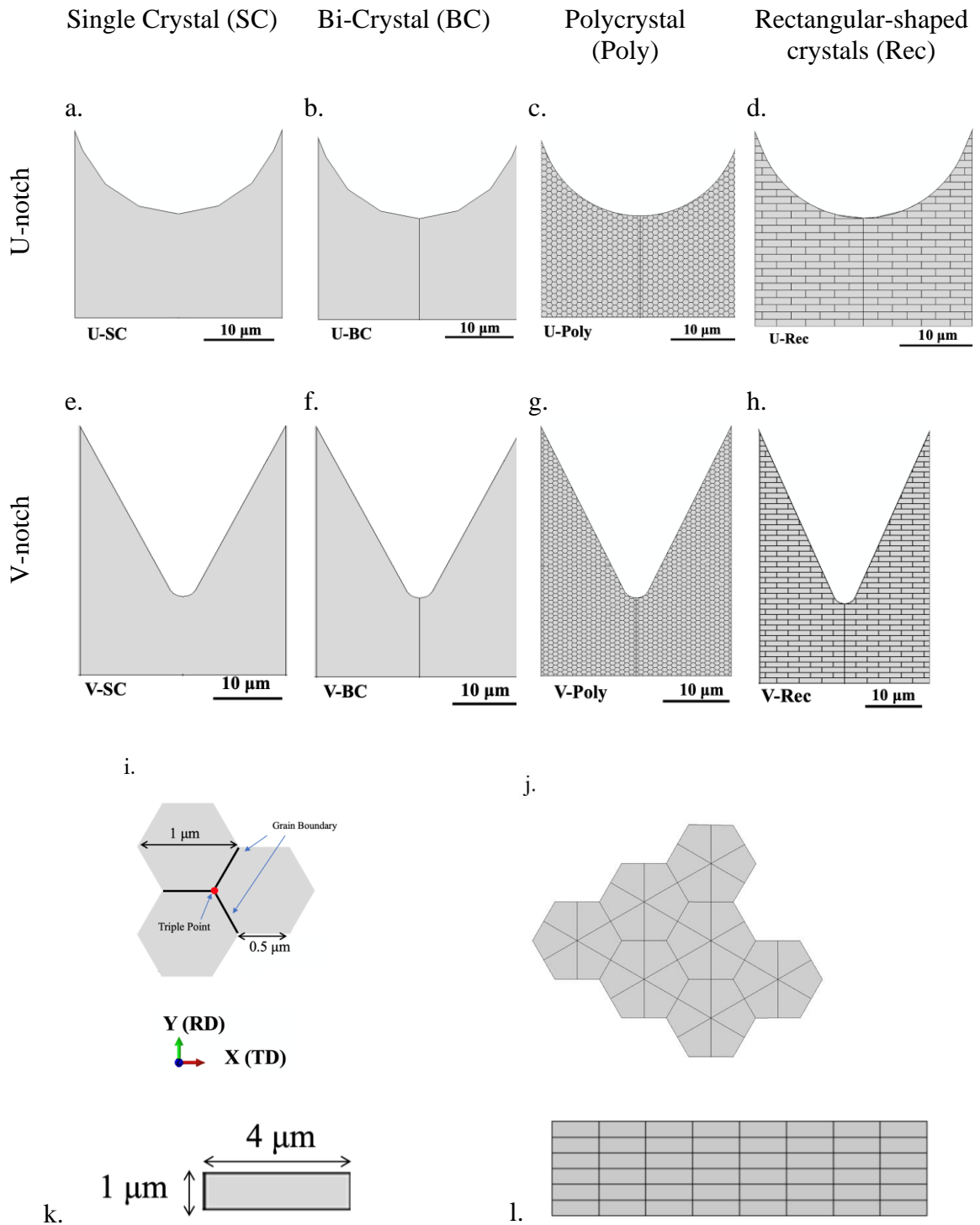
**Fig. 4-2 – The configurations of notch tips described in Table 4-2 for (a) U-SC, (b) U-BC, (c) U-Poly, (d) U-Rec, (e) V-SC, (f) V-BC, (g) V-Poly and (h) V-Rec models. Dimensions of (i) hexagonal-shaped grains and (k) rectangular-shaped grains. All grains are extruded through the sample thickness. Mesh discretization for hexagonal-shaped grains and rectangular-shaped grains are shown respectively in (j) and (l).**

**Table 4-2 - Model setup for studying hydrogen transport towards the notch tips**

| Model name | Notch shape | Number of grains at the notch tip | Notch tip texture / Euler angles of grain(s) |
|---|---|---|---|
| U-SC-1 | U | 1 | (90 90 0) |
| U-SC-2 | U | 1 | (45 90 0) |
| U-BC-1 | U | 2 | (90 90 0) & (45 90 0) |
| U-BC-2 | U | 2 | (0 90 0) & (45 90 0) |
| U-Poly-R | U | 945 | Random texture |
| U-Poly-T | U | 945 | Textured along X (TD) |
| U-Poly-T* | U | 117 | Textured along X (TD) |
| U-Rec-R | U | 172 | Random texture |
| U-Rec-T | U | 172 | Textured along X (TD) |
| V-SC-1 | V | 1 | (90 90 0) |
| V-SC-2 | V | 1 | (45 90 0) |
| V-BC-1 | V | 2 | (90 90 0) & (45 90 0) |
| V-Poly-R | V | 1565 | Random texture |
| V-Poly-T | V | 1565 | Textured along X (TD) |
| V-Rec-T | V | 320 | Textured along X (TD) |

The (0002) pole figure of the models with "random texture", mentioned in Table 4-2, is shown in Fig. 4-3a. For the "textured" models, on the other hand, the measured texture of CANDU pressure tube shown in Fig. 4-3b is used, i.e., the c-axis of most of the grains are

oriented towards the transverse direction (X-axis) (Holt and Zhao, 2004; Vicente Alvarez et al., 2012; Holt and Aldridge, 1985).

a.                                                      b.
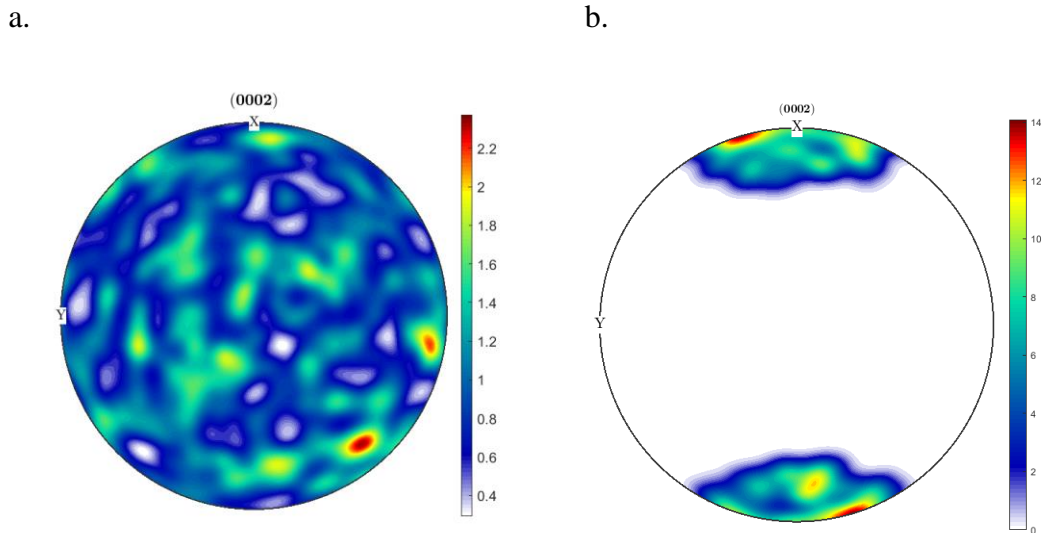


**Fig. 4-3 – The pole figures of the notch tip microstructures for (a) "random texture" and (b) "textured" models.**

## 4.3 Results

The results of the U-models are presented first, starting from the SC models, followed by the BC, Poly, and Rec models. Then, a comparison between different configurations in the ROI of the U- and V-notches is presented. It should be noted that all the results presented in this work are for the surface of the specimen, with HCP schematics showing grain orientations before any deformation is applied.

## 4.3.1 Single Crystals

The results of the single crystal models for the ROI of the U-notched specimen are presented in this section. The orientation of the HCP crystal used for each model is schematically shown. Fig. 4-4 shows the distribution of hydrogen concentration and hydrostatic stress for models U-SC-1 and U-SC-2.
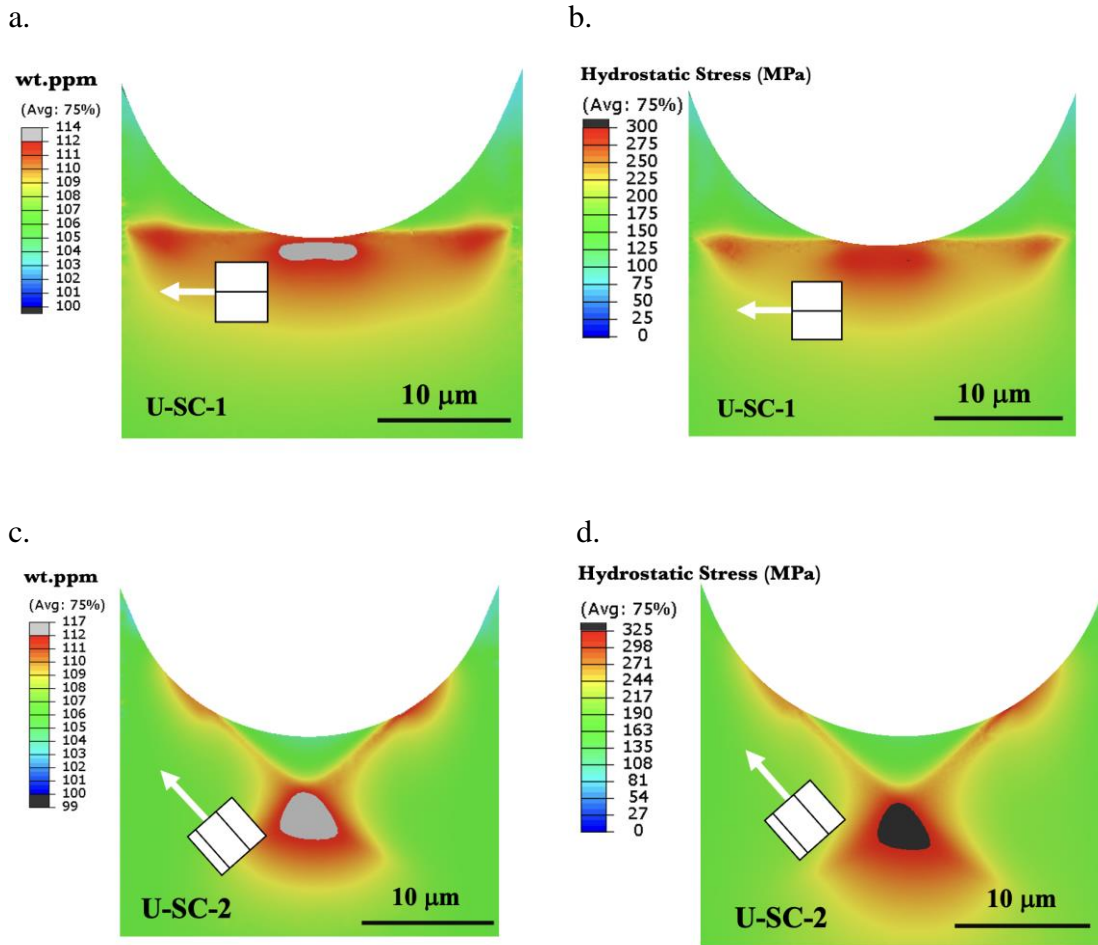
**Fig. 4-4 – The distributions of (a, c) hydrogen concentration, and (b, d) hydrostatic stress near the notch tips of the single crystal models. The schematic of grain orientation is provided in each figure. The distributions are for $\Delta Y_{external} = 42$ μm.**

The distributions of hydrogen concentration and hydrostatic stress for models U-SC-1 and U-SC-2 show that the crystal orientation significantly alters the location of peak hydrogen concentration. For U-SC-1, it is very close to the notch tip while for U-SC-2, it is further away from the notch tip. This is interesting as the texture of extruded tubes are generally close to U-SC-1, indicating that their susceptibility to hydride formation is higher. This happens when the crystal c-axis is along the X direction- comparing to the case where the c-axis is at an angle with the X-axis, e.g., U-SC-2. Hence, hydride nucleation sites will be closer to notch tip for U-SC-1 in comparison to U-SC-2. In addition, the shapes of the two different hydrogen fields are different, where in U-SC-2 an "X" type distribution is

observed, but in both models, the direction of maximum hydrogen concentration follows the crystal c-axis due to the activation of different slip modes. In U-SC-1, most of the plastic deformation at the notch tip is accommodated by the pyramidal $\langle c+a \rangle$ slip system whereas in U-SC-2 both basal and prism $\langle a \rangle$ slip systems are active.

## 4.3.2 Bi-crystal models

A combination of the two single crystals presented in the previous section is studied here. The results for hydrogen concentration and hydrostatic stress for U-BC-1 are shown in Fig. 4-5a and b. It can be seen that the grain orientation and grain-grain interaction change the location of the peak hydrogen concentration. For this model, the grain-grain interaction pushed the peak of hydrogen concentration to take place right at the notch tip and in the left grain which is oriented towards the X-axis. In the right grain, on the other hand, the hydrogen concentration peaks in the grain interior, away from the notch tip. In fact, there is a depletion of hydrogen atoms at the notch tip in the right grain. Similar to the single crystal cases, the direction of maximum hydrogen concentration in both crystals follows the crystal c-axis. The same trend is calculated for the distribution of hydrostatic stress as well.

The model U-BC-1 is an extreme case of grain orientations at the notch tips of a CANDU pressure tube where grains are oriented towards TD (X-axis) with a minor population of grains rotated away from TD towards RD (Y-axis). This model indicates that peaks of hydrogen concentration take place right at the notch tip within the grains oriented towards the X-axis. This is consistent with many experimental observations of hydride nucleation in notched CANDU pressure tube specimens (Allen et al., 2012; Sagat et al., 1994; Cui et al., 2009).
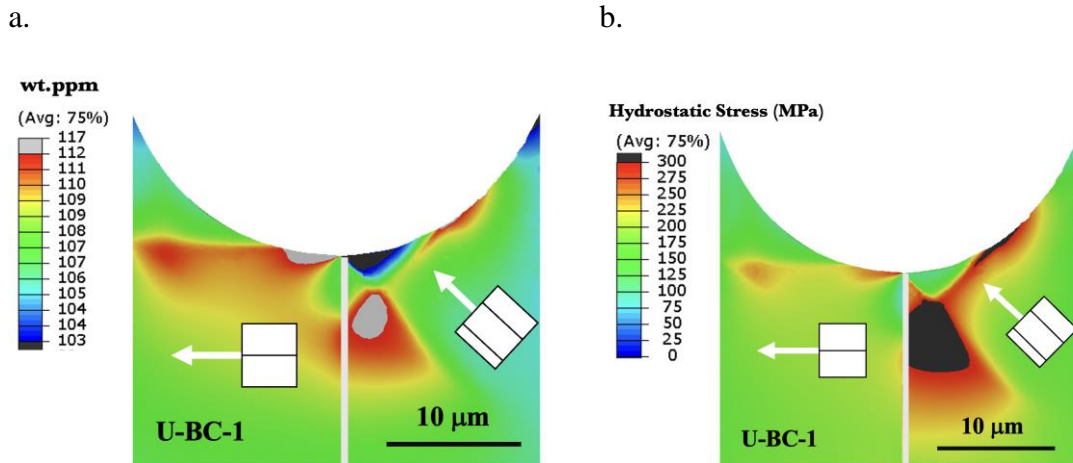
**Fig. 4-5 – (a) The distribution of hydrogen and (b) hydrostatic stress fields at the notch tip region of model U-BC-1. Results are for $\Delta Y_{external} = 42$ μm.**

U-BC-2 is another hypothetical bi-crystal model studied here in which the left grain of the model U-BC-1 is rotated such that the c-axis of the HCP crystal coincides with the Y-axis. The results for hydrogen concentration as well as hydrostatic stress for this model are presented in Fig. 4-6a and b, respectively. The comparison of the hydrogen concentration at the notch tips of model U-BC-1 and U-BC-2 reveals that this concentration is higher in the grain with its c-axis aligned with the loading direction (see Fig. 4-6a). The gradient of hydrogen concentration along the crystal c-axis is also higher in this grain. The same color bar is used for both models to provide a better comparison.
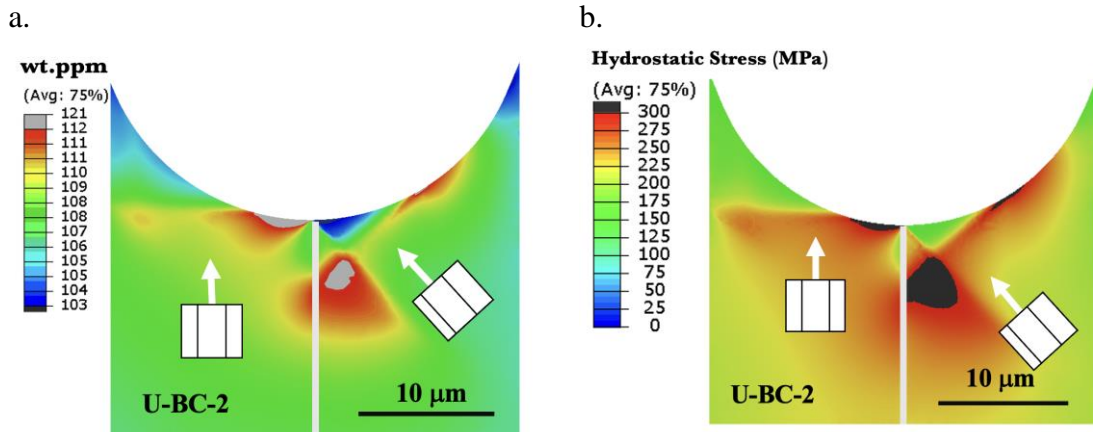
**Fig. 4-6 – The distributions of (a) hydrogen concentration and (b) hydrostatics stress at the notch tip of model U-BC-2. Results are for $\Delta Y_{external}$ = 42 µm.**

## 4.3.3 Polycrystals: hexagonal grains

Fig. 4-7a shows the distribution of hydrogen atoms in the ROI of U-Poly-R model. As shown in Table 4-2, a random texture is assigned to the 945 hexagonal grains located in the ROI. A comparison of this model and U-Poly-T is presented in section 4.4.1. The area A1 is magnified for a more detailed investigation of hydrogen concentration. It can be seen that hydrogen atoms "preferentially" diffuse to specific grains in the ROI, as well as to grain boundaries and triple points. This is in agreement with experimental observations on Zircaloy-4 (Kiran Kumar et al., 2010). In addition, a few hydrogen depletion sites can be seen at some of the triple points. The location of maximum and minimum hydrogen concentration in combination with hydride induced transformation strain ($\Delta\varepsilon^{trH}$) might explain the trajectory of the hydrides forming at notch tips (see section 4.4.1.1).

The analysis of the results reveals that the frequency of hydrogen concentration peaks is the highest along the dashed arrow shown in Fig. 4-7a. These grains are closer to the middle part of the ROI and are shown with the black circle A2. This is interesting because in agreement with the results of U-SC-2, the peak of hydrogen concentration does not exactly take place at the notch tip.

Our analysis does not reveal any distinct or general relationship between the locations of maximum or minimum hydrogen concentration with grain orientation or grain

neighborhood; however, these peaks take place at specific sites, depending on both the interaction of the surrounding grains as well as orientation of each grain with respect to the loading direction.

The results presented in this section agree with the results of Díaz et al. (2017). They carried out FE simulations of stress-assisted diffusion and concluded that hydrogen is concentrated at the sites where hydrostatic stress is high. Also, in the numerical study conducted by Hussein et al. (2021), it was shown that the peaks of hydrogen concentration take place at the triple points and grain boundaries. In addition, Mani Krishna et al. (2006) used transmission electron microscopy (TEM) and electron backscatter diffraction (EBSD) and showed that hydrides in Zircaloy-2 predominantly form at the grain boundaries. The contribution of different parameters in the formation of hydrides within the microstructure was quantified, especially at the grain boundaries. This was also supported in another experimental study on hydrogen embrittlement of Zr-Nb alloys with different Nb content (Oh et al., 2010).

a.                                                          b.
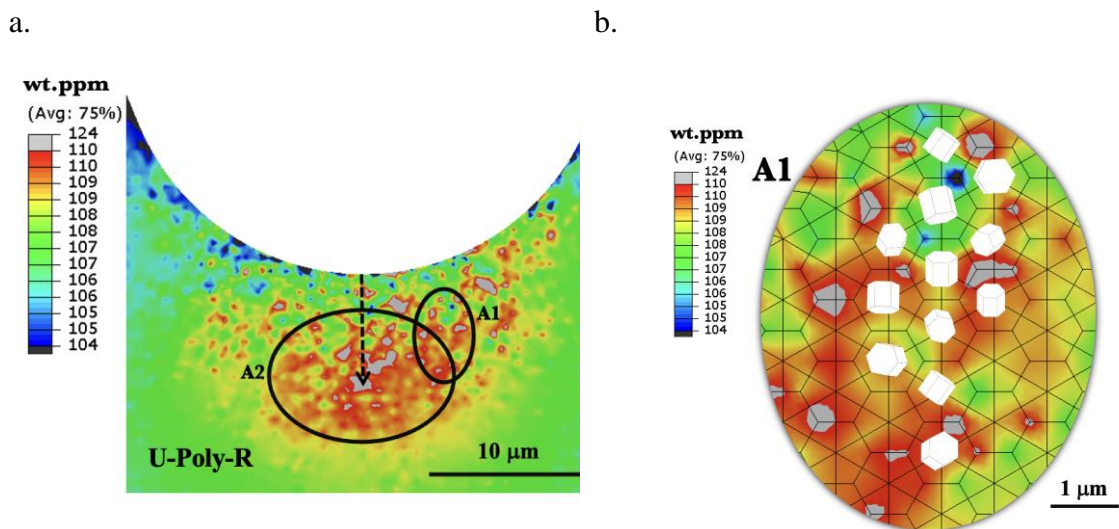


**Fig. 4-7 – (a) The distribution of hydrogen at the notch tip of U-Poly-R model. (b) The enlarged area A1 with overlaid grain orientations. Results are for $\Delta Y_{external} = 42$ μm.**

## 4.3.4 V-notch vs. U-notch models

Service-induced flaws can have different shapes and geometries. Two different notch shapes, V- and U-notches, and their effects on the process of hydrogen transport are

investigated in this section. Comparisons are made between single crystals, bi-crystals, hexagonal-grain, and rectangular-grain polycrystals.

## 4.3.4.1 Single and bi-crystal models

The effects of notch shape on hydrogen diffusion in single and bi-crystal models are discussed in this section. The results for hydrogen concentration in the ROIs of models U-SC-2 and V-SC-2 after 30 µm of $\Delta Y_{external}$ are shown in Fig. 4-8a and b. The color scales are nearly the same in both plots to enable visual comparison. Due to having a higher hydrostatic stress and steeper gradients near the notch tip, hydrogen atoms are more concentrated at the tip of the notch with a smaller radius.
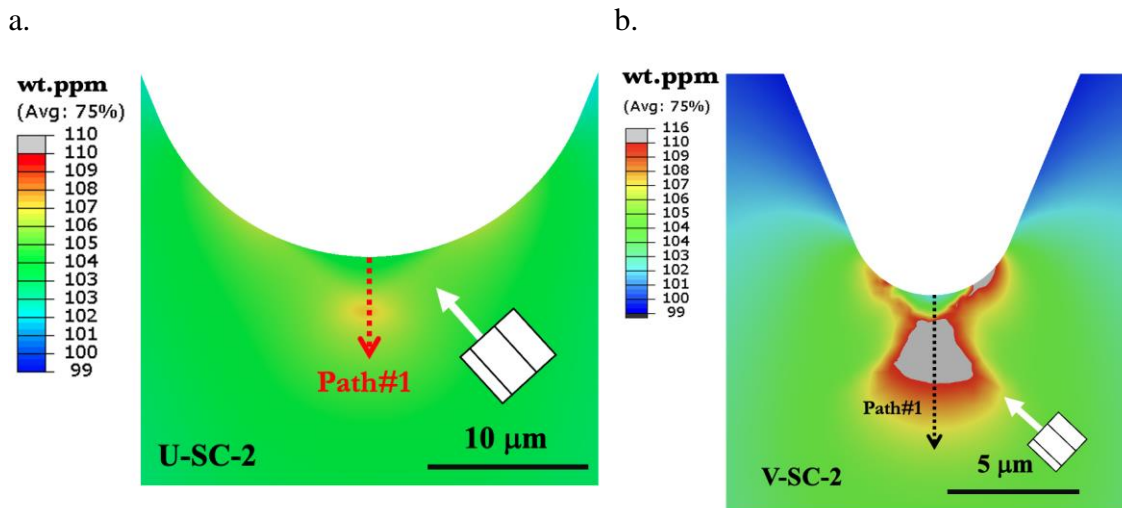


**Fig. 4-8 – The distribution of hydrogen atoms at the notch tips of (a) U-SC-2 and (b) V-SC-2 models. Grain orientations are shown schematically. Results are for $\Delta Y_{external} = 30$ µm.**

The hydrogen concentration fields for U-SC-1 and V-SC-1 models are respectively shown in Fig. 4-9a and b where a higher hydrogen concentration in the V-notch model is observed. The peaks of hydrogen concentration are much closer to the notch tip comparing to those shown in Fig. 4-8. Path#1 is introduced to compare the results presented. This path is shown in both Fig. 4-9 and Fig. 4-8. Distributions of hydrogen atoms along Path#1 for U-SC-1 and U-SC-2 models are plotted in Fig. 4-9c, where it is shown that hydrogen concentration uniformly decreases in U-SC-1, whereas in U-SC-2, it peaks at a distance

from the notch tip. Similarly, the hydrogen concentrations for models V-SC-1 and -2 along Path#1 are plotted in Fig. 4-9d. It can be seen that the maximum of hydrogen concentration does not take place right at the notch tip (distance=0), but at 0.6 µm from it in the model V-SC-1. The results presented in Fig. 4-9d agree well with those presented in Lufrano et al. (1998) for hydrogen concentration in the vicinity of a notched specimen, although a macroscale FE model was used.

The maximum of hydrogen concentration from V-SC-1 takes place at different location when compared with that of U-SC-1. Since grain orientations in both models are the same, this difference is due to the notch geometry.
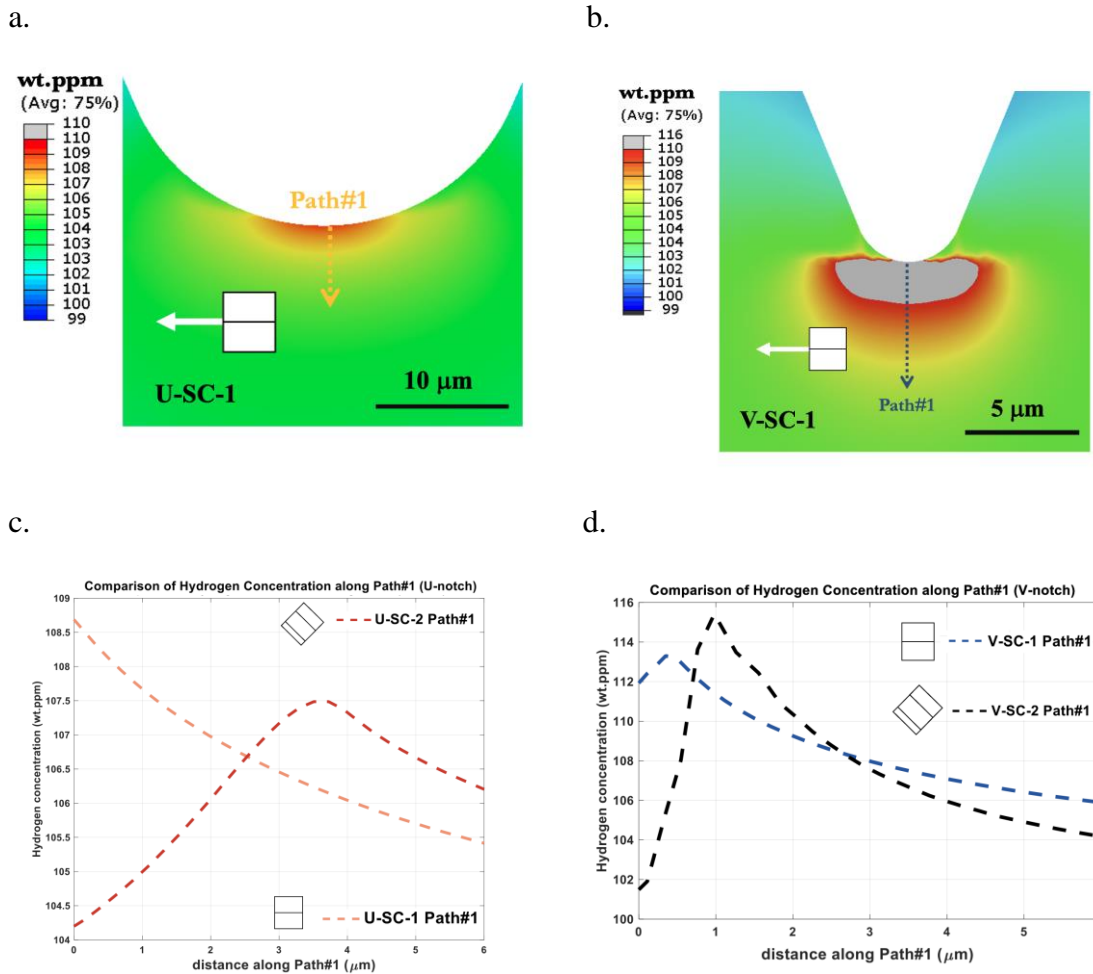
**Fig. 4-9 – The distribution of hydrogen concentration in the notch tip region of (a) U-SC-1 and (b) V-SC-1 models. (c) Hydrogen concentration along Path#1 for U-SC-1 and U-SC-2 models. The distribution of hydrogen concentration for V-SC-1 and V-SC-2 models along Path#1 is plotted in (d). Starting points of the plots (distance = 0) coincide with the starting points of the arrows. Path#1 is shown in (a) and (b). Results are for $\Delta Y_{external} = 30$ μm.**

To investigate the effect of applied displacement, the hydrogen concentration from V-SC-1 model along the crystal basal plane (Path#1) at different applied displacements are plotted in Fig. 4-10. At lower macroscopic strains, the hydrogen concentration steadily decreases with distancing from the notch tip. The lower two curves belong to the elastic zone where minimum plasticity is observed at the notch tip. Once a certain level of macroscopic strain is reached and plastic deformation occurs in the ROI, a peak of hydrogen concentration forms which moves further away from the notch tip as the external displacement is increased. As the material hardens, this peak intensifies with increasing the applied

displacement. This is consistent with the trends reported in the numerical studies by Aslan (2015) and Olden et al. (2008), as well as those reported in an experiment conducted by Gong et al. (2018).



Comparison of Hydrogen Concentration for different strains (V-notch)
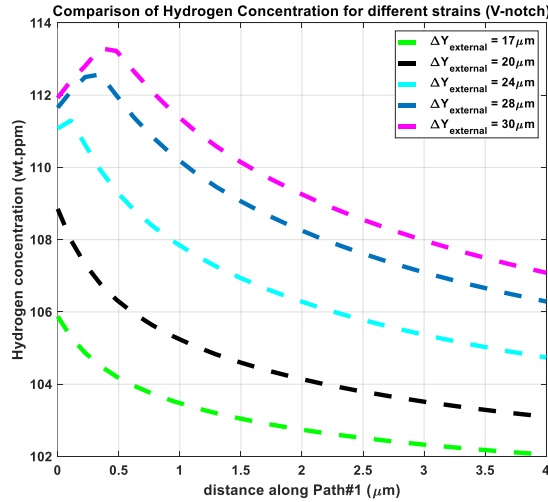
**Fig. 4-10 − Comparison of hydrogen concentration from V-SC-1 model along Path#1 at different applied external displacements. Path#1 is shown in Fig. 4-9b.**

The results of the bicrystal models U-BC-1 and V-BC-1 at the $\Delta Y_{external}$= 40 μm are presented in Fig. 4-11. The locations of maximum hydrogen concentration are shown using blue arrows. It can be seen that with decreasing notch radius, the location of maximum hydrogen concentration moves from the left grain to the right one. Also, this position moves along the Y-axis from the notch tip in the model U-BC-1 to a position further away from the notch. For V-BC-1, it moves to the right-hand side of the model. This agrees with the results of Depover et al. (2019) for hydrogen embrittlement of steel alloys. Using both experimentation and numerical modeling, it was shown that specimens with sharper notch geometries contained higher hydrogen concentrations. They also showed that the area affected by hydrogen charging was broader in samples with larger notch tip radii.
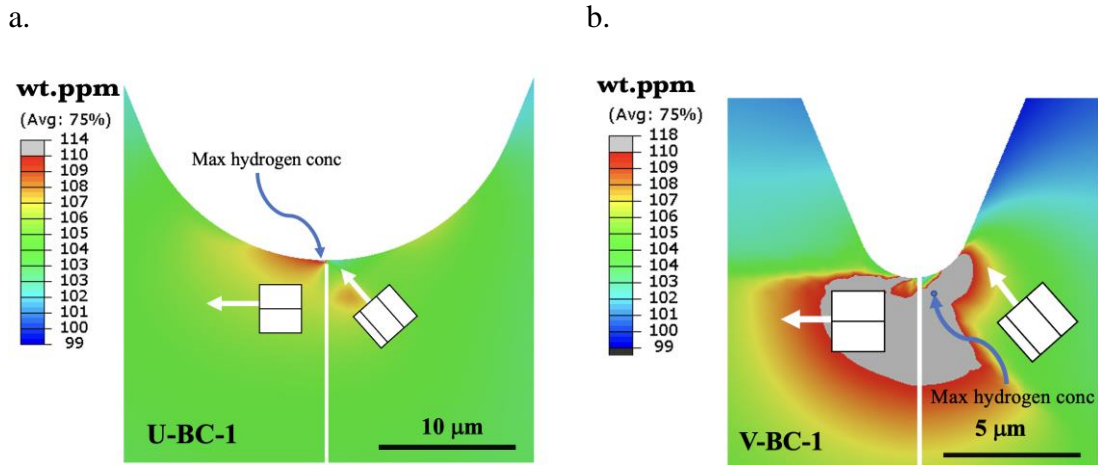
**Fig. 4-11 – Hydrogen concentration fields at the notch tip of (a) U-BC-1 and (b) V-BC-1 models. The locations of the maximum hydrogen concentration are shown using the blue arrows. Results are for $\Delta Y_{external} = 40$ μm.**

## 4.3.4.2 Polycrystals: maximum hydrogen concentration

The U- and V-notched polycrystal models are compared in this section. In the following models, the texture of CANDU pressure tubes is used and up to 17μm displacement is applied to the models. Hydrogen concentration fields in the ROIs of U-Poly-T and V-Poly-T models as well as U-Rec-T and V-Rec-T models are shown in Fig. 4-12. The maximum hydrogen concentrations for V-notch models are considerably higher in comparison to those of U-notch models. Also, comparing to the models with rectangular grains, a slightly higher hydrogen concentration is calculated close to the notch tip in the models with hexagonal grains. This is due to a higher ratio of grain boundaries to grain interiors in the model with hexagonal grains. A higher number of grains in addition to more grain boundaries and grain neighbors lead to more heterogeneity in the hydrogen distribution field at the notch tip. This trend is also observed for the U-notch models. Therefore, it can be concluded that grain size might also affect the magnitude of maximum hydrogen concentration. This is further discussed in section 4.4.4.

The results of this section indicate that the notch radius has an important role in determining hydrogen concentration. This is consistent with the results of the study conducted by Shang et al. (2020), where it was shown that increasing stress intensity factor through decreasing

notch tip radius leads to a faster hydrogen-induced degradation through increasing hydrogen concentration at the notch tip.
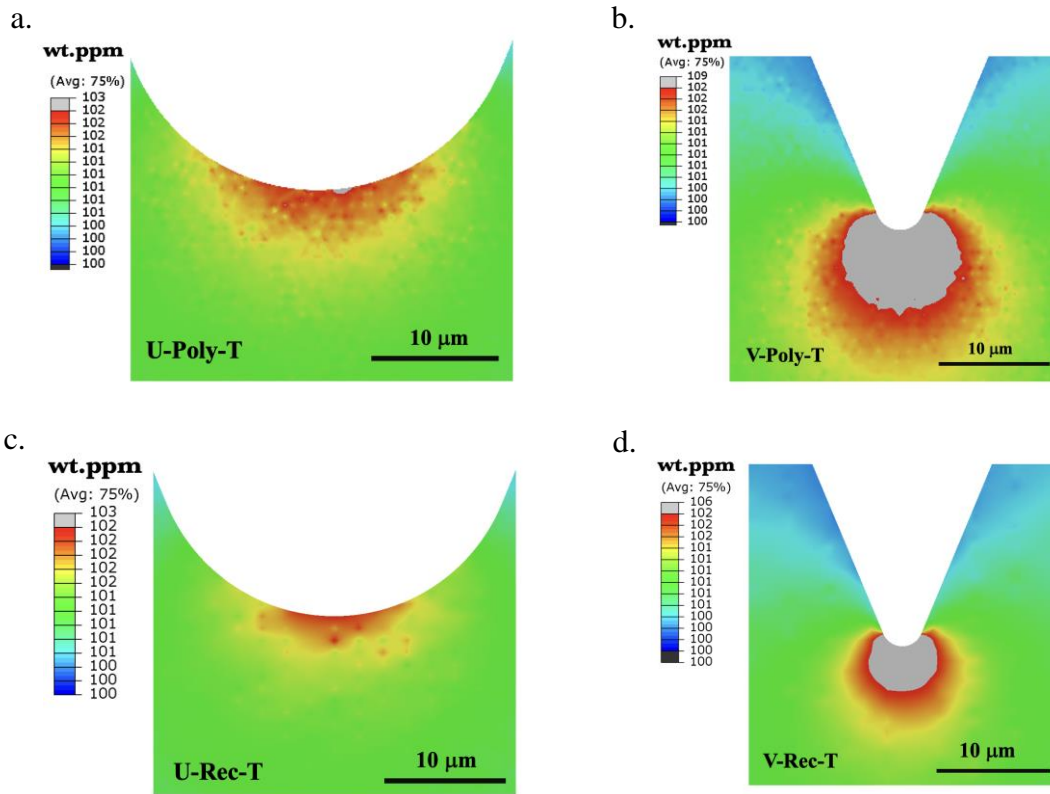


**Fig. 4-12– Hydrogen concentration fields at the notch tip regions of (a) U-Poly-T, (b) V-Poly-T, (c) U-Rec-T and (d) V-Rec-T models. The details of the models are listed in Table 4-2 and the results are for $\Delta Y_{external} = 17\mu m$.**

## 4.4 Discussion

In the following sections, the effects of the parameters that can contribute to hydrogen transport towards the notch tips are discussed in detail. For this purpose, all the other parameters, except for the one being investigated, are kept constant in the comparisons presented. These parameters include texture, grain size and applied external displacement. Lastly, the effects of dislocations on hydrogen concentration in trap sites are also discussed.

### 4.4.1 The effects of texture

#### 4.4.1.1 Hexagonal grains

As shown in the previous sections, texture can greatly affect the distribution of hydrogen atoms at the notch tips. Here, numerical results obtained using two different textures in the

ROIs are discussed. Fig. 4-13 compares the distribution of the maximum principal strain for the U-Poly-R and U-Poly-T models. The textured model has higher localized strains but accommodates less average strain within the ROI. To further investigate the effects of texture, the hydrogen concentrations, vonMises stresses and the maximum principal strains of both models are compared and presented in Fig. 4-14. Results presented are for $\Delta Y_{external}$ = 42 µm. Fig. 4-14a and b show that grains closer to the notch tip have higher hydrogen content in the "textured" model compared to the model with random texture. It can be concluded that random-textured notch tips are less susceptible to hydrogen embrittlement. Fig. 4-14c compares the variation of hydrogen concentration along Path#2, shown in Fig. 4-14a and b. These results show that grains of the textured model have higher hydrogen concentration than those of the random model, particularly towards the middle of the path plot. Also, Path#1, similar to the one introduced for U-SC and V-SC models, is used in both models to compare the state of strains and stresses. Fig. 4-14d and 4-14e respectively show the variations of the maximum principal strains and vonMises stresses along Path#1. The results show that the model with random texture is more strained compared to the "textured" model since there are some soft orientated grains in the random textured model. All in all, the textured model develops higher stresses and higher hydrogen concentrations at the notch tip leading to more susceptibility to hydrogen embrittlement.
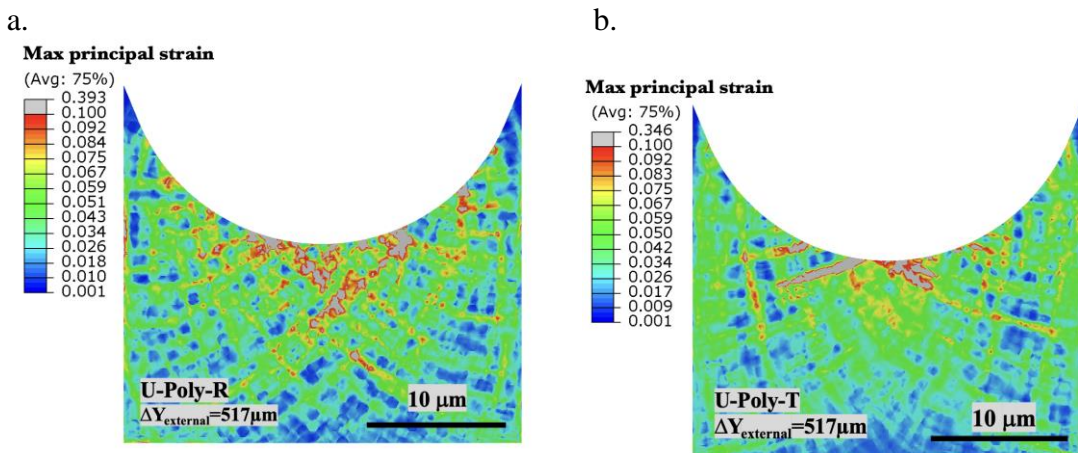


**Fig. 4-13 – The maximum principal strain for models (a) U-Poly-R and (b) U-Poly-T. Results are for $\Delta Y_{external}$ =517 µm.**
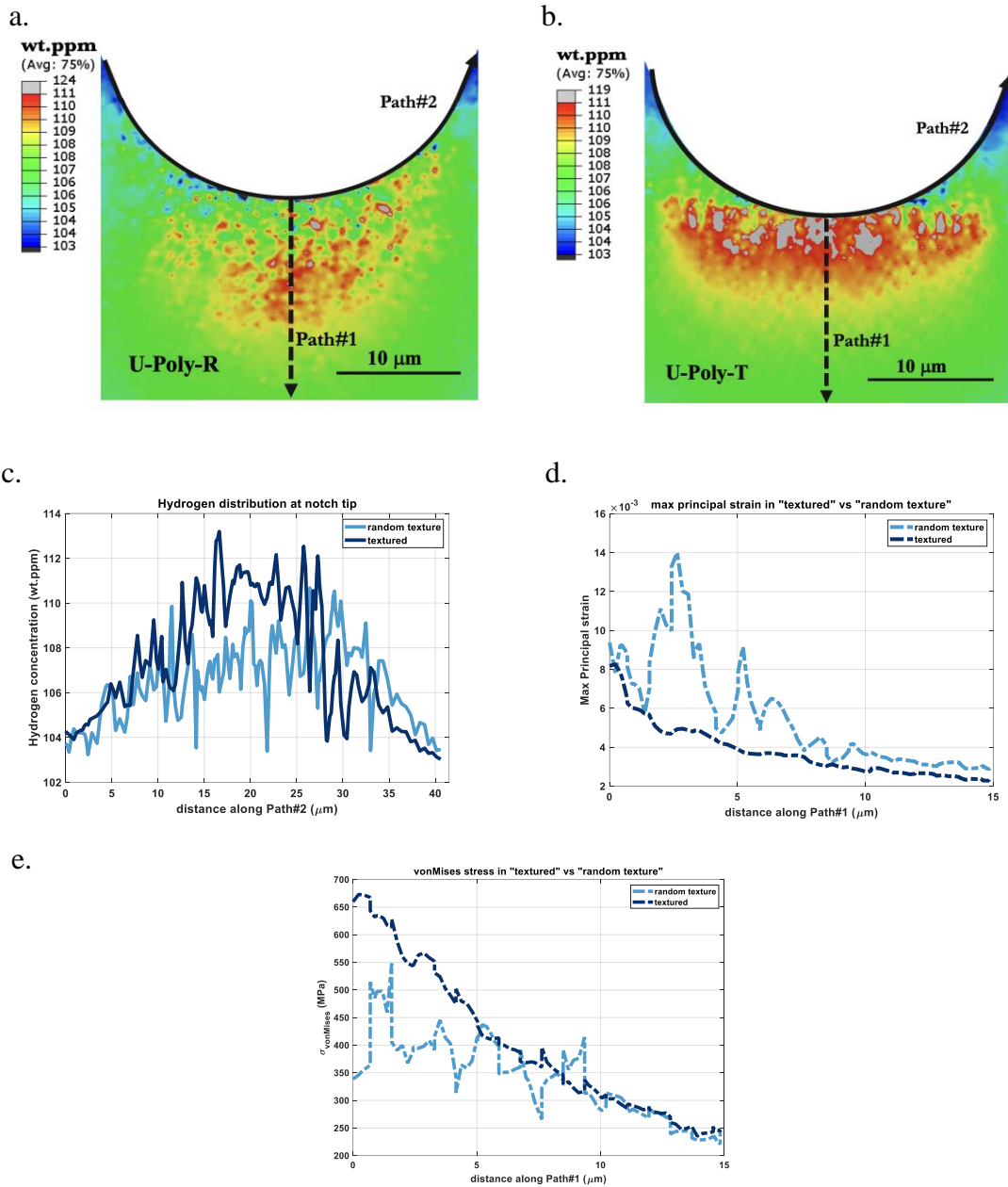
**Fig. 4-14 – Hydrogen concentration fields at the notch tip regions of (a) U-Poly-R and (b) U-Poly-T models. (c) The variation of hydrogen concentrations from both models and along Path#2. Path#2 is shown in (a). The variation of (d) the maximum principal strains and (e) vonMises stresses along Path#1. Results are for $\Delta Y_{external}$ =42μm.**

## 4.4.1.2 Rectangular-shaped grains

The effects of texture are further investigated in models in which the ROI is partitioned with rectangular-shaped grains. The distribution of hydrogen concentration in the ROI of

the U-Rec-R model is shown in Fig. 4-15a. In this model, a random texture is assigned to 172 grains located in the ROI. Similar to U-Poly-R with random texture and hexagonal grains, grain boundaries and triple points are the main sites at which the peaks of hydrogen concentration take place (see the intersection of grain boundaries in Fig. 4-15a and b). In addition, the distribution of hydrogen in the ROI of model U-Rec-T is shown in Fig. 4-15b. In the "textured" model, the peaks of hydrogen concentration generally occur along the horizontal grain boundaries. In comparison to the model with a random texture, the grains at the notch tip of the textured model accommodate more hydrogen atoms. This is consistent with the results presented for the textured model and the one with a random texture and hexagonal grains. Therefore, this strong texture facilitates the transport of hydrogen atoms towards the notch tip. This could be the reason for the formation of mesoscale hydrides in strongly textured specimens reported by Jia et al. (2021) and Motta et al. (2019). In addition, grain boundaries in both models, specifically horizontal ones, and triple points are the first places at which hydrogen concentration peaks. Results of this section are also in agreement with the experimental observations of Oh et al. (2010), where it was shown that grains that are aligned with the rolling direction are more susceptible to hydride formation than the equiaxed ones.

a.



b.
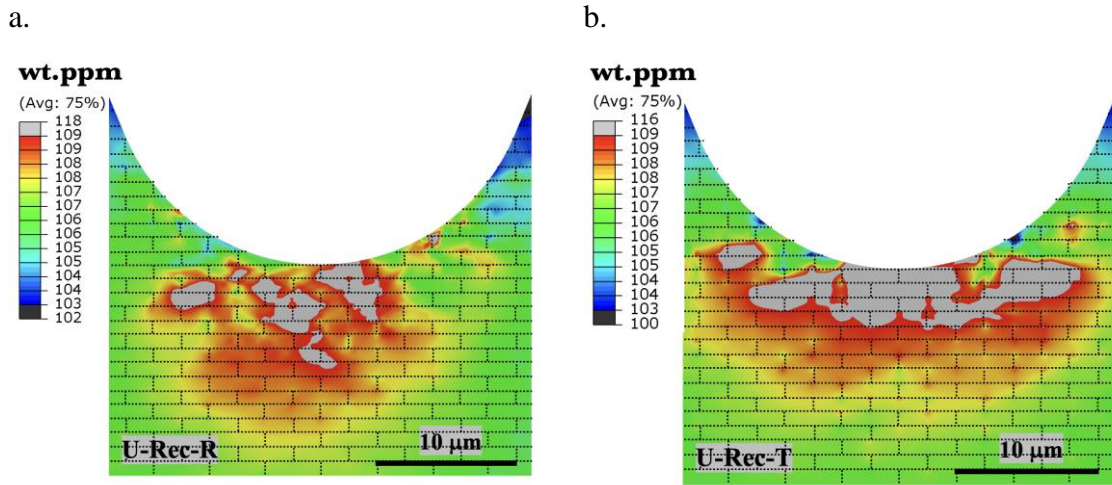
**Fig. 4-15 – The distribution of hydrogen within the notch tip regions of (a) U-Rec-R and (b) U-Rec-T models. Grain boundaries are shown using the dashed lines. Results are for $\Delta Y_{external} = 42\mu m$.**

## 4.4.2 The effects of texture: localization in V-notch models

In this section, the effects of texture on the localization of stress, strain and hydrogen concentration in the ROIs of the V-notch models are discussed and presented. The models are deformed to $\Delta Y_{external} = 172\mu m$. As shown in Fig. 4-16b, stresses are localized close to the notch tip in the textured model (V-Poly-T). V-Poly-R model has a more homogenous distribution of vonMises stress, although higher stresses are observed near its notch tip (Fig. 4-16a). Also, Fig. 4-16c and d show that strains are more localized in the textured model but are higher in the V-Poly-R model with a random texture. That is, the textured model undergoes less amount of deformation due to the alignment of most of its crystals c-axis with the loading direction.
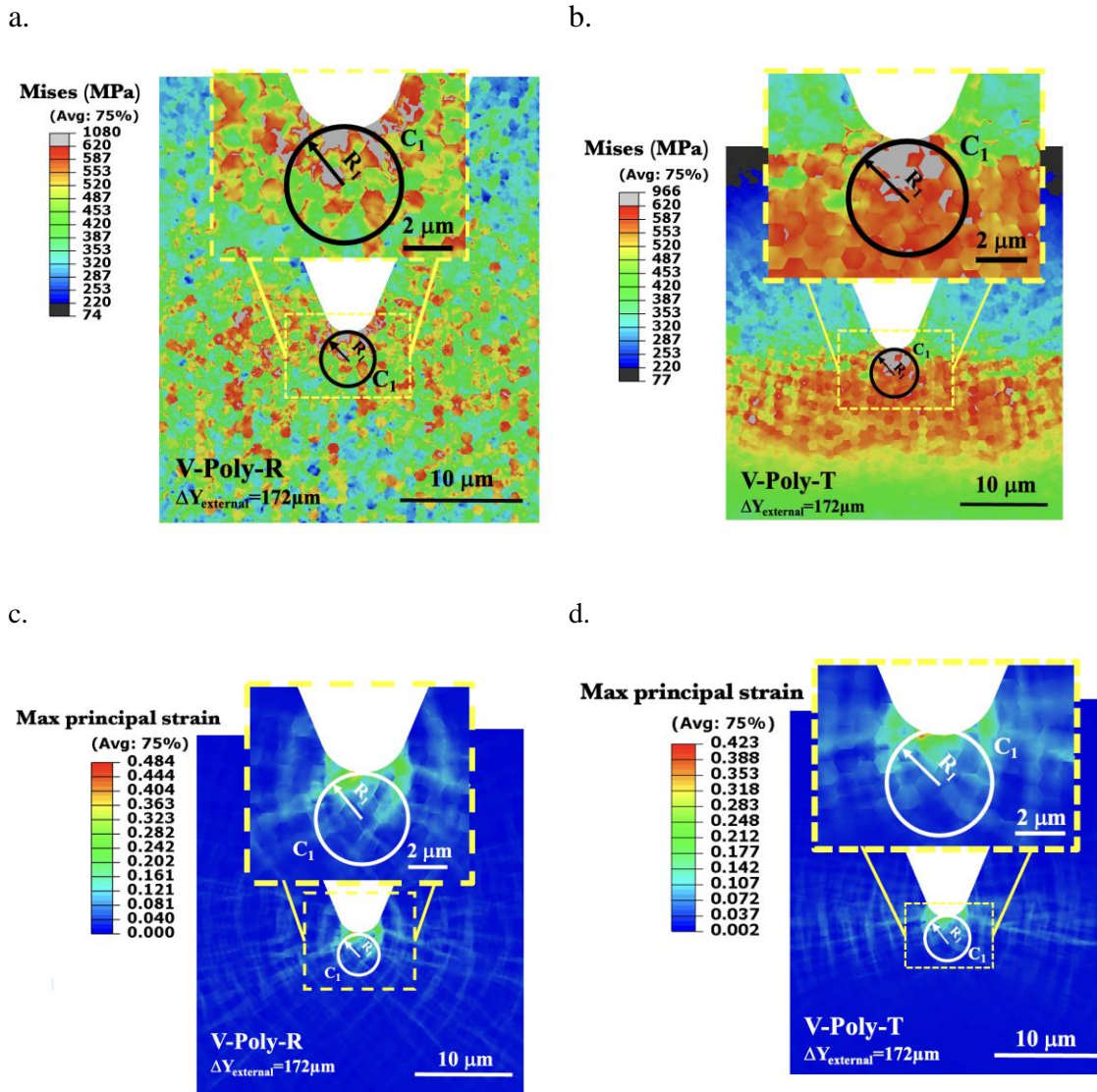
**Fig. 4-16 – The distribution of vonMises stress at the notch tip regions of (a) V-Poly-R, (b) V-Poly-T models. The maximum principal strains of (c) V-Poly-R and (d) V-Poly-T models. Results are for $\Delta Y_{external}$=172μm.**

To quantify the localization of stress, hydrogen, and strain in the vicinity of notch tips, the circle $C_1$ is defined where these values are averaged, compared, and divided by the average values from the ROI to determine the concentration factor (CF). The circle $C_1$ is shown in Fig. 4-16, and the results are shown in Table 4-3. It was previously shown in section 4.4.1 that in U-notch models, texture plays a very important role in redistributing hydrogen atoms in the ROI, especially at the notch tip. However, the data presented in Table 4-3

shows that with sharpening the notch tip, the contribution of notch tip radius overshadows that of texture.

**Table 4-3 - Effects of texture on the localization of stress, strain and hydrogen concentration.**

| $\Delta Y_{external}$ =172μm | V-Poly-T (textured) | | | V-Poly-R (random) | | |
|---|---|---|---|---|---|---|
| | C1 | ROI | $CF = \frac{c_1}{ROI}$ | C1 | ROI | $CF = \frac{c_1}{ROI}$ |
| $Mises_{avg}$ (MPa) | 700.11 | 354.24 | **1.97** | 578.21 | 389.79 | **1.48** |
| $\varepsilon_{avg}^{max\ principal}$ | 0.107 | 0.0174 | **6.14** | 0.126 | 0.0198 | **6.36** |
| $\sigma_{H\ avg}(MPa)$ | 516.41 | 367.02 | **1.40** | 489.01 | 360.25 | **1.35** |
| Hydrogen Concentration$_{avg}$ (wt.ppm) | 118.37 | 110.94 | **1.07** | 116.19 | 110.36 | **1.05** |

## 4.4.3 The effects of applied strain

Depending on the service conditions, zirconium might undergo different levels of mechanical loads which directly affect the process of hydrogen embrittlement. Here, the effects of applied strain as well as texture are studied by deforming the models U-Poly-R and U-Poly-T to $\Delta Y_{external}$ = 42μm and 65μm. The hydrogen concentrations calculated for $\Delta Y_{external}$ = 65μm are presented in Fig. 4-17a and 4-17c. In comparison to grains of U-Poly-R, grains of U-Poly-T uniformly have high hydrogen concentration but with a lower peak. The variation of hydrogen concentration for the two applied displacement of U-Poly-R model along Path#2 is shown in Fig. 4-17b. It is not surprising that hydrogen concentration has increased with the applied displacement. However, the difference in hydrogen concentration for the two applied displacements becomes more pronounced when the distributions are plotted along Path#1 and for the U-Poly-T model (Fig. 4-17d). The difference in hydrogen concentration increases as the path goes through inner grains, further from the notch tip. This growing difference between the two plots is shown using

the solid arrows. Although, ~5 μm into the path, the difference between the two plots remains generally constant.

The results of this section are in agreement with those reported in the study by Toribio et al. (2020) where it is mentioned that the peak of hydrogen concentration is shifted towards the inner points of the specimen by increasing the applied load. As a result of significant elastic and plastic anisotropy in zirconium crystals, it is shown in Fig. 4-17a and d that the distribution of hydrogen atoms, even in the area that experience highest concentrations, is not uniform.

a.



b.



c.



d.
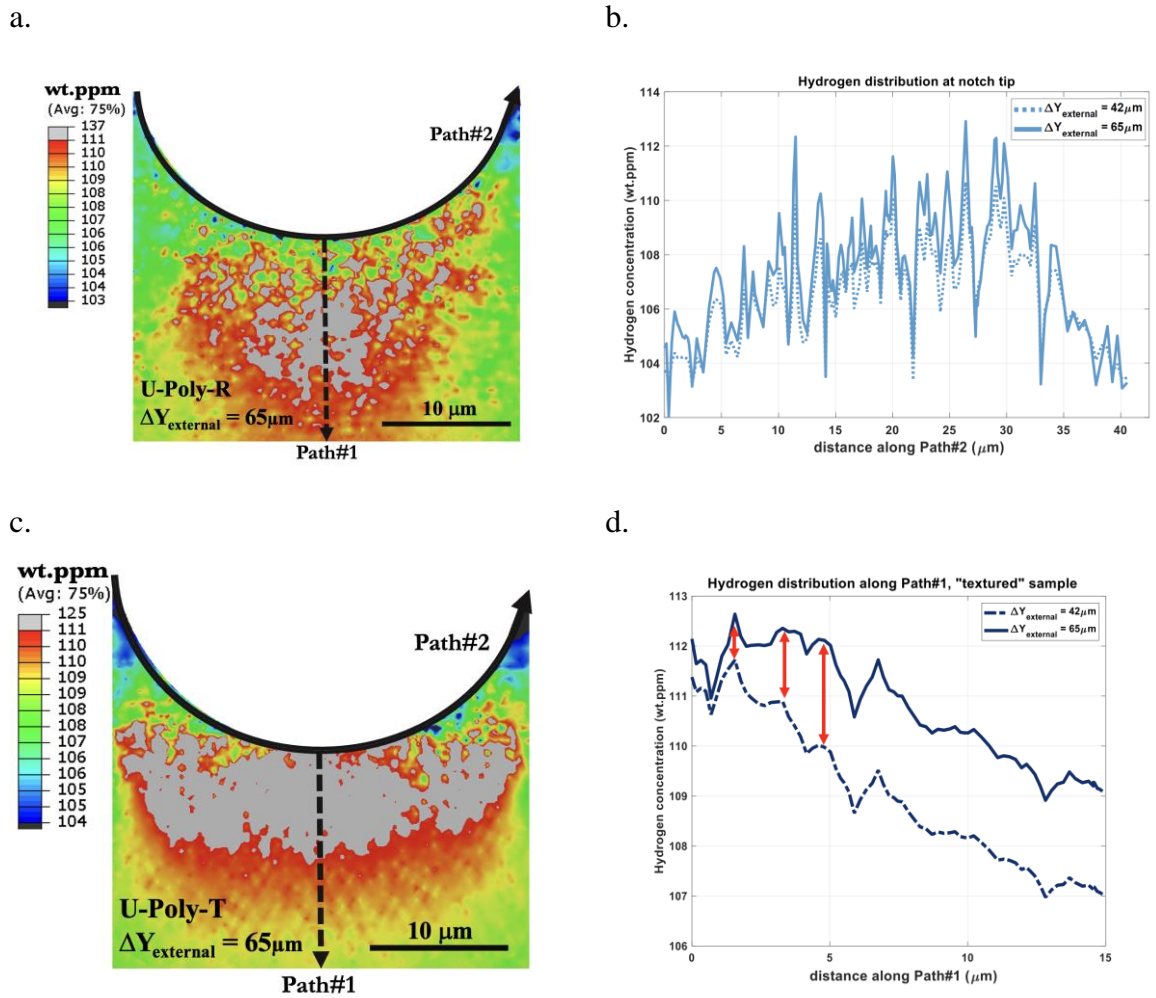


**Fig. 4-17– Hydrogen distribution fields of (a) U-Poly-R and (c) U-Poly-T models for $\Delta Y_{external}$ = 65μm. (b) The variation of hydrogen concentration from U-Poly-R and along Path#2, shown in (a). (d) The variation of hydrogen concentration along Path#1 and for $\Delta Y_{external}$ = 42μm, and 65μm. Path#1 is shown in (c).**

## 4.4.4 Effects of grain size

It was shown in section 4.4.1 that grain morphologies may change the distribution and the flux of hydrogen atoms towards the notch tips. The effects of grain size are discussed in this section using the results of models U-poly-T and U-poly-T*, both of which have "textured" ROI, but with different grain sizes. These models respectively comprised of 945 and 179 grains at the notch tip, which makes the average size in the latter model almost 5 times bigger than that of the former. Consequently, the grain boundary area of U-Poly-T*

is considerably less than that of U-Poly-T. Fig. 4-18a and b, respectively show the hydrogen concentrations at the notch tips of models U-Poly-T and U-Poly-T*.

a.

b.
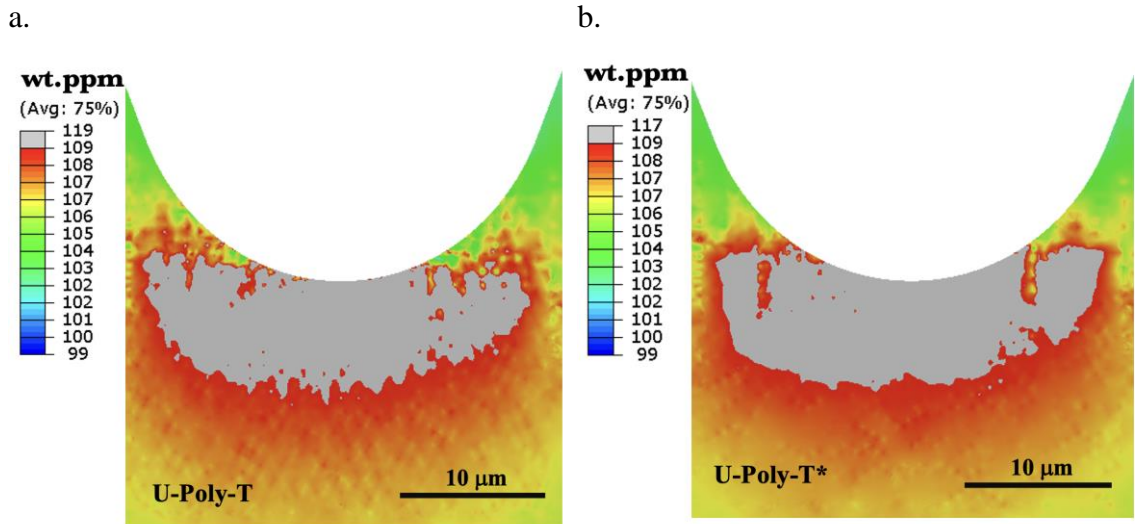


**Fig. 4-18– The effects of grain size on the distribution of hydrogen at the notch tip: Hydrogen map for models (a) U-Poly-T and (b) U-Poly-T*. Average grain size in the U-Poly-T* model is 5 times bigger than that of U-Poly-T model. Results are for $\Delta Y_{external} = 42\mu m$.**

The analysis of the results shows that hydrogen in U-Poly-T* is distributed more homogenously than in U-Poly-T, since the propensity of grain misorientations is lower in U-Poly-T*. Also, the maximum of hydrogen concentration in U-Poly-T is higher than U-Poly-T*. This is due to having more grain boundaries in this model, which act as hydrogen accumulation sites. Overall, the differences are very small mainly because only the hydrogen atoms in the lattice sites are studied here. Grain boundaries can act as trap sites, the effects of which are ignored in this analysis.

## 4.4.5 Hydrogen concentration in lattice sites vs. trap sites

All the concentration results presented so far are for hydrogen atoms located in the lattice sites ($C_L$). It is known that defects can play an important role in determining the concentration of hydrogen atoms. The contribution of dislocations to hydrogen contents ($C_T$) generally can be estimated using the following equation (Sofronis and McMeeking, 1989):

$$C_T = \theta_T \beta N_T \qquad \qquad (4\text{-}15)$$

where $\theta_T$ can be determined by assuming that the hydrogen in the lattice sites is in equilibrium with those in the trap sites. The value of $\theta_T$ is always less than or equal to one. We pick up one to calculate an upper bound for hydrogen contents in dislocations. The value of $\beta$ for cubic crystals is suggested to be $\sqrt{2}$ to $\sqrt{3}$ (Dadfarnia et al., 2014), but here, for HCP crystal is considered to be 2 which is the minimum number reported in Wimmer et al. (2020) for hydrogen in vacancies. the number of trap sites ($N_T$) correlates with dislocation density following Eq. 4-16:

$$N_T = \frac{\rho_{dis}}{d_{hkl}} \qquad \qquad (4\text{-}16)$$

where $d_{hkl}$ is the interatomic spacing for a given *hkl* plane. This equation is adapted from the trap model proposed in Oriani (1970) and Krom and Bakker (2000). Here we assume that the maximum dislocation density that can develop in zirconium alloys is $10^{17}$ m$^{-2}$ which is consistent with those measured with the HR-EBSD method. The value of $d_{hkl}$ for prism slip systems is 0.2796 nm which is in between that of pyramidal and basal slip systems. Hence, the maximum of C$_T$ can be calculated to be $7.15 \times 10^{26}$ atoms.m$^{-3}$. Considering that the density of zirconium is 6.49 gr.cm$^{-3}$, the value of C$_T$ in heavily deformed areas will be 183 wt.ppm per slip system. Also, this value could be an order of magnitude higher than the one calculated here, considering that a higher number of hydrogen atoms can be located per trap site (Wimmer et al., 2020). This means that dislocations help the process of hydrogen diffusion by trapping the hydrogen atoms in the lattice and enhancing more hydrogen diffusion towards the notch tip to counterbalance the induced concentration gradient.

In addition to dislocations, grain boundaries and vacancies are other hydrogen trap sites, the effects of which are ignored in this study, but will be included in future studies. The contribution of vacancies particularly become important for irradiated zirconium. Generally, there is a lack of experimental data on determining the sink strength of grain

boundaries or vacancies in zirconium. Lastly, the effects of (thermal) residual stresses that will develop in zirconium as well as the actual 3D grain shapes are ignored as well.

## 4.5 Conclusions

A coupled diffusion-crystal plasticity finite element model is used to conduct a parametric study on the effects of microstructure and texture on the stress-assisted hydrogen diffusion towards notch tips in HCP zirconium polycrystals. A 3-point bending configuration is used and it is shown that:

1. The texture at the notch tip region significantly affects the distribution of hydrogen atoms as well as the location of peak hydrogen concentration.

2. Single crystal simulations show that the patterning of stress fields depends upon the crystal orientation, which subsequently affects the location of peak hydrogen concentration.

3. For single and bi-crystals, the hydrogen concentration generally peaks along the HCP crystal c-axis, regardless of the assigned notch shapes.

4. The use of random texture moves the peak of hydrogen concentration away from the notch tip. In contrast, when a typical texture of pressure tube material is used, this peak moves towards the notch tip and increases the susceptibility of the tube to hydrogen embrittlement. In comparison to the examined random texture models, more hydrogen atoms concentrate at the notch tip of the "textured" models.

5. The location of peak hydrogen concentration in the lattice is significantly affected by the magnitude of plastic deformation as well as the activity of slip systems. Applying higher macroscopic strains moves the peak hydrogen concentration further away from the notch tip towards inner grains.

6. Hydrogen concentration monotonically decreases along the Y-axis, in the absence of plastic deformation around the notch tip. This Y-axis goes through the center of the tube and notch.

7. For the range of the applied displacements studied here, both hydrogen concentration and hydrostatic stress ahead of the notch tip peak along the Y-axis once plastic deformation occurs.

8. The location of maximum hydrogen concentration is affected by the notch geometry. A sharper notch accelerates the diffusion of hydrogen atoms towards the notch tip due to the increase in the magnitudes of the localized stresses.

9. As the notch tip radius decreases, the effects of texture on hydrogen localization at the notch tip become less significant.

10. Decreasing grain size while using the same texture increases hydrogen diffusion towards grain boundaries due to the higher ratio of grain boundaries to grain interiors.

The advantage of using CPFE framework is shown to be in quantifying stress heterogeneities and their subsequent effects on the nonuniform distribution of hydrogen atoms. Such stress heterogeneities originate from the significant elastic and plastic anisotropy of zirconium single crystals. The implemented framework allows us to study the effects of materials texture, grain morphologies, and notch geometries on the hydrogen diffusion in the lattice, but the important effects of traps, e.g., dislocations, are ignored which will be the focus of future studies.

# Chapter 5

## 5 Modeling the interaction of zirconium hydrides

The zirconium alloys used in the core of nuclear reactors are susceptible to hydride formation and hydrogen embrittlement. Depending on the loading condition, zirconium hydrides usually form in different directions and with various configurations. This study focuses on the development of the stress fields resulting from the interaction of hydrides, and the subsequent redistribution of hydrogen atoms. The effects of the separation distance between the hydrides formed in parallel and perpendicular configurations are investigated using a coupled diffusion-crystal plasticity finite element approach. The effects of hydride length and width on the stress-assisted diffusion of hydrogen atoms towards hydrides tips are also studied. It is shown that, due to the alignment of growth direction of hydrides, stress fields in the vicinity of two parallel hydrides interact more significantly compared to those of perpendicular hydrides. It is further shown that hydrides with a width of 1 μm propagate faster than those having lower or higher widths.

## 5.1 Introduction

Due to their good mechanical properties, resistance to corrosion at elevated temperatures, and most importantly, low neutron absorption cross-section, zirconium (Zr) alloys have been widely used in the core of various types of nuclear reactors. During the operation of nuclear reactors, the hot water coolant reacts with zirconium, releasing hydrogen (H) atoms into the zirconium lattice. Once hydrogen concentration surpasses the terminal solid solubility (TSS) limit of hydrogen in zirconium, a brittle phase known as zirconium hydride forms. TSS highly depends on the operating temperature of the reactor, therefore, formation of hydrides is more likely to occur during a reactor shutdown. Formation of hydrides can potentially deteriorate the integrity and in-service performance of zirconium cladding material. It is known that hydrogen atoms tend to diffuse towards regions with high tensile stresses, e.g., hydride tips and stress risers such as flaw tips through a process known as stress-assisted diffusion (SAD) (Blackmur et al., 2016; Courty et al., 2014a; Eadie et al., 1991; Motta et al., 2019). The development of such localized stress fields is affected by the elastic and plastic anisotropy of zirconium single crystals- which mainly

have a hexagonal close-packed (HCP) crystal structure. It is also known that formation of hydrides depends on the microstructure of zirconium (Wang et al., 2019). Therefore, depending on the local microstructure or stress state, hydrides could form in different directions and interact with one another. This study focuses on the numerical simulation of the interactions of hydrides as well as the effects of hydride geometry on the diffusion of hydrogen atoms.

Experimental characterization of hydrides has been the focus of many studies in the literature. For instance, it is shown that both the cooling rate and hydrogen content affect the type of hydrides forming within zirconium (Cameron and Duncan, 1977; Nath et al., 1975). Also, cooling rate is shown to affect the size and distribution of hydrides (Lee and Hong, 2002). With the use of X-ray diffraction (XRD), four different types of hydrides with different crystal structures are reported (Lumley et al., 2014). The stability of the hydride phases is debated in the literature (Lanzani and Ruch, 2004), however, the most frequent and stable phases are suggested to be δ- and γ-hydrides with face-centered cubic (FCC) and face-centered tetragonal (FCT) crystal structures, respectively (Domain et al., 2002; Zheng et al., 2015). In this work, we focus specifically on δ-hydrides which precipitate during slow cooling rates ($< 2$ °C/min) and is known to be one of the most stable hydride phases. The transformation of HCP α-zirconium to FCC δ-hydride is accompanied by 17.2% volumetric strain (Carpenter, 1973), which is known as hydride-induced transformation strain (HITS).

XRD has been used to study the orientation relationship of different phases. For example, in a study conducted by Vicente Alvarez et al. on a hydrided Zr-2.5Nb pressure tube, it was shown that selective precipitation occurs within the grains of α-Zr (Vicente Alvarez et al., 2011). Also, the orientation relationship of α-zirconium and δ-hydride is reported to be α (0 0 0 1)// δ (1 1 1) and α [1 1 -2 0]// δ [1 -1 0]. The direction along which hydrides form could greatly affect the toughness of nuclear pressure tubes (Gopalan et al., 2021). For example, zirconium is shown to be more susceptible to failure when interlinked hydrides align towards the radial direction of the tube (Kiran Kumar and Szpunar, 2011). Using XRD, Vizcaíno et al. studied the effects of the parent grain orientation on δ-hydride precipitation (Vizcaíno et al., 2014). It was reported that the precipitation of δ-hydrides

occurs mostly in two groups of HCP grains: (i) those having their c-axis oriented towards the hoop direction of the tube, and (ii) those having their c-axis oriented towards an intermediate direction in hoop-radial plane of the tube. In nuclear pressure tubes, the c-axis of most of the HCP crystals are oriented towards the hoop direction. In a later study by Jia et al., a preferential hydride precipitation was reported (Jia et al., 2021). It was shown that grain boundaries with c-axis misorientation of <15°, in between 55° to 60°, and >85° are preferred for hydride precipitation. Generally, three distinct locations are suggested for hydride nucleation: (1) at grain boundaries, which result in intergranular hydrides, (2) inside grains, which result in intragranular hydrides, and (3) twin boundary hydrides (Kiran Kumar et al., 2010; Silva et al., 2019; Tunes et al., 2019; Wang et al., 2019). The shared plane between α-zirconium crystals and the hydride phase is called the habit plane. The habit plane of δ-hydride in pure zirconium and zirconium alloys, including Zircaloy-2 and -4, are respectively reported to be $\{1\,0\,\bar{1}\,0\}$ and $\{1\,0\,\bar{1}\,7\}$ (Kim et al., 2015; Perovic et al., 1983; Pshenichnikov et al., 2016; Westlake, 1968). It is also known that intragranular hydrides are more likely to precipitate within the grains with larger areas (Wang et al., 2019). Similarly, El Chamaa et al. showed that the likelihood of intragranular hydrides formation within larger grains is higher than that of smaller grains (El Chamaa et al., 2018).

In service, hydrides generally tend to precipitate along the circumferential direction of nuclear pressure tubes. However, hydrides might reorient towards the radial direction due to a variety of reasons including temperature and stress gradients (Colas et al., 2011), hydrogen content (Hardie and Shanahan, 1975), neutron irradiation (Jang and Kim, 2017) and oxygen content (Cha et al., 2015a). A detailed study on the contributing parameters to hydride reorientation by Cha et al. shows that slower cooling rate and higher tensile hoop stresses lead to formation of larger radial hydrides (Cha et al., 2015b). This phenomenon might cause extensive damages and premature failures to nuclear reactors through cladding embrittlement (Bell and Duncan, 1975; Simon et al., 2021). For example, Raynaud et al. studied the effects of temperature on the crack growth of Zircaloy-4 (Raynaud et al., 2012). It was reported that material's fracture toughness decreases at low temperatures with higher fraction of radial hydrides causing accelerated crack growth. The ductility of cladding materials can also be affected by hydride reorientation (Auzoux et al., 2017). Recently, the microstructure and crystallographic features of hydride reorientation have been

comprehensively studied by Li et al. (Li et al., 2020). It was shown that even after hydride reorientation, the habit plane of microscale hydrides remains unchanged. On the other hand, the growth direction of macroscopic hydrides changes due to the presence of hoop stresses. Direction of growth along the radial direction is more favorable since it accommodates the large mismatch between the two phases along the $(0001)_\alpha//\{111\}_\delta$.

Hydride precipitation and reorientation have also been studied using numerical methods. One of the methods that has been used to study hydride formation is phase field modeling (Ma et al., 2002; Xiao et al., 2015). For example, Lin and Heuser developed a phase-field model to simulate hydrogen solvus in zirconium where it was shown that δ-hydrides tend to precipitate within the grains with lower strain energies (Lin and Heuser, 2019). In a study by Qin et al., it was shown that hydrides tend to connect and form an interlinked structure (Qin et al., 2014). As well, it was reported that the development of tensile stresses at the tips of hydrides contributes to further hydride propagation, affecting other neighboring grains and hydrides. Phase field modeling has also been used to address hydride reorientation in zirconium alloys (Shin and Chang, 2020; Toghraee et al., 2021). For example, Han et al. showed that δ-hydrides form in stacks that are nearly parallel to the basal planes of zirconium crystals (Han et al., 2019). It was further shown that pre-existing hydrides tend to grow from their tips where the driving force for hydride nucleation is the highest. In addition, Welland and Hanlon studied the hysteresis effects during precipitation and dissolution of hydrides, where it was concluded that such effects depend on nucleation barriers (Welland and Hanlon, 2020). Another numerical method used for studying the precipitation of hydrides is discrete dislocation dynamics (DDD) (Reali et al., 2021). For example, this method was used to quantify the state of stresses near δ-hydrides (Tummala et al., 2018). It was shown that hydride-matrix interface can act as a nucleation site for new hydrides because of the nucleated dislocation.

Crystal plasticity finite element modeling (CPFEM) is another method that can be used to investigate the deformation of materials at the grain scale (Abdolvand et al., 2018; Feather et al., 2021; Wang et al., 2020). This method has been used to study the state of stresses in hydrides and deformation twins (Abdolvand et al., 2020, 2015c; G. Liu et al., 2021; Louca et al., 2021; Tondro and Abdolvand, 2021). It is further used to study the dependency of

yield strength of Zr-2.5Nb on its texture, where the results suggest that the anisotropy of yield strength along different directions mainly depends on texture and partially on grain morphology (Ahn et al., 2021). Furthermore, conventional finite element modeling (FEM) and CPFEM have been used to study the effects of stress fields on the diffusion of hydrogen atoms (Cui et al., 2017; Ilin et al., 2014; Y. Liu et al., 2021a). For example, Hussein et al. studied the redistribution of hydrogen atoms as a result of heterogenous micromechanical stresses using a coupled crystal plasticity and diffusion model (Hussein et al., 2021). It was shown that hydrogen is depleted from regions with compressive hydrostatic stresses and diffuses towards regions with tensile hydrostatic stresses. Abdolvand studied the effects of thermal residual stresses on the redistribution of hydrogen atoms in zirconium lattice (Abdolvand, 2019). It was concluded that the sequence of hydride nucleation is affected by the state of grain-scale stresses. Furthermore, the effects of texture on hydrogen transport towards micro-scale notches are studied by Tondro and Abdolvand (Tondro and Abdolvand, 2022). It was suggested that highly textured pressure tubes are more susceptible to hydride precipitation. Similarly, Tondro and Abdolvand studied the effects of grain orientations on stress-assisted diffusion and concluded that hydride growth is more likely to take place within crystallographically "harder" grains, i.e., the grains with their c-axis aligned with the external loading direction (Tondro and Abdolvand, 2021).

There are hardly any studies in the literature focusing on the interaction of hydrides, despite their importance in hydrides propagation or shaping hydride interlinks. Interlinked hydride structures can span over several neighboring grains and form a continuous chain of hydride which could extend a few hundred microns. This can potentially deteriorate the integrity of zirconium and accelerate the premature failure of pressure tubes. Numerical studies in the literature usually ignore the effects of HITS and its subsequent stresses that develop in the vicinity of hydrides. In this chapter, the interaction of hydrides with different orientations is studied using a coupled diffusion (D)-CPFE approach. While the hydrides are embedded in zirconium single crystals, the effects of HITS on the SAD of hydrogen atoms are investigated. The aim of this chapter is to understand (a) the importance of hydride growth direction on their interaction with surrounding hydrides and (b) the effects of hydride morphology on hydride propagation. First, the constitutive equations used in the D-CPFE model are presented followed by the results for parallel and perpendicular

hydrides. Lastly, the effects of hydride geometry and mechanical properties of hydrides on the hydrogen redistribution are discussed.

## 5.2 Modeling

### 5.2.1 Crystal plasticity formulation

In this section, the key equations implemented in the D-CPFE model are described. Here, tensors are presented with bold fonts and vectors with an arrow on the top. The details of D-CPFE model used here can be found in the study by Abdolvand (Abdolvand, 2019). A User MATerial (UMAT) subroutine is coupled with a UMATHT subroutine to simulate the diffusion of atoms in an anisotropic polycrystal. The UMAT subroutine calculates stress increments and updates the solution dependent state variables based on the inputs provided by the FE solver, i.e., strain, rotation, time, and temperature increments. The total strain increment ($\Delta \boldsymbol{\varepsilon}$ ) can be written as:

$$\Delta \boldsymbol{\varepsilon} = \Delta \boldsymbol{\varepsilon}^{el} + \Delta \boldsymbol{\varepsilon}^{pl} + \Delta \boldsymbol{\varepsilon}^{trH} \tag{5-1}$$

where $\Delta \boldsymbol{\varepsilon}^{el}$ and $\Delta \boldsymbol{\varepsilon}^{pl}$ respectively represent the increments of elastic strain, and the plastic strain resulting from crystallographic slip. $\Delta \boldsymbol{\varepsilon}^{trH}$ is the hydride-induced transformation strain (HITS). This strain is applied to the domain that undergoes phase transformation while hydride is precipitating. In this chapter, we focus on δ-hydrides. The formulation below is used to calculate the plastic strain increment which uses the integration of the plastic part of the deformation rate ($\boldsymbol{D}^{pl}$) over each time increment, i.e.:

$$\dot{\boldsymbol{\varepsilon}}^{pl} = \boldsymbol{D}^{pl} = \sum_{\alpha=1}^{N^{spl}} \boldsymbol{P}^{\alpha} \dot{\gamma}^{\alpha} \tag{5-2}$$

$$\boldsymbol{P}^{\alpha} = sym(\boldsymbol{S}^{\alpha}) \ where \ \boldsymbol{S}^{\alpha} = \vec{d}^{\alpha} \otimes \vec{n}^{\alpha}$$

where $\boldsymbol{P}^{\alpha}$ is the symmetric part of the Schmid tensor ($\boldsymbol{S}^{\alpha}$), $\dot{\gamma}^{\alpha}$ is the shear rate on the slip system $\alpha$, and $\vec{d}^{\alpha}$ and $\vec{n}^{\alpha}$ are respectively the slip direction and normal to the slip plane. Shear rate of each slip system is calculated using the following equation (Needleman et al., 1985):

$$\dot{\gamma}^\alpha = \dot{\gamma}_0 \left|\frac{\tau^\alpha}{g^\alpha}\right|^n sign\left(\frac{\tau^\alpha}{g^\alpha}\right) \tag{5-3}$$

where $\dot{\gamma}_0$ is a reference shear strain rate and $n$ controls the rate dependency. $\tau^\alpha$ and $g^\alpha$ are the resolved shear stress on the slip system $\alpha$ and the strength of this system, respectively. An extended Voce hardening law is used for $g^\alpha$:

$$g^\alpha = g_0^\alpha + (g_1^\alpha + \theta_1^\alpha \Gamma)\left(1 - exp\left(-\frac{\theta_0^\alpha \Gamma}{g_1^\alpha}\right)\right) \tag{5-4}$$

where $g^\alpha$ is the current critical resolved shear stress (CRSS), $g_0^\alpha$ is the initial CRSS, $\Gamma$ is the shear accumulated on all slip systems, $\theta_0^\alpha$ is the initial hardening rate, and $g_1^\alpha$ and $\theta_1^\alpha$ determine asymptotic characteristics of hardening.

The resolved shear stress used in Eq. 5-3 is proportional to the Kirchhoff stress ($\mathbf{\Psi}$) through (Peirce et al., 1983):

$$\tau^\alpha = \mathbf{P}^\alpha : \mathbf{\Psi} \tag{5-5}$$

The Jaumann rate of Kirchhoff stress ($\overset{\smile}{\mathbf{\Psi}}$) correlates with the elastic part of the deformation rate tensor ($\mathbf{D}^{el}$) and the elastic stiffness tensor ($\mathbb{C}$) through the following equation:

$$\overset{\smile}{\mathbf{\Psi}} = \mathbb{C} : \mathbf{D}^{el} \ where \ \overset{\smile}{\mathbf{\Psi}} = \dot{\mathbf{\Psi}} - \mathbf{\Omega}^{el}\mathbf{\Psi} + \mathbf{\Psi}\mathbf{\Omega}^{el} \tag{5-6}$$

where $\mathbf{\Omega}^{el}$ is the elastic part of the spin tensor. The unconstrained misfit strain associated with the formation of δ-hydrides were calculated to be 4.58% and 7.2% along the HCP crystal a-axis and c-axis, respectively (Carpenter, 1973):

$$\varepsilon^{trH} = \begin{bmatrix} 0.0458 & 0 & 0 \\ 0 & 0.0458 & 0 \\ 0 & 0 & 0.072 \end{bmatrix} \tag{5-7}$$

This transformation strain is applied incrementally over the time period of 3600 seconds to the domain that undergoes phase transformation. When two hydrides are modeled, the HITS is applied to both hydride domains in the same time step.

## 5.2.2 Stress-assisted hydrogen diffusion

The flux of hydrogen atoms ($\vec{J}$) within zirconium matrix depends on the concentration (C) and velocity of hydrogen atoms ($\vec{v}$):

$$\vec{J} = \vec{v}C \tag{5-8}$$

The velocity of hydrogen is proportional to its mobility ($M$) and the gradient of the chemical potential ($\mu$):

$$\vec{v} = -M\vec{\nabla}\mu$$

$$M = \frac{D}{RT} \text{ where } D = \begin{bmatrix} D_a & & \\ & D_a & \\ & & D_c \end{bmatrix} \tag{5-9}$$

where R is the universal gas constant, $\mu$ is the chemical potential of hydrogen in zirconium, and T is the absolute temperature ($K$). The diffusivity of hydrogen atoms along the a-axis ($D_a$) and c-axis ($D_c$) of the HCP zirconium crystals for the temperature range of 300K-1100 K is presented in Zhang et al. and can be written as (Zhang et al., 2017):

$$D_c = 1.08 \exp\left(-\frac{0.46}{8.6 \times 10^{-5}T}\right)$$

$$D_a = D_c(-3.3 \times 10^{-7}T^2 + 7 \times 10^{-4}T + 0.8298)^{-1} \tag{5-10}$$

in which diffusivities are in units of mm$^2$/s. The chemical potential of the diffusing hydrogen can be written as:

$$\mu = \mu_0 + RTlnC - \frac{\sigma_{kk}}{3}\bar{V}_H \tag{5-11}$$

where $\mu_0$ is the reference chemical potential, $\frac{\sigma_{kk}}{3}$ represents the hydrostatic stress, and $\bar{V}_H$ is the partial molar volume of the hydrogen atoms in the Zr lattice and is 1670 mm$^3$/mol.

Combining equations 5-8, 5-9 and 5-11, the equation for hydrogen flux can be rewritten as:

$$\vec{J} = -\boldsymbol{D} . \left[ \vec{\nabla} C + C . lnC \frac{\vec{\nabla} T}{T} - C \frac{\bar{V}_H}{3.RT} \vec{\nabla} \sigma_{kk} \right] \tag{5-12}$$

where $\frac{\vec{\nabla} \sigma_{kk}}{3}$ represents the gradient of hydrostatic stress. According to Eq. 5-12, the three parameters affecting mass flux are the gradient of mass concentration, the gradient of temperature (known as temperature-driven diffusion), and the gradient of hydrostatic stress (known as stress-assisted diffusion). When diffusion happens under constant temperature, the second term on the right-hand side of Eq. 5-12 will be zero. In this chapter, the focus is solely on the effects of stress on mass diffusion, i.e., we solve for isothermal case where the gradient of temperature is zero. The general form of diffusion equation derived from a control volume can be written as:

$$\frac{\partial C}{\partial t} = -\nabla . \vec{J} \tag{5-13}$$

For the steady state condition, the derivative of concentration with respect to time will be zero.

The format of Eqs. 5-12 and 5-13 is very similar to the conductive heat transfer equations used for calculating temperature distribution in the presence of heat sinks and sources. In Abaqus FE solver, UMATHT can be used for modeling coupled temperature-displacement problems, but by replacing temperature with concentration (C), this subroutine can be used for coupled diffusion-displacement problems. Following the method discussed in the study by Abdolvand (Abdolvand, 2019), Eqs. 5-9 to 5-13 are implemented in a UMATHT subroutine to solve for hydrogen concentration.

To summarize, the total strain and time increments provided at the beginning of each time increment are used to calculate stress increment using Eqs. 5-1 to 5-6 (Abaqus Documentation, 2020). If a domain undergoes hydride formation, the HITS provided in Eq. 5-7 is applied to the domain to replicate the strain fields around the δ-hydride. The updated stress matrix at each IP is then used to calculate hydrostatic stress, and with the

use of current coordinates of the same IP, the gradients of hydrostatic stress are calculated. The calculated $\vec{\nabla}\sigma_{kk}$ is subsequently sent to UMATHT to calculate hydrogen concentration using Eqs. 5-12 and 5-13.

## 5.2.3 Input models

All simulations are conducted at the constant temperature of 603K to replicate the nominal operation temperature of nuclear reactors. Hydrogen is known to be very mobile at this temperature (Kearns, 1967; Puls, 2012). In the following simulations, it is assumed that the initial hydrogen concentration is 100 wt.ppm, which is consistent with the solubility limit of hydrogen in zirconium lattice at 603K. Due to the high diffusivity of hydrogen atoms in zirconium at elevated temperatures, all simulations are conducted assuming the steady state condition. Unless hydride reorientation is studied, the parent-precipitate relationship reported in the literature is used, which indicates that δ-hydrides form nearly parallel to the basal plane of the parent crystal. Unless otherwise is stated, the parent grain within which the hydride region is embedded has the Euler angles of (45 90 0). That is, the misorientation of the crystal c-axis and the loading direction is 45° (see Fig. 5-2). The Euler angles presented in this work follow the Bunge convention for $\varphi_1, \varphi$, and $\varphi_2$ with crystals rotating about Z, X and Z axes, respectively. The parent grain orientation considered in this work implies an intermediate "hard-soft" behavior. Lastly, the c-axis of the HCP crystals in nuclear pressure tubes are mainly oriented towards the transverse direction with some variation towards the radial direction. Here, the Euler angles are selected such that the HCP crystal c-axis represents a point in between the two directions.

The elastic modulus of zirconium single crystal used in this study are those reported in Fisher and Renken: $C_{11}$=143.5 GPa, $C_{33}$=164.9 GPa, $C_{12}$=72.5 GPa, $C_{13}$=65.4 GPa, and $C_{44}$=32.1 GPa (Fisher and Renken, 1964). Plastic behavior of zirconium is modelled using the Voce hardening parameters reported in the study by Abdolvand and Daymond and are summarized in Table 5-1 (Abdolvand and Daymond, 2013).

**Table 5-1 - The single crystal parameters used for zirconium (Abdolvand and Daymond, 2013)**

| Slip system | n | $\dot{\gamma}_0(s^{-1})$ | $g_0^\alpha$ (Gpa) | $g_1^\alpha$ (GPa) | $\theta_0^\alpha$ (GPa) | $\theta_1^\alpha$ (GPa) |
|---|---|---|---|---|---|---|
| Prism | 20 | $3.5 \times 10\text{-}4$ | 0.12 | 0.33 | 0.01 | 0 |
| Basal | 20 | $3.5 \times 10\text{-}4$ | 0.168 | 0.22 | 0.05 | 0 |
| Pyramidal <c+a> | 20 | $1.0 \times 10\text{-}4$ | 0.331 | 0.27 | 0.62 | 0.28 |

The material property of the continuous δ-hydride domain is considered to be linear elastic and isotropic with E=100 GPa and ν = 0.33, as reported in Puls et al. (Puls, 2012; Puls et al., 2005). It should be noted that the hydride domains in this study are considered continuous, which are referred as "macroscopic" hydrides in the literature. The effects of stacking of hydride platelets, which are referred as "microscopic" hydrides, are discussed in section 5.4.2.

## 5.2.3.1 The interaction of parallel hydrides

Previous studies have shown that hydride tips undergo higher levels of tensile stresses compared to the inner parts of the parent grain, further from the hydride domain (Tondro and Abdolvand, 2021). Also, compressive stresses develop along the hydride sides. Hence, hydrogen atoms tend to diffuse towards hydride tips, and away from hydride sides, which further leads to propagation of hydrides from their tips. Initially, most of the precipitated hydrides in pressure tubes are oriented along the transverse direction, resulting in formation of parallel hydrides. Furthermore, neighboring hydrides interact with one another due to their stress fields and form interlinked hydride structures. These structures are shown by SEM images (Chu et al., 2008), an example of which is shown in Fig. 5-1. The FE model of this section is designed to simulate the interaction of stress fields of two parallel hydrides. For this purpose, two elongated hydrides, as illustrated by the white boundaries of Fig. 5-2, are embedded in a zirconium single crystal. Both hydrides form nearly on the basal plane of the parent grain and hence are parallel. Therefore, this model will be referred to "Par-DH" (standing for parallel direction hydrides) in the rest of the chapter. The size of the model along X and Y axis is 200 μm, and the thickness of the sample is set to be 1 μm

(see Fig. 5-2). The distance "d" between the tips of the hydrides is studied to understand the probability of hydrides interlinking. The value of "d" is set to vary between 5 μm and 70 μm. Also, the hydride regions are densely meshed, especially close to the tips of the hydrides. The element type used in all simulations is second order coupled "displacement-concentration" brick elements (C3D20RT). It should be noted that the width and length of the hydrides are 0.5 μm and 50 μm, and are kept constant in order to neutralize their effects, but the effects of hydride geometry are discussed in section 5.4.1. A summary of the model specifications for this section is presented in Table 5-2.
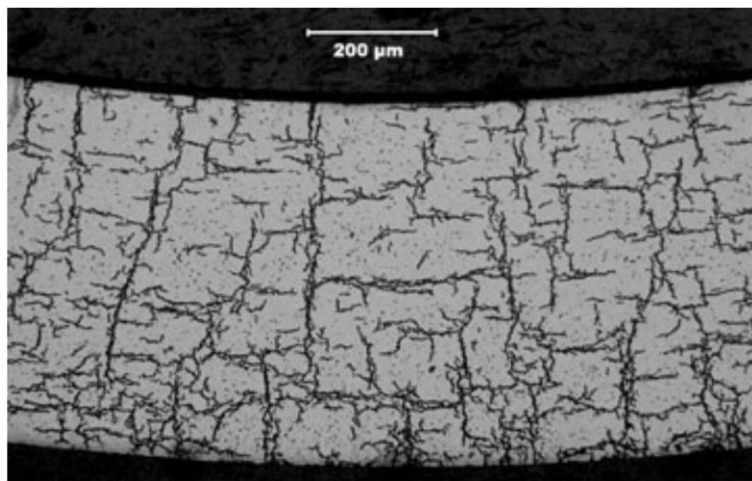


**Fig. 5-1 – Microscopic image of a pressure tube showing the formation of both transverse hydrides and reoriented radial hydrides (Bilone et al., 2012).**

**Table 5-2 - Finite element models for parallel hydrides and their corresponding hydrides distances**

| Model No. | Distance between hydrides, d (µm) | Model No. | Distance between hydrides, d (µm) |
|-----------|-----------------------------------|-----------|-----------------------------------|
| Par-DH-1  | 5    | Par-DH-8  | 30 |
| Par-DH-2  | 7.5  | Par-DH-9  | 35 |
| Par-DH-3  | 10   | Par-DH-10 | 45 |
| Par-DH-4  | 12.5 | Par-DH-11 | 50 |
| Par-DH-5  | 15   | Par-DH-12 | 60 |
| Par-DH-6  | 20   | Par-DH-13 | 70 |
| Par-DH-7  | 25   |           |    |

The simulation steps can be summarized as:

Step-1: mechanical boundary conditions (BC) are applied to the model. The boundary conditions of the left and bottom surfaces of the model are $U_x=0$ and $U_y=0$, respectively. Here, $U_i$ represents displacement along the i$^{th}$ direction. Also, $U_z=0$ is applied to the top edge of the model. These boundary conditions remain active throughout the entire simulation. For the diffusion boundary condition, the four surfaces perpendicular to the X and Y axis are set to have 100 wt.ppm of hydrogen throughout the simulation.

Step-2: the model is loaded up to 0.3% ($\varepsilon_x$) using the strain rate of $5 \times 10^{-5}\ s^{-1}$.

Step-3: Over 3600 s, the HITS is applied onto the domains determined as δ-hydrides to replicate the volumetric strain of hydriding using a quasi-static strain rate of $5 \times 10^{-5}\ s^{-1}$. The applied load in the previous step is kept constant, i.e., HITS is applied under constant strain. The concentration of hydrogen atoms and vonMises stress are studied at the end of this step.
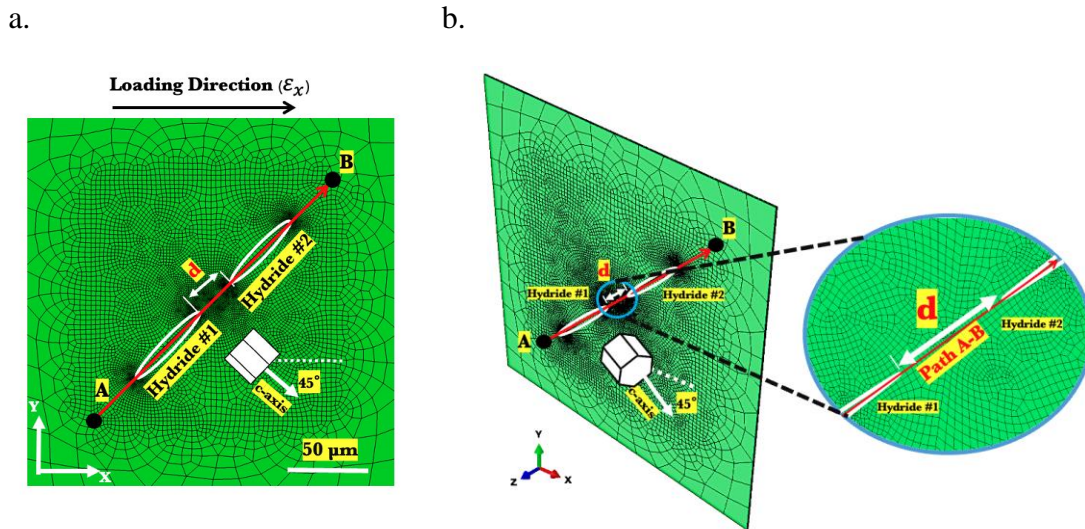
**Fig. 5-2 – (a) The XY plane view and (b) the 3D view of the finite element input models used for simulating the interaction of parallel hydrides. The two hydrides form on the basal plane of the parent grain. The parent grain orientation is shown schematically. The hydrides widths are exaggerated for a better visualization.**

The HITS is applied under constant applied strain, but the effects of this external load during hydride formation are discussed in section 5.4.3.

## 5.2.3.2 Interaction of perpendicular hydrides

Depending on temperature gradients and external loading conditions, zirconium hydrides may reorient during the service of nuclear reactors from a transverse configuration to a radial configuration (Cinbiz et al., 2016; Singh et al., 2004; Weekes et al., 2016). The configuration used in this section is based on the SEM images in the literature showing the presence of both initial hydride precipitates and reoriented hydrides (Chu et al., 2008). The input model described in this section aims to study the interaction of a reoriented hydride with a neighboring hydride which has not yet reoriented. For this purpose, Hydride#1 region is reoriented towards the c-axis of the parent grain so that the two hydrides take a perpendicular position with respect to each other (see Fig. 5-3). The models described in this section will be referred to as "Per-DH" in the rest of this chapter. The schematic of the setup is shown in Fig. 5-3. The BCs and hydride geometries are the same as the ones described for the model representing parallel hydrides. Similarly, "d" represents the

distance in between the lower tips of the two hydrides and varies between 5 µm and 70 µm (see Fig. 5-3). A summary of the FE input models is listed in Table 5-3.

**Table 5-3 – Finite element models for perpendicular hydrides and their corresponding hydride distances**

| Model No. | Distance between hydrides, d (µm) | Model No. | Distance between hydrides, d (µm) |
|---|---|---|---|
| Per-DH-1 | 5 | Per-DH-7 | 30 |
| Per-DH-2 | 7.5 | Per-DH-8 | 35 |
| Per-DH-3 | 10 | Per-DH-9 | 45 |
| Per-DH-4 | 15 | Per-DH-10 | 50 |
| Per-DH-5 | 20 | Per-DH-11 | 60 |
| Per-DH-6 | 25 | Per-DH-12 | 70 |

The simulation steps for this model can be summarized as:

Step-1: mechanical BCs similar to the case of parallel hydrides are applied to the model.

Step-2: the model is loaded up to 0.3% of strain ($\varepsilon_x$) using the strain rate of $5 \times 10^{-5} \ s^{-1}$.

Step-3: HITS is applied to the Hydride#2 domain, which is the hydride formed on the basal plane of the parent grain.

Step-4: the model is further loaded to 1.0% of strain ($\varepsilon_x$).

Step-5: HITS is applied to the domain representing Hydride#1. This hydride is formed after the extension of external loading to simulate the role of "reoriented" hydrides in nuclear pressure tubes.
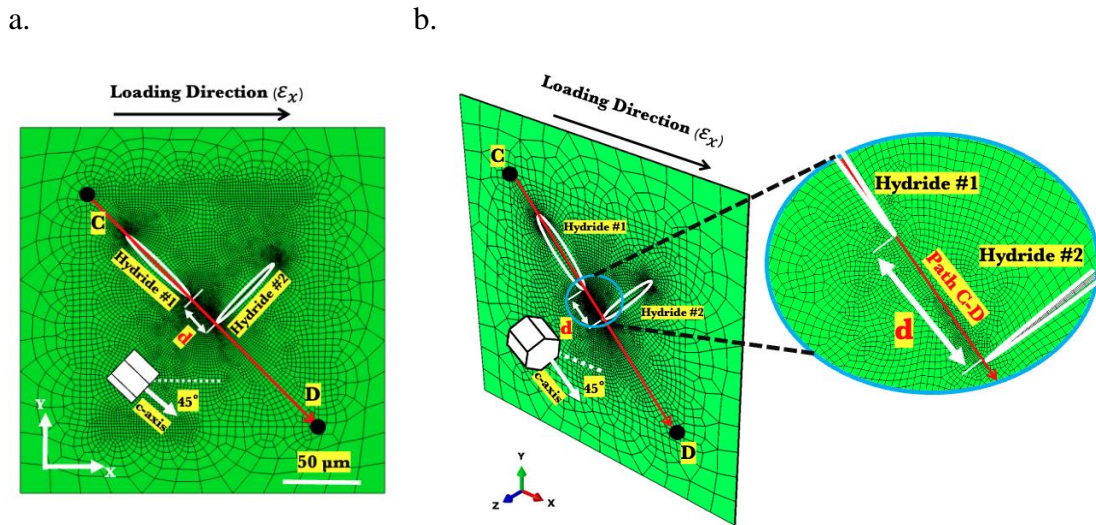
**Fig. 5-3– (a) The XY view and (b) the 3D view of the finite element input models used for simulating the interaction of perpendicular hydrides. Hydride#2 is on the basal plane of the parent grain, while Hydride#1 is reoriented towards its c-axis. The parent grain is shown schematically. Distance "d" is along Path C-D, between the lower tips of the hydrides. The hydrides widths are exaggerated for better visualization.**

The extra loading step in this model is to deform the parent grain to the stress state above which reorientation is reported to happen, i.e., ~ 300 MPa.

## 5.3 Results

### 5.3.1 The interaction of parallel hydrides

The results for the interaction of zirconium hydrides formed in parallel are presented in this section. The state of vonMises stress is presented first as a representative for the extent of interaction between the stress fields from the two hydrides. A comparison of vonMises stress contours for six models with different "d" values is presented in Fig. 5-4. It is shown that the field of interaction between the hydrides gradually weakens as "d" increases. The stress fields for other models are not shown to avoid busy figures but follow the same trend.
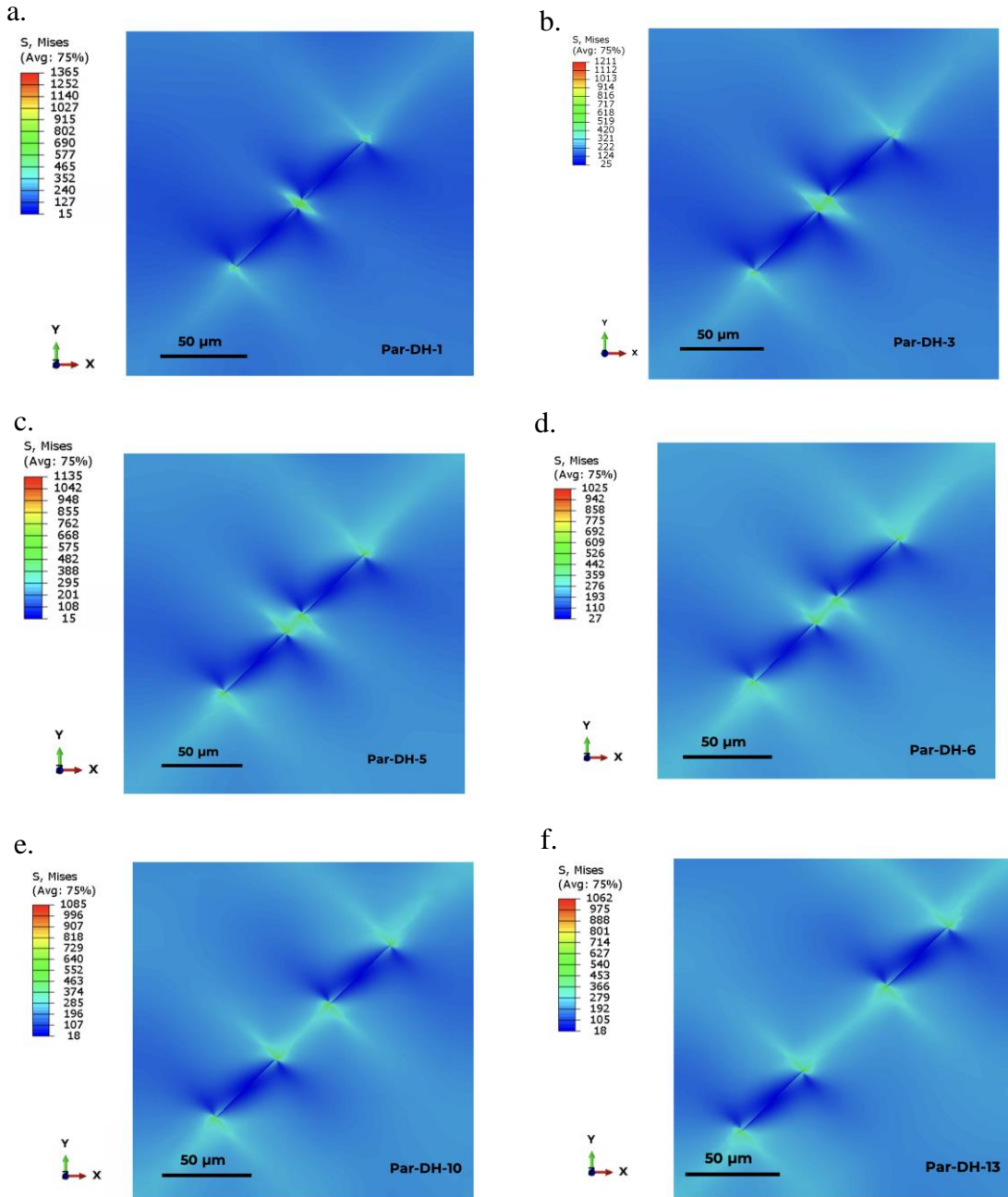
**Fig. 5-4 – The distributions of vonMises stresses for Par-DH models with parallel hydrides. vonMises stresses are shown at various hydride distances: (a) Par-DH-1 (d=5 μm), (b) Par-DH-3 (d=10 μm), (c) Par-DH-5 (d=15 μm), (d) Par-DH-6 (d=20 μm), (e) Par-DH-10 (d=45 μm), and (f) Par-DH-13 (d=70 μm).**

The distribution of vonMises stresses along the Path A-B and between the hydrides for various "d" values is presented in Fig. 5-5a and b. In these figures, the x-axis represents the normalized distance between the upper tip of Hydride#1 and the lower tip of Hydride#2,

along Path A-B (see Fig. 5-2). It is shown that hydride stress fields highly interact when "d" is small, but with increasing the distance between the hydrides, vonMises stress starts to converge, suggesting the interaction of hydrides becomes less significant. Fig. 5-6 shows the relationship between "d" and the magnitudes of vonMises stresses at the midpoint in between the two hydrides, i.e., normalized distance of 0.5. The results of this figure show that the variation of vonMises stress is the steepest at distances less than 20 µm. At distances beyond 45 µm, the variation in the magnitude of vonMises stress is less than 3%. It can also be seen that hydride stress fields are affected the most at distances less than 20 µm, but stabilizes between distances of 20 µm to 30 µm, with hydride interaction becoming negligible for the distances beyond 45 µm.

a.



b.
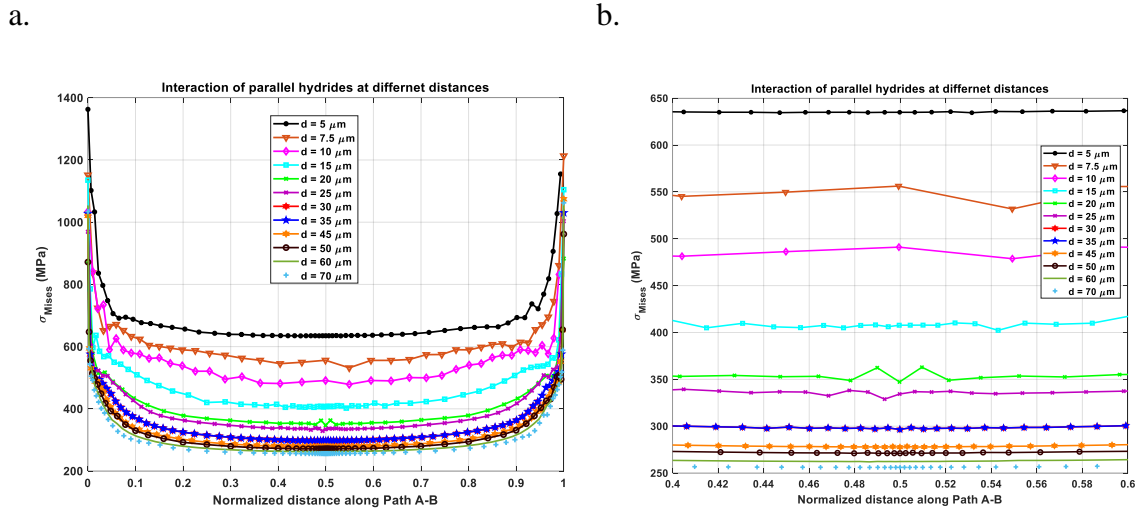


**Fig. 5-5 – (a) The distribution of vonMises stresses along the Path A-B vs. the normalized distance "d". A zoomed-in view of the same plots between the normalized distances of [0.4, 0.6] is shown in (b). Path A-B and "d" are shown in Fig. 5-2.**

It is expected that vonMises stress peaks in between the normalized distances of [0, 0.1] and [0.9, 1]. This is due to the formation of highly localized plasticity zones near the tips of the hydrides. Hydride interaction likely occurs closer to the center, in between the two hydrides, e.g., at the normalized distance of 0.5. This is where the two stress fields from hydrides overlap. In the model with d = 5 µm (Par-DH-1), for instance, vonMises stress between the hydrides is relatively a straight line because the tips of the hydrides are very close. As such, the vonMises stress is constantly high and does not decrease along the 5 µm distance. As the distance between the hydrides increases, e.g., in Par-DH-2 model, the vonMises stress decreases at some points along the Path A-B.
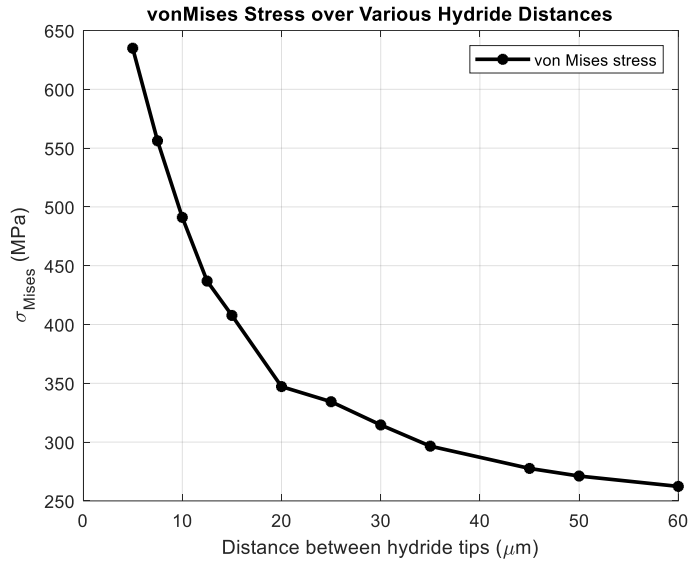
**Fig. 5-6 – vonMises stress at the middle of path A-B vs. "d", the distance between the hydrides. Results are for parallel hydrides.**

The distributions of hydrogen concentration between the tips of the parallel hydrides are shown in Fig. 5-7. As shown in Fig. 5-7a, the interaction between the hydrides in the model with d = 5 µm (Par-DH-1) is the highest and gradually weakens and barely exists beyond d = 20 µm (Par-DH-6). This is consistent with the results shown previously for the distribution of vonMises stress. Results for the rest of the models follow the same trend.
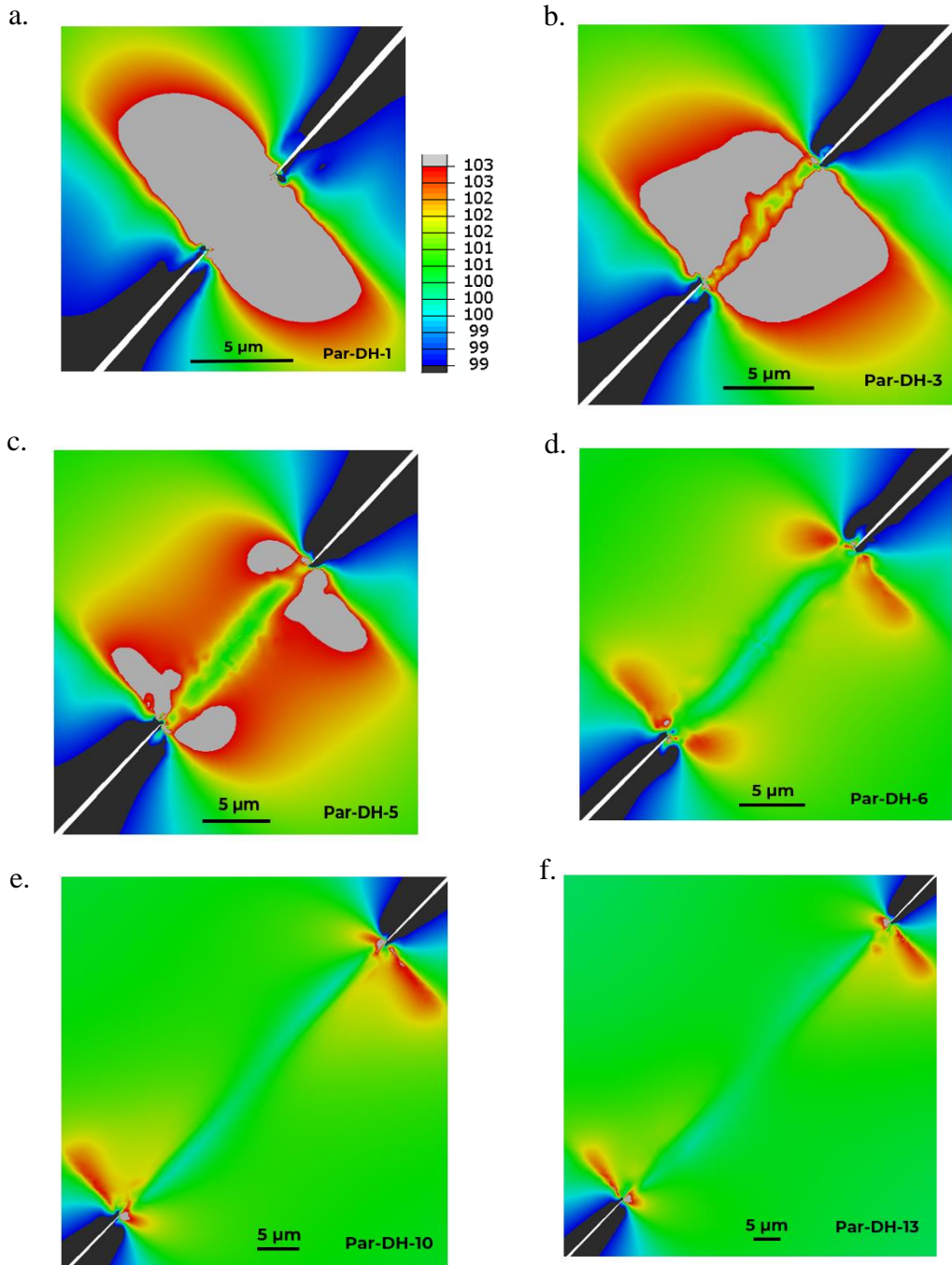
**Fig. 5-7 – The distributions of hydrogen concentration for Par-DH models with parallel hydrides: (a) Par-DH-1 (d=5 μm), (b) Par-DH-3 (d=10 μm), (c) Par-DH-5 (d=15 μm), (d) Par-DH-6 (d=20 μm), (e) Par-DH-10 (d=45 μm), and (f) Par-DH-13 (d=70 μm). The same hydrogen concentration limits are used in all the subfigures for a better comparison. All numbers are in wt.ppm.**

The interaction of hydrides is also investigated by averaging the concentration of hydrogen atoms in between the hydrides. In the results presented below, hydrogen concentration is

the average of the calculated values in the area A1, between the upper tip of Hydride#1 and the lower tip of Hydride#2, as shown with the red box in Fig. 5-8b. The width of A1 is chosen to be 0.5 μm, to be consistent with the width of the hydride domains. In agreement with the results obtained from comparison of vonMises stresses as well as the hydrogen distributions shown in Fig. 5-7, results obtained using averaging hydrogen concentrations also imply that interaction of hydrides decreases exponentially and is most significant at d < 20 μm.

a.



b.
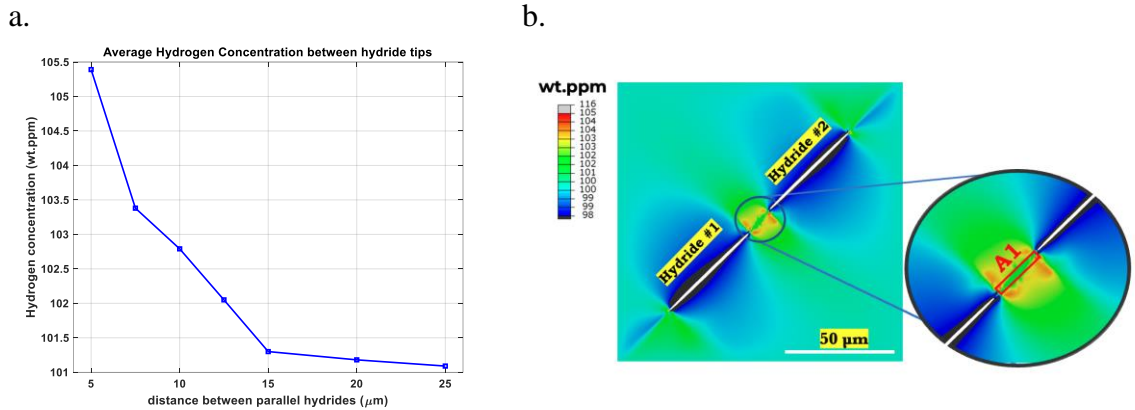


**Fig. 5-8 – (a) The average hydrogen concentration as a function of "d"- the distance between parallel hydrides. Hydrogen concentrations are averaged in the area A1, shown in (b).**

## 5.3.2 The interaction of perpendicular hydrides

Similar to the previous section, vonMises stresses are compared to study the interaction of perpendicular hydrides. The results for six representative models with different "d" values are presented in Fig. 5-9. It can be seen from the distribution of vonMises stresses that field of interaction between the hydrides gradually weakens with "d" increasing.
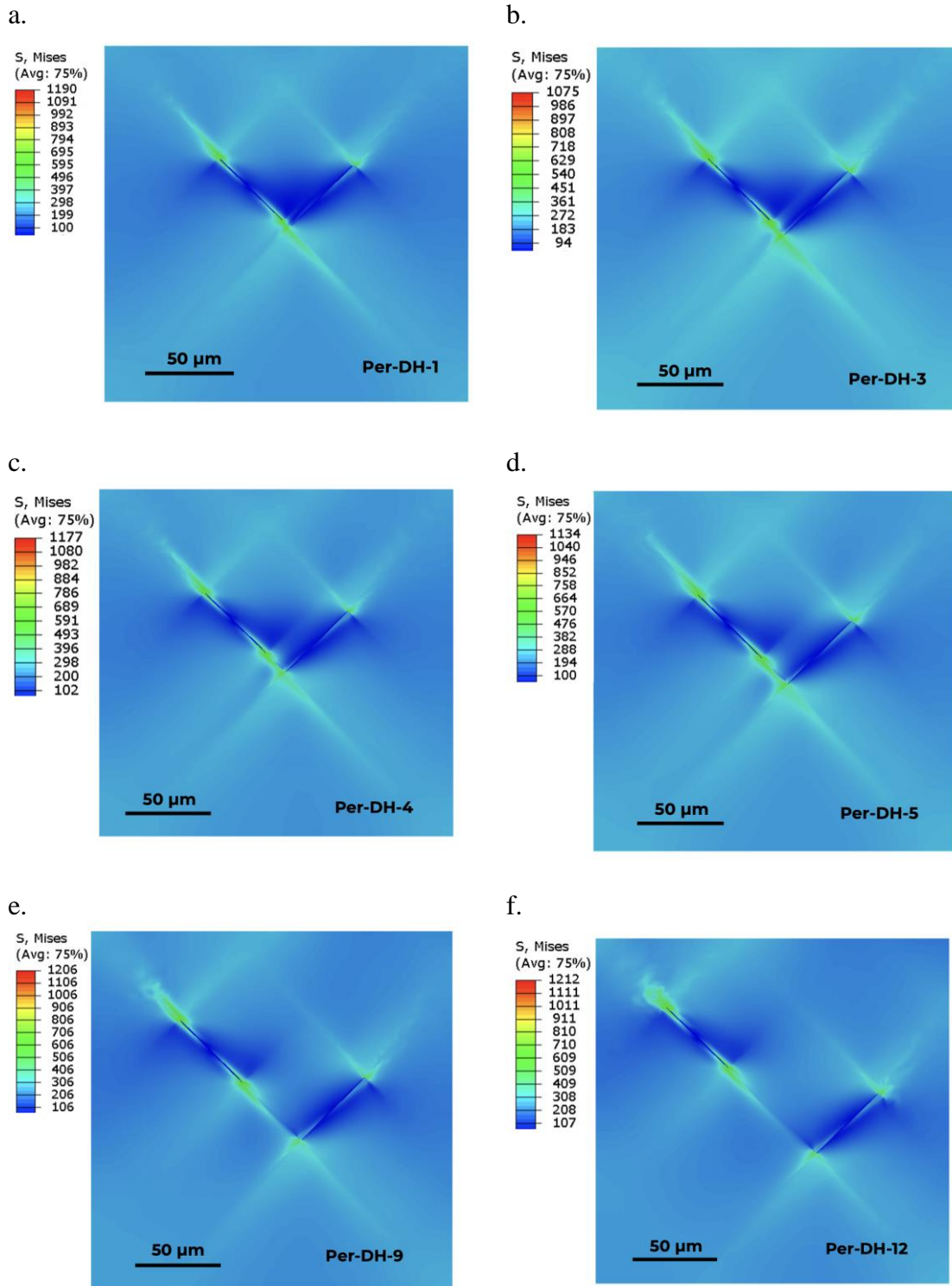
**Fig. 5-9 – The distributions of vonMises stresses for Per-DH models with perpendicular hydrides. vonMises stresses are shown at various hydride distances: (a) Per-DH-1 (d=5 μm), (b) Per-DH-3 (d=10 μm), (c) Per-DH-4 (d=15 μm), (d) Per-DH-5 (d=20 μm), (e) Per-DH-9 (d=45 μm), and (f) Per-DH-13 (d=70 μm).**

Fig. 5-10 shows the distribution of vonMises stresses for different hydride distances along the Path C-D (shown in Fig. 5-3). The starting point of the x-axis in Fig. 5-10 is where the lower tip of Hydride#1 is located (see Fig. 5-3). With moving further away from the hydride tip, the magnitude of vonMises stress decreases. However, the rate of stress decrease is different for different models, e.g., a steeper decrease rate indicates a reduced interaction between the two hydrides. After a certain "d", the interaction of hydrides can be considered negligible. As shown in Fig. 5-10, it can be concluded that the interaction of hydrides in the perpendicular configuration is most significant at distances < 15 μm, and can be considered negligible beyond distances of 20 μm.

In comparison to parallel hydrides, perpendicular hydrides are less likely to propagate and interlink. Also, a stronger interaction is observed between parallel hydrides since their growth directions are aligned increasing the possibility of further hydride precipitation.

a.                                          b.
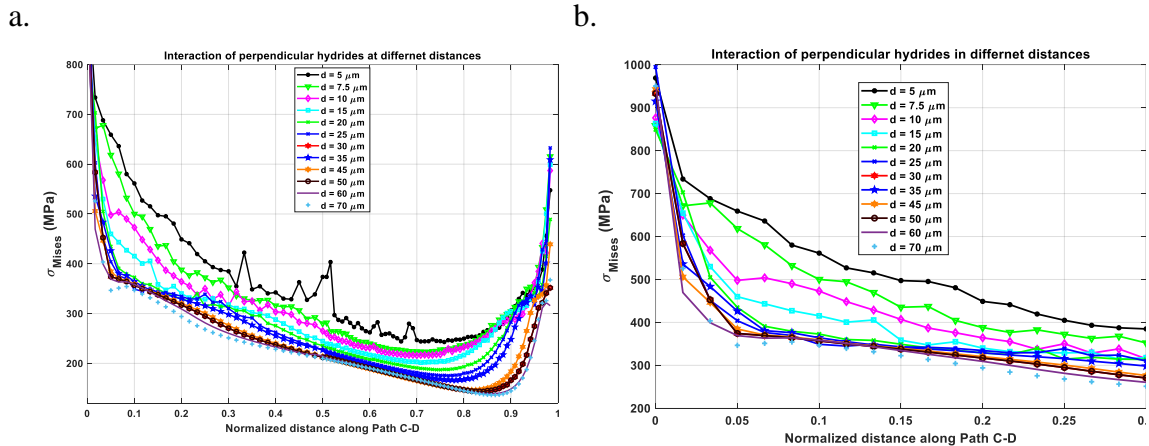


**Fig. 5-10 – (a) The distribution of vonMises stress vs. normalized distance "d" along the Path C-D for perpendicular hydrides. (b) A zoomed-in view of (a) for the normalized distance of [0, 0.3] where most of the interactions take place.**

The distributions of hydrogen concentrations for models with d < 20 μm are shown in Fig. 5-11. In this figure, in agreement with the results obtained from comparison between the vonMises stresses, the interaction of two perpendicular hydrides is significant at d < 15 μm and becomes negligible beyond d = 20 μm. Furthermore, the hydrogen concentration peaks along the axial direction of the radial hydride, implying that the propagation of hydride is more likely to happen along the radial direction.

122
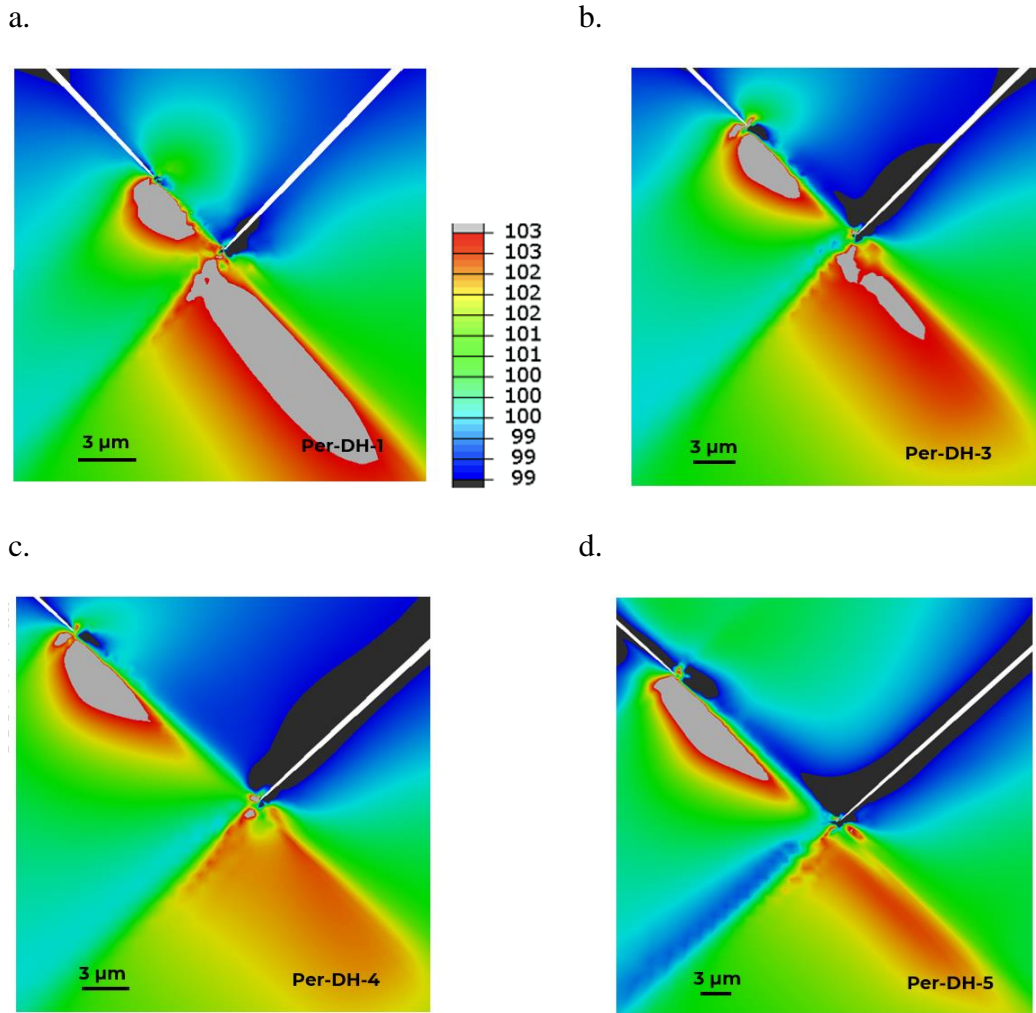
**Fig. 5-11 – The distributions of hydrogen concentration for Per-DH models with perpendicular hydrides: (a) Per-DH-1 (d=5 μm), (b) Par-DH-3 (d=10 μm), (c) Par-DH-4 (d=15 μm), (d) Par-DH-5 (d=20 μm). The same hydrogen concentration limits are used in all the subfigures for a better comparison. All numbers are in wt. ppm.**

## 5.4 Discussion

The stress and hydrogen distribution fields shown so far are affected by the size of the hydride and the applied BCs. Hence, in this section, a parametric study is conducted to discuss the effects of hydride size, stacking of micro-hydrides, and applied BCs on the results.

## 5.4.1 The effects of hydride geometry

One single hydride embedded in a zirconium single crystal is used to study the effects of hydride size on the results presented. The geometry and set-up of the parent grain is the same as the ones used so far, i.e., the Euler angles of the parent grain are (45 90 0), and the hydride is extruded throughout the sample thickness. There are three parameters affecting the results: length of the hydride (L), width of the hydride (W), and the applied external load. As such, models with different hydrides widths and lengths are simulated with and without external loads. A schematic of the model setup and the hydride domain is shown in Fig. 5-12. A summary of the conducted simulations is presented in Table 5-4. In this table, SH stands for models with single hydride.
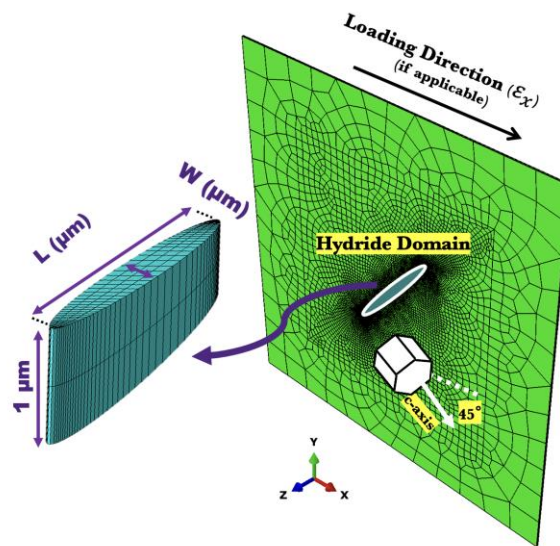


**Fig. 5-12 – 3D view of the finite element input model used for studying the effects of hydride geometry. The width (W) and length (L) of the hydride are shown schematically. The hydride geometry is exaggerated for better visualization.**

**Table 5-4– Finite element models of zirconium hydrides with different lengths and widths**

| Model No. | External Loading | Hydride Length (μm) | Hydride Width (μm) | Aspect Ratio (L/W) |
|---|---|---|---|---|
| SH-1 | no load | 50 | 0.5 | 100 |
| SH-2 | no load | 70 | 0.5 | 140 |
| SH-3 | no load | 90 | 0.5 | 180 |
| SH-4 | no load | 110 | 0.5 | 220 |
| SH-5 | $\varepsilon_x = 1.0\%$ | 50 | 0.5 | 100 |
| SH-6 | $\varepsilon_x = 1.0\%$ | 70 | 0.5 | 140 |
| SH-7 | $\varepsilon_x = 1.0\%$ | 90 | 0.5 | 180 |
| SH-8 | $\varepsilon_x = 1.0\%$ | 110 | 0.5 | 220 |
| SH-9 | no load | 90 | 1 | 90 |
| SH-10 | $\varepsilon_x = 1.0\%$ | 90 | 1 | 90 |
| SH-11 | no load | 70 | 1 | 70 |
| SH-12 | $\varepsilon_x = 1.0\%$ | 70 | 1 | 70 |
| SH-13 | no load | 90 | 2 | 45 |
| SH-14 | no load | 90 | 3 | 30 |
| SH-15 | $\varepsilon_x = 1.0\%$ | 70 | 2 | 35 |
| SH-16 | no load | 70 | 2 | 35 |
| SH-17 | no load | 70 | 3 | 23 |
| SH-18 | $\varepsilon_x = 1.0\%$ | 90 | 2 | 45 |
| SH-19 | $\varepsilon_x = 1.0\%$ | 90 | 3 | 30 |

The calculated hydrogen concentration and hydrostatic stress at the hydride tip for case studies with a constant width of 0.5 µm and different hydride lengths are respectively

shown in Fig. 5-13a and b. In these figures, only the length of hydride is changed. As hydride length increases from 50 µm to 110 µm, both hydrogen concentration and hydrostatic stress slightly increase. The models with externally applied loads demonstrate higher values of hydrogen concentrations because of the accelerated diffusion of hydrogen atoms. The difference in hydrostatic stress with applying external loads is 70 MPa to 100 MPa higher than the cases where no external load is applied. As the hydride length increases and since there exists more surface area of the hydride in contact with the surrounding zirconium matrix, higher hydrogen concentration and hydrostatic stress are calculated.

Hydrogen Concentration                    Hydrostatic Stress

a.

**Effect of Hydride Lengths at W=0.5 $\mu$m on Hydrogen Concentr**



b.

**Effect of Hydride Lengths at W=0.5 $\mu$m on Hydrostatic**



c.

**Effect of Hydride Width at L=90 $\mu$m on Hydrogen Concentra**



d.

**Effect of Hydride Widths at L=90 $\mu$m on Hydrostatic Stre**
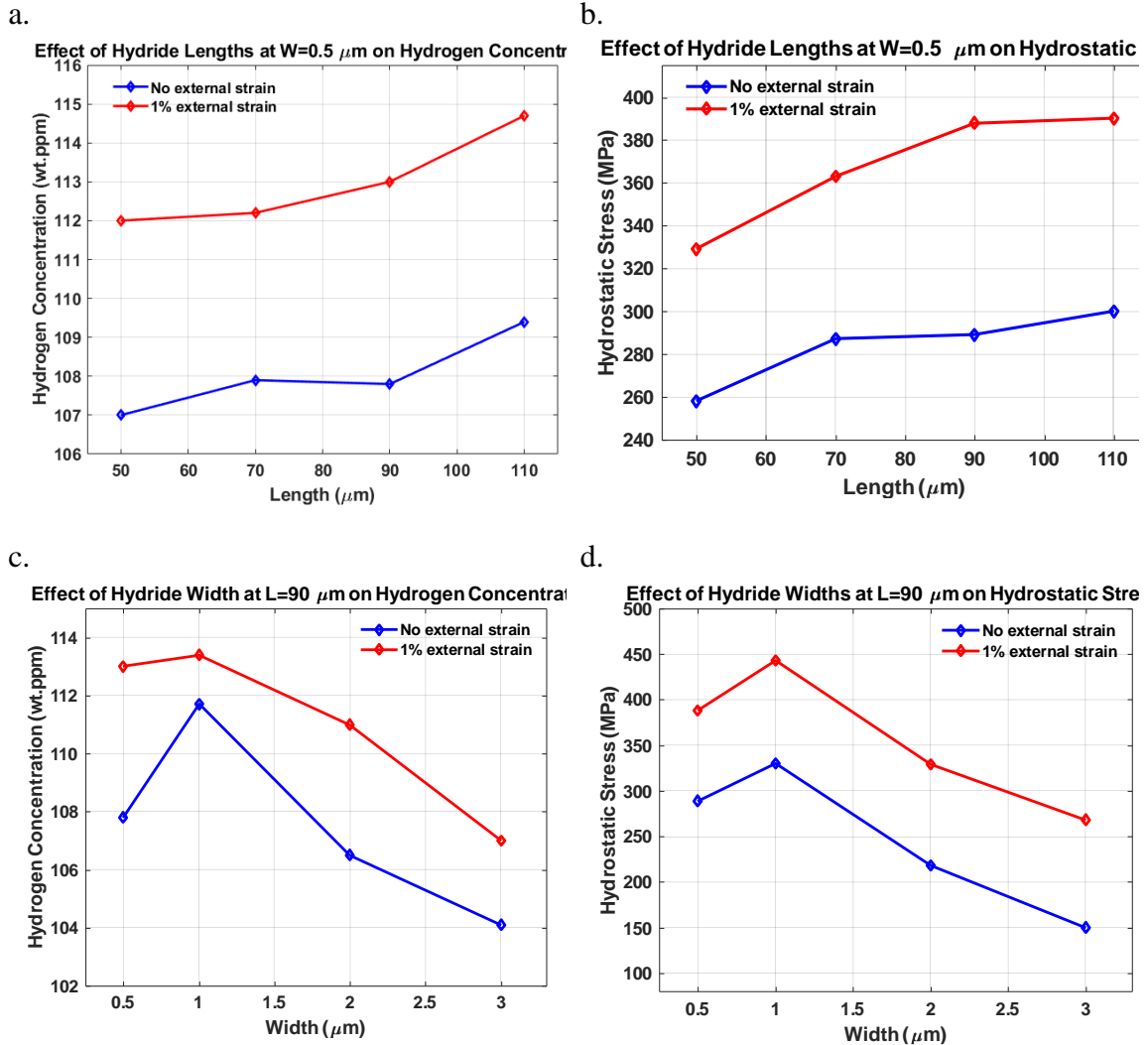


**Fig. 5-13- (a) Hydrogen concentration and (b) hydrostatic stress for different hydride lengths at the constant width of 0.5 µm. Hydrogen concentration and hydrostatic stress for a constant length of 90 µm and different hydride widths are shown in (c) and (d). Each figure contains the data for both no external load as well as 1% applied strain.**

The calculated results for hydrogen concentration and hydrostatic stress at a constant hydride length of 90 µm but different widths are respectively shown in Fig. 5-13c and d. As shown, a width of 1 µm is where the hydrogen concentration peaks and as the width is increased further, the concentration decreases. The same trend is also captured for the hydrostatic stress. As the width of the hydride increases, the volume of the hydride increases as well, but the hydride tips become less sharp. Therefore, the surface area of the

hydride tip, which is in contact with the zirconium matrix, increases and a more distributed hydrogen is calculated at the tip of the hydrides. It can be concluded that beyond the widths of 1 µm, the effects of hydride sharpness are overshadowed by those of hydride volume.

## 5.4.2 The effects of hydride platelets: macro-hydrides vs. micro-hydrides

In this section, the assumption of modeling a hydride as a continuous domain is examined. Two case studies are considered for this purpose: (1) a single crystal with a continuous macro-hydride, as the one used in this chapter and studied in section 5.4.1, and (2) a single crystal with parallel platelets of micro-hydrides. The orientation of the single crystal for both models is the same as the one used previously, and is schematically shown in Fig. 5-14a. All the other contributing parameters in both models are considered the same. A comparison of the hydride regions used in these models is shown in Fig. 5-14b. It should be noted that in the latter model, the micro-hydrides platelets are modelled such that their habit planes are parallel to their basal planes and their packets growth direction is at 14.7° away from the basal plane (parallel to $\{10\bar{1}7\}$ planes), as reported in the literature (Motta et al., 2019; Weekes et al., 2015). The length of the hydride is chosen as 50 µm and width of the macro-hydride is chosen to be the most critical width (W = 1 µm) calculated in section 5.4.1. The dimensions and the "stack separation" parameter, referred with $\lambda_H$, for hydride platelets are the ones reported in the study by Patel et al. and are summarized in Fig. 5-14b (Patel et al., 2021).
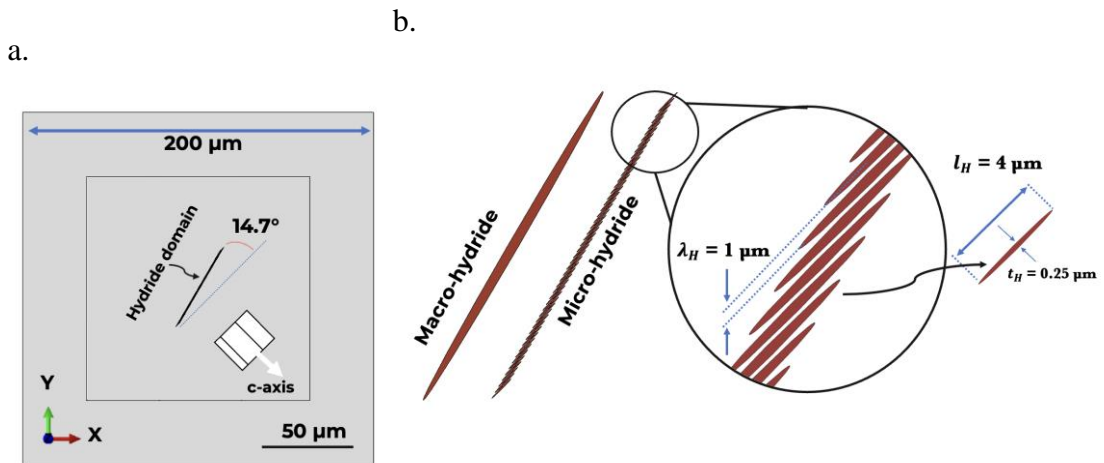
**Fig. 5-14 – (a) The schematic of the model used for comparing macro-hydrides and micro-hydrides. The growth direction of hydride packet in both models is oriented at 14.7° away from the basal plane. A comparison between the macro- and micro-hydride regions is shown in (b). The dimensions of the micro-hydride platelet are shown in (b). In both models, the length and width of the "hydride packet" are considered 50 μm and 1 μm, respectively.**

The comparison between the results of hydrogen concentration and hydrostatic stress is presented in Fig. 5-15. As shown, the tips of the "hydride packet" in the micro-hydride model and the tips of the macro-hydride are both the sites at which hydrogen concentration and hydrostatic stress peak. This shows that, in both cases, the growth of hydrides takes place along the axial direction and at the tip of the "hydride packet". Results of this section imply that simulating hydrides either as a continuous medium or as discontinuous hydride platelets could both lead to higher stresses and hydrogen concentrations in the vicinity of hydrides; however, the macro-hydride model calculates higher hydrostatic stresses and higher hydrogen concentration at the tips of the hydride packet. This is due to a higher volume of the model undergoing HITS.

Hydrogen Concentration　　　　　　Hydrostatic Stress
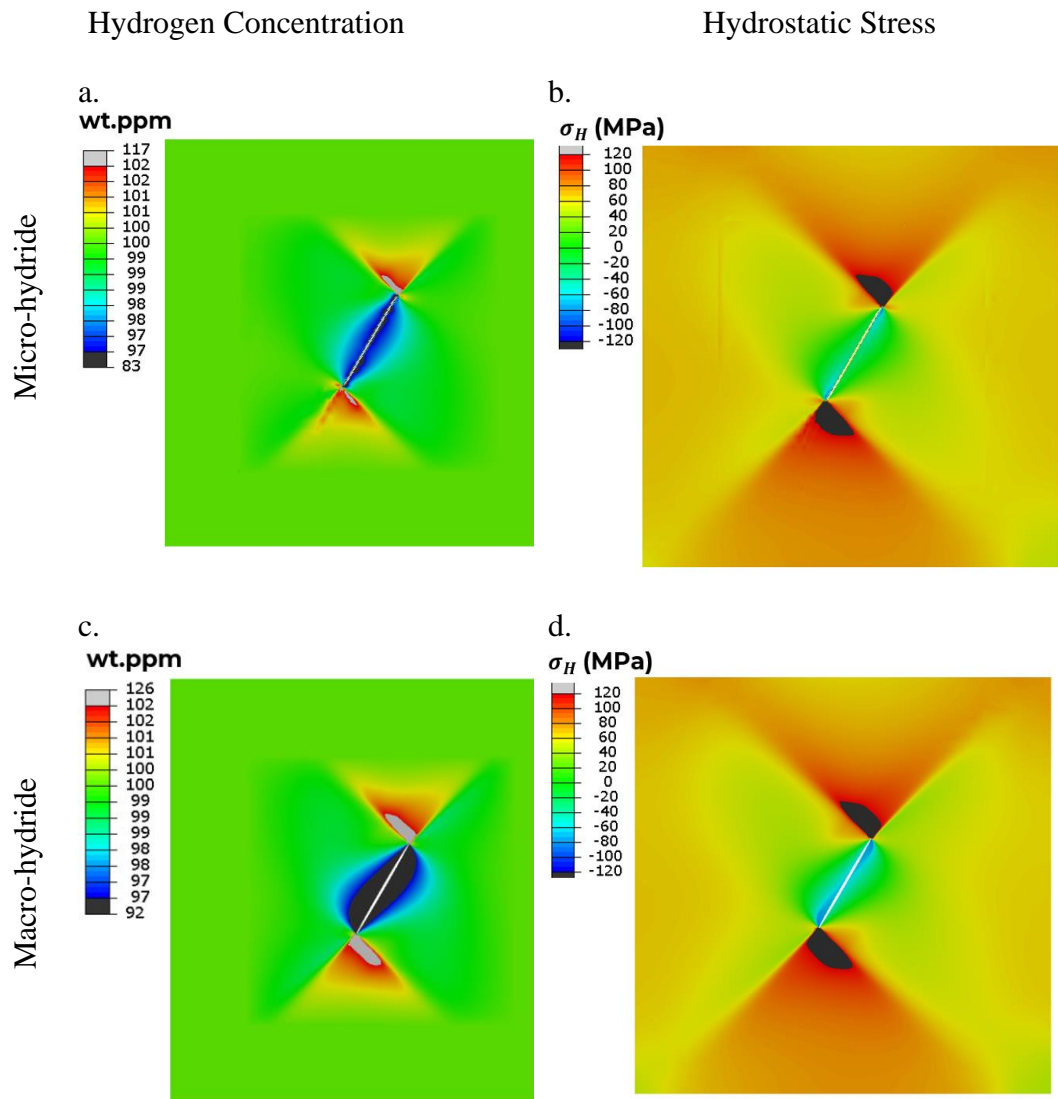


**Fig. 5-15- Hydrogen concentration of the single crystal model with (a) micro-hydride and (c) macro-hydride. The corresponding hydrostatic stress fields are shown in (b) and (d), respectively.**

## 5.4.3 The effects of applied boundary conditions

In the simulations presented so far, it is assumed that hydride formation takes place under a constant applied strain. However, since the internal pressure in the nuclear pressure tubes can be considered constant, it can be argued that hydrides form under constant applied stress. In this section, the combined effects of external loading condition and hydride precipitation is studied. For this purpose, the model with parallel hydrides and with 20 µm

hydride distance is chosen for further analysis. Two cases are compared: (1) Par-DH-6 model which is loaded to $\varepsilon_x = 0.3\%$, at which the applied strain is kept constant and hydride is allowed to form by applying HITS to the hydriding domain, and (2) Par-DH-6-S model which is deformed to 300 MPa applied stress in the x-direction, at which the applied stress is kept constant and hydride is allowed to form. The applied stress of 300 MPa is chosen as this stress corresponds to the 0.3% applied strain in the single crystal simulations and is higher than the stress under which hydrides are reported to reorient (Cinbiz et al., 2016).

The distributions of hydrogen atoms for both models with constant strain and constant stress are respectively presented in Fig. 5-16a and b. As shown, hydrogen concentration from the model with constant stress is more homogenous near the hydrides. Also, a higher peak of hydrogen concentration is calculated in the constant stress model, yet a more localized hydrogen concentration is captured at the hydride tips in the constant strain model (shown with dashed arrows near the tips). Fig. 5-16c shows the distribution of hydrogen along Path A-B and in between the hydride tips. The max value of hydrogen concentration is higher in the model undergoing constant stress. The results of this section suggest that hydrogen diffusion is accelerated when a constant stress assumption is used. Accelerated hydrogen diffusion subsequently leads to faster propagation of hydrides.

a.



b.



c.
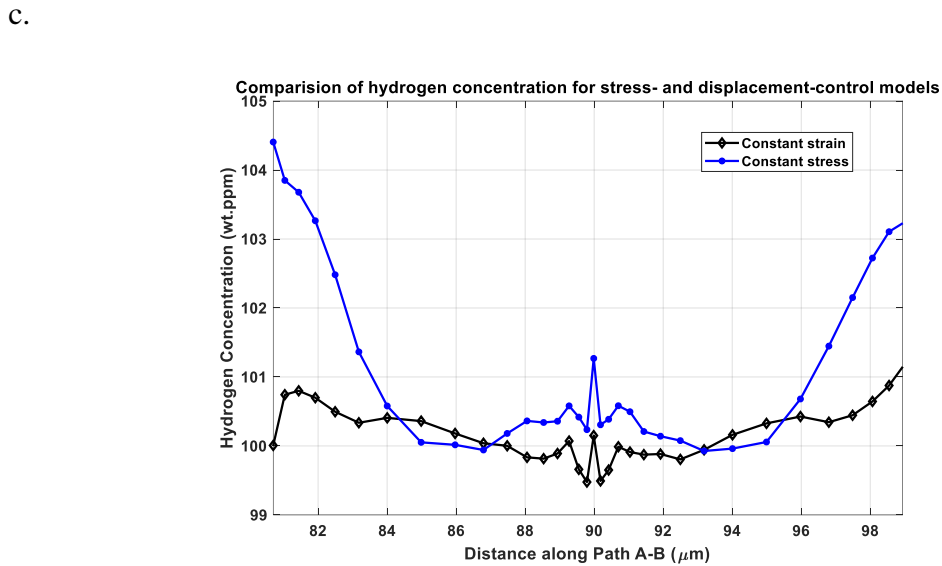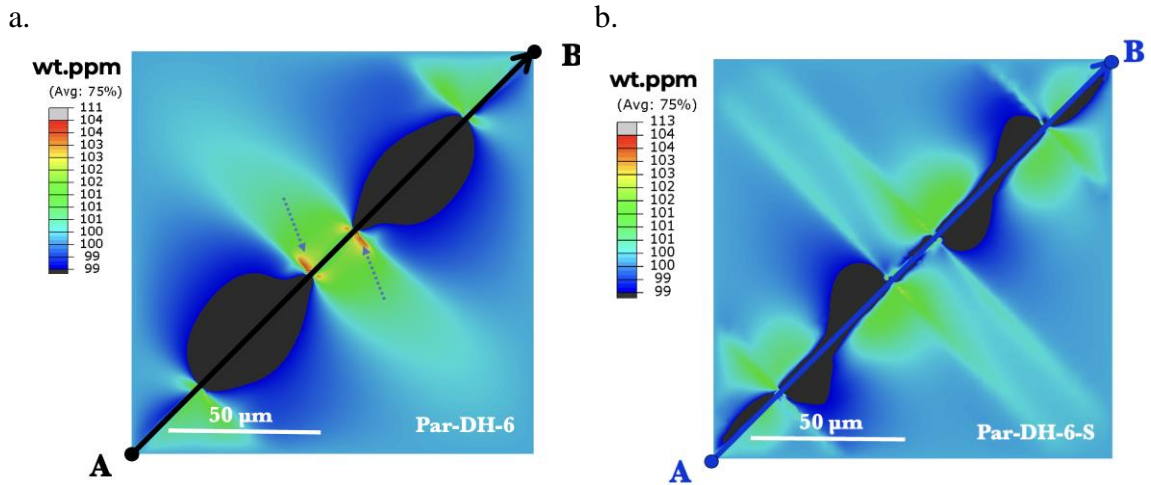


**Fig. 5-16 – The distribution of hydrogen atoms in models (a) Par-DH-6 and (b) Par-DH-6-S.  (c) The variation of hydrogen concentration along the Path A-B shown in (a).**

## 5.5  Conclusions

The interaction of hydrides in a zirconium single crystal is studied using a coupled diffusion and crystal plasticity finite element model. The effects of the distance between hydrides on the interaction of stress fields in the vicinity of hydrides are investigated. It is shown that:

1. the interaction of two hydrides is more significant in the parallel configuration compared to the perpendicular configuration. This is due to the alignment of the stress fields forming at the tips of the two parallel hydrides.

2. stress and hydrogen concentration fields of parallel hydrides are significantly higher than those of perpendicular hydrides. For the same distance *d,* parallel hydrides have a higher probability of connecting and propagating.

3. hydrides interact the most at distances less than 20 µm in the parallel configuration. The interaction remains but weakens for distances between 20 µm and 30 µm. The interaction between parallel hydrides is negligible for distances above 45 µm.

4. a circumferential and a radial hydride interact the most at distances less than 15 µm, where perpendicular hydrides have the highest probability of connecting. The interaction of perpendicular hydrides becomes negligible at distances greater than 20 µm.

5. hydrides are most likely to propagate when their width is 1 µm.

6. the width of the hydride has a great impact on the redistribution of hydrogen. Above a certain width where the hydrogen concentration and hydrostatic stress peak, there is a decrease in both values due to the reduced sharpness of the hydride.

7. length of the hydride has rather negligible effects on hydrogen diffusion. As the length of the hydride increases, hydrogen concentration and hydrostatic stress slightly increase.

8. simulating the formation of hydrides either as a continuous medium or as discrete "hydride micro platelets" both lead to the same trend in hydrogen distribution around the tips of the hydride packets.

9. due to the accumulation of more hydrogen at the tips of the hydrides, formation of hydrides under constant stress is more likely in comparison to using a constant strain assumption.

# Chapter 6

# 6 Diffusion and redistribution of hydrogen atoms in the vicinity of localized deformation zones

The presence of hydrogen atoms in the lattice of polycrystalline metals can lead to hydrogen embrittlement. The diffusion of hydrogen atoms and formation of hydrides depend on several parameters such as the microstructure of the metal alloy, the presence of stress risers, and the applied loading condition. In this study, a non-local crystal plasticity finite element model is coupled with hydrogen diffusion equations to study the effects of such parameters on the stress-assisted diffusion of hydrogen atoms in zirconium polycrystals. The concentrations of hydrogen atoms in the lattice and dislocation trap sites under different scenarios are studied to deconvolute the effects of texture, microstructure, and applied strain on hydrogen diffusion. It is shown that the concentration of hydrogen in the lattice peaks in the vicinity of grain boundaries and most importantly, at the triple-junction points. It is further shown that in localized deformation zones, such as twin or notch tips where dislocations concentrate, the effects of trapped hydrogen content can be significant.

## 6.1 Introduction

Zirconium (Zr) and its alloys are widely used in the core of light and heavy water nuclear reactors due to their good mechanical properties, corrosion resistance, and low neutron absorption cross-section. During the operation of reactors, corrosion occurs at the water/metal interface leading to the formation of zirconium oxide and the release of hydrogen atoms. The released hydrogen can ingress into the zirconium lattice, accumulate with time, and exceed the hydrogen solid solubility limit which leads to the precipitation of a brittle phase called zirconium hydride (Bair et al., 2015; Courty et al., 2014b; Puls, 2012). The dissolved hydrogen atoms in zirconium can either reside in Normal Interstitial Lattice Sites (NILS) or inside the imperfections in the medium such as vacancies, dislocation cores, and grain boundaries, which are commonly referred to as the "trap sites" (Krom and Bakker, 2000; Turnbull, 1993). In some cases, the hydrogen concentration within traps can be a significant portion of the total hydrogen concentration. The effect of

trapped hydrogen content on zirconium polycrystals is rarely discussed in the literature, especially using mesoscale models. In addition, α-zirconium has a hexagonal close-packed (HCP) crystal structure with a high degree of elastic and plastic anisotropy that results in the development of highly localized stress and strain fields (Abdolvand et al., 2020; Louca et al., 2021; Sedaghat and Abdolvand, 2021). In this study, the effects of texture and dislocations on the concentration of hydrogen in zirconium polycrystals are studied using a strain gradient crystal plasticity finite element (CPFE) model coupled with hydrogen diffusion equations.

Many different aspects of hydrogen embrittlement have been studied using experimental methods. For example, it is shown that the existence of hydrogen deteriorates the mechanical performance of steel (Strakosova et al., 2021). Due to hydrogen-induced dislocation pinning, a reduction in ductility and an increase in yield and ultimate tensile stresses in hydrogen-charged steel specimens have been reported (Wang et al., 2021). The presence of hydrogen can also affect the performance of metals through hydrogen enhanced localized plasticity (HELP), hydrogen enhanced strain-induced void formation (HESIV), or hydrogen-enhanced decohesion (HEDE) which are shown through experiments. The state of hydrostatic stress and its gradients can also affect the diffusion of hydrogen atoms within the metal. This process is known as stress-assisted diffusion (SAD) and is being studied experimentally (Blackmur et al., 2016; Motta et al., 2019; Simpson and Ells, 1974; Wang et al., 2019). The diffusion of hydrogen atoms and their accumulation with time can lead to a process known as delayed hydride cracking (DHC). Here, hydrogen concentration exceeds the solid solubility limit of hydrogen in the metal resulting in the precipitation of hydrides and cracking. The repetition of this process is known as DHC (Puls, 2012).

Considering that the development of localized plastic zones and hydrostatic stresses affect hydrogen diffusion, it is essential to account for the contribution of trap sites to the development of highly concentrated hydrogen zones. Several studies have already investigated the relationship between plasticity and hydrogen diffusion in metals such as zirconium or steel (Arakawa et al., 2021; Gu and El-Awady, 2018; Jones et al., 2021; Kapci et al., 2021; Moshtaghi et al., 2021; Wimmer et al., 2020; Ye et al., 2021). In addition,

several numerical studies have focused on including the effects of trap sites on hydrogen diffusion in metals. For example, Sofronis and McMeeking (1989) developed a model to investigate hydrogen transport in the lattice of steel, which was coupled with a trapping mechanism. It was suggested that the trapped hydrogen concentration is directly proportional to plastic strain and dislocation density, while it should be in equilibrium with lattice hydrogen concentration through the equilibrium equations developed by Oriani (1970). Sofronis and McMeeking (1989) also used Sievert's law to determine the lattice hydrogen concentration from hydrostatic stress. The Oriani's equilibrium condition and the assumptions used for fast kinetics have been consistently and frequently used (Dadfarnia et al., 2014; Krom and Bakker, 2000; Salvadori et al., 2018; Sofronis and McMeeking, 1989). Lufrano et al. (1998) also incorporated an elastoplastic model into a finite element framework to solve a coupled hydrogen diffusion problem for a 4-point bending beam made of an X-750 alloy. The effects of both lattice and trap sites, hydrogen-induced lattice dilatation, and stress-assisted diffusion were considered in this study. In addition, Krom et al. (1999) used a plastically-deformed model in the finite element framework to study the effects of strain rate on hydrogen diffusion in the lattice and hydrogen content in the traps. Further, Krom and Bakker (2000) described the effects of hydrogen trapping in steel by considering dislocation cores as saturable and reversible trap sites, while using the Sievert's law for determining the lattice hydrogen content from the state of hydrostatic stress. A relationship between dislocation density and number of trap sites in BCC crystals was also introduced and it was shown that, with hydrogen trapping, diffusivity decreases whereas hydrogen solubility increases.

The coupled effects of hydrogen diffusion and thermomechanical loads were studied by Anand (2011), where a large viscoelastic deformations model for metals was used. The effects of traps were subsequently added to the same model by Di Leo and Anand (2013), but a new equilibrium condition for hydrogens in traps and NILS was introduced which was not constrained to the Oriani's equilibrium condition. Similarly, Dadfarnia et al. (2015) used an elastoplastic material model for steel that accounts for the effects of dislocation densities on hydrogen diffusion towards notch tips. It was shown that the effects of traps on hydrogen content can be significant. Recently, Yang et al. (2020) used a coupled diffusion-elastoplastic material model to investigate the effects of hydrogen in titanium.

With considering the effects of hydrogen atoms in traps and NILS, it was shown that elastoplastic behavior of the material significantly affects the sites at which the peaks of hydrogen concentration take place. To study the effects of hydrogen atoms on HELP and HESIV in steel, Depraetere et al. (2021) used a hydrogen diffusion model coupled with the Gurson damage model in which the effects of hydrogen atoms in traps and NILS were considered along with the strain rate effects. This model showed the loss of ductility due to the presence of hydrogen atoms. The concept of hydrogen trapping is also used to model hydrogen-induced decohesion (HEDE) of the carbide-matrix interface, using micro-mechanical modeling (Novak et al., 2010). Although these models are comprehensive and provide useful information regarding hydrogen diffusion and its subsequent effects on the performance of metals and alloys, the effects of materials microstructures and textures are not explicitly accounted for and are generally ignored.

Other modeling approaches are also used to study the effects of hydrogen atoms on the mechanical properties of metals. For example, discrete dislocation plasticity is used to study the behavior of hydrogen in face-centered cubic (FCC) materials. With the use of this technique, Yu et al. (2020) showed that hydrogen promotes dislocation pile-up and softens the global behavior of the material, which is in agreement with the theory of HELP. Phase-field models are also used to simulate the effects of hydrogen diffusion on the fatigue performance of metals (Golahmar et al., 2022). For instance, Zhang et al. (2021) used a phase-field modeling approach to simulate hydrogen diffusion in polycrystalline iron. It was concluded that grain boundaries have a significant impact on the distribution of hydrogen atoms and the subsequent hydriding process. Golahmar et al. (2021) also developed a phase-field model to study hydrogen embrittlement under fatigue loading. The fatigue crack growth rate for specimens with different geometries and loading conditions were studied. At lower length scales, atomic models are widely used to study various effects of hydrogen in metals, such as the interaction between hydrogen atoms and grain boundaries (Chen et al., 2021; Oudriss et al., 2012a), the diffusivity of hydrogen atoms in nickel alloys (Martin et al., 2012), or preferred migration path for hydrogen in FCC crystals (Tang et al., 2021). Furthermore, Patel et al. (2021) developed an efficient multiscale approach to simulate the precipitation and reorientation of hydrides under the steady-state diffusion condition. A multiscale extended FEM-based discrete dislocation dynamic model

was developed to study the effects of hydrogen on the transition of ductile fracture to brittle cleavage in aluminum and nickel alloys (Liang et al., 2021). It was shown that depending on the grain boundary type or grain boundary misorientation, different hydrogen embrittlement mechanism can become active.

Crystal plasticity finite element (CPFE) modeling can be used to simulate the effects of materials microstructures on their macroscopic behaviors. CPFE has been used in the literature to study the strain rate sensitivity, creep, or hydrogen diffusion effects on the performance of polycrystals. For example, Abdolvand (2019) developed a coupled diffusion- crystal plasticity finite element framework (D-CPFE) to study the stress-assisted-diffusion of hydrogen atoms in zirconium polycrystals. It was reported that local residual stresses affect the redistribution of hydrogen atoms and that the hydrogen atoms tend to reside at grain boundaries. Similarly, Arnaudov et al. (2020) used a coupled diffusion-CPFE approach to study fatigue behavior of steel. The effects of strain rates and hydrogen in trap sites were considered and it was shown that hydrogen atoms tend to enhance the formation of localized strain fields. Tondro and Abdolvand (2021) used a D-CPFE framework to study the effects of microstructure on the behavior of zirconium hydrides and the state of the stresses imposed on the medium by the formation of hydrides. It was reported that due to the formation of tensile hydrostatic stress fields at the hydride tips, hydrides tend to propagate along their longitudinal direction. Furthermore, the interaction of hydrides stress fields and their subsequent effects on hydrogen distribution were studied by Tondro et al. (2022). It was shown that in comparison to perpendicular hydrides, parallel hydrides are more likely to connect. The effects of microstructure and texture at the notch tips of zirconium polycrystals were studied by (Tondro and Abdolvand, 2022), where it was shown that the susceptibility to hydriding depends on both materials texture and microstructure. In addition, Liu et al. (2021) used a CPFE approach to predict the location of hydrides in the vicinity of a notch tip in a thermomechanically loaded zirconium beam. Hussein et al. (2021) incorporated a representative volumetric element and a D-CPFE framework to study hydrogen diffusion in steel. By considering the effects of hydrogen in traps and NILS, it was shown that even when grain boundaries are not modeled explicitly, hydrogen atoms tend to concentrate at grain boundaries. With the use of CPFE modeling, it is shown that defects, such as cracks and notches, drive creep-induced

stress changes and accelerate hydrogen transport further encouraging DHC, even at room temperature (Y. Liu et al., 2021b). Strain-gradient CPFE modeling has also been used to investigate the effects of microstructure on hydrogen content in FCC polycrystals. It was shown that grain size reduction promotes the trapping of hydrogen atoms (Kumar and Mahajan, 2020).

While hydrogen embrittlement of zirconium is an important concept, the effects of trap sites on hydrogen diffusion and concentration are rarely studied. This study focuses on addressing this knowledge gap by updating a strain-gradient CPFE model to study the effects of the elastic and plastic anisotropy of zirconium crystals on stress-assisted hydrogen diffusion. Subroutines are developed to account for the effects of hydrogen atoms in NILS and traps while solving for the coupled diffusion-CPFE equations. Attention is given to the effects of texture, grain size, and temperature on hydrogen redistribution in the lattice and dislocation trapping sites. First, the mathematical formulation and the FE input models are described. This is followed by assessing the performance of the model for bi- and polycrystal models. The distributions of hydrogen in NILS and traps sites are subsequently analyzed and discussed.

## 6.2 Formulation and input models

A strain-gradient CPFE model is updated and coupled with diffusion equations to simulate the stress-assisted diffusion of hydrogen atoms in polycrystalline zirconium. The strain-gradient model, also known as non-local model, was validated against a comprehensive set of data measured in neutron diffraction and high resolution electron backscatter diffraction experiments, the results of which can be found in Sedaghat and Abdolvand (2021a). In the following sections, the formulation used in the CPFE model and the model updates for correlating the calculated total dislocation densities to hydrogen concentration in the trap sites, and the effects of local hydrostatic stresses on hydrogen in NILS are presented.

In the following sections, tensors are shown using bold fonts, and vectors are shown using an arrow.

## 6.2.1 Crystal Plasticity

Generally, the total deformation gradient ($F$) can be decomposed to elastic ($F^e$) and plastic ($F^p$) parts following:

$$F = F^e F^p \tag{6-1}$$

The total velocity gradient tensor ($L$) in the current configuration can be decomposed to elastic ($L^e$) and plastic ($L^p$) parts as:

$$L = \dot{F}F^{-1} = \dot{F}^e F^{e-1} + F^e \dot{F}^p F^{p-1} F^{e-1} = L^e + L^p \tag{6-2}$$

The total velocity gradient tensor can be divided into the symmetric part, i.e., deformation rate tensors ($D^e, D^p$), and asymmetric part, i.e., spin tensors ($\Omega^e, \Omega^p$). The integration of deformation rate and spin tensor with respect to time provides the increments of strain and rotation tensors, respectively. During crystallographic slip, dislocations move on a particular plane, in a particular direction. The plastic part of the velocity gradient can be calculated from the summation of crystallographic slips on all active slip systems (Asaro and Needleman, 1985):

$$L^p = D^p + \Omega^p = \sum_{\alpha=1}^{N} \dot{\gamma}^\alpha \vec{m}^\alpha \otimes \vec{n}^\alpha \tag{6-3}$$

where $\vec{m}^\alpha$, $\vec{n}^\alpha$ and $\dot{\gamma}^\alpha$ represent the slip direction, the slip plane normal, and the shear rate on the $\alpha^{\text{th}}$ slip system for the $N$ number of slip systems, respectively. $\vec{m}^\alpha \otimes \vec{n}^\alpha$ is the dyadic product of the slip plane direction and the slip plane normal, known as the Schmid tensor of the slip system $\alpha$. The plastic part of the deformation rate and spin tensors can be calculated using the following equations:

$$D^p = \sum_{\alpha=1}^{N} P^\alpha \dot{\gamma}^\alpha$$

$$\Omega^p = \sum_{\alpha=1}^{N} W^\alpha \dot{\gamma}^\alpha$$

(6-4)

where $P^\alpha$ and $W^\alpha$ are the symmetric and asymmetric parts of the Schmid tensor, respectively. A rate-dependent equation is used to calculate the shear rate on the slip system $\alpha$, based on the resolved shear stress ($\tau^\alpha$) that acts on the same slip system (Asaro and Needleman, 1985):

$$\dot{\gamma}^\alpha = \dot{\gamma}_0^\alpha \, sign\left(\frac{\tau^\alpha}{g^\alpha}\right) \left|\frac{\tau^\alpha}{g^\alpha}\right|^n$$

(6-5)

where $\dot{\gamma}_0$ is a reference shear strain rate, $n$ represents the sensitivity of the material to a strain-rate and $g^\alpha$ is the critical resolved shear stress (CRSS) of the slip system $\alpha$. The resolved shear stress acting on the slip system $\alpha$ is proportional to Kirchhoff stress ($\psi$) through the following equation (Asaro, 1983):

$$\tau^\alpha = P^\alpha : \psi$$

(6-6)

The Jaumann rate of the Kirchhoff stress ($\breve{\psi}$) is related to the elastic part of the deformation rate tensor ($D^e$) as:

$$\breve{\psi} = \mathbb{C} : D^e$$

(6-7)

where $\mathbb{C}$ is the elastic stiffness tensor of the HCP crystal after rotation to the deformed configuration. The objective rate of Kirchhoff stress, in Eq. 6-8, is defined with respect to an observer attached to the crystal lattice:

$$\breve{\psi} = \dot{\psi} - \Omega^e \psi + \psi \Omega^e$$

(6-8)

The current strength of each slip system is assumed to correlate with the square root of the density of dislocations (Evers et al., 2004; A. Ma et al., 2006; Sedaghat and Abdolvand, 2021):

$$g^\alpha = g_0^\alpha + \zeta G b^\alpha \sqrt{\sum_{\beta=1}^{N} q^{\alpha\beta}\left(\rho_{GND}^\beta + \rho_{SSD}^\beta\right)} \qquad (6\text{-}9)$$

where, $g^\alpha$ is the updated CRSS, and $g_0^\alpha$ is the initial CRSS. $G$ is the shear modulus, $b^\alpha$ is the size of the Burgers vector for the slip system $\alpha$, and $\zeta$ is a material constant. $\rho_{GND}^\beta$ is the density of geometrically necessary dislocations (GNDs), $\rho_{SSD}^\beta$ is the density of statistically stored dislocations (SSDs) for the slip system $\beta$, and $q^{\alpha\beta}$ represents the self and latent hardening coefficients. Calculating the densities of GNDs and SSDs requires the use of a strain-gradient formulation the details of which are provided in Sedaghat and Abdolvand (2021). Here, a brief description of underlying equations is provided. The density of GNDs depends on the local lattice curvature through Nye tensor (Nye, 1953), which can be formulated as (Arsenlis and Parks, 1999):

$$\left(curl\left(\boldsymbol{F}^{pT}\right)\right)^T = \sum_{\alpha=1}^{N} \left(\rho_{GND,s}^\alpha\, \vec{b}_\alpha \otimes \vec{m}_\alpha + \rho_{GND,et}^\alpha\, \vec{b}_\alpha \otimes \vec{t}_\alpha + \rho_{GND,en}^\alpha\, \vec{b}_\alpha \otimes \vec{n}_\alpha\right) \qquad (6\text{-}10)$$

in which $N$ is the number of slip systems, $\rho_{GND,s}^\alpha$ is the density of screw dislocations with the Burger's vector parallel to the slip direction $\vec{m}_\alpha$, $\rho_{GND,en}^\alpha$ and $\rho_{GND,et}^\alpha$ are the edge dislocation densities along with the slip plane normal $\vec{n}_\alpha$ and $\vec{t}_\alpha = \vec{m}_\alpha \times \vec{n}_\alpha$ respectively. The GND densities can be calculated using the following equation:

$$\{\rho_{GND}^\alpha\} = \boldsymbol{A}^T(\boldsymbol{A}\boldsymbol{A}^T)^{-1}\boldsymbol{B} \qquad (6\text{-}11)$$

where $\boldsymbol{B}$ contains the components of the tensor in the left-hand side of the Eq. (6-10), and $\boldsymbol{A}$ contains the basis tensors of the right-hand side of Eq. (6-10). The evolution of SSDs is calculated using the following equation:

$$\dot{\rho}_{SSD}^{\alpha} = \frac{|\dot{\gamma}^{\alpha}|}{b^{\alpha}} \left( K^{\alpha} \sqrt{\rho_{SSD}^{\alpha} + \rho_{GND}^{\alpha}} - 2y_c^{\alpha} \rho_{SSD}^{\alpha} \right) \tag{6-12}$$

where $K^{\alpha}$ is a material constant for the accumulation of SSDs, and $y_c^{\alpha}$ is the critical annihilation length of the dislocations with opposite Burgers vectors.

## 6.2.2 Hydrogen diffusion

Hydrogen atoms reside either in NILS or in trap sites e.g., dislocation cores, grain boundaries, voids, and other flaws in the zirconium matrix. The Fick's second law can be used for the diffusion of hydrogen atoms:

$$\frac{\partial C_H}{\partial t} = -\vec{\nabla} . \vec{J} \tag{6-13}$$

where, $C_H$ is the total hydrogen concentration, and $\vec{J}$ is the hydrogen flux. The total hydrogen concentration can be decomposed to those hydrogen atoms located in NILS, here called $C_L$, and those trapped in dislocations, called $C_T$. Hydrogen diffusion is assumed to be only through NILS, while trapped hydrogens are assumed to be immobile (Krom and Bakker, 2000). Hence, the hydrogen flux can be defined as:

$$\vec{J} = -\frac{\boldsymbol{D}_L C_L}{RT} \vec{\nabla} \mu \tag{6-14}$$

where $\boldsymbol{D}_L$ is the diffusion constant for the hydrogen atoms in NILS ($C_L$), $T$ is temperature, and $R$ is the universal gas constant. The chemical potential of metal-solvent is:

$$\mu = \mu_0 + RT \ln C_L - \frac{\sigma_{kk}}{3} \bar{V}_H \tag{6-15}$$

in which $\mu_0$ is the reference chemical potential and is considered constant, $\bar{V}_H$ is the partial molar volume of hydrogen in the host metal, and $\sigma_{kk}$ represents the summation of normal stresses. For the length scale that is the focus of this study, i.e., a few micrometers, the variation of temperature is negligible. Hence, with using Eqs. (6-14) and (6-15), and in the absence of temperature gradients, the flux of NILS hydrogens in the zirconium matrix can be written as:

$$\vec{J} = -\mathbf{D}_L \cdot \left[ \vec{\nabla} C_L - C_L \frac{\bar{V}_H}{RT} \frac{\vec{\nabla} \sigma_{kk}}{3} \right] \qquad (6\text{-}16)$$

According to Eq. (6-16), the hydrogen flux in zirconium matrix is affected by the gradients of hydrogen concentration and hydrostatic stress ($\frac{\vec{\nabla} \sigma_{kk}}{3}$), where the latter is known as stress-assisted diffusion (SAD).

In this work, the possible directional effects of the stress tensor or resolved stresses as the driving force for diffusion are neglected and it is assumed that only hydrostatic stress contributes to SAD. It was previously shown that there exists a fairly accurate match between the locations of hydrogen peaks, the locations of hydride precipitates, and the profiles of hydrostatic stresses (Abdolvand, 2019).

Since the total hydrogen content is decomposed to those in NILS ($C_L$) and those trapped in dislocations ($C_T$), the change of total hydrogen content with respect to time is:

$$\frac{\partial C_H}{\partial t} = \frac{\partial C_L}{\partial t} + \frac{\partial C_T}{\partial t} \qquad (6\text{-}17)$$

The concentration of hydrogen in NILS and traps can be defined as (Di Leo and Anand, 2013):

$$C_L = \theta_L \, N_L \qquad (6\text{-}18)$$

$$C_T = \theta_T \, N_T \qquad (6\text{-}19)$$

in which $\theta_L$ and $\theta_T$ are the occupancy fractions of NILS and trap sites, respectively. $N_L$ is the number of solvent atoms per unit lattice volume, and $N_T$ is the number of traps per unit lattice volume. Eqs. (6-18) and (6-19) describe the concentration of hydrogen in NILS and traps based on the condition of lattice. The values of $N_L$ and $N_T$ can be determined using the following equations (Krom and Bakker, 2000):

$$N_L = \frac{N_A \cdot \beta \cdot \rho}{A_r} \tag{6-20}$$

$$N_T = \sum_{\alpha} \frac{\rho_{dis}^{\alpha}}{d_{hkl}^{\alpha}} \tag{6-21}$$

in which $N_A$ is the Avogadro's number, $\rho$ is the density of solvent, $\beta$ is the number of available NILS per solvent atom, and $A_r$ is the atomic weight of the host lattice. $\rho_{dis}$ is the total dislocation density and $d_{hkl}$ is the interplanar spacing between the hkl planes. To correlate the concentration of hydrogen atoms in NILS with those trapped, an equilibrium condition was introduced by Oriani (1970), and used in later studies in the literature (Sofronis and McMeeking, 1989), which is also used in the current study:

$$\frac{1-\theta_L}{\theta_L}\frac{\theta_T}{1-\theta_T} = K = exp\left(\frac{\overline{\Delta H_B}}{RT}\right) \tag{6-22}$$

in which $\overline{\Delta H_B}$ is the trap binding energy of hydrogen atoms in the zirconium matrix. Assuming that the occupancy of NILS is small, i.e., $\theta_L \ll 1$, the following equation can be derived:

$$if\ \theta_L \ll 1 \xrightarrow{(6-22)} \theta_T = \frac{\theta_L K}{1+\theta_L K} \rightarrow C_T = \frac{N_T \frac{C_L}{N_L} K}{1 + \frac{C_L}{N_L} K} \rightarrow \frac{\partial C_T}{\partial C_L} = \omega$$

$$= \frac{C_T(1-\theta_T)}{C_L} \tag{6-23}$$

and:

$$\frac{\partial C_H}{\partial t} = \frac{\partial C_L}{\partial t} + \frac{\partial C_T}{\partial t} = \frac{\partial C_L}{\partial t} + \overbrace{\frac{\partial C_T}{\partial C_L}}^{\omega}\frac{\partial C_L}{\partial t} \rightarrow \frac{\partial C_H}{\partial t} = \frac{\partial C_L}{\partial t}[1+\omega] \tag{6-24}$$

Combining Eqs. (6-13), (6-16), and (6-24) yields:

$$\frac{\partial C_L}{\partial t}[1 + w] = \nabla.\left[ \boldsymbol{D}_L . \left[ \vec{\nabla} C_L - C_L \frac{\bar{V}_H}{RT} \frac{\vec{\nabla} \sigma_{kk}}{3} \right] \right] \tag{6-25}$$

which can be rearranged to:

$$\frac{\partial C_L}{\partial t} = \nabla.\left[ \boldsymbol{D}_{eff} . \left[ \vec{\nabla} C_L - C_L \frac{\bar{V}_H}{RT} \frac{\vec{\nabla} \sigma_{kk}}{3} \right] \right] \tag{6-26}$$

where

$$\tag{6-27}$$

$$\boldsymbol{D}_{eff} = \frac{\boldsymbol{D}_L}{1 + w}$$

It should be noted that effects of pipe diffusion by dislocations on the diffusivity of hydrogen in zirconium are neglected in this work (Nordin et al., 2019).

It should be noted that the effects of pipe diffusion within dislocations as well as grain boundaries on the diffusivity of hydrogen in zirconium are neglected in this chapter. These assumptions are based on the previous experimental measurements. For example, the measurements reported in Kearns (1972) show that the diffusivity of hydrogen in zirconium is independent from zirconium grain size. Similarly, it has been shown that the difference between the diffusivity of hydrogen in heavily deformed and undeformed zirconium polycrystals is not significant, particularly at 300 ˚C (Nordin et al., 2019). It should be noted that since the diffusion length of hydrogen at the temperature used in our simulations (600 K) is quite high, and since we will mainly focus on the steady state condition, the assumptions made above do not considerably affect the results reported here.

To summarize the steps followed in the simulations, $C_L$ is solved using Eq. (6-26) which is coupled with the mechanical (CPFE) model. $\theta_L$ is subsequently computed using the resulting value for $C_L$ through Eqs. (6-18) and (6-20). The value of $\theta_L$ and Eq. 6-22 is then used to determine the magnitude of $\theta_T$. This is followed by using the magnitude of total dislocation density from CPFE and interplanar spacing to calculate $N_T$ through Eq. (6-21). In the last step $C_T$ is obtained using the calculated values of $N_T$ and $\theta_T$. It is acknowledged

that more than one hydrogen atom can reside in a dislocation core (P. Yu et al., 2020), however, due to the uncertainties regarding this number, simulations are carried out assuming that on average, only one hydrogen atom can reside in a dislocation core, i.e., there is no multiplication factor in Eq. (6-21). The diffusion equations are solved using a UMATHT subroutine that is fully coupled with the mechanical model and the UMAT subroutine. The details of this process can be found in Abdolvand (2019).

The material properties used in this study are those of the alpha phase of Zr-2.5Nb CANDU pressure tube. The elastic modulus of the HCP crystals are (Fisher and Renken 1964) $C_{11}=$ 143.5 GPa, $C_{33}$=164.9 GPa, $C_{12}$=72.5 GPa, $C_{13}$=65.4 GPa, $C_{44}$=32.1 GPa. The slip systems used in this study are prism, basal, and pyramidal <c+a> (Cai et al., 2009). The parameters for strain gradient plasticity, dislocation evolution, and strain rate for a single crystal are listed in Table 6-1. Also, $\zeta$ is assumed to be 0.5 and $G$ is the average of $C_{44}, C_{55}$, and $C_{66}$. The $g_0^\alpha$ values used for Zr-2.5Nb are the ones reported in a study by Cai et al. (2009). Other parameters are extracted from the study by Sedaghat and Abdolvand (2021a) for α-zirconium. Also, it is assumed that the elastic and plastic response of the material is not affected by hydrogen concentration. The yield stress of zirconium at 300 ˚C only slightly change with hydrogen concentration (Tung et al., 2016).

**Table 6-1 – CPFE parameters**

| Slip system | $|\vec{b}|$ ($nm$) | $g_0^\alpha$ ($GPa$) | $n$ | $\dot{\gamma}_0^\alpha$ | $K^\alpha$ | $y_c^\alpha$ ($nm$) |
|---|---|---|---|---|---|---|
| Prism | 0.323 | 0.12 | 20 | $3.5\times10^{-4}$ | 0.05 | 5 |
| Basal | 0.323 | 0.15 | 20 | $3.5\times10^{-4}$ | 0.05 | 5 |
| Pyramidal | 0.608 | 0.3 | 20 | $1.0\times10^{-4}$ | 0.3 | 10 |

The initial dislocation density is set to be $5\times10^{12}$ m$^{-2}$ representing fully annealed samples. The interplanar spacings ($d$) used for the calculations of the number of trap sites in Eq. (6-21) can be obtained from the formulation for a hexagonal unit cell for any ($hkl$) plane:

$$\frac{1}{d^2} = \frac{4}{3}\left[\frac{h^2 + hk + k^2}{a^2}\right] + \frac{l^2}{c^2} \qquad (6\text{-}28)$$

For an HCP crystal of zirconium, $a$ and $c$ in Eq. 6-28 are respectively 0.3229 nm and 0.5141 nm.

The diffusion rate of hydrogen in α-zirconium depends on the direction of hydrogen flow (Zhang et al., 2017):

$$D_c = 1.08\, exp\left(-\frac{0.46}{K_b T}\right)$$

$$D_a = \frac{D_c}{(P_1 T^2 + P_2 T + P_3)} \qquad\qquad (6\text{-}29)$$

$$K_b = 8.61733 \times 10^{-5}$$

$$P_1 = -3.323 \times 10^{-7}, P_2 = 7.025 \times 10^{-4}, P_3 = 0.8298$$

where T is the absolute temperature. $D_c$ and $D_a$ are respectively the diffusivities along the HCP crystal "a" and "c" axis, and in mm²/s. The partial molar volume of hydrogen atoms in zirconium ($\bar{V}_H$) is 1670 mm³/mol. Here, all simulations are conducted at 603 K which is the nominal temperature of zirconium in nuclear reactors. Trap binding energy of hydrogen atoms in zirconium ($\overline{\Delta H_B}$) is set at 25 kJ/mol, but the effects of $\overline{\Delta H_B}$ are further discussed in section 6.4.1. Also, the density of the zirconium and its molar mass are considered to be 6.49 gr/cm³ and 91.22 gr/mol, respectively. Generally, there are one octahedral site and two tetrahedral sites per atom in α-zirconium (Connétable et al., 2011); therefore, $\beta$ should theoretically be 3. Although, experimental measurements suggest that zirconium atoms may not be fully saturated (Courty et al., 2014b). In addition, with the use of inelastic neutron scattering, it was shown that at 600 °C, hydrogen atoms tend to reside at tetrahedral sites, and the octahedral sites remain mostly vacant (Khoda-Bakhsh and Ross, 1982). In this study, the number of possible hydrogen atoms per Zr atom is taken from δ-hydride at 300°C with $ZrH_{1.66}$ composition (Puls, 2012). Therefore, there should be $\beta$ =1.66 NILS available per Zr atom.

## 6.2.3 Input models

Four input models are prepared, the details of which are provided below.

## 6.2.3.1 The bi-crystal model

The bi-crystal model is used to study the effects of misorientation between two neighboring grains, so as the effects of model constants as well as grain size. This model is shown in Fig. 6-1 and consists of two $0.5\times0.5\times0.5$ $\mu m^3$ grains. In all simulations presented, the c-axis of the grain located in the back of the model is kept unchanged and parallel to the loading direction. The c-axis of the front grain, on the other hand, is rotated about the global Y-axis. Both the global coordinate and the schematic of HCP crystals are shown in Fig. 6-1a. In this study, $\psi$ refers to the misorientation between the c-axis of the two crystals. Unless otherwise is stated, the model is loaded to 5% uniaxial strain along the global Z-direction in 900 seconds. 8000 cubic elements (C3D20RT) are used to mesh the model, where a higher mesh density is used closer to the grain bounday (Fig. 6-1b). The details of the applied boundary conditions (BC) are provided in Fig. 6-1a. For diffusion BC, hydrogen concentration is set to be constant and equal to 100 wt. ppm which is assigned to the "ijkl" face shown in Fig. 6-1a. The choice of 100 wt.ppm is to resemble the nominal solid solubility limit of hydrogen atoms in zirconium at the operative temperatures of nuclear reactors. The effects of diffusion boundary conditions on the results are discussed in section 6.4.2. Lastly, unless otherwise stated, the results of this chapter are presented along the Path#1 shown in Fig. 6-1a which starts from point "p" and ends at point "q".
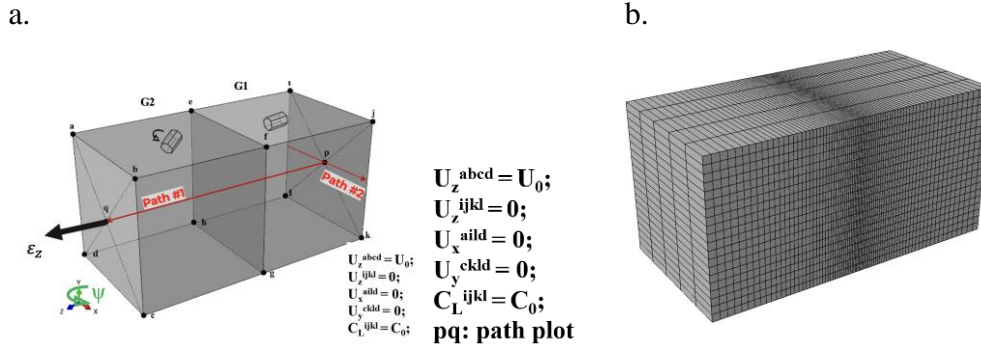
**Fig. 6-1- (a) The geometry and applied boundary conditions and (b) the assigned mesh to the bi-crystal model.**

## 6.2.3.2 The tri-crystal model and twinning

The model in this section is to study the effects of deformation twinning on the redistribution of hydrogen atoms both in trap sites and NILS. The model set-up is shown in Fig. 6-2a and Fig. 6-2b. The model is comprised of three grains where a twinning domain, with a denser mesh, is embedded in the middle grain. The dimensions of the model are shown in Fig. 6-2b and all three grains are the same size along X-axis. The model is confined along X and Y, respectively on the left and bottom faces. Also, the top edge of the model is confined along Z. For the mass diffusion boundary condition, all four sides of the model are set as 100 wt.ppm throughout the simulation. The grain specifications for different model configurations are listed in Table 6-2. The external strain is applied using a strain rate of $5.5 \times 10^{-5}$ s$^{-1}$. The orientation of the surrounding elements is set the same as that of Grain#2. Following the method discussed in Abdolvand and Wilkinson (2016), the embedded twinning domain in the middle crystal is reoriented using the crystallographic orientation relationship of twin and parent. The tips of the embedded twin domain are located right at the grain boundaries, and it is assumed that the twin domain does not thicken throughout the simulation.

**Table 6-2 – The tri-crystal model specifications.**

| Model No. | Grain #1 | Grain #2 | Grain #3 | Twin orientation | Applied strain |
|---|---|---|---|---|---|
| Tri-twin-1 | (95 85 65) | (95 85 65) | (0 90 0) | (4 90 0) | $\varepsilon_x = 2.0\%$ |
| Tri-twin-2 | (95 85 65) | (95 85 65) | (45 90 0) | (4 90 0) | $\varepsilon_x = 2.0\%$ |
| Tri-twin-3 | (95 85 65) | (95 85 65) | (90 90 0) | (4 90 0) | $\varepsilon_x = 2.0\%$ |

a.　　　　　　　　　　　　　　　　b.
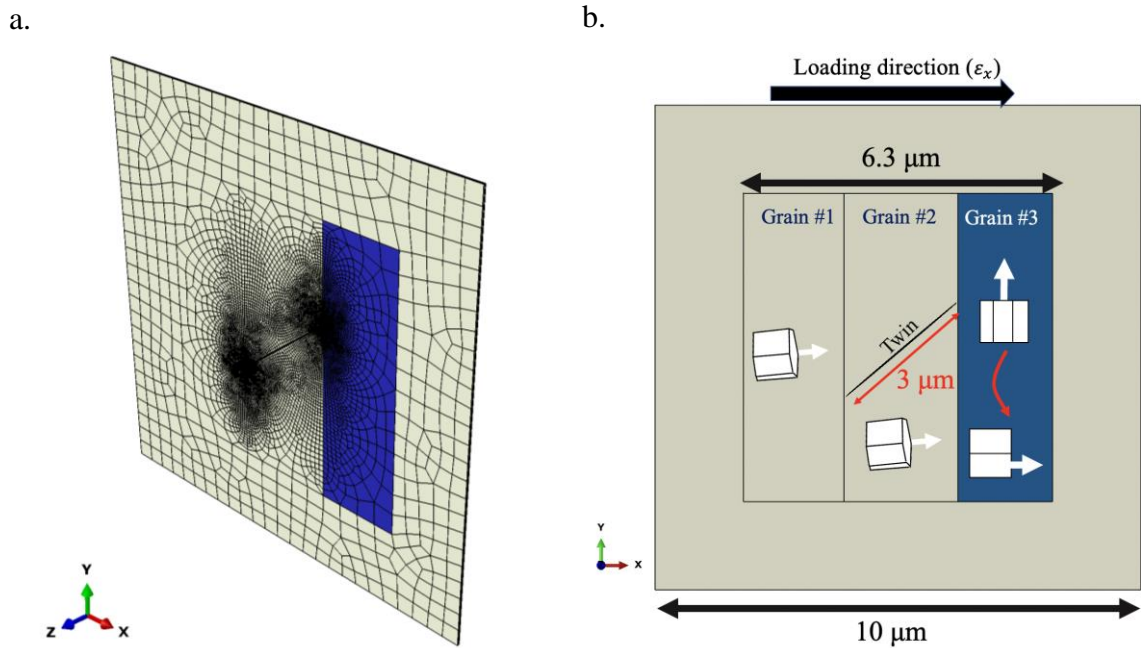


**Fig. 6-2-(a) 3D and (b) 2D view of the tri-crystal model with a twin embedded within Grain #2. The schematics of the grain orientations are shown in (b).**

The steps of the simulation conducted in this section can be summarized as:

- Step-1: mechanical boundary conditions are applied to the model, including a 2.0% strain along the global x-axis, with the strain rate of $5.5 \times 10^{-5}$ s$^{-1}$.

- Step-2a: reorientation of the twinning domain using a reflection against the $\{10\bar{1}2\}$ plane.

- Step-2b: the twin transformation strain of 16.9% is applied incrementally to the twin domain.

- Step-3: concentration of hydrogen in NILS and trap sites are extracted and reported at this step.

## 6.2.3.3 The polycrystal model

To study the effects of texture on the distribution of dislocation densities and hydrogen concentration, a qausi-3D model consisting of 176 grains is prepared. This model is shown in Fig. 6-3a and Fig. 6-3b with the details of the grain dimensions and applied BCs respectively shown in in Fig. 6-3c and Fig. 6-3d. The dimension of the model is $10{\times}10\ \mu m^2$ on the XY plane and 0.5 µm along the Z direction. This will result in grains that are 1 µm in their longest diagonal direction (Fig. 6-3c). The choice of grain size is to resemble the fine microstructure of CANDU pressure tubes that are ~ $0.5 \times 1\ \mu m^2$ on the transverse-radial direction of the tube.

The model is uniaxially strained to 5% along the X-axis in 900 seconds to simulate a quasi-static loading condition with the strain rate of $5.5{\times}10^{-5}\ s^{-1}$. The initial hydrogen concentration of 100 wt.ppm ($C_0$) is prescribed on all nodes. The boundary condition used for this model is the constant concentration of hydrogen on "efgh" face throughout the simulations. More than 11k C3D20RT elements are used to mesh the model.

c.                                                      d.



$$U_x^{abcd} = U_0$$
$$U_x^{efgh} = 0;$$
$$U_z^f = U_z^g = 0;$$
$$U_y^{intersection\ (eg\ and\ fh)} = 0;$$
$$C_L^{efgh} = C_0$$
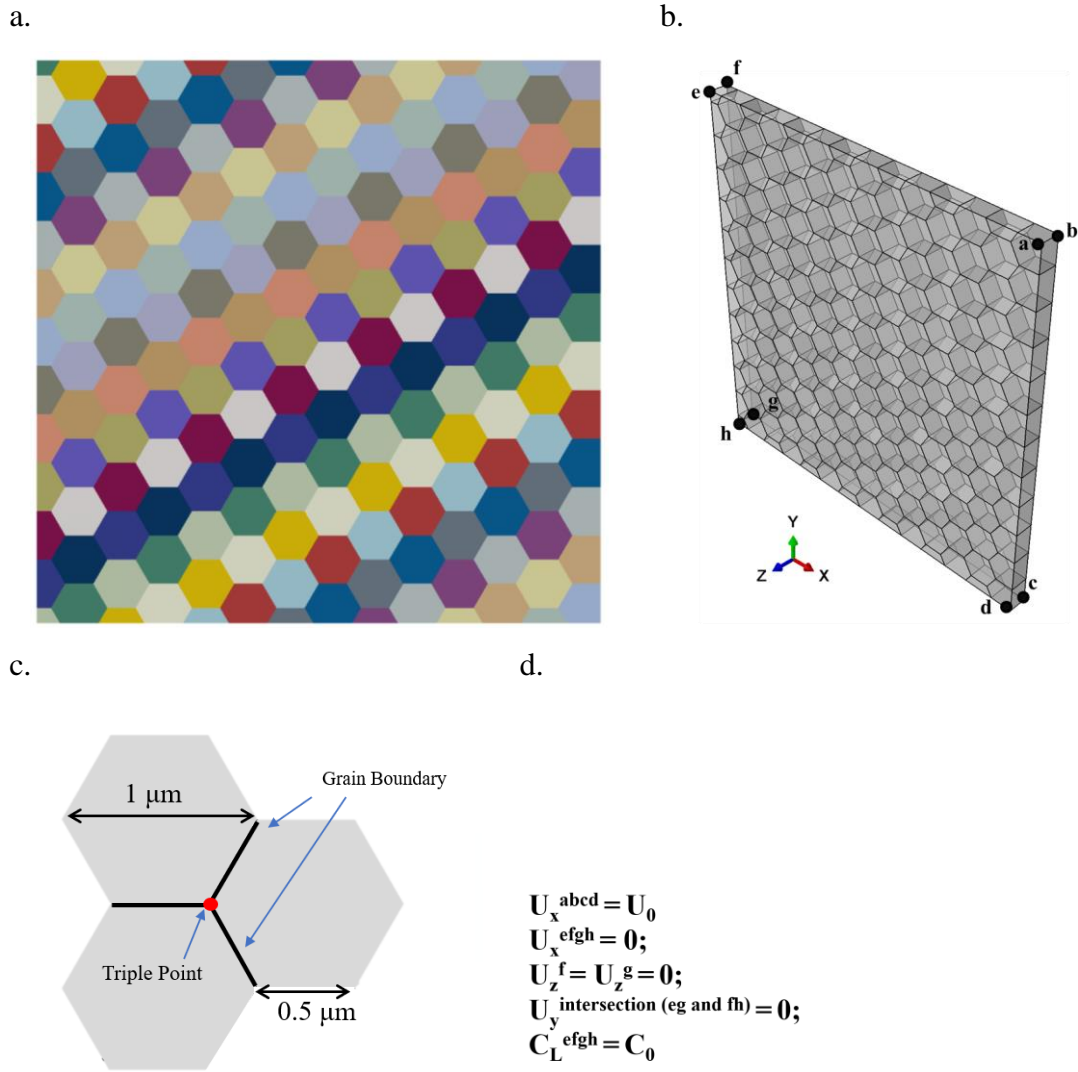
**Fig. 6-3- (a) The grains, (b) 3D view, (c) grain size, and (d) boundary conditions of the polycrystal model with no notch.**

## 6.2.3.4 The three-point bending model

Three-point bending of notched specimens, cut from the nuclear pressure tubes, is a common method that has been used to study hydrogen embrittlement of zirconium alloys (Cui et al., 2009b). A three-point bending model, similar to the one introduced in the study by Shek et al. (2005) and Cui et al. (2009), is introduced to study the state of hydrogen distribution in the vicinity of the notched region. The dimensions of the specimen are the ones from CANDU Zr-2.5Nb pressure tube and are consistent with the mentioned references. The model set-up is shown in Fig. 6-4a. The model is loaded using an externally

applied displacement field ($\Delta Y_{external}$) on the bottom surface of the sample. The boundary conditions (BC) applied to the model are the ones for a typical three-point bending experiment and are summarized in Fig. 6-4b. In this figure, $C_L$ represents the concentration of hydrogen at NILS in wt.ppm and $U_i$ represents displacement BCs along the $i^{th}$ direction where i=1, 2, and 3 respectively represent the global X, Y, and Z-axis shown in Fig. 6-4a. The width of the specimen along Z-axis is 6mm (AB in Fig. 6-4a) and other dimensions of the model are shown in Fig. 6-4c. The dimensions of the notched area in this figure are shown in Fig. 6-4d. The light gray region in Fig. 6-4d is called the Region of Interest (ROI) in the rest of this chapter. The ROI of the model in this section is partitioned into hexagonal-shaped grains (see Fig. 6-4d), the dimensions of which are shown in Fig. 6-3c.
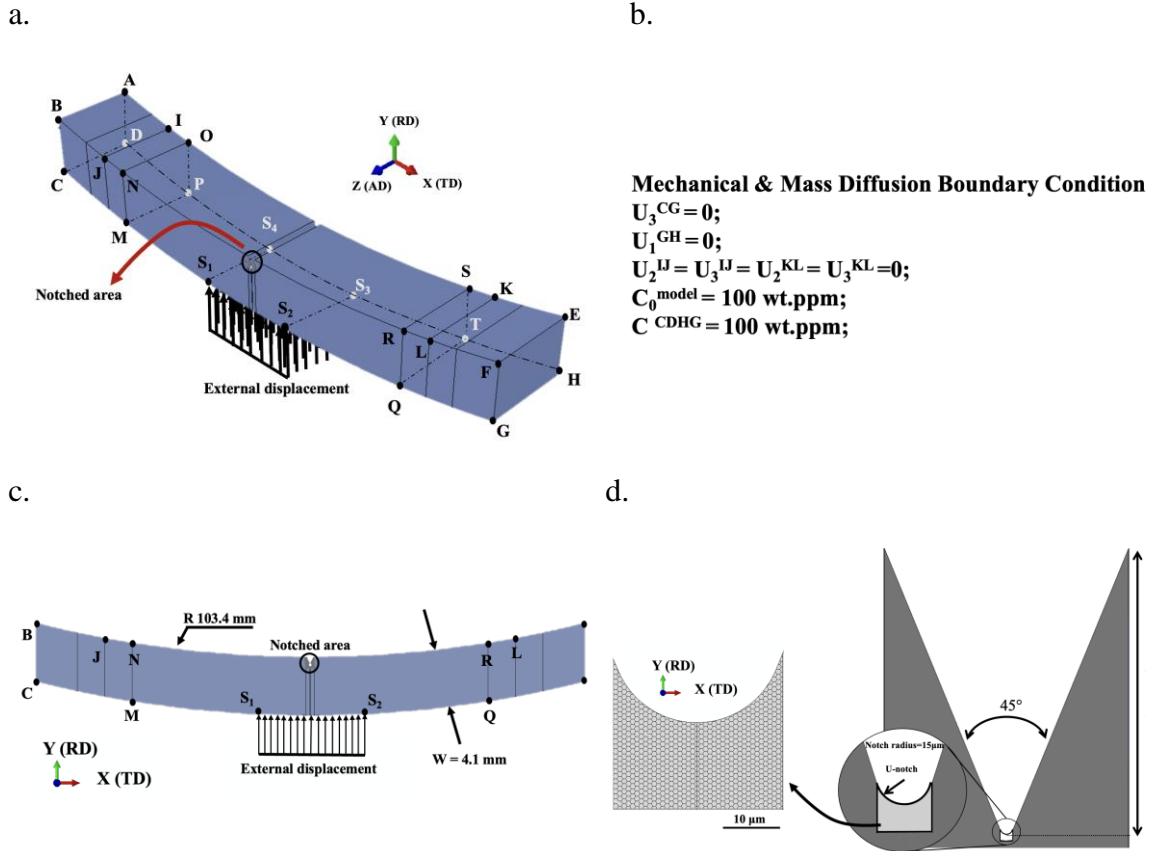
**Fig. 6-4- (a) and (c) the macroscopic set-up of the three-point bending model. (b) The mechanical and mass diffusion boundary conditions of the model. (d) Dimensions of the notched area and configuration of hexagonal-shaped grains used at the notched region. Dimensions of the hexagonal-shaped grains are shown in Fig. 6-3c.**

In all the simulations conducted in this section, the temperature of the model is kept at 603 K to replicate the in-service condition of nuclear reactors. The mass diffusion BC used is constant concentration, applied on the outer surface of the model ($C_L^{CDHG} = 100 \ wt.ppm$). The model is deformed using a quasi-static displacement rate of $0.50 \ \frac{\mu m}{s}$. Also, the c-axis orientation of the elements outside the ROI for all the simulations are set along global X-axis, which coincides with the transverse direction (TD) of the pressure tube. Two different crystallographic textures, similar to the ones introduced in Tondro and Abdolvand (2022) are used to study the state of deformation and subsequent hydrogen distribution near the notch: (1) "random texture" and (2) "textured". For the latter, most of the grains are oriented towards TD, similar to the orientation of grains in a CANDU pressure tube. The

simulations are conducted in one coupled displacement-diffusion step with the use of steady-state condition for hydrogen diffusion. The concentration of hydrogen in NILS and trap sites are reported at the end of this step.

## 6.3 Results

First, the results of the bi-crystal model for the steady state condition are provided which are followed by a transient analysis. The results of the tri-crystal and polycrystal models are subsequently presented.

### 6.3.1 The bi-crystal model: steady-state analysis

The results of the bi-crystal model for the steady state condition and after applying 5% strain along the Z-direction are presented in this section. Unless otherwise stated, all path plots follow the "pq" line shown in Fig. 6-1a with point "p" representing the starting point of the path plot. Since the c-axis of the grain located in the back of the model is parallel to the loading direction, only pyramidal slip system can become active; however, this slip activity occurs at higher stresses since the CRSS of pyramidal <c+a> is the highest among the three slip systems (Table 6-1). That is, this grain resembles a crystallographically "hard grain". On the other hand, the front grain is relatively "soft" where basal and prism slip systems can become active, depending on the magnitude of the applied strain. The activation of different slip systems results in significant deformation heterogeneity between the two grains. This can be seen in Fig. 6-5a where the variation of calculated dislocation density for both grains and for two different $\psi$ angles are illustrated. Since the hard grain barely deforms, the "soft" grain accommodates most of the applied strain and will have higher dislocation density. This will result in significant load sharing, the effects of which is reflected in the redistribution of hydrogen concentration in the lattice sites (Fig. 6-5b). It can be seen that lattice hydrogen concentration, $C_L$, decreases from the hard grain towards the softest grain ($\psi=80˚$) where 15 wt.ppm of hydrogen reduction is observed. Due to the significant elastic and plastic anisotropy of HCP single crystals and the development of triaxial stresses in the vicinity of grain boundaries, this trend changes as a function of $\psi$. For example, when $\psi=45˚$, the reduction in hydrogen concentration $C_L$ is only 5 wt.ppm.
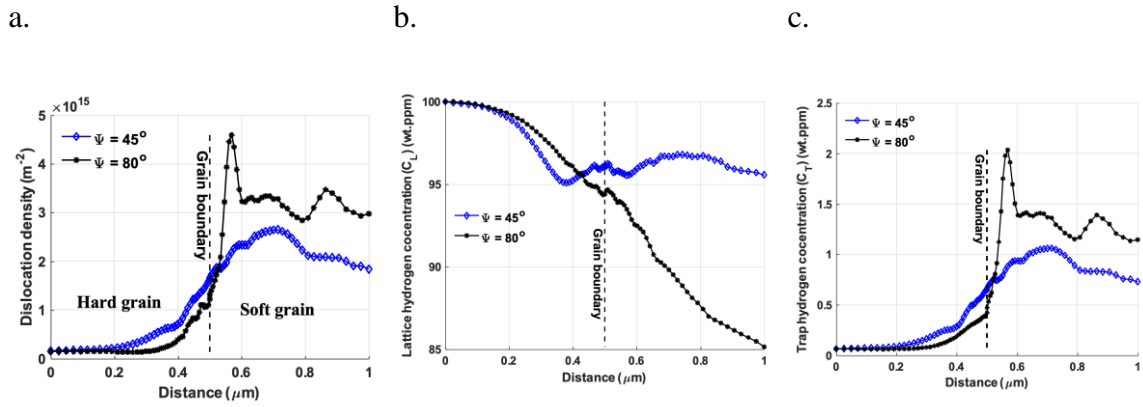
**Fig. 6-5- The results of the bi-crystal model: (a) total dislocation density, (b) hydrogen concentration in the lattice sites, and (c) the trapped hydrogen concentration. All results are for the steady state condition and after applying 5% macroscopic strain in the Z direction.**

The calculated total dislocation densities ($\sum_\alpha \rho_{GND}^\alpha + \rho_{SSD\,GND}^\alpha$) are presented in Fig. 6-5a. Since the "hard" grain does not deform plastically as much as the "soft" grains, higher levels of dislocation densities are recorded in both soft grains. This trend affects the magnitude of calculated trapped hydrogen concentration $C_T$ in the bi-crystal (Fig. 6-5c). As opposed to the trend observed for $C_L$, higher trapped hydrogen concentration $C_T$ is recorded in the soft grains as more dislocations are calculated due to higher levels of plasticity. In addition, the change in the magnitude of $C_T$ is in the order of 2 wt.ppm which is less than 15 wt.ppm observed for $C_L$ at $\psi=80°$, but is comparable to the 5 wt.ppm observed for $C_L$ at $\psi=45°$. It is expected that the contribution of $C_T$ to the total hydrogen concentration increases with plasticity and dislocation density, which takes place at higher applied strains, yet there will be a limit to $C_T$ due to the saturation of dislocation densities.

Fig. 6-5a and 6-5c reveal a peak in both dislocation density and $C_T$ curves of $\psi=80°$ case study, at distance 0.55 µm. This peak is due to the formation of highly localized deformation zones near grain boundaries that resemble slip bands and is the outcome of using a strain-gradient formulation. To further investigate such localization of hydrogen atoms, two other path plots are prepared and presented in Fig. 6-6a. The distribution of total dislocation density is shown in Fig. 6-6b, where it is observed that several "slip bands", or highly deformed zones, are formed in the vicinity of the grain boundaries but

within the soft grain. It has been shown that the directions of calculated "slip bands" are generally parallel to the experimentally observed slip bands (Sedaghat and Abdolvand, 2021), and for this particular case, they are parallel to the prism slip systems. Similar peaks are observed for $C_T$ which are shown in Fig. 6-6c and Fig. 6-6d along Path-A and -B (defined in Fig. 6-6b). It can be seen that the magnitude of $C_T$ at the peak observed along Path-A is ~6 wt.ppm which exceeds the variation calculated for the maximum of $C_L$, showing the significance of trapped hydrogen atoms, especially in the highly deformed zones. In these zones, trapped hydrogen concentration will represent a major part of the total hydrogen content and will significantly affect the materials performance. The results presented in this section are consistent with those reported in Aubert et al. (2012), Girardin et al. (2015), Jagodzinski et al. (2000), where it is observed that local hydrogen concentration correlated with slip bands. It is also stated that high hydrogen concentration that results in hydrogen-induced damage most likely happens in dislocation pile-ups (Ulmer and Altstetter, 1991).
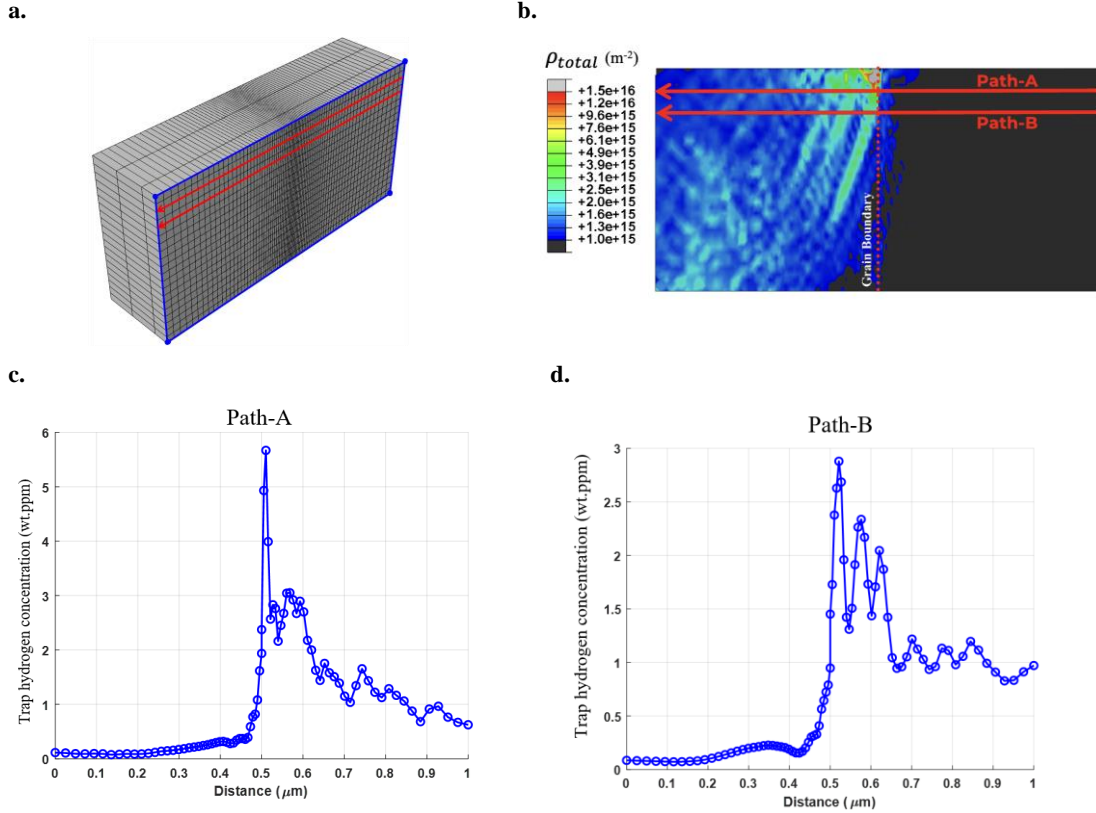
**Fig. 6-6- The localization of trapped hydrogen concertation $C_T$ in the vicinity of slip bands: (a) the two path plots, (b) the calculated dislocation densities (m$^{-2}$). Variation of $C_T$ along (c) Path-A and (d) Path-B. The misorientation between the two grains is ψ=80˚.**

## 6.3.2 The bi-crystal model: transient analysis

Considering the grain size used and the size of the model, a steady state analysis was used in the previous section. According to Zhang et al. (2017), the average diffusivities of hydrogen in zirconium along the crystal c- and a-axis at 603 K is 1.45x10$^{-4}$ mm$^2$/s. Hence, the diffusion length of hydrogen $\left(L_D = \sqrt{D.t}\right)$ at this temperature is ~1.7 µm in 0.02 seconds. This diffusion length is larger than the 1µm length of the model and indicates that hydrogen diffusion happens at much shorter time scales than the one used for applying the mechanical BC. Therefore, it is acceptable to use the steady state condition for calculating the redistribution of hydrogen atoms; however, as shown in Eq. 6-26, the effective diffusivity ($D_{eff}$) depends on the magnitudes of $C_T$ and $C_L$. Hence, in this section, the variations of such parameters in the first 0.02 seconds of the analysis are studied using a

coupled diffusion-displacement transient analysis. The bi-crystal model with a $\psi=45^o$ is used for this purpose, but the trends presented below hold for other angles, as well.

Fig. 6-7a and Fig. 6-7b show the changes in the fractions of lattice ($\theta_L$) and trap ($\theta_T$) sites that are occupied with hydrogen atoms. Results are provided at different time steps and along Path#1 in Fig. 6-1a. It can be seen that both $\theta_L$ and $\theta_T$ reach the steady-state condition as time approaches 0.02 seconds. In addition, the boundary value for $\theta_L$ is the 100 wt.ppm assigned as BC divided by the theoretical value for maximum hydrogen in the zirconium lattice, which is 18,200 wt.ppm for zirconium δ-hydrides (Courty et al., 2014b). Hence, the maximum value of $\theta_L$ is $5.5 \times 10^{-3}$ which is significantly lower than 1, reinforcing the assumption made in Eq. 6-23. Once $\theta_L$ is determined, the value of $\theta_T$ can be extracted from the Oriani's equilibrium condition (Eq. 6-22). Although, value of $\theta_T$ depends on the temperature and the trap binding energy of hydrogen in zirconium ($\overline{\Delta H_B}$)- the effects of which are further discussed in section 6.4.1.

Fig. 6-7- c demonstrates the ratio of effective diffusivity ($D_{eff}$) to lattice diffusivity ($D_L$) which is equal to $1/(1 + \omega)$, according to Eq. 6-27. This value increases with hydrogen diffusing into each available space and plateaus at about $t = 0.02$ seconds. This trend agrees with the results presented in the study by Krom and Baker (2000).

a.



b.



c.
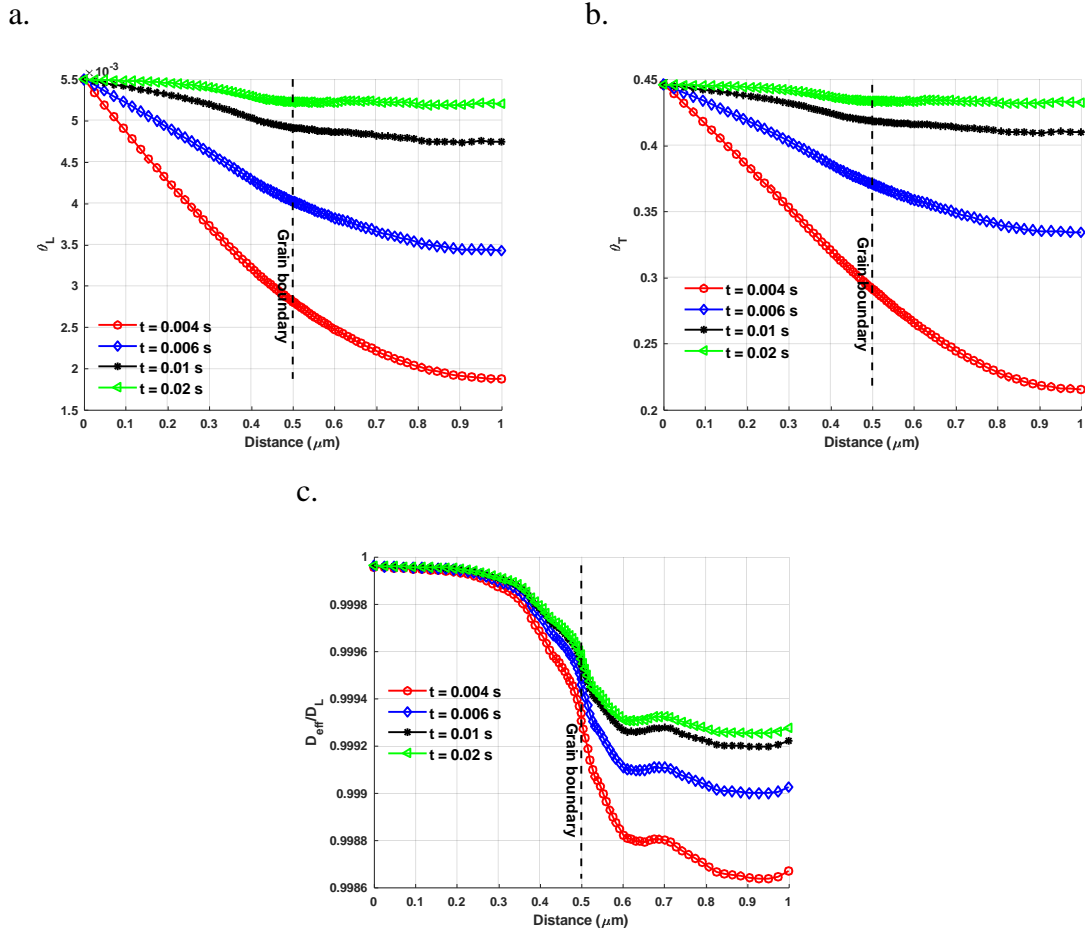


**Fig. 6-7- The occupancy of hydrogen in (a) lattice sites, and (b) trap sites. (c) The ratio of effective diffusivity to lattice diffusivity from Eq. 6-27. All results are for the bi-crystal model, along path "pq" shown in Fig. 6-1a.**

## 6.3.3 The tri-crystal model and twinning

In this section, the results of the tri-crystal models with an embedded twinning domain in the middle grain is presented. This is to show how $C_H$, $C_L$, and $C_T$ vary in localized deformation zones, such as the ones that develop in the vicinity of twin tips (Abdolvand and Wilkinson, 2016b). The results are shown only for the three adjacent crystals, where the surrounding buffer region is removed.

a.

b. Lattice hydrogen concentration at twin tips

c. Trap hydrogen concentration at twin tips

d. Total hydrogen concentration at twin tips
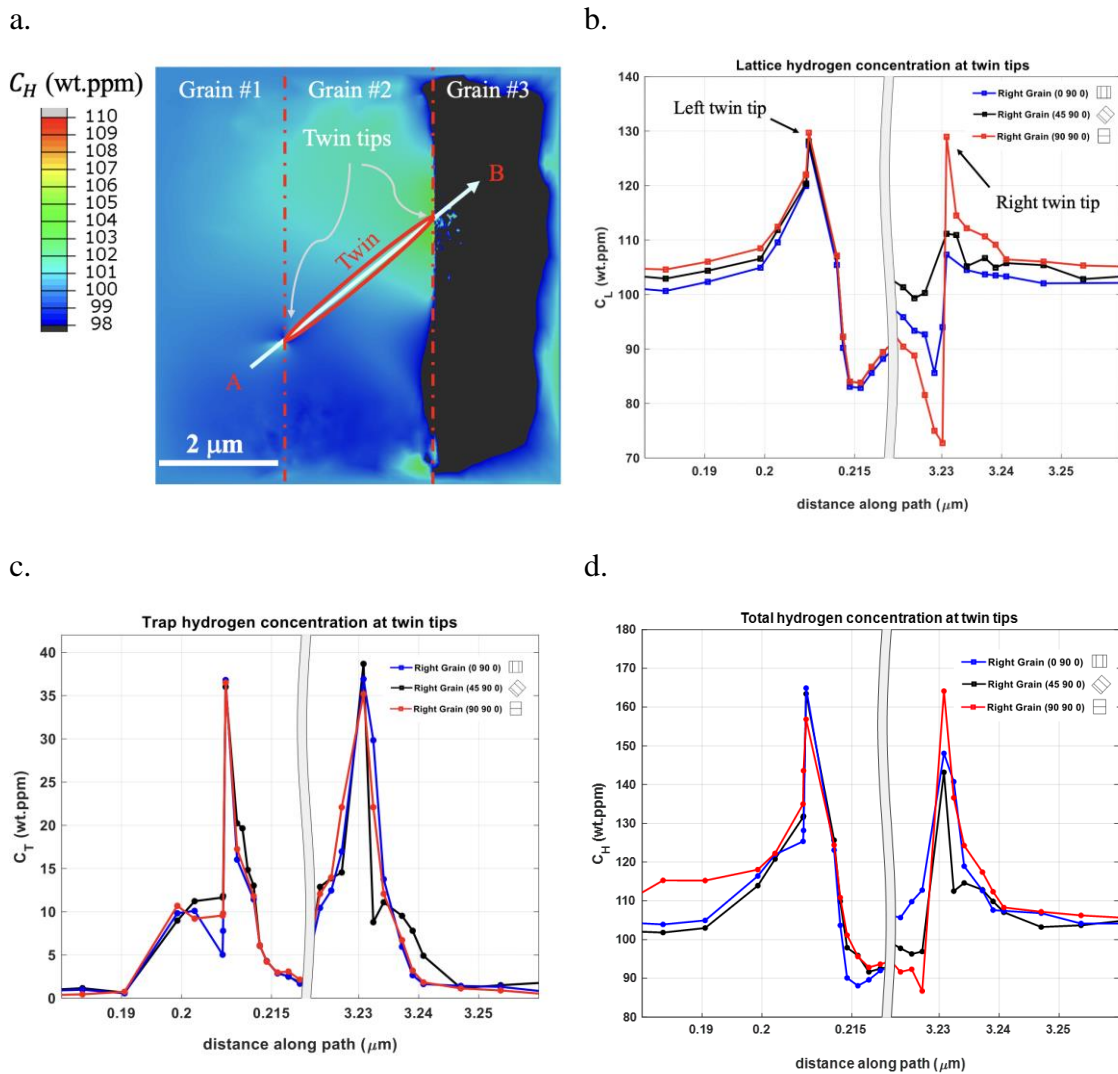
**Fig. 6-8- The results of the tri-crystal model with a twin domain: (a) the distribution of total hydrogen concentration. The distribution of (b) lattice hydrogen concentration, (c) trapped hydrogen, and (d) total hydrogen concentrations along the Path A-B. Path A-B is shown in (a).**

The distribution of $C_H$ is shown in Fig. 6-8a. Both twin tips, regardless of the assigned orientations are the sites at which $C_H$ peaks. Path A-B is introduced in this figure to investigate local variations. This path starts from Grain #1 and passes through the tips of the twin, located in Grain #2, and stops inside Grain #3. It can be seen that the left twin tip, located in the hard grain, is the site at which the lattice hydrogen concentration has the highest magnitude (see Fig. 6-8b); This is due to the development of higher localized

hydrostatic stresses in Grain #1. Furthermore, the tips of the twin domain are highly deformed regions where $C_T$ also spikes (see Fig. 6-8c), regardless of the assigned grain orientation; however, results of Fig. 6-8d suggest that the total hydrogen concentration at twin tips are still governed by the local stresses at the twin tips- which depend on the orientation of neighboring grain. The distribution of $C_T$ in these models show that trapped hydrogen might increase in excess of 40% of the initial hydrogen concentration. Results of this section suggest that as the material undergoes higher levels of plasticity, $C_T$ plays more important role in determining the state of hydrogen concentration.

## 6.3.4 The polycrystal model

In this section, the results of the polycrystal model are presented to investigate the effects of texture on hydrogen redistribution. The model is assumed to be heavily textured with most of the crystals c-axis oriented towards the loading direction, which is parallel to the x-axis. This model is named "X-texture". Both applied texture and the coordinate system of the model are shown in Fig. 6-9a. This texture resembles the heavy texture of CANDU pressure tubes where the crystals c-axis are mainly oriented towards the tube's transverse direction, although, other textures are further discussed in section 6.4.3. Attention is given to the biased, stress-driven concentration of hydrogen atoms at grain boundaries, in addition to the relationship between the hydrogen concentration and c-axis misorientations at the grain boundaries.
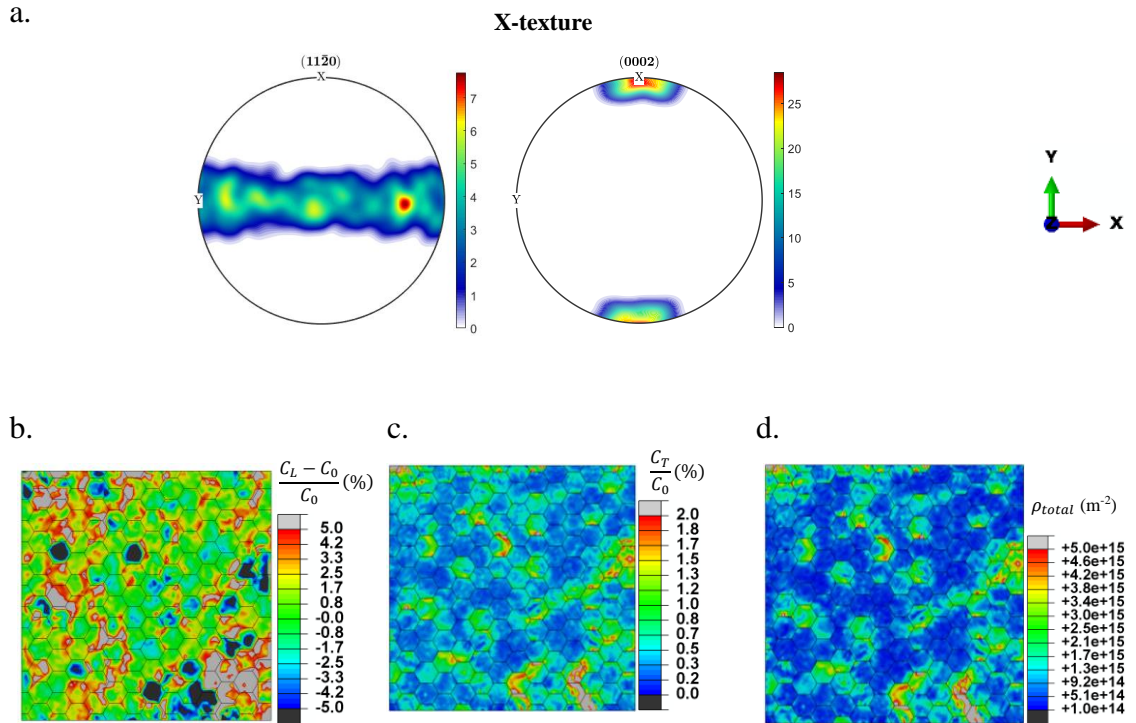
**Fig. 6-9- The results of the polycrystal model: (a) $(0002)$ and $(11\bar{2}0)$ pole figures. (b) The variation of lattice hydrogen concertation $C_L$. (c) The variation of trapped hydrogen concentration $C_T$. (d) The distribution of total dislocation density. The coordinate system of the model is shown in the right-hand side and $C_0$ represents the initial hydrogen concentration of 100 wt.ppm that is applied as a boundary condition.**

The results of the polycrystal model at the applied strain of 5% are presented in Fig. 6-9b-d. To provide a better comparison between $C_T$ and $C_L$, the results for hydrogen concentrations are normalized with respect to the applied BC ($C_0$), i.e., 100 wt. ppm. It is shown that the elastic and plastic anisotropy of HCP crystals result in significant stress heterogeneity, the effects of which are reflected in the heterogeneous distribution of hydrogen atoms. For example, Fig. 6-9b shows that in the areas where tensile hydrostatic stresses develop, the concentration of hydrogen in the lattice ($C_L$) increases up to 5%, i.e., 5 wt.ppm. This is clear evidence showing that some grain boundaries are more prone to hydrogen embrittlement. While the magnitude of $C_L$ can both increase or decrease, the value of trapped hydrogen concentration $C_T$ is shown to always increase due to the increase in total dislocation density (Fig. 6-9c and 6-9d). In addition, while the applied strain is only

5%, the calculated increase for $C_T$ is comparable to that of $C_L$ indicating the contribution of dislocations to hydrogen embrittlement. It is evident that the magnitude of plastic strain can be significantly higher near notch tips, resulting in stronger contribution of dislocations and traps to hydrogen embrittlement (see section 6.3.5).

The distributions shown in Fig. 6-9 reveal that hydrogen atoms tend to diffuse towards grain boundaries. Generally, the distribution of hydrogen atoms is relatively more uniform inside the grains, compared to that of grain boundaries, where there seems to be more fluctuations of hydrogen concentration. To further analyze the distribution of hydrogen atoms, the nodes of the model are divided into three categories, which are shown in Fig. 6-10a: nodes residing within grains, nodes residing at grain boundaries, and nodes residing at triple points.

The distributions of lattice hydrogen concentration $C_L$ for all three types of nodes are plotted in Fig. 6-10b. While the calculated average $C_L$ is the highest for triple points and lowest for internal nodes, a distinct variation is observed for the calculated standard deviations (SDs). It is evident that the standard deviation of the triple-junction nodes is the highest, with those of the grain boundary and internal nodes being lower and the lowest, respectively. Therefore, the numerical results indicate that when hydrogen diffusion is solely driven by stress, there is a higher probability for hydride precipitation and hydrogen-induced damage at grain boundaries compared to grain interiors. These results are in agreement with the EBSD-measured experimental data that shows that hydrides tend to preferentially precipitate along grain boundaries rather than inside the grains of an α-zirconium polycrystal (Kiran Kumar et al., 2010).

**X-texture**

a.

b.

Internal nodes (46255 nodes), Mean = 100.7,  SD =3.06

Grain-boundary nodes (12619 nodes), Mean = 100.9,  SD =3.42

Triple-junction nodes (2093 nodes), Mean = 101.3,  SD =4.78
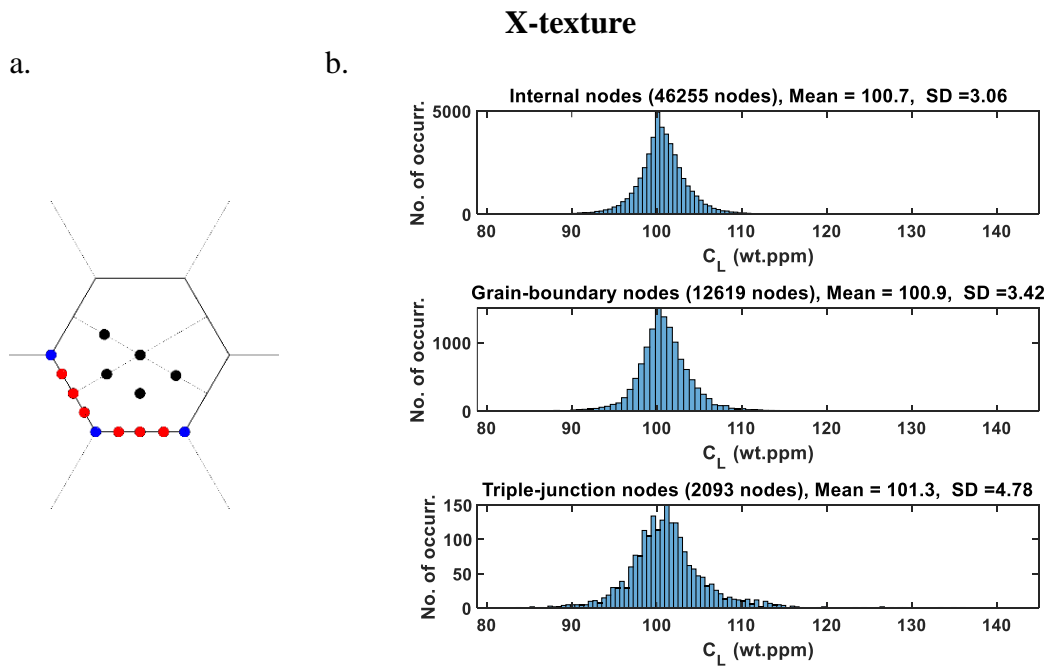
**Fig. 6-10- (a) The three categories of finite element nodes: black dots represent internal nodes, red dots represent grain boundary nodes, and blue dots represent triple points. (b) The distribution of lattice hydrogen concentration $C_L$ for the three types of nodes. SD represents standard deviation.**

The effects of c-axis misorientation between any two neighboring grains on the hydrogen concentration at the grain boundary are investigated to determine any possible relationships between the two. Fig. 6-11a shows the distribution of lattice hydrogen concentration $C_L$ as a function of basal plane misorientation. To be able to demonstrate the otherwise unobvious relationship in the dotted graph, four regions are considered based on the misorientations. The distribution of lattice hydrogen concentration for each section is plotted in Fig. 6-11b. The number of points in each population, the mean, and standard deviation (SD) values are mentioned above each distribution. Although the mean values only slightly increase towards higher misorientations, the increase in the standard deviations is more tangible. That is, the probability for hydrogen accumulation and the subsequent hydride formation or hydrogen-induced damage increases with increasing misorientation between the two neighboring grains. This effect is associated with the elevated levels of stress triaxiality and hydrostatic stress gradients due to compatibility-induced stresses in the vicinity of the

grain boundary, which results in more severe fluctuations in hydrogen content at such places compared to the inside of the grains.

a.

b.
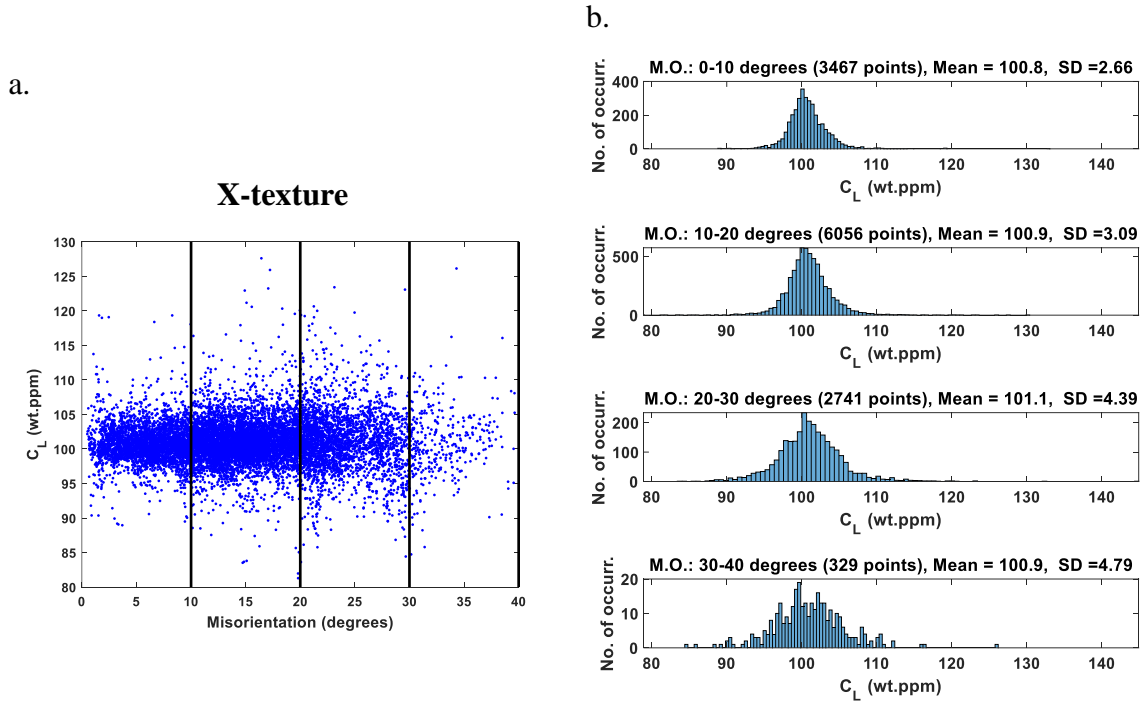


**Fig. 6-11-** **(a) The distribution of lattice hydrogen concentration C$_L$ as a function of the basal plane misorientation (M.O.) of any two neighboring grains. The data shown in (a) are divided into four categories: misorientations between 0° to 10°, 10° to 20°, 20° to 30°, and 30° to 40° with the histogram of each category shown in (b). SD represents standard deviation.**

The results presented in this section are in agreement with those reported in the literature. For instance, Fu et al. (2021) have shown that hydrogen-induced cracking in steel mainly happens along grain boundaries. He et al. (2021) have reported similar results for austenite, but in agreement with the numerical results presented here, it is also shown that a higher misorientation between neighboring grains will increase the tendency of segregation of hydrogen atoms from the lattice into the grain boundary. The preferential stress-assisted diffusion of hydrogen atoms towards grain boundaries in materials with cubic crystals is also reported by Ilin (2014). Similarly, with the use of molecular dynamics (MD) modeling, Lloyd et al. (2019) have shown that due to the state of the stress, hydrogen atoms tend to diffuse towards grain boundaries of zirconium crystals. Also, with using a critical nucleation energy analysis, Qin et al. (2011) have shown that grain boundaries with higher

misorientation are preferential sites for hydride nucleation than those with lower misorientation.

## 6.3.5 The three-point bending model

The results for $C_L$ and total hydrogen concentration in the ROI of the three-point bending model are investigated. All figures are for the applied displacement of $\Delta Y_{external} = 130$ μm. The distributions of dislocation density for the "random texture" (U-Poly-R) and "textured" (U-Poly-T) models are respectively shown in Fig. 6-12a and Fig. 6-12b. As shown, the textured model undergoes lower plasticity, and hence has less dislocation density near the notch, and vice versa for the random texture model. Also, Path-N is introduced in both models to better understand the distribution of hydrogen along the notch tip. The distributions of $C_L$ and $C_H$ are respectively shown in Fig. 6-12c and Fig. 6-12d, for both models along Path-N. Since the textured model develops higher stresses, as a results of developing less plasticity, it hosts more hydrogen atoms in its lattice sites. This can be seen in the peak of hydrogen concentration along Path-N. On the other and, since the random model develops higher plasticity and, hence, dislocation density, the peak of $C_H$ will be associated with this model, indicating the significant role of dislocations to trapping hydrogen and affecting total hydrogen concentration.
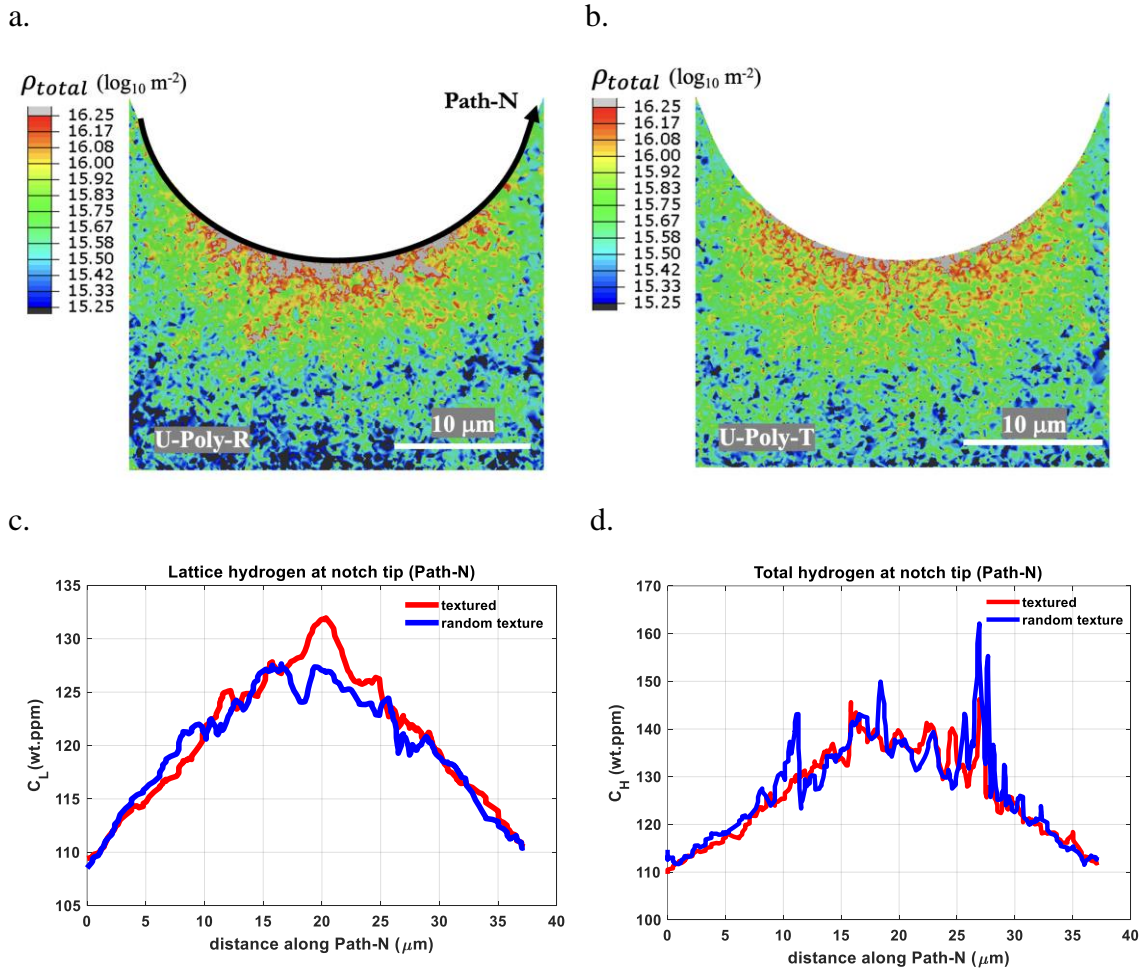
**Fig. 6-12- The results of the three-point bending model: the distribution of total dislocation density in (a) random texture and (b) textured models. The variation of (c) lattice hydrogen concentration and (d) total hydrogen concentration for both models along Path-N, shown in (a).**

## 6.4 Discussion

In this section, the parameters affecting the distribution of trapped hydrogen concentration are studied. The effects of trap binding energy, temperature, external load, initial hydrogen concentration, grain size, and diffusion boundary conditions are studied first using the bi-crystal model. This is followed by using the polycrystal model to study the effects of texture. Lastly, a comparison between the simulation results with those published in the literature is provided.

## 6.4.1 Binding energy and temperature effects

Two of the parameters that affect the magnitude of the calculated trapped hydrogen concentration $C_T$ are the trap binding energy of hydrogen in the zirconium lattice $(\overline{\Delta H_B})$ and temperature, the effects of which are studied here. The Oriani's (1970) equilibrium condition was used to determine $C_T$ based on $\overline{\Delta H_B}$ and applied temperature (Eq. 6-22). It is reported that $\overline{\Delta H_B}$ varies from 16.7 kJ/mol to 35.2 kJ/mol (Wimmer et al., 2020), while in the current study, $\overline{\Delta H_B}= 25$ kJ/mol is used as a mid-point value in between the two extremes. This number was also previously reported in the study by Swan et al. (2022). In Fig. 6-13a, the variation of trap sites occupancy fraction $\theta_T$ is plotted as a function of $\overline{\Delta H_B}$, considering constant lattice occupancy for $C_L=100$ wt.ppm. It is shown that for $\overline{\Delta H_B}$ less than 15 kJ/mol, less than 10% of trap sites are occupied by hydrogen while for $\overline{\Delta H_B}$ higher than 40 kJ/mol, more than 90% of trap sites are occupied. The subsequent effects of $\overline{\Delta H_B}$ and $\theta_T$ on $C_T$ are shown in Fig. 6-13c where the variation of $C_T$ along the "pq" path of the bi-crystal model for different $\overline{\Delta H_B}$ are plotted. It can be seen that when the trap binding energy increases, the trapping mechanism becomes more favorable and the magnitude of $C_T$ increases, particularly in the softer grain with more dislocations. In addition, the magnitude of $C_T$ increases by an order of magnitude from $\overline{\Delta H_B}=15$ kJ/mol to 35 kJ/mol.

a.



b.



c.



d.
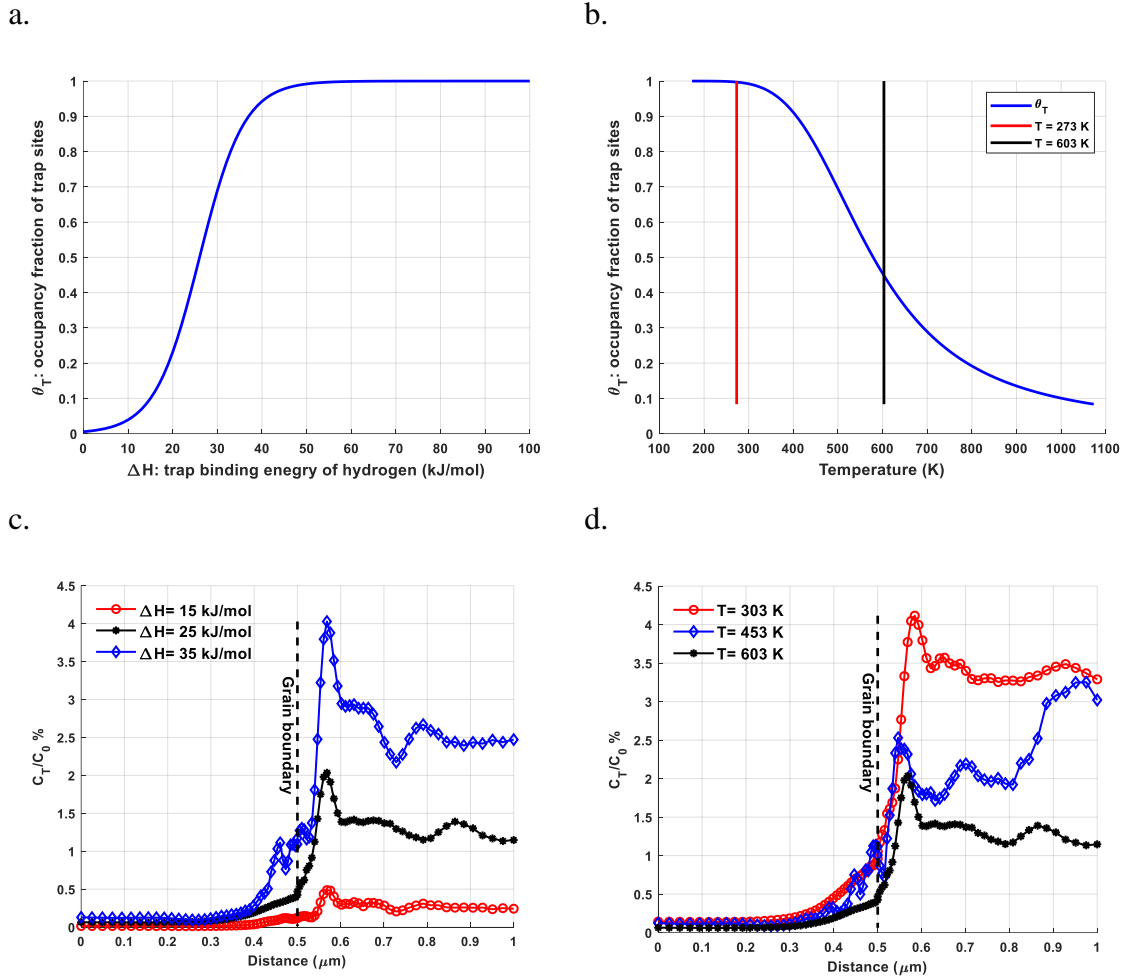


**Fig. 6-13- The variation of trap occupancy fraction as a function of (a) trap binding energy and (b) temperature. The variation of trapped hydrogen concentration as a function of (c) trap binding energy and (b) temperature for the bi-crystal model for ψ=80˚.**

The variation of $\theta_T$ with respect to temperature is plotted in Fig. 6-13b, where it is shown that, the trapping mechanism is more favorable at room temperatures. At operative temperatures of nuclear reactors, i.e., ~600 K, only 50% of trap sites can be occupied by hydrogen atoms. Similarly, due to the development of higher dislocation densities in the soft grain, more tangible effects can be observed in the soft grain where the magnitude of $C_T$ is increased two-fold from 30 ˚C to 330 ˚C (Fig. 6-13d). It is worth mentioning that while solid solubility of hydrogen in zirconium is about 100 wt.ppm at 600 K, it reduces to about 10 wt.ppm at room temperature, resulting in the precipitation of excessive hydrides. That is, by reducing temperature, while trap sites become more favorable for

171

hydrogen atoms, precipitation will take place reducing hydrogen concentration in the lattice.

## 6.4.2 The effects of model parameters and boundary conditions

The effects of applied boundary conditions, namely, external load and initial hydrogen concentration are investigated and shown in Fig. 6-14. Fig. 6-14a shows the effect of initial hydrogen concentration $C_0$. All results are normalized with respect to $C_0$ for a better comparison. It is shown that the trapped hydrogen concentration plays more important role at lower $C_0$, which takes place at the early years of nuclear pressure tubes lifetime. Fig. 6-14b shows the effects of applied load on the magnitude of trapped hydrogen concentration, which has a direct relationship with the calculated dislocation densities. At higher plastic deformations, more dislocation density will be generated, increasing the trapped hydrogen concentration. Therefore, there is a direct relationship between applied load and trapped hydrogen concentration, which indicates the significance of dislocation trapping in highly strained regions, e.g., crack-tips, slip bands, and notch tips.

a.



b.



c.



d.
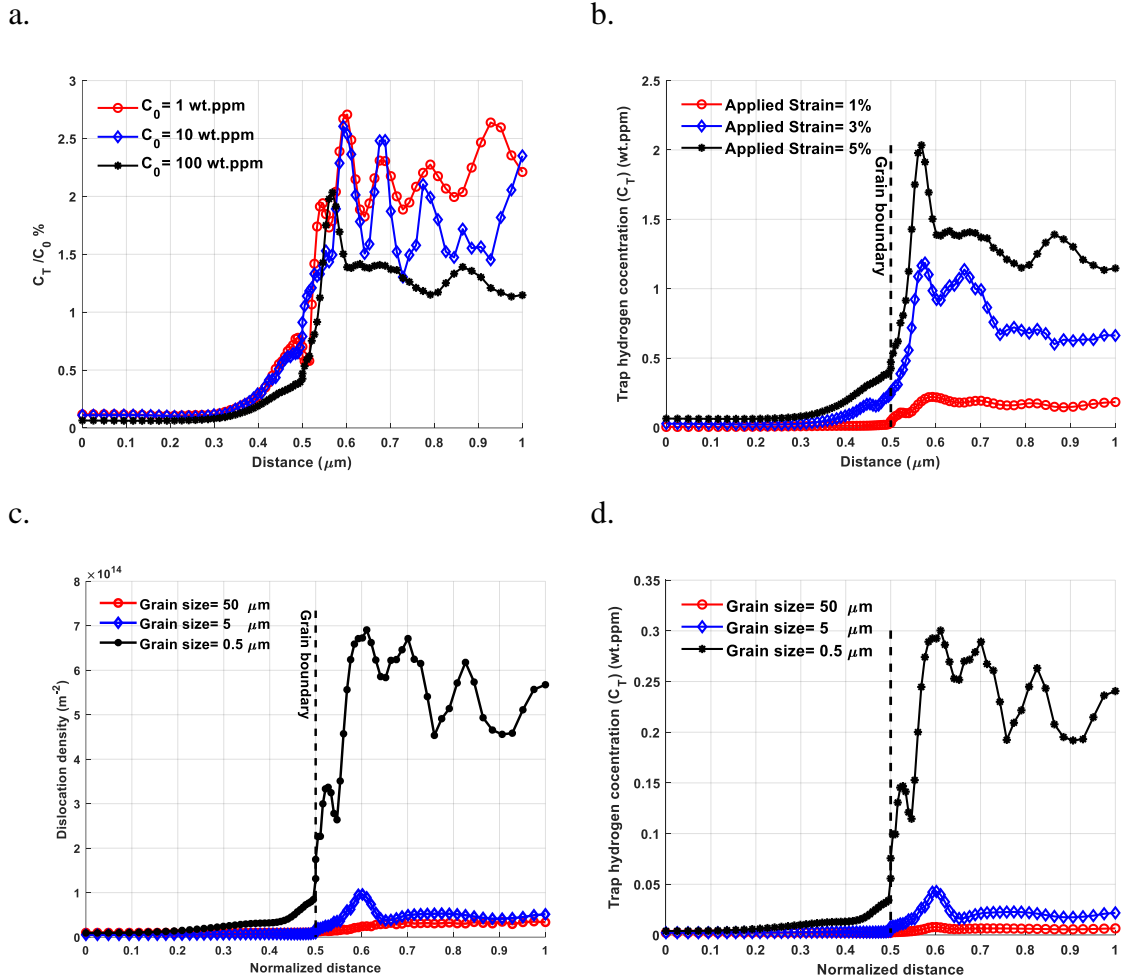


**Fig. 6-14- The effects of (a) boundary condition C₀, and (b) applied strain on the trapped hydrogen concentration C_T. The effects of grain size on (c) calculated dislocation densities, and (d) the trapped hydrogen concentration C_T after 1% of external strain. The distance in (c) and (d) are normalized with respect to the total size of the bi-crystal model. All results are for bi-crystal with ψ=80˚.**

The magnitude of dislocation densities is affected by the size of grains. This is due to the geometrical constrains that affect the determination of GND densities and it is well-studied in the literature (Acharya and Bassani, 2000; Arsenlis and Parks, 1999). Here such variations for the calculated dislocation densities are investigated by changing grain size from 50 µm to 0.5 µm. In Fig. 6-14c, it is shown that the calculated total dislocation density is increased by an order of magnitude in the softer grain (ψ=80˚) when smaller grains are used, but such variations become negligible for bigger grains. The corresponding hydrogen concentrations in trap sites for the applied strain of 1% are provided in Fig. 6-14d. It can

173

be seen that grain size greatly affects the value of $C_T$ for submicron grains. This is important as the average grain size for nuclear pressure tubes are generally in the order of micron or sub-microns.

These results are in agreement with the ones from the literature discussing the effects of grain size on hydrogen embrittlement rate. For example, Qin et al (2012), showed that an increase in the grain boundary area results in more nucleation sites for hydride precipitation in Zircaloy-4. EBSD measurements have also indicated that hydrogen content in a Zircaloy-4 specimen will increase when grain size is reduced (Silva et al., 2019).

In all simulations presented so far, a constant hydrogen concentration of 100 wt.ppm was imposed onto one of the model surfaces. This diffusion boundary condition has been used in other studies (Krom and Bakker, 2000; Sofronis and McMeeking, 1989), but constant chemical potential might also be a suitable condition (Di Leo and Anand 2013). In this section, the results of the model for these two cases are compared and discussed.

The bi-crystal model presented in Fig. 6-1a is used. The misorientation between the two crystals is set at 80° and the model is deformed to $\varepsilon=1\%$. Two cases are examined, where for the first case, a constant lattice hydrogen concentration is applied onto the back surface of the model, i.e., $C_L^{ijkl} = 100$ wt.ppm. In the second case, a constant chemical potential, $\mu - \mu_0 = RT\ln(\hat{c}_0) - \frac{\hat{\sigma}_{kk}^0}{3}\overline{V}_H$, is applied on the same surface. In this equation, $\hat{c}_0$ and $\frac{\hat{\sigma}_{kk}^0}{3}$ are the hydrogen concentration and hydrostatic stress of a reference point within the model and away from the boundaries. Considering that the actual value of $\mu - \mu_0$ is not known, and that the trends observed are independent from the value of $\mu - \mu_0$, this reference point is selected within the first case model such that the results of both models for $C_L$ converge.

Fig. 6-15a shows the distribution of hydrogen concentration on the mid-plane along the Y-axis of both models with different diffusion boundary conditions. Path#1 to #4 are defined along different directions to study the distributions of hydrogen concentrations. As seen in Fig. 6-15a and Fig. 6-15c, hydrogen concentration along Path#2 located on the back surface of the model is not constant when a constant chemical potential is used. However, Fig. 6-15b indicates that the observed trends for hydrogen concentration are not influenced by

the type of boundary condition used. In addition, the hydrogen concentration fields are not affected except for the region where the boundary condition is applied. This region is shown using the dotted ellipses in Fig. 6-15a. The calculated values near this region are magnified in Fig. 6-15b. It can be concluded that the trends presented in this work are not substantially dependent on the implemented diffusion boundary conditions.

a.
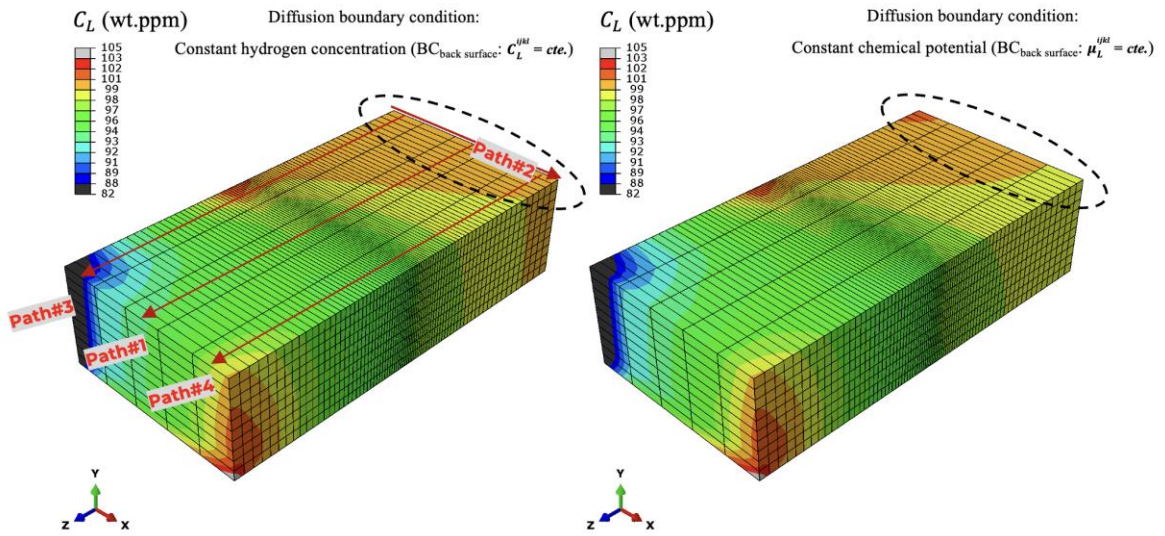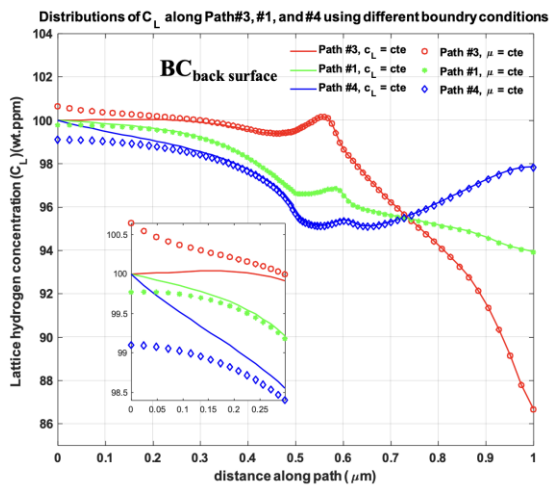


b.                        c.
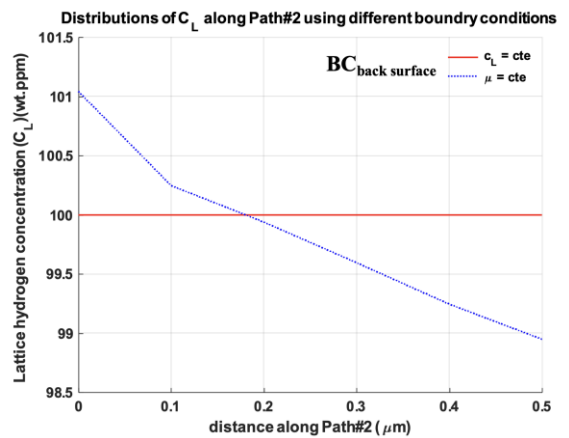


**Fig. 6-15 - (a) The effects of boundary conditions on hydrogen concentration. Distributions of hydrogen concentration along (b) Path #1, #3, #4 and (b) Path #2 for constant concentration and constant chemical potential. Path#1 to #4 are shown in (a).**

## 6.4.3 The effects of texture

To study the effects of materials texture on the redistribution of trapped hydrogen atoms, two models are prepared. The first model is identical to the polycrystal model presented in section 6.3.4 with most of the crystals c-axis oriented towards the X-axis, which is parallel to the loading direction (see Fig. 6-9a). This model is called X-texture and has crystallographically "hard" grains. The setup of the second model is identical to the first, except that a "soft" texture is assigned to its grains, i.e., the pole figure of the first model presented in Fig. 6-9a is rotated about the Y-axis so that most of the crystals have their c-axis oriented towards the Z-axis. This model is called Z-texture model. The distributions of total dislocation density and trapped hydrogen concentration are shown in Fig. 6-16, following 0.5% of external strain along global X-direction. The distributions show that in comparison to the Z-texture model with soft grains, the X-texture model has lower mean dislocation density as well as trapped hydrogen concentration. Also, it has lower standard deviation for trapped hydrogen which indicates a more localized hydrogen distribution. This highlights the importance of trapped hydrogen concentration in softer textures.

a.
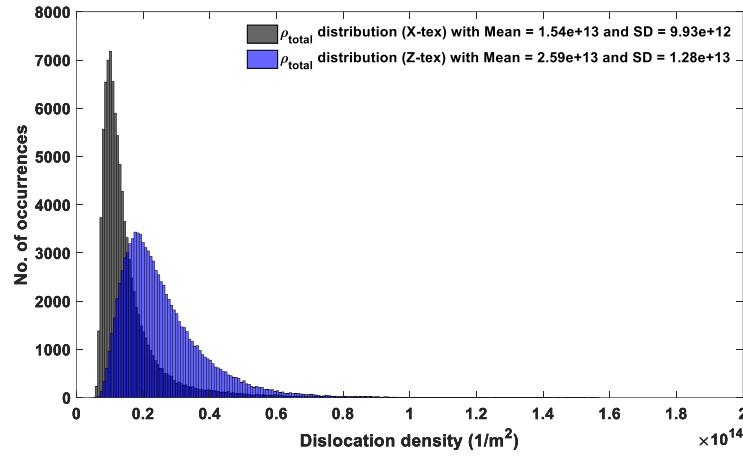


b.
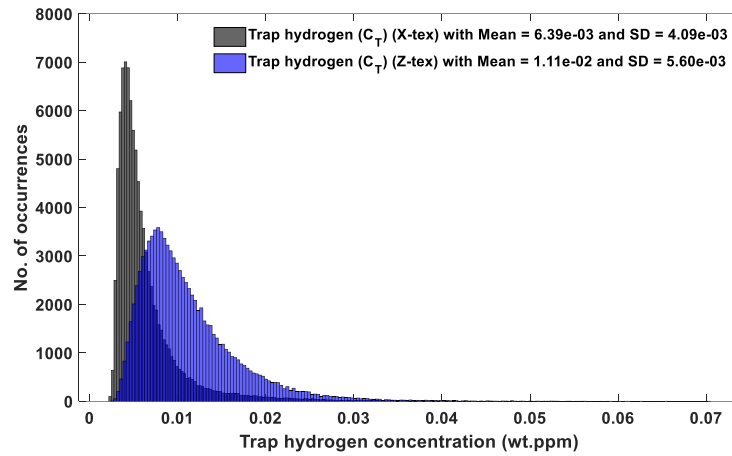


**Fig. 6-16- The distribution of (a) total dislocation densities (b) trapped hydrogen concentrations. Results are shown for both X-texture model Z-texture model.**

## 6.4.4 General Discussion

Very few studies have focused on measuring hydrogen concentration within traps and NILS. Since the focus of our study is on the contribution of dislocations to $C_T$, we first start by comparing the calculated dislocation densities to those previously measured. By using transmission electron microscopy and neutron diffraction, Long et al. (2017a) measured the dislocation density in a Zr-2.5Nb specimen deformed to $\varepsilon$=5%. It was reported that $\rho_{total}$ varies from $6.93\times10^{14}$ to $11.1\times10^{14}$ m$^{-2}$, depending on the measurement direction. For the polycrystal model shown in Fig. 6-9d and under 5% applied strain, the non-local

CPFE model used in this work calculates an average dislocation density of $\rho_{total} = 9.67 \times 10^{14}$ m$^{-2}$, which falls in between the boundaries determined by Long et al. (2017).

In a recent study by Swan et al. (2022), the concentration of hydrogen atoms in the trap and lattice sites were measured using synchrotron X-ray diffraction. A Zircaloy-4 specimen was used that was cold worked to 80%. It was reported that the peak of trapped hydrogen concentration takes place at ~300 °C. At temperatures higher than 300 °C, hydrogen atoms start to reside in NILS due to their release from both trap sites and from hydrides. Below 300 °C, the hydrogen concentration within hydrides increases. The trapped hydrogen concentration of ~20 wt.ppm for this extremely deformed specimen was reported at ~300 °C. This value is comparable and consistent with the results presented in section 6.3.3 and 6.3.5 for trapped hydrogen concentration in highly deformed zones.

## 6.5 Conclusions

A hydrogen diffusion subroutine coupled with a non-local CPFE framework was developed to deconvolute the contribution of hydrostatic stress as well as dislocation densities on lattice and trapped hydrogen concentrations. It is shown that:

1. The load sharing between hard and soft grains significantly affects the patterning of hydrogen distribution within grains.
2. Generally, hard grains develop higher hydrostatic stresses and hence higher hydrogen concentration within the lattice, but less dislocations and hydrogen within the trap sites.
3. On the other hand, soft grains develop less hydrostatic stresses, but higher dislocation densities that leads to hosting more trapped hydrogen.
4. In the localized deformation zones such as in the vicinity of grain boundaries, at the interface of hard-soft grain combinations, or in the vicinity of twin tips, the variation of hydrogen concentration within trap sites can easily exceed that of lattice sites. This will increase the susceptibility of such locations to hydrogen embrittlement.
5. Due to the patterning of stress and dislocation fields, triple junctions have the highest hydrogen content and hence the highest susceptibility to hydrogen

embrittlement, followed by grain boundaries. Also, the patterning of stress fields could cause hydrogen depletion at some grain boundaries, depending on local grain neighborhood.

6. Generally, in textured materials that have hard grains, the hydrogen in lattice contributes the most to the total hydrogen concentration. However, depending on the level of applied strain, in textured materials with soft grains, the variation of trapped hydrogen concentration might exceed that of lattice hydrogen concentration.

7. The effects of trapping sites are more significant when the initial hydrogen concentration is lower.

# Chapter 7

## 7   Conclusions and future works

## 7.1  Conclusions

A coupled diffusion-crystal plasticity finite element model was used to study stress-assisted hydrogen diffusion in zirconium alloys. Diffusion equations were coupled with mechanical user subroutines in Abaqus (Abdolvand, 2019). Various case studies were conducted to gain a better understanding of the effects of grain-grain interactions, load sharing, texture, notch geometry, phase transformation, and dislocation densities on the redistribution of hydrogen atoms. All simulations were focused on zirconium alloys, due to their application in nuclear reactors. The main conclusions of this thesis are summarized in this section, followed by stating the key limitations of the current work and some suggestions for future works.

In chapter 3, the effects of hydride-induced transformation strain on the stress field as well as on the redistribution of hydrogen atoms in the vicinity of zirconium hydrides were studied. The results showed that there exists a direct correlation between the gradient of hydrostatic stress and the gradient of hydrogen concentration within the lattice. It was further shown that hydrogen diffusion occurs from regions with compressive hydrostatic stress towards those undergoing tensile stresses. In agreement with the results of the bi-crystal models, hydrides were shown to have tensile and compressive hydrostatic stresses near the tips and near the sides, respectively. This suggests the tendency of the hydrides to grow axially. Furthermore, the effects of the orientation of the parent and neighboring grains on the propagation of hydrides were studied, and it was shown that hydrides tend to grow within mechanically harder grains, i.e., those having their c-axis aligned with the direction of the external loads.

In chapter 4, a model similar to a typical three-point bending experiment of a CANDU pressure tube was designed to understand the contribution of notch geometry, texture, external loads, and grain size on hydrogen transport towards notch tips. Results of this chapter highlighted the importance of microstructure variation on the state of deformation and hydrogen diffusion, especially near geometrical irregularities such as notch tips. Using

simulations with different macroscopic strains, it was shown that the location of peak hydrogen concentration is influenced by the magnitude of plastic deformation as well as the activity of slip systems. In the absence of plastic deformation, the peak occurs right at the notch root and hydrogen concentration profile monotonically decreases along the radial axis. However, the peak is located at a distance from the notch root in the presence of plastic deformation. Results of this chapter also indicated that texture plays an important role in hydrogen transport towards notches. The use of a random texture moves the peak of hydrogen concentration away from the notch tip. In contrast, a typical CANDU pressure tube texture has a peak concentration much closer to the notch root. Moreover, it was revealed that as the sharpness of the notch increases, the effects of texture become less significant in terms of hydrogen localization at the notch root.

Chapter 5 studied the interactive effects of neighboring hydrides due to hydride-induced transformation strain and consequently the intensity of interaction as a function of distance between the hydrides. The two main models considered for this chapter were (1) parallel hydrides – which is applicable to circumferentially-oriented hydrides and (2) perpendicular hydrides – which is applicable to hydrides which are reoriented towards radial direction of pressure tubes. It is shown that parallel hydrides interact the most at distances less than 20 μm. The interaction remains, but weakens for distances between 20 μm and 30 μm. The interaction becomes negligible at distances above 45 μm. For the case of perpendicular hydrides, the interaction occurs the most at distances less than 15 μm, but becomes negligible at distances greater than 20 μm.

Chapter 5 also discussed a set of D-CPFE simulations of hydride growth in a single crystal domain with various thickness and length of hydride. It was shown that length of hydrides does not significantly affect the probability of hydride growth. On the other hand, it was shown that thickness of hydride considerably affects the state of deformation and subsequent hydrogen distribution in the vicinity of the hydrided domain. It was concluded that hydrides with thickness of 1 μm are the ones with highest likelihood of propagation.

In chapter 6, the effects of dislocation densities on hydrogen concentration were studied using a newly-developed non-local D-CPFE model. It was shown that, as softer grains

undergo higher levels of plasticity, a higher hydrogen concentration in trap sites is calculated compared to that of harder grains. The patterning of stress and dislocation fields presented in this chapter showed that triple junctions host the highest hydrogen content and hence are the most susceptible locations to hydrogen embrittlement. It was also shown that the effects of trapped hydrogen could become quite significant in textured materials with soft grains, especially in highly deformed zones, e.g., twin tips and near the notch root.

In summary, this work sheds light on coupling effects of microstructure-dependent deformation and diffusion of hydrogen at micro-scale. The effects of transformation strain associated with the phase transformation of zirconium to zirconium hydrides are studied using an in-house D-CPFE approach. Different configurations of hydride precipitation are studied to investigate the state of hydrogen redistribution. Also, this thesis comprehensively studies the contribution of texture, grain morphology and notch geometry on hydrogen transport towards geometrical irregularities and micro-scale notches. This greatly helps the nuclear industry understand the significance of each of these contributing parameters on transport of hydrogen towards these stress-riser sites. Another industrial-oriented work that is studied in this thesis is the interaction between zirconium hydrides formed within the CANDU pressure tube. Two cases of interaction between circumferentially- and radially-oriented hydrides are studied as well as effects of hydride geometry. Furthermore, Oriani's theory of equilibrium of lattice and trap sites hydrogen concentration is studied for the first time in the case of zirconium alloys (Oriani, 1970), where great potential impact of dislocations on hydrogen diffusion is highlighted.

## 7.2 Limitations of this work

It should be noted that the work presented in this thesis is based on some simplifying assumption, and it is acknowledged that this thesis is accompanied by some limitations, some of which are listed below:

1. The effects of temperature gradients through the thickness of the pressure tubes are neglected. This could contribute to the diffusion equations and change the distributions of hydrogen concentration. Also, the effects of thermal residual stresses associated with temperature gradients and fluctuations are ignored.

2.  The mechanism of hydride precipitation and propagation as well as existing secondary precipitates are not modelled in this work. These effects could cause sharper stress gradients and subsequently accelerate diffusion of hydrogen.

3.  The interface of hydrides and zirconium matrix, as well as notch tip region, are the main sites at which crack initiation and propagation take place. The effects brittleness of the hydrides are not considered in this work.

4.  All the external displacements applied on the models in this work are monotonic loads and the effects of cyclic loading are neglected. Also, all the loads are simulated assuming that the model undergoes quasi-static deformation. Higher strain rates and dynamic deformation are not studied in this thesis.

5.  The effects of grain boundary and trap site diffusivities are not taken into account in this work. Such effects, known as pipe diffusion effects, are not implemented in the presented model.

## 7.3 Future works

In future, the following topics can be studied using both experimentation and numerical modeling:

1.  Adding the effects of grain boundaries to the non-local D-CPFE model to investigate diffusion of hydrogen atoms and trapping at grain boundaries. This directly influences the results for trapped hydrogen concentration.

2.  Studying the transient diffusion of hydrogen atoms across polycrystalline material using anisotropic diffusivity.

3.  Including the dual-phase effects (effects of beta phase) in Zr-2.5Nb and how it affects the deformation and subsequent hydride propagation.

4.  Studying in-situ heating of the matrix which discovers the initiation points at which hydride dissolution/precipitation takes place.

5.  Studying twinning in hydrided samples using both EBSD and D-CPFE. The effect of twining transformation strain and its interactive effects on hydride precipitation is of great importance which has barely been studied. This directly influences the

propagation of hydrides at different sites of the microstructure, including twin-parent interface.

# References

Abaqus Documentation, 2020.

Abdolvand, H., 2022. Development of microstructure-sensitive damage models for zirconium polycrystals. Int. J. Plast. 149, 103156. https://doi.org/10.1016/J.IJPLAS.2021.103156

Abdolvand, H., 2019. Progressive modelling and experimentation of hydrogen diffusion and precipitation in anisotropic polycrystals. Int. J. Plast. 116, 39–61. https://doi.org/10.1016/j.ijplas.2018.12.005

Abdolvand, H., Daymond, M.R., 2013. Multi-scale modeling and experimental study of twin inception and propagation in hexagonal close-packed materials using a crystal plasticity finite element approach; Part II: Local behavior. J. Mech. Phys. Solids 61, 803–818. https://doi.org/10.1016/j.jmps.2012.10.017

Abdolvand, H., Daymond, M.R., Mareau, C., 2011. Incorporation of twinning into a crystal plasticity finite element model: Evolution of lattice strains and texture in Zircaloy-2. Int. J. Plast. 27, 1721–1738. https://doi.org/10.1016/j.ijplas.2011.04.005

Abdolvand, H., Louca, K., Mareau, C., Majkut, M., Wright, J., 2020. On the nucleation of deformation twins at the early stages of plasticity. Acta Mater. 196, 733–746. https://doi.org/10.1016/J.ACTAMAT.2020.07.010

Abdolvand, H., Majkut, M., Oddershede, J., Schmidt, S., Lienert, U., Diak, B.J., Withers, P.J., Daymond, M.R., 2015a. On the deformation twinning of Mg AZ31B: A three-dimensional synchrotron X-ray diffraction experiment and crystal plasticity finite element model. Int. J. Plast. 70, 77–97. https://doi.org/10.1016/j.ijplas.2015.03.001

Abdolvand, H., Majkut, M., Oddershede, J., Wright, J.P., Daymond, M.R., 2015b. Study of 3-D stress development in parent and twin pairs of a hexagonal close-packed polycrystal: Part I - In-situ three-dimensional synchrotron X-ray diffraction measurement. Acta Mater. 93, 246–255. https://doi.org/10.1016/j.actamat.2015.04.020

Abdolvand, H., Majkut, M., Oddershede, J., Wright, J.P., Daymond, M.R., 2015c. Study of 3-D stress development in parent and twin pairs of a hexagonal close-packed polycrystal: Part II - Crystal plasticity finite element modeling. Acta Mater. 93, 235–245. https://doi.org/10.1016/j.actamat.2015.04.025

Abdolvand, H., Wilkinson, A.J., 2016a. On the effects of reorientation and shear transfer during twin formation: Comparison between high resolution electron backscatter diffraction experiments and a crystal plasticity finite element model. Int. J. Plast. 84, 160–182. https://doi.org/10.1016/j.ijplas.2016.05.006

Abdolvand, H., Wilkinson, A.J., 2016b. Assessment of residual stress fields at deformation

twin tips and the surrounding environments. Acta Mater. 105, 219–231. https://doi.org/10.1016/j.actamat.2015.11.036

Abdolvand, H., Wright, J.P., Wilkinson, A.J., 2018. On the state of deformation in a polycrystalline material in three-dimension: Elastic strains, lattice rotations, and deformation mechanisms. Int. J. Plast. 106, 145–163. https://doi.org/10.1016/j.ijplas.2018.03.006

Acharya, A., Bassani, J.L., 2000. Lattice incompatibility and a gradient theory of crystal plasticity. J. Mech. Phys. Solids 48, 1565–1595. https://doi.org/10.1016/S0022-5096(99)00075-7

Ahn, D.H., Lee, G.G., Moon, J., Kim, H.S., Chun, Y.B., 2021. Analysis of texture and grain shape effects on the yield anisotropy of Zr-2.5wt%Nb pressure tube alloy using crystal plasticity finite element method. J. Nucl. Mater. 555, 153112. https://doi.org/10.1016/J.JNUCMAT.2021.153112

Alawadi, A., Abdolvand, H., 2020. Measurement and modeling of micro residual stresses in zirconium crystals in three dimension. J. Mech. Phys. Solids 135, 103799. https://doi.org/10.1016/j.jmps.2019.103799

Aldridge, S.A., Cheadle, B.A., 1972. Age hardening of Zr-2.5 wt % Nb slowly cooled from the (α +β) phase field. J. Nucl. Mater. 42, 32–42. https://doi.org/10.1016/0022-3115(72)90004-9

Allen, G.B., Kerr, M., Daymond, M.R., 2012. Measurement and modeling of strain fields in zirconium hydrides precipitated at a stress concentration. J. Nucl. Mater. 430, 27–36. https://doi.org/10.1016/J.JNUCMAT.2012.06.037

Anand, L., 2011. A thermo-mechanically-coupled theory accounting for hydrogen diffusion and large elastic-viscoplastic deformations of metals. Int. J. Solids Struct. 48, 962–971. https://doi.org/10.1016/j.ijsolstr.2010.11.029

Arakawa, K., Kageyama, A., Hiroshima, H., Yasuda, H., Ogata, S., 2021. Hydrogen Effects on the Migration of Nanoscale Cavities in Iron. ISIJ Int. 61, 2305–2307. https://doi.org/10.2355/isijinternational.isijint-2021-140

Arnaudov, N., Kolyshkin, A., Weihe, S., 2020. Micromechanical modeling of fatigue crack initiation in hydrogen atmosphere. Mech. Mater. 149, 103557. https://doi.org/10.1016/j.mechmat.2020.103557

Arsenlis, A., Parks, D.M., 1999. Crystallographic aspects of geometrically-necessary and statistically-stored dislocation density. Acta Mater. 47, 1597–1611. https://doi.org/10.1016/S1359-6454(99)00020-8

Arul Kumar, M., Kanjarla, A.K., Niezgoda, S.R., Lebensohn, R.A., Tomé, C.N., 2015. Numerical study of the stress state of a deformation twin in magnesium. Acta Mater. 84, 349–358. https://doi.org/10.1016/j.actamat.2014.10.048

Arunachalam, V.S., Lehtinen, B., Östberg, G., 1967. The orientation of zirconium hydride on grain boundaries in zircaloy-2. J. Nucl. Mater. 21, 241–248. https://doi.org/10.1016/0022-3115(67)90174-2

Asaro, R.J., 1983. Crystal plasticity. J. Appl. Mech. Trans. ASME 50, 921–934. https://doi.org/10.1115/1.3167205

Asaro, R.J., Needleman, A., 1985. Overview no. 42 Texture development and strain hardening in rate dependent polycrystals. Acta Metall. 33, 923–953. https://doi.org/10.1016/0001-6160(85)90188-9

Aslan, O., 2015. ScienceDirect Numerical modeling of hydrogen diffusion in metals accounting for large deformations. Int. J. Hydrogen Energy 40, 15227–15235.

Aubert, I., Saintier, N., Olive, J.M., 2012. Crystal plasticity computation and atomic force microscopy analysis of the internal hydrogen-induced slip localization on polycrystalline stainless steel. Scr. Mater. 66, 698–701. https://doi.org/10.1016/J.SCRIPTAMAT.2012.01.019

Auzoux, Q., Bouffioux, P., Machiels, A., Yagnik, S., Bourdiliau, B., Mallet, C., Mozzani, N., Colas, K., 2017. Hydride reorientation and its impact on ambient temperature mechanical properties of high burn-up irradiated and unirradiated recrystallized Zircaloy-2 nuclear fuel cladding with an inner liner. J. Nucl. Mater. 494, 114–126. https://doi.org/10.1016/J.JNUCMAT.2017.07.022

Ayas, C., Deshpande, V.S., Fleck, N.A., 2014. A fracture criterion for the notch strength of high strength steels in the presence of hydrogen. J. Mech. Phys. Solids 63, 80–93. https://doi.org/10.1016/j.jmps.2013.10.002

Bailey, J.., 1963. Electron microscope observations on the precipitation of zirconium hydride in zirconium. Acta Metall.

Bair, J., Asle, M., Tonks, M., 2015. A review on hydride precipitation in zirconium alloys. J. Nucl. Mater. J. 466, 12–20.

Barrow, a. T.W., Korinek, a., Daymond, M.R., 2013. Evaluating zirconium-zirconium hydride interfacial strains by nano-beam electron diffraction. J. Nucl. Mater. 432, 366–370. https://doi.org/10.1016/j.jnucmat.2012.08.003

Baudoin, P., Hama, T., Takuda, H., 2019. Influence of critical resolved shear stress ratios on the response of a commercially pure titanium oligocrystal: Crystal plasticity simulations and experiment. Int. J. Plast. 115, 111–131. https://doi.org/10.1016/j.ijplas.2018.11.013

Bell, L.G., Duncan, R.G., 1975. Hydride orientation in Zr-2.5%Nb; how it is affected by stress, temperature and heat treatment - AECL-5110, Canada.

Bilone, M.., Burtseva, T.A., Dobrzynski, J.P., McGann, D.P., Byrne, K., Han, Z., Liu,

Y.Y., 2012. Used Fuel Disposition Campaign Phase I Ring Compression Testing of High-Burnup Cladding.

Blackmur, M.S., Preuss, M., Robson, J.D., Zanellato, O., Cernik, R.J., Ribeiro, F., Andrieux, J., 2016. Strain evolution during hydride precipitation in Zircaloy-4 observed with synchrotron X-ray diffraction. J. Nucl. Mater. 474, 45–61. https://doi.org/10.1016/j.jnucmat.2016.01.039

Bradbrook, J.S., Lorimer, G.W., Ridley, N., 1972. The precipitation of zirconium hydride in zirconium and zircaloy-2. J. Nucl. Mater. 42, 142–160. https://doi.org/10.1016/0022-3115(72)90021-9

Breen, A.J., Mouton, I., Lu, W., Wang, S., Szczepaniak, A., Kontis, P., Stephenson, L.T., Chang, Y., da Silva, A.K., Liebscher, C.H., Raabe, D., Britton, T.B., Herbig, M., Gault, B., 2018. Atomic scale analysis of grain boundary deuteride growth front in Zircaloy-4. Scr. Mater. 156, 42–46. https://doi.org/10.1016/j.scriptamat.2018.06.044

Bronkhorst, C.A., Hansen, B.L., Cerreta, E.K., Bingert, J.F., 2007. Modeling the microstructural evolution of metallic polycrystalline materials under localization conditions. J. Mech. Phys. Solids 55, 2351–2383. https://doi.org/10.1016/j.jmps.2007.03.019

Busso, E.P., Meissonnier, F.T., O'Dowd, N.P., 2000. Gradient-dependent deformation of two-phase single crystals. J. Mech. Phys. Solids 48, 2333–2361. https://doi.org/10.1016/S0022-5096(00)00006-5

Cai, S., Daymond, M.R., Holt, R.A., 2009. Modeling the room temperature deformation of a two-phase zirconium alloy. Acta Mater. 57, 407–419. https://doi.org/10.1016/j.actamat.2008.09.020

Cameron, D.J., Duncan, R.G., 1977. On the existence of a memoty effect in hydride precipitation in cold-worked Zr-2.5% Nb. J. Nucl. Mater. 68, 340–344. https://doi.org/10.1016/0022-3115(77)90260-4

Carpenter, G.J.C., 1973. The dilatational misfit of zirconium hydrides precipitated in zirconium. J. Nucl. Mater. 48, 264–266. https://doi.org/10.1016/0022-3115(73)90022-6

Cha, H.J., Jang, K.N., An, J.H., Kim, K.T., 2015a. The effect of hydrogen and oxygen contents on hydride reorientations of zirconium alloy cladding tubes. Nucl. Eng. Technol. 47, 746–755. https://doi.org/10.1016/J.NET.2015.06.004

Cha, H.J., Won, J.J., Jang, K.N., An, J.H., Kim, K.T., 2015b. Tensile hoop stress-, hydrogen content- and cooling rate-dependent hydride reorientation behaviors of Zr alloy cladding tubes. J. Nucl. Mater. 464, 53–60. https://doi.org/10.1016/J.JNUCMAT.2015.04.027

Chen, J., Zhu, Y., Huang, M., Zhao, L., Liang, S., Li, Z., 2021. Study on hydrogen-affected

interaction between dislocation and grain boundary by MD simulation. Comput. Mater. Sci. 196, 110562. https://doi.org/10.1016/j.commatsci.2021.110562

Cheng, J., Ghosh, S., 2017. Crystal plasticity finite element modeling of discrete twin evolution in polycrystalline magnesium. J. Mech. Phys. Solids 99, 512–538. https://doi.org/10.1016/j.jmps.2016.12.008

Cheong, K.S., Busso, E.P., 2006. Effects of lattice misorientations on strain heterogeneities in FCC polycrystals. J. Mech. Phys. Solids 54, 671–689. https://doi.org/10.1016/j.jmps.2005.11.003

Chernov, I.I., Staltsov, M.S., Kalin, B.A., Guseva, L.Y., 2017. Some problems of hydrogen in reactor structural materials: A review. Inorg. Mater. Appl. Res. 8, 643–650. https://doi.org/10.1134/S2075113317050094

Chu, H.C., Wu, S.K., Kuo, R.C., 2008. Hydride reorientation in Zircaloy-4 cladding. J. Nucl. Mater. 373, 319–327. https://doi.org/10.1016/J.JNUCMAT.2007.06.012

Cinbiz, M.N., Koss, D.A., Motta, A.T., 2016. The influence of stress state on the reorientation of hydrides in a zirconium alloy. J. Nucl. Mater. 477, 157–164. https://doi.org/10.1016/J.JNUCMAT.2016.05.013

Colas, K.B., Motta, A.T., Daymond, M.R., Kerr, M., Almer, J.D., 2011. Hydride platelet reorientation in zircaloy studied with synchrotron radiation diffraction. J. ASTM Int. 8, 1–17. https://doi.org/10.1520/JAI103033

Connétable, D., Huez, J., Andrieu, É., Mijoule, C., 2011. First-principles study of diffusion and interactions of vacancies and hydrogen in hcp-titanium. J. Phys. Condens. Matter 23, 405401. https://doi.org/10.1088/0953-8984/23/40/405401

Courty, O., Motta, A.T., Hales, J.D., 2014a. Modeling and simulation of hydrogen behavior in Zircaloy-4 fuel cladding. J. Nucl. Mater. 452, 311–320. https://doi.org/10.1016/j.jnucmat.2014.05.013

Courty, O., Motta, A.T., Hales, J.D., 2014b. Modeling and simulation of hydrogen behavior in Zircaloy-4 fuel cladding. J. Nucl. Mater. 452, 311–320. https://doi.org/10.1016/j.jnucmat.2014.05.013

Cox, B., 1990. Environmentally-induced cracking of zirconium alloys - A review. J. Nucl. Mater. 170, 1–23. https://doi.org/10.1016/0022-3115(90)90321-D

Cui, J., Shek, G.K., Scarth, D.A., Wang, Z., 2009a. Delayed hydride cracking initiation at notches in Zr-2.5Nb alloys. J. Press. Vessel Technol. Trans. ASME 131, 1–12. https://doi.org/10.1115/1.3141433

Cui, J., Shek, G.K., Wang, Z., 2009b. Overload fracture of hydrided region at simulated blunt flaws in Zr-2.5nb pressure tube material. J. Press. Vessel Technol. Trans. ASME 131, 1–15. https://doi.org/10.1115/1.3147743

Cui, T.C., Liu, P.F., Gu, C.H., 2017. Finite element analysis of hydrogen diffusion/plasticity coupled behaviors of low-alloy ferritic steel at large strain. Int. J. Hydrogen Energy 42, 20324–20335. https://doi.org/10.1016/J.IJHYDENE.2017.06.059

Dadfarnia, M., Martin, M.L., Nagao, A., Sofronis, P., Robertson, I.M., 2014. Modeling hydrogen transport by dislocations. J. Mech. Phys. Solids 78, 511–525. https://doi.org/10.1016/j.jmps.2015.03.002

Dadfarnia, M., Somerday, B.P., Sofronis, P., Robertson, I.M., Stalheim, D., 2009. Interaction of hydrogen transport and material elastoplasticity in pipeline steels. J. Press. Vessel Technol. Trans. ASME 131, 1–13. https://doi.org/10.1115/1.3027497

Daum, R.S., Chu, Y.S., Motta, A.T., 2009. Identification and quantification of hydride phases in Zircaloy-4 cladding using synchrotron X-ray diffraction. J. Nucl. Mater. 392, 453–463. https://doi.org/10.1016/j.jnucmat.2009.04.004

Depover, T., Hertelé, S., Verbeken, K., 2019. The effect of hydrostatic stress on the hydrogen induced mechanical degradation of dual phase steel: A combined experimental and numerical approach. Eng. Fract. Mech. 221, 106704. https://doi.org/10.1016/j.engfracmech.2019.106704

Depraetere, R., De Waele, W., Hertelé, S., 2021. Fully-coupled continuum damage model for simulation of plasticity dominated hydrogen embrittlement mechanisms. Comput. Mater. Sci. 200, 110857. https://doi.org/10.1016/J.COMMATSCI.2021.110857

Desquines, J., Drouan, D., Billone, M., Puls, M.P., March, P., Fourgeaud, S., Getrey, C., Elbaz, V., Philippe, M., 2014. Influence of temperature and hydrogen content on stress-induced radial hydride precipitation in Zircaloy-4 cladding. J. Nucl. Mater. 453, 131–150. https://doi.org/10.1016/j.jnucmat.2014.06.049

Di Leo, C. V., Anand, L., 2013. Hydrogen in metals: A coupled theory for species diffusion and large elastic-plastic deformations. Int. J. Plast. 43, 42–69. https://doi.org/10.1016/j.ijplas.2012.11.005

Díaz, A., Alegre, J.M., Cuesta, I.I., 2017. Numerical simulation of hydrogen embrittlement and local triaxiality effects in notched specimens. Theor. Appl. Fract. Mech. 90, 294–302. https://doi.org/10.1016/j.tafmec.2017.06.017

Domain, C., Besson, R., Legris, A., 2002. Atomic-scale Ab-initio study of the Zr-H system: I. Bulk properties. Acta Mater. 50, 3513–3526. https://doi.org/10.1016/S1359-6454(02)00173-8

Duda, F.P., Ciarbonetti, A., Sánchez, P.J., Huespe, A.E., 2014. A phase-field/gradient damage model for brittle fracture in elastic-plastic solids. Int. J. Plast. 65, 269–296. https://doi.org/10.1016/j.ijplas.2014.09.005

Duda, F.P., Ciarbonetti, A., Toro, S., Huespe, A.E., 2018. A phase-field model for solute-

assisted brittle fracture in elastic-plastic solids. Int. J. Plast. https://doi.org/10.1016/j.ijplas.2017.11.004

Eadie, R.L., Mok, D., Scarth, D., Léger, M., 1991. The hydrostatic stress field around the crack tip in zirconium 2.5% niobium and implications for delayed hydride cracking. Scr. Metall. Mater. 25, 497–502. https://doi.org/10.1016/0956-716X(91)90217-O

El Chamaa, S., Patel, M., Davies, C.M., Wenman, M.R., 2018. The Effect of Grain Boundaries and Second-Phase Particles on Hydride Precipitation in Zirconium Alloys. MRS Adv. 3, 1749–1754. https://doi.org/10.1557/adv.2018.111

Ells, C.E., 1968. Hydride precipitates in zirconium alloys (A review). J. Nucl. Mater. 28, 129–151. https://doi.org/10.1016/0022-3115(68)90021-4

Evers, L.P., Brekelmans, W.A.M., Geers, M.G.D., 2004. Non-local crystal plasticity model with intrinsic SSD and GND effects. J. Mech. Phys. Solids 52, 2379–2401. https://doi.org/10.1016/J.JMPS.2004.03.007

Feather, W.G., Savage, D.J., Knezevic, M., 2021. A crystal plasticity finite element model embedding strain-rate sensitivities inherent to deformation mechanisms: Application to alloy AZ31. Int. J. Plast. 143, 103031. https://doi.org/10.1016/J.IJPLAS.2021.103031

Fisher, E.S., Renken, C.J., 1964. Single-crystal elastic moduli and the hcp $\rightarrow$ bcc transformation in Ti, Zr, and Hf. Phys. Rev. 135. https://doi.org/10.1103/PhysRev.135.A482

Fong, R.W.L., 2013. Phase Transformation, Texture and Mechanical Anisotropy in Zirconium Alloys. thesis.

Fu, H., Chen, X., Wang, W., Pia, G., Zhang, J., Li, J., 2021. Statistical study on the effects of heterogeneous deformation and grain boundary character on hydrogen-induced crack initiation and propagation in twining-induced plasticity steels. Corros. Sci. 192, 109796. https://doi.org/10.1016/j.corsci.2021.109796

Girardin, G., Huvier, C., Delafosse, D., Feaugas, X., 2015. Correlation between dislocation organization and slip bands: TEM and AFM investigations in hydrogen-containing nickel and nickel-chromium. Acta Mater. 91, 141–151. https://doi.org/10.1016/j.actamat.2015.03.016

Golahmar, A., Kristensen, P.K., Niordson, C.F., Martínez-Pañeda, E., 2022. A phase field model for hydrogen-assisted fatigue. Int. J. Fatigue 154, 106521. https://doi.org/10.1016/J.IJFATIGUE.2021.106521

Gong, W., Trtik, P., Valance, S., Bertsch, J., 2018. Hydrogen diffusion under stress in Zircaloy: High-resolution neutron radiography and finite element modeling. J. Nucl. Mater. 508, 459–464. https://doi.org/10.1016/j.jnucmat.2018.05.079

Gopalan, A., Bind, A.K., Sunil, S., Murty, T.N., Sharma, R.K., Samanta, A., Soren, A., Singh, R.N., 2021. Effect of radial hydride on room temperature fracture toughness of Zr-2.5Nb pressure tube material. J. Nucl. Mater. 544, 152681. https://doi.org/10.1016/J.JNUCMAT.2020.152681

Gu, Y., El-Awady, J.A., 2018. Quantifying the effect of hydrogen on dislocation dynamics: A three-dimensional discrete dislocation dynamics framework. J. Mech. Phys. Solids 112, 491–507. https://doi.org/10.1016/j.jmps.2018.01.006

Guo, X.H., Shi, S.Q., Zhang, Q.M., Ma, X.Q., 2008. An elastoplastic phase-field model for the evolution of hydride precipitation in zirconium. Part I: Smooth specimen. J. Nucl. Mater. 378, 110–119. https://doi.org/10.1016/j.jnucmat.2008.05.008

Han, G.M., Zhao, Y.F., Zhou, C.B., Lin, D.Y., Zhu, X.Y., Zhang, J., Hu, S.Y., Song, H.F., 2019. Phase-field modeling of stacking structure formation and transition of δ-hydride precipitates in zirconium. Acta Mater. 165, 528–546. https://doi.org/10.1016/j.actamat.2018.12.009

Hardie, D., Shanahan, M.W., 1975. Stress reorientation of hydrides in zirconium−2.5% niobium. J. Nucl. Mater. 55, 1–13. https://doi.org/10.1016/0022-3115(75)90132-4

Hassan, H. ul, Govind, K., Hartmaier, A., 2019. Micromechanical modelling of coupled crystal plasticity and hydrogen diffusion. Philos. Mag. 99, 92–115. https://doi.org/10.1080/14786435.2018.1530466

He, Y., Su, Y., Yu, H., Chen, C., 2021. First-principles study of hydrogen trapping and diffusion at grain boundaries in γ-Fe. Int. J. Hydrogen Energy 46, 7589–7600. https://doi.org/10.1016/J.IJHYDENE.2020.11.238

Holt, R.A., Aldridge, S.A., 1985. Effect of extrusion variables on crystallographic texture of Zr-2.5 wt% Nb. J. Nucl. Mater. 135, 246–259. https://doi.org/10.1016/0022-3115(85)90084-4

Holt, R.A., Zhao, P., 2004. Micro-texture of extruded Zr-2.-5Nb tubes. J. Nucl. Mater. 335, 520–528. https://doi.org/10.1016/j.jnucmat.2004.07.043

Hussein, A., Krom, A.H.M., Dey, P., Sunnardianto, G.K., Moultos, O.A., Walters, C.L., 2021. The effect of hydrogen content and yield strength on the distribution of hydrogen in steel: a diffusion coupled micromechanical FEM study. Acta Mater. 209, 116799. https://doi.org/10.1016/j.actamat.2021.116799

Ilin, D., 2014. Simulation of hydrogen diffusion in fcc polycrystals . Effect of deformation and grain boundaries : effect of deformation and grain boundaries. PhD Thesis, Univ. Bordeaux.

Ilin, D.N., Saintier, N., Olive, J.M., Abgrall, R., Aubert, I., 2014. Simulation of hydrogen diffusion affected by stress-strain heterogeneity in polycrystalline stainless steel. Int. J. Hydrogen Energy 39, 2418–2422. https://doi.org/10.1016/j.ijhydene.2013.11.065

Jagodzinski, Y., Hänninen, H., Tarasenko, O., Smuk, S., 2000. Interaction of hydrogen with dislocation pile-ups and hydrogen induced softening of pure iron. Scr. Mater. 43, 245–251. https://doi.org/10.1016/S1359-6462(00)00398-5

Jang, K.N., Kim, K.T., 2017. The effect of neutron irradiation on hydride reorientation and mechanical property degradation of zirconium alloy cladding. Nucl. Eng. Technol. 49, 1472–1482. https://doi.org/10.1016/J.NET.2017.05.006

Jia, Y.J., Beyerlein, I.J., Han, W.Z., 2021. Precipitation characteristics and distributions of subsurface hydrides in zirconium. Acta Mater. 216, 117146. https://doi.org/10.1016/J.ACTAMAT.2021.117146

Jones, C., Tuli, V., Shah, Z., Gass, M., Burr, P.A., Preuss, M., Moore, K.L., 2021. Evidence of hydrogen trapping at second phase particles in zirconium alloys. Sci. Rep. 11, 4370. https://doi.org/10.1038/s41598-021-83859-w

Judge, C.D., Li, W., Mayhew, C., Buyers, A., Bickel, G.A., 2017. Adopting Transmission Kikuchi Diffraction To Characterize Grain Structure and Texture of Zr-2.5Nb Candu Pressure Tubes. CNL Nucl. Rev. 1–7. https://doi.org/10.12943/cnr.2017.00010

Kanayama, H., Ogino, M., Miresmaeili, R., Nakagawa, T., Toda, T., 2008. Hydrogen Transport in a Coupled Elastoplastic-Diffusion Analysis near a Blunting Crack Tip. J. Comput. Sci. Technol. 2, 499–510. https://doi.org/10.1299/jcst.2.499

Kapci, M.F., Schön, J.C., Bal, B., 2021. The role of hydrogen in the edge dislocation mobility and grain boundary-dislocation interaction in α-Fe. Int. J. Hydrogen Energy 46, 32695–32709. https://doi.org/10.1016/J.IJHYDENE.2021.07.061

Kearns, J.J., 1972. Diffusion coefficient of hydrogen in alpha zirconium, Zircaloy-2 and Zircaloy-4. J. Nucl. Mater. 43, 330–338. https://doi.org/10.1016/0022-3115(72)90065-7

Kearns, J.J., 1967. Terminal solubility and partitioning of hydrogen in the alpha phase of zirconium, Zircaloy-2 and Zircaloy-4. J. Nucl. Mater. 22, 292–303. https://doi.org/10.1016/0022-3115(67)90047-5

Kearns, J.J., Woods, C.., 1966. Effect of texture, grain size and cold work on the precipitaiton of oriented hydrides in zircaloy tubes and plate 20, 241–261.

Kerr, M., Daymond, M.R., Holt, R.A., Almer, J.D., Stafford, S., 2010. Observation of growth of a precipitate at a stress concentration by synchrotron X-ray diffraction. Scr. Mater. 62, 341–344. https://doi.org/10.1016/j.scriptamat.2009.10.031

Kerr, M., Daymond, M.R., Holt, R.A., Almer, J.D., Stafford, S., Colas, K.B., 2009. Fracture of a minority phase at a stress concentration observed with synchrotron X-ray diffraction. Scr. Mater. 61, 939–942. https://doi.org/10.1016/j.scriptamat.2009.07.030

Khoda-Bakhsh, R., Ross, D.K., 1982. Determination of the hydrogen site occupation in the α phase of zirconium hydride and in the α and β phases of titanium hydride by inelastic neutron scattering. J. Phys. F Met. Phys. 12, 15–24. https://doi.org/10.1088/0305-4608/12/1/003

Kim, J.S., Kim, S.D., Yoon, J., 2016. Hydride formation on deformation twin in zirconium alloy. J. Nucl. Mater. 482, 88–92. https://doi.org/10.1016/j.jnucmat.2016.10.020

Kim, S.D., Rhyim, Y., Kim, J.S., Yoon, J., 2015. Characterization of zirconium hydrides in Zircaloy-4 cladding with respect to cooling rate. J. Nucl. Mater. 465, 731–736. https://doi.org/10.1016/J.JNUCMAT.2015.07.006

Kim, S.S., 2006. The texture dependence of KIH in Zr–2.5%Nb pressure tube materials. J. Nucl. Mater. 349, 83–95. https://doi.org/10.1016/j.jnucmat.2005.09.027

Kim, S.S., Kim, Y.S., 2000. KIH in radial textured Zr-2.5%Nb pressure tube. J. Nucl. Mater. 279, 286–292. https://doi.org/10.1016/S0022-3115(99)00284-6

Kim, Y.S., Kim, S.J., Im, K.S., 2004. Delayed hydride cracking in Zr-2.5Nb tube with the cooling rate and the notch tip shape. J. Nucl. Mater. 335, 387–396. https://doi.org/10.1016/j.jnucmat.2004.07.046

Kiran Kumar, N.A.P., Szpunar, J.A., 2011. EBSD studies on microstructure and crystallographic orientation of δ-hydrides in Zircaloy-4, Zr–1% Nb and Zr–2.5% Nb. Mater. Sci. Eng. A 528, 6366–6374. https://doi.org/10.1016/J.MSEA.2011.05.022

Kiran Kumar, N.A.P., Szpunar, J.A., He, Z., 2010. Preferential precipitation of hydrides in textured zircaloy-4 sheets. J. Nucl. Mater. 403, 101–107. https://doi.org/10.1016/J.JNUCMAT.2010.06.005

Klinsmann, M., Rosato, D., Kamlah, M., McMeeking, R.M., 2015. An assessment of the phase field formulation for crack growth. Comput. Methods Appl. Mech. Eng. 294, 313–330. https://doi.org/10.1016/j.cma.2015.06.009

Kotake, H., Matsumoto, R., Taketomi, S., Miyazaki, N., 2008. Transient hydrogen diffusion analyses coupled with crack-tip plasticity under cyclic loading. Int. J. Press. Vessel. Pip. 85, 540–549. https://doi.org/10.1016/j.ijpvp.2008.02.002

Kristensen, P.K., Niordson, C.F., Martínez-Pañeda, E., 2020. A phase field model for elastic-gradient-plastic solids undergoing hydrogen embrittlement. J. Mech. Phys. Solids 143, 104093. https://doi.org/10.1016/j.jmps.2020.104093

Krom, A.H.M., Bakker, A.D., 2000. Hydrogen trapping models in steel. Metall. Mater. Trans. B Process Metall. Mater. Process. Sci. 31, 1475–1482. https://doi.org/10.1007/s11663-000-0032-0

Krom, A.H.M., Koers, R.W.J., Bakker, A., 1999a. Hydrogen transport near a blunting crack tip. J. Mech. Phys. Solids 47, 971–992. https://doi.org/10.1016/S0022-

5096(98)00064-7

Krom, A.H.M., Maier, H.J., Koers, R.W.J., Bakker, A., 1999b. The effect of strain rate on hydrogen distribution in round tensile specimens. Mater. Sci. Eng. A 271, 22–30. https://doi.org/10.1016/s0921-5093(99)00276-2

Kubo, T., Kobayashi, Y., 2013. Effects of δ-hydride precipitation at a crack tip on crack propagation in delayed hydride cracking of Zircaloy-2. J. Nucl. Mater. 439, 202–211. https://doi.org/10.1016/j.jnucmat.2013.04.015

Kumar, R., Mahajan, D.K., 2020. Hydrogen distribution in metallic polycrystals with deformation. J. Mech. Phys. Solids 135, 103776. https://doi.org/10.1016/j.jmps.2019.103776

Lanzani, L., Ruch, M., 2004. Comments on the stability of zirconium hydride phases in Zircaloy. J. Nucl. Mater. 324, 165–176. https://doi.org/10.1016/J.JNUCMAT.2003.09.013

Lee, K.W., Hong, S.I., 2002. Zirconium hydrides and their effect on the circumferential mechanical properties of Zr-Sn-Fe-Nb tubes. J. Alloys Compd. 346, 302–307. https://doi.org/10.1016/S0925-8388(02)00527-3

Li, J., Wang, Z., Wu, H., Chen, G., 2020. Microstructural and crystallographic analysis of hydride reorientation in a zirconium alloy cladding tube. J. Nucl. Mater. 537, 152232. https://doi.org/10.1016/J.JNUCMAT.2020.152232

Liang, S., Huang, M., Zhao, L., Zhu, Y., Li, Z., 2021. Effect of multiple hydrogen embrittlement mechanisms on crack propagation behavior of FCC metals: Competition vs. synergy. Int. J. Plast. 143, 103023. https://doi.org/10.1016/j.ijplas.2021.103023

Lin, J. li, Heuser, B.J., 2019. Modeling hydrogen solvus in zirconium solution by the mesoscale phase-field modeling code Hyrax. Comput. Mater. Sci. 156, 224–231. https://doi.org/10.1016/j.commatsci.2018.09.051

Liu, G., Mo, H., Wang, J., Shen, Y., 2021. Coupled crystal plasticity finite element-phase field model with kinetics-controlled twinning mechanism for hexagonal metals. Acta Mater. 202, 399–416. https://doi.org/10.1016/J.ACTAMAT.2020.11.002

Liu, Y., Chamaa, S. El, Wenman, M.R., Davies, C.M., Dunne, F.P.E., 2021a. Hydrogen concentration and hydrides in Zircaloy-4 during cyclic thermomechanical loading. Acta Mater. 117368. https://doi.org/10.1016/J.ACTAMAT.2021.117368

Liu, Y., Wan, W., Chamaa, S. El, Wenman, M.R., Davies, C.M., 2021b. Characterisation of microstructural creep , strain rate and temperature sensitivity and computational crystal plasticity in Zircaloy-4.

Lloyd, A.L., Smith, R., Wootton, M.J., Andrews, J., Arul, J., Muruva, H.P., Vinod, G.,

2019. Modelling the effect of hydrogen on crack growth in zirconium. Nucl. Instruments Methods Phys. Res. Sect. B Beam Interact. with Mater. Atoms 455, 13–20. https://doi.org/10.1016/j.nimb.2019.06.017

Long, F., Balogh, L., Daymond, M.R., 2017a. Evolution of dislocation density in a hot rolled Zr–2.5Nb alloy with plastic deformation studied by neutron diffraction and transmission electron microscopy. Philos. Mag. 97, 2888–2914. https://doi.org/10.1080/14786435.2017.1356940/SUPPL_FILE/TPHM_A_1356940_SM6099.ZIP

Long, F., Kerr, D., Domizzi, G., Wang, Q., Daymond, M.R., 2017b. Microstructure characterization of a hydride blister in Zircaloy-4 by EBSD and TEM. Acta Mater. 129, 450–461. https://doi.org/10.1016/j.actamat.2017.03.016

Louca, K., Abdolvand, H., Mareau, C., Majkut, M., Wright, J., 2021. Formation and annihilation of stressed deformation twins in magnesium. Commun. Mater. 2, 1–11. https://doi.org/10.1038/s43246-020-00105-y

Lufrano, J., Sofronis, P., Symons, D., 1998. Hydrogen transport and large strain elastoplasticity near a notch in alloy X-750. Eng. Fract. Mech. 59, 827–845. https://doi.org/10.1016/S0013-7944(97)00142-2

Lumley, S.C., Grimes, R.W., Murphy, S.T., Burr, P.A., Chroneos, A., Chard-Tuckey, P.R., Wenman, M.R., 2014. The thermodynamics of hydride precipitation: The importance of entropy, enthalpy and disorder. Acta Mater. 79, 351–362. https://doi.org/10.1016/j.actamat.2014.07.019

Ma, A., Roters, F., Raabe, D., 2006. A dislocation density based constitutive model for crystal plasticity FEM including geometrically necessary dislocations. J. Mech. Phys. Solids 54, 2169–2179. https://doi.org/10.1016/j.actamat.2006.01.005

Ma, X.Q., Shi, S.Q., Woo, C.H., Chen, L.Q., 2006. The phase field model for hydrogen diffusion and γ-hydride precipitation in zirconium under non-uniformly applied stress, in: Mechanics of Materials. Elsevier, pp. 3–10. https://doi.org/10.1016/j.mechmat.2005.05.005

Ma, X.Q., Shi, S.Q., Woo, C.H., Chen, L.Q., 2002. Phase-field simulation of hydride precipitation in bi-crystalline zirconium. Scr. Mater. 47, 237–241. https://doi.org/10.1016/S1359-6462(02)00131-8

Mani Krishna, K. V., Sain, A., Samajdar, I., Dey, G.K., Srivastava, D., Neogy, S., Tewari, R., Banerjee, S., 2006. Resistance to hydride formation in zirconium: An emerging possibility. Acta Mater. 54, 4665–4675. https://doi.org/10.1016/J.ACTAMAT.2006.06.004

Martin, M.L., Somerday, B.P., Ritchie, R.O., Sofronis, P., Robertson, I.M., 2012. Hydrogen-induced intergranular failure in nickel revisited. Acta Mater. 60, 2739–2745. https://doi.org/10.1016/J.ACTAMAT.2012.01.040

Martínez-Pañeda, E., Del Busto, S., Niordson, C.F., Betegón, C., 2016. Strain gradient plasticity modeling of hydrogen diffusion to the crack tip, in: International Journal of Hydrogen Energy. Elsevier Ltd, pp. 10265–10274. https://doi.org/10.1016/j.ijhydene.2016.05.014

Martínez-Pañeda, E., Golahmar, A., Niordson, C.F., 2018. A phase field formulation for hydrogen assisted cracking. Comput. Methods Appl. Mech. Eng. 342, 742–761. https://doi.org/10.1016/j.cma.2018.07.021

McRae, G.A., Coleman, C.E., 2018. Precipitates in metals that dissolve on cooling and form on heating: An example with hydrogen in alpha-zirconium. J. Nucl. Mater. 499, 622–640. https://doi.org/10.1016/j.jnucmat.2017.09.017

McRae, G.A., Coleman, C.E., Leitch, B.W., 2010. The first step for delayed hydride cracking in zirconium alloys. J. Nucl. Mater. 396, 130–143. https://doi.org/10.1016/j.jnucmat.2009.08.019

Moshtaghi, M., Safyari, M., Kuramoto, S., Hojo, T., 2021. Unraveling the effect of dislocations and deformation-induced boundaries on environmental hydrogen embrittlement behavior of a cold-rolled Al–Zn–Mg–Cu alloy. Int. J. Hydrogen Energy 46, 8285–8299. https://doi.org/10.1016/j.ijhydene.2020.12.028

Motta, A.T., Capolungo, L., Chen, L.Q., Cinbiz, M.N., Daymond, M.R., Koss, D.A., Lacroix, E., Pastore, G., Simon, P.C.A., Tonks, M.R., Wirth, B.D., Zikry, M.A., 2019. Hydrogen in zirconium alloys: A review. J. Nucl. Mater. https://doi.org/10.1016/j.jnucmat.2019.02.042

Nath, B., Lorimer, G.W., Ridley, N., 1975. Effect of hydrogen concentration and cooling rate on hydride precipitation in α-zirconium. J. Nucl. Mater. 58, 153–162. https://doi.org/10.1016/0022-3115(75)90101-4

Needleman, A., Asaro, R.J., Lemonds, J., Peirce, D., 1985. Finite element analysis of crystalline solids. Comput. Methods Appl. Mech. Eng. 52, 689–708. https://doi.org/10.1016/0045-7825(85)90014-3

Nordin, H., Ulaganathan, J., Hanlon, S., Broad, D., 2019. Effect of cold work on hydrogen diffusion in Zr-2.5%Nb alloys at reactor temperatures. 19th Int. Conf. Environ. Degrad. Mater. Nucl. Power Syst. - Water React. EnvDeg 2019 103–109.

Novak, P., Yuan, R., Somerday, B.P., Sofronis, P., Ritchie, R.O., 2010. A statistical, physical-based, micro-mechanical model of hydrogen-induced intergranular fracture in steel. J. Mech. Phys. Solids 58, 206–226. https://doi.org/10.1016/j.jmps.2009.10.005

Nye, J.., 1953. Some geometrical relations in dislocated crystals. Acta Metall. 1, 153–162. https://doi.org/10.1016/0001-6160(53)90054-6

Oh, S., Jang, C., Kim, J.H., Jeong, Y.H., 2010. Effect of Nb on hydride embrittlement of

Zr–xNb alloys. Mater. Sci. Eng. A 527, 1306–1313. https://doi.org/10.1016/J.MSEA.2009.11.024

Olden, V., Thaulow, C., Johnsen, R., 2008. Modelling of hydrogen diffusion and hydrogen induced cracking in supermartensitic and duplex stainless steels. Mater. Des. 29, 1934–1948. https://doi.org/10.1016/J.MATDES.2008.04.026

Ontario Power Generation Darlington Fuel Channel Fitness for Service Report, 2015.

Oriani, R.A., 1970. The diffusion and trapping of hydrogen in steel. Acta Metall. 18, 147–157. https://doi.org/10.1016/0001-6160(70)90078-7

Oudriss, A., Creus, J., Bouhattate, J., Conforto, E., Berziou, C., Savall, C., Feaugas, X., 2012a. Grain size and grain-boundary effects on diffusion and trapping of hydrogen in pure nickel. Acta Mater. 60, 6814–6828. https://doi.org/10.1016/j.actamat.2012.09.004

Oudriss, A., Creus, J., Bouhattate, J., Savall, C., Peraudeau, B., Feaugas, X., 2012b. The diffusion and trapping of hydrogen along the grain boundaries in polycrystalline nickel. Scr. Mater. 66, 37–40. https://doi.org/10.1016/j.scriptamat.2011.09.036

Patel, M., Reali, L., Sutton, A.P., Balint, D.S., Wenman, M.R., 2021. A fast efficient multi-scale approach to modelling the development of hydride microstructures in zirconium alloys. Comput. Mater. Sci. 190, 110279. https://doi.org/10.1016/j.commatsci.2021.110279

Peirce, D., Asaro, R.J., Needleman, a., 1983. Material rate dependence and localized deformation in crystalline solids. Acta Metall. 31, 1951–1976. https://doi.org/10.1016/0001-6160(83)90014-7

Perovic, V., Weatherly, G.C., Simpson, C.J., 1983. Hydride precipitation in α/β zirconium alloys. Acta Metall. 31, 1381–1391. https://doi.org/10.1016/0001-6160(83)90008-1

Pshenichnikov, A., Stuckert, J., Walter, M., 2016. Hydride precipitation, fracture and plasticity mechanisms in pure zirconium and Zircaloy-4 at temperatures typical for the postulated loss-of-coolant accident. Nucl. Eng. Des. 301, 366–377. https://doi.org/10.1016/J.NUCENGDES.2016.03.024

Puls, M.P., 2012. The Effect of Hydrogen and Hydrides on the Integrity of Zirconium Alloy Components. Springer. https://doi.org/10.1007/978-1-4471-4195-2

Puls, M.P., Shi, S.Q., Rabier, J., 2005. Experimental studies of mechanical properties of solid zirconium hydrides. J. Nucl. Mater. 336, 73–80. https://doi.org/10.1016/j.jnucmat.2004.08.016

Qin, W., Kiran Kumar, N.A.P., Szpunar, J.A., Kozinski, J., 2011. Intergranular δ-hydride nucleation and orientation in zirconium alloys. Acta Mater. 59, 7010–7021. https://doi.org/10.1016/j.actamat.2011.07.054

Qin, W., Szpunar, J.A., Kozinski, J., 2012. Hydride-induced degradation of hoop ductility in textured zirconium-alloy tubes: A theoretical analysis. Acta Mater. 60, 4845–4855. https://doi.org/10.1016/j.actamat.2012.06.003

Qin, W., Szpunar, J.A., Kumar, N.A.P.K., Kozinski, J., 2014. Microstructural criteria for abrupt ductile-to-brittle transition induced by d -hydrides in zirconium alloys. Acta Mater. 81, 219–229. https://doi.org/10.1016/j.actamat.2014.08.010

Raykar, N.R., Singh Raman, R.K., Maiti, S.K., Choudhary, L., 2012. Investigation of hydrogen assisted cracking of a high strength steel using circumferentially notched tensile test. Mater. Sci. Eng. A 547, 86–92. https://doi.org/10.1016/j.msea.2012.03.086

Raynaud, P.A., Koss, D.A., Motta, A.T., 2012. Crack growth in the through-thickness direction of hydrided thin-wall Zircaloy sheet. J. Nucl. Mater. 420, 69–82. https://doi.org/10.1016/J.JNUCMAT.2011.09.005

Reali, L., Balint, D.S., Sutton, A.P., Wenman, M.R., 2021. Plastic relaxation and solute segregation to β-Nb second phase particles in Zr-Nb alloys: A discrete dislocation plasticity study. J. Mech. Phys. Solids 156, 104581. https://doi.org/10.1016/J.JMPS.2021.104581

Rico, A., Martin-rengel, M.A., Ruiz-hervias, J., Rodriguez, J., Gomez-sanchez, F.J., 2014. Nanoindentation measurements of the mechanical properties of zirconium matrix and hydrides in unirradiated pre-hydrided nuclear fuel cladding. J. Nucl. Mater. 452, 69–76. https://doi.org/10.1016/j.jnucmat.2014.04.045

Root, J.H., Small, W.M., Khatamian, D., Woo, O.T., 2003. Kinetics of the δ to γ zirconium hydride transformation in Zr-2.5Nb. Acta Mater. 51, 2041–2053. https://doi.org/10.1016/S1359-6454(03)00004-1

Sagat, S., Shi, S.Q., Puls, M.P., 1994. Crack initiation criterion at notches in Zr-2.5Nb alloys. Mater. Sci. Eng. A 176, 237–247. https://doi.org/10.1016/0921-5093(94)90981-4

Salvadori, A., McMeeking, R., Grazioli, D., Magri, M., 2018. A coupled model of transport-reaction-mechanics with trapping. Part I – Small strain analysis. J. Mech. Phys. Solids 114, 1–30. https://doi.org/10.1016/j.jmps.2018.02.006

Scarth, D.A., Smith, T., 2002. The effect of plasticity on process-zone predictions of DHC initiation at a flaw in CANDU reactor Zr-Nb pressure tubes. 2002 ASME Press. Vessel. Pip. Conf.

Sedaghat, O., Abdolvand, H., 2021. A non-local crystal plasticity constitutive model for hexagonal close-packed polycrystals. Int. J. Plast. 136, 102883. https://doi.org/10.1016/j.ijplas.2020.102883

Shang, J., Zheng, J., Hua, Z., Li, Y., Gu, C., Cui, T., Meng, B., 2020. Effects of stress

concentration on the mechanical properties of X70 in high-pressure hydrogen-containing gas mixtures. Int. J. Hydrogen Energy 45, 28204–28215. https://doi.org/10.1016/j.ijhydene.2020.02.125

Shek, G.K., Cui, J., Perovic, V., Holt, R., Strasser, A., 2005. Overload fracture of flaw tip hydrides in Zr-2.5Nb pressure tubes. ASTM Spec. Tech. Publ. 2, 729–758. https://doi.org/10.1520/stp37533s

Shi, S.Q., Puls, M.P., 1994. Criteria for fracture initiation at hydrides in zirconium alloys I. Sharp crack tip. J. Nucl. Mater. 208, 232–242. https://doi.org/10.1016/0022-3115(94)90332-8

Shiman, O. V., Tulk, E., Daymond, M.R., 2018. Synchrotron X-ray diffraction study of zirconium hydride distribution in Zr-2.5%Nb and its redistribution during thermal cycling. Mater. Charact. 136, 183–195. https://doi.org/10.1016/j.matchar.2017.12.012

Shin, W., Chang, K., 2020. Phase-field modeling of hydride reorientation in zirconium cladding materials under applied stress. Comput. Mater. Sci. 182, 109775. https://doi.org/10.1016/J.COMMATSCI.2020.109775

Shinohara, Y., Abe, H., Iwai, T., Sekimura, N., Kido, T., Yamamoto, H., Taguchi, T., 2009. In situ TEM observation of growth process of zirconium hydride in Zircaloy-4 during hydrogen ion implantation. J. Nucl. Sci. Technol. 46, 564–571. https://doi.org/10.1080/18811248.2007.9711563

Silva, C.M., Ibrahim, F., Lindquist, E.G., McMurray, J.W., Bryan, C.D., 2019. Brittle nature and the related effects of zirconium hydrides in Zircaloy-4. Mater. Sci. Eng. A 767, 138396. https://doi.org/10.1016/J.MSEA.2019.138396

Simon, P.C.A., Frank, C., Chen, L.Q., Daymond, M.R., Tonks, M.R., Motta, A.T., 2021. Quantifying the effect of hydride microstructure on zirconium alloys embrittlement using image analysis. J. Nucl. Mater. 547, 152817. https://doi.org/10.1016/J.JNUCMAT.2021.152817

Simpson, C.J., Ells, C.E., 1974. Delayed hydrogen embrittlement in Zr-2.5 wt % Nb. J. Nucl. Mater. 52, 289–295. https://doi.org/10.1016/0022-3115(74)90174-3

Singh, A., Pal, S., 2020. Coupled chemo-mechanical modeling of fracture in polycrystalline cathode for lithium-ion battery. Int. J. Plast. 127, 102636. https://doi.org/10.1016/j.ijplas.2019.11.015

Singh, R.N., Kishore, R., Singh, S.S., Sinha, T.K., Kashyap, B.P., 2004. Stress-reorientation of hydrides and hydride embrittlement of Zr-2.5 wt% Nb pressure tube alloy. J. Nucl. Mater. 325, 26–33. https://doi.org/10.1016/j.jnucmat.2003.10.009

Singh, R.N., Lala Mikin, R., Dey, G.K., Sah, D.N., Batra, I.S., Ståhle, P., 2006. Influence of temperature on threshold stress for reorientation of hydrides and residual stress

variation across thickness of Zr-2.5Nb alloy pressure tube. J. Nucl. Mater. 359, 208–219. https://doi.org/10.1016/j.jnucmat.2006.09.004

Sofronis, P., McMeeking, R.M., 1989. Numerical analysis of hydrogen transport near a blunting crack tip. J. Mech. Phys. Solids 37, 317–350. https://doi.org/10.1016/0022-5096(89)90002-1

Strakosova, A., Roudnická, M., Ekrt, O., Vojtěch, D., Michalcová, A., 2021. Hydrogen Embrittlement of the Additively Manufactured High-Strength X3NiCoMoTi 18-9-5 Maraging Steel. Materials (Basel). 14, 5073. https://doi.org/10.3390/ma14175073

Suman, S., Khan, M.K., Pathak, M., Singh, R.N., 2017. Effects of Hydride on Crack Propagation in Zircaloy-4. Procedia Eng. 173, 1185–1190. https://doi.org/10.1016/j.proeng.2016.12.105

Sung, Z.H., Wang, M., Polyanskii, A.A., Santosh, C., Balachandran, S., Compton, C., Larbalestier, D.C., Bieler, T.R., Lee, P.J., 2017. Development of low angle grain boundaries in lightly deformed superconducting niobium and their influence on hydride distribution and flux perturbation. J. Appl. Phys. 121, 0–11. https://doi.org/10.1063/1.4983512

Swan, H., Styman, P., Wilcox, H., Bowden, N., Ungar, T., Connor, L., Garner, A., Cole-Baker, A., Binks, P., Smith, C., Sikotra, S., Hawes, J., Ortner, S., 2022. Measurement of hydrogen trapping in cold-work dislocations using synchrotron X-ray diffraction. J. Nucl. Mater. 571, 154012. https://doi.org/10.1016/J.JNUCMAT.2022.154012

Taha, A., Sofronis, P., 2001. A micromechanics approach to the study of hydrogen transport and embrittlement. Eng. Fract. Mech. 68, 803–837. https://doi.org/10.1016/S0013-7944(00)00126-0

Tang, J., Qiu, R., Chen, J., Liu, P., Ao, B., 2021. Hydrogen diffusion in plutonium hydrides from first principles. J. Nucl. Mater. 557, 153247. https://doi.org/10.1016/j.jnucmat.2021.153247

Toghraee, A., Bair, J., Asle Zaeem, M., 2021. Effects of applied load on formation and reorientation of zirconium hydrides: A multiphase field modeling study. Comput. Mater. Sci. 192, 110367. https://doi.org/10.1016/J.COMMATSCI.2021.110367

Tondro, A., Abdolvand, H., 2022. On the effects of texture and microstructure on hydrogen transport towards notch tips: A CPFE study. Int. J. Plast. 103234. https://doi.org/10.1016/J.IJPLAS.2022.103234

Tondro, A., Abdolvand, H., 2021. Quantifying hydrogen concentration in the vicinity of zirconium hydrides and deformation twins. J. Mech. Phys. Solids 148, 104287. https://doi.org/10.1016/j.jmps.2020.104287

Tondro, A., Bidyk, B., Ho, I., Abdolvand, H., 2022. Modelling the interactions of zirconium hydrides. Mater. Today Commun. 103933.

https://doi.org/10.1016/J.MTCOMM.2022.103933

Tondro, A., Taherijam, M., Abdolvand, H., 2023. Diffusion and redistribution of hydrogen atoms in the vicinity of localized deformation zones. Mech. Mater. 177, 104544. https://doi.org/10.1016/J.MECHMAT.2022.104544

Toribio, J., González, B., Matos, J.C., 2020. Hydrogen embrittlement and notch tensile strength of pearlitic steel: a numerical approach. Procedia Struct. Integr. 28, 2444–2449. https://doi.org/10.1016/J.PROSTR.2020.11.095

Tummala, H., Capolungo, L., Tomé, C.N., 2018. Quantifying the stress state in the vicinity of a δ-hydride in α-zirconium. J. Nucl. Mater. 511, 406–416. https://doi.org/10.1016/j.jnucmat.2018.08.050

Tunes, M.A., Silva, C.M., Edmondson, P.D., 2019. Site specific dependencies of hydrogen concentrations in zirconium hydrides. Scr. Mater. 158, 136–140. https://doi.org/10.1016/J.SCRIPTAMAT.2018.08.044

Tung, H.M., Chen, T.C., Tseng, C.C., 2016. Effects of hydrogen contents on the mechanical properties of Zircaloy-4 sheets. Mater. Sci. Eng. A 659, 172–178. https://doi.org/10.1016/J.MSEA.2016.02.051

Turnbull, A., 1993. Modelling of environment assisted cracking. Corros. Sci. 34, 921–960.

Ulmer, D.G., Altstetter, C.J., 1991. Hydrogen-induced strain localization and failure of austenitic stainless steels at high hydrogen concentrations. Acta Metall. Mater. 39, 1237–1248. https://doi.org/10.1016/0956-7151(91)90211-I

Une, K., Nogita, K., Ishimoto, S., Ogata, K., 2004. Crystallography of zirconium hydrides in recrystallized zircaloy-2 fuel cladding by electron backscatter diffraction. J. Nucl. Sci. Technol. 41, 731–740. https://doi.org/10.1080/18811248.2004.9715540

Vicente Alvarez, M.A., Santisteban, J.R., Domizzi, G., Almer, J., 2011. Phase and texture analysis of a hydride blister in a Zr-2.5%Nb tube by synchrotron X-ray diffraction. Acta Mater. 59, 2210–2220. https://doi.org/10.1016/j.actamat.2010.12.024

Vicente Alvarez, M.A., Santisteban, J.R., Vizcaino, P., Flores, A. V., Banchik, A.D., Almer, J., 2012. Hydride reorientation in Zr2.5Nb studied by synchrotron X-ray diffraction. Acta Mater. 60, 6892–6906. https://doi.org/10.1016/j.actamat.2012.07.029

Vizcaíno, P., Santisteban, J.R., Vicente Alvarez, M.A., Banchik, A.D., Almer, J., 2014. Effect of crystallite orientation and external stress on hydride precipitation and dissolution in Zr2.5%Nb. J. Nucl. Mater. 447, 82–93. https://doi.org/10.1016/j.jnucmat.2013.12.025

Von Pezold, J., Lymperakis, L., Neugebeauer, J., 2011. Hydrogen-enhanced local plasticity at dilute bulk H concentrations: The role of H-H interactions and the formation of

local hydrides. Acta Mater. 59, 2969–2980. https://doi.org/10.1016/j.actamat.2011.01.037

Wang, M., Akiyama, E., Tsuzaki, K., 2007. Effect of hydrogen on the fracture behavior of high strength steel during slow strain rate test. Corros. Sci. 49, 4081–4097. https://doi.org/10.1016/j.corsci.2007.03.038

Wang, M., Akiyama, E., Tsuzaki, K., 2006. Determination of the critical hydrogen concentration for delayed fracture of high strength steel by constant load test and numerical calculation. Corros. Sci. 48, 2189–2202. https://doi.org/10.1016/j.corsci.2005.07.010

Wang, Q., Cochrane, C., Skippon, T., Wang, Z., Abdolvand, H., Daymond, M.R., 2020. Orientation-dependent irradiation hardening in pure Zr studied by nanoindentation, electron microscopies, and crystal plasticity finite element modeling. Int. J. Plast. 124, 133–154. https://doi.org/10.1016/J.IJPLAS.2019.08.007

Wang, S., Giuliani, F., Britton, T. Ben, 2019. Microstructure and formation mechanisms of δ-hydrides in variable grain size Zircaloy-4 studied by electron backscatter diffraction. Acta Mater. 169, 76–87. https://doi.org/10.1016/j.actamat.2019.02.042

Wang, T., Zhang, H., Liang, W., 2021. Hydrogen embrittlement fracture mechanism of 430 ferritic stainless steel: The significant role of carbides and dislocations. Mater. Sci. Eng. A 142043. https://doi.org/10.1016/J.MSEA.2021.142043

Wang, Y., Li, X., Dou, D., Shen, L., Gong, J., 2016. FE analysis of hydrogen diffusion around a crack tip in an austenitic stainless steel. Int. J. Hydrogen Energy 41, 6053–6063. https://doi.org/10.1016/j.ijhydene.2016.03.003

Weatherly, G.C., 1980. the precipitation of γ-hydride plates in zirconium. Acta Metall. 29, 501–512.

Weck, P.F., Kim, E., Tikare, V., Mitchell, J.A., 2015. Mechanical properties of zirconium alloys and zirconium hydrides predicted from density functional perturbation theory 1–3. https://doi.org/10.1039/x0xx00000x

Weekes, H.E., Jones, N.G., Lindley, T.C., Dye, D., 2016. Hydride reorientation in Zircaloy-4 examined by in situ synchrotron X-ray diffraction. J. Nucl. Mater. 478, 32–41. https://doi.org/10.1016/J.JNUCMAT.2016.05.029

Weekes, H.E., Vorontsov, V.A., Dolbnya, I.P., Plummer, J.D., Giuliani, F., Britton, T.B., Dye, D., 2015. In situ micropillar deformation of hydrides in Zircaloy-4. Acta Mater. 92, 81–96. https://doi.org/10.1016/j.actamat.2015.03.037

Welland, M.J., Hanlon, S.M., 2020. Prediction of the zirconium hydride precipitation barrier with an anisotropic 3D phase-field model incorporating bulk thermodynamics and elasticity. Comput. Mater. Sci. 171, 109266. https://doi.org/10.1016/j.commatsci.2019.109266

Westlake, D.G., 1968. The habit planes of zirconium hydride in zirconium and zircaloy. J. Nucl. Mater. 26, 208–216.

Wimmer, E., Christensen, M., Wolf, W., Howland, W.H., Kammenzind, B., Smith, R.W., 2020. Hydrogen in zirconium: Atomistic simulations of diffusion and interaction with defects using a new embedded atom method potential. J. Nucl. Mater. 532, 152055. https://doi.org/10.1016/J.JNUCMAT.2020.152055

Wook, T., Colas, K.B., Motta, A.T., Chen, L., 2019. A phase-field model for hydride formation in polycrystalline metals : Application to δ -hydride in zirconium alloys. Acta Mater. 181, 262–277. https://doi.org/10.1016/j.actamat.2019.09.047

Wu, Q., Zikry, M.A., 2015. Prediction of diffusion assisted hydrogen embrittlement failure in high strength martensitic steels. J. Mech. Phys. Solids 85, 143–159. https://doi.org/10.1016/j.jmps.2015.08.010

Xiao, Z., Hao, M., Guo, X., Tang, G., Shi, S.Q., 2015. A quantitative phase field model for hydride precipitation in zirconium alloys: Part II. Modeling of temperature dependent hydride precipitation. J. Nucl. Mater. 459, 330–338. https://doi.org/10.1016/j.jnucmat.2014.12.110

Xie, F., Li, H., Zhang, W., Ma, Q., 2020. A coupled model of stress, creep, and diffusion in the film/substrate system. J. Appl. Phys. 128, 145106. https://doi.org/10.1063/5.0018968

Yamanaka, S., Yoshioka, K., Uno, M., Katsura, M., Anada, H., Matsuda, T., Kobayashi, S., 1999. Thermal and mechanical properties of zirconium hydride 295, 23–29.

Yang, F., Zhan, W., Yan, T., Zhang, H., Fang, X., 2020. Numerical Analysis of the Coupling between Hydrogen Diffusion and Mechanical Behavior near the Crack Tip of Titanium. Math. Probl. Eng. 2020, 1–15. https://doi.org/10.1155/2020/3618589

Ye, F., Zhu, T., Mori, K., Xu, Q., Song, Y., Wang, Q., Yu, R., Wang, B., Cao, X., 2021. Effects of dislocations and hydrogen concentration on hydrogen embrittlement of austenitic 316 stainless steels. J. Alloys Compd. 876, 160134. https://doi.org/10.1016/j.jallcom.2021.160134

Yokobori, A.T., Nemoto, T., Satoh, K., Yamada, T., 1996. Numerical analysis on hydrogen diffusion and concentration in solid with emission around the crack tip. Eng. Fract. Mech. 55, 47–60. https://doi.org/10.1016/0013-7944(96)00002-1

Yu, H., Cocks, A., Tarleton, E., 2019. Discrete dislocation plasticity HELPs understand hydrogen effects in bcc materials. J. Mech. Phys. Solids 123, 41–60. https://doi.org/10.1016/j.jmps.2018.08.020

Yu, H., Cocks, A.C.F., Tarleton, E., 2020. Simulating hydrogen in fcc materials with discrete dislocation plasticity. Int. J. Hydrogen Energy 45, 14565–14577. https://doi.org/10.1016/j.ijhydene.2020.01.118

Yu, P., Cui, Y., Zhu, G. zhen, Shen, Y., Wen, M., 2020. The key role played by dislocation core radius and energy in hydrogen interaction with dislocations. Acta Mater. 185, 518–527. https://doi.org/10.1016/j.actamat.2019.12.033

Zhang, J., Su, J., Zhang, B., Zong, Y., Yang, Z., Zhang, C., Chen, H., 2021. Phase-Field Modeling of Hydrogen Diffusion and Trapping in Steels. Acta Metall. Sin. (English Lett. https://doi.org/10.1007/s40195-021-01241-1

Zhang, Y., Jiang, C., Bai, X., 2017. Anisotropic hydrogen diffusion in α-Zr and Zircaloy predicted by accelerated kinetic Monte Carlo simulations. Sci. Rep. 7, 1–13. https://doi.org/10.1038/srep41033

Zheng, J., Zhou, X., Mao, L., Zhang, H., Liang, J., Sheng, L., Peng, S., 2015. First-principles study of the relative stability of various zirconium hydrides using the special quasirandom structures approach. Int. J. Hydrogen Energy 40, 4597–4604. https://doi.org/10.1016/J.IJHYDENE.2015.02.045

<h1 style="text-align: center;">Curriculum Vitae</h1>

| | |
|---|---|
| **Name:** | Alireza Tondro |

| | |
|---|---|
| **Post-secondary Education and Degrees:** | Amirkabir University of Technology (Tehran Polytechnic) Tehran, Iran 2015-2019 B.Sc. in Mechanical Engineering – Manufacturing |
| | The University of Western Ontario London, Ontario, Canada 2019-2023 Ph.D. in Mechanical and Material Engineering |

**Honours and Awards:**

Dean's Honor List, School of Mechanics, Tehran Polytechnic, Tehran, Iran
2016-2019

| | |
|---|---|
| **Related Work Experience** | Research and Teaching Assistant The University of Western Ontario 2019-2023 |

**Publications:**

A. Tondro, H. Abdolvand, Quantifying hydrogen concentration in the vicinity of zirconium hydrides and deformation twins, Journal of the Mechanics and Physics of Solids, Volume 148, March 2021, 104287, https://doi.org/10.1016/j.jmps.2020.104287

A. Tondro, H. Abdolvand, On the effects of texture and microstructure on hydrogen transport towards notch tips: A CPFE study, International Journal of Plasticity, Volume 152, May 2022, 103234, https://doi.org/10.1016/j.ijplas.2022.103234

A. Tondro, B. Bidyk, I. Ho, H. Abdolvand, Modelling the interaction of zirconium hydrides, Materials Today Communications, Volume 32, August 2022, 103933, https://doi.org/10.1016/j.mtcomm.2022.103933

A. Tondro, M. Taherijam, H. Abdolvand, Diffusion and redistribution of hydrogen atoms in the vicinity of localized deformation zones, Mechanics of Materials, Volume 177, February 2023, 104544, https://doi.org/10.1016/j.mechmat.2022.104544

S. Marashi, K. Louca, A. Tondro, E. Tulk, H. Abdolvand, Journal of Nuclear Materials, Volume 577, April 2023, 154321, https://doi.org/10.1016/j.jnucmat.2023.154321